Chair of Functional Materials and Materials Systems

Doctoral Thesis

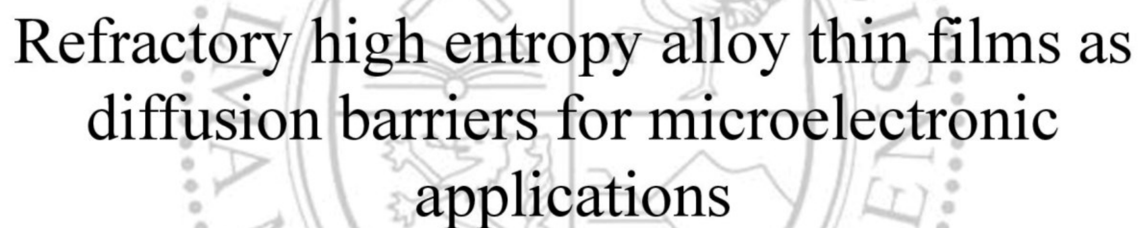

Refractory high entropy alloy thin films as diffusion barriers for microelectronic applications

Dipl.-Ing. Georg Christoph Gruber, BSc

April 2023

MONTANUNIVERSITÄT LEOBEN

www.unileoben.ac.at

AFFIDAVIT

I declare on oath that I wrote this thesis independently, did not use other than the specified sources and aids, and did not otherwise use any unauthorized aids.

I declare that I have read, understood, and complied with the guidelines of the senate of the Montanuniversität Leoben for "Good Scientific Practice".

Furthermore, I declare that the electronic and printed version of the submitted thesis are identical, both, formally and with regard to content.

Date 18.04.2023

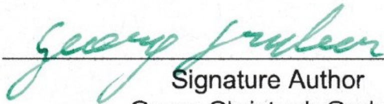

Signature Author
Georg Christoph Gruber

ACKNOWLEDGMENTS

The funding from the Austrian Research Promotion Agency (FFG) (project number: 871687, PowerHEA) is gratefully acknowledged.

I am very grateful to Univ.-Prof. DI Dr. Christian Mitterer, Head of the Chair of Functional Materials and Materials Systems, for giving me the opportunity to execute this work at his Chair and for all the support I got from him.

Further I would like to thank Dr. Robert Franz for always supporting me during my work and for the many good discussions. Many good ideas included in this work would not have been possible without these discussions. I also want to thank Priv.Doz Dr. Megan J. Cordill for co-supervising as a mentor of this thesis and all the help I got from her during this thesis, especially when measurements at the Erich Schmid Institute needed to be arranged. I also want to thank her and all the attendees of the regular project meetings for the fruitful discussions during those meetings. I'm grateful to Dr. Alice Lassnig, Dr. Stanislav Zak, Dr. Stefan Wurster and Dr. Christoph Gammer for being a part of this project and all the measurements, they have done for this work.

I want to thank Sabrina Hirn and Magdalena Kirchmair for the help with the film deposition and measurements and Sabrina Hirn for the introduction to Esmeralda, the used deposition system in this thesis. Additional I want to thank all my colleagues at the Chair of Functional Materials and Materials System, for helping me out with every kind of problem and providing a pleasant working atmosphere.

Many thanks also to all friends outside of the institute, I gained during my studies in Leoben for making this such a wonderful time. Especially I want to thank, Cornelius Amann, Nikolas Natter, Johannes Schloffer, Clemens Lughofer, Fabian Wiebogen, Anton Seidl und Maximilian Mader.

I also want to thank my family for all the support I got during my whole life. Additionally, I'm grateful to my parent for always believing in me, even though some teacher didn't.

Last but not least I want to thank my fiancé Romana Bojar, for always being there for me and all the encouraging words after all setbacks during my thesis. Thanks for being the person I love to spend my time with.

CONTENT

1 Introduction 1

2 Thin Film Synthesis 3

2.1 Magnetron Sputtering 3

2.2 High Power Impulse Magnetron Sputtering 5

3 Thin Film Growth and Stress 18

3.1 Thin Film Growth 18

3.2 Residual Stress 21

4 High Entropy Alloy Films 26

4.1 Survey on High Entropy Alloys 26

4.2 Refractory High Entropy Alloys 31

5 Diffusion Barriers for Microelectronic Systems 33

5.1 General Purpose of Diffusion Barriers 33

5.2 Overview For Used Material Systems 35

5.3 High Entropy Alloys for Diffusion Barriers 37

6 Summary and Conclusion 41

7 References 43

8 Publications 61

8.1 List of Included Publications 61

Publication I 63

Publication II 89

Publication III 121

Publication IV 141

Publication V 167

1 INTRODUCTION

In the early 2000s high entropy alloys (HEAs) where introduced by Yeh [1] and Cantor [2] and since then the scientific interest for HEAs has been increasing each year. HEAs are alloys which consist of at least five elements and have a configurational entropy of at least $1.5R$ [3], where R is the gas constant. These high entropy values lead to the formation of simple, face centered cubic (fcc), body centered cubic (bcc) or hexagonal solid solution phases, instead of the formation of intermetallic phases [3]. Refractory HEAs (RHEAs) are HEAs which consist mainly of refractory elements and are promising candidates for future high temperature applications, due to their good thermal stability. Many studied RHEAs are based on MoNbTaW alloyed with several other elements, such as MoNbTaVW introduced by Senkov et al. [4,5], which is the most prominent representative. This RHEA is known for its good thermal stability and high strength at elevated temperatures, which exceeds the performance of Ni-based superalloys in vacuum [5]. The substitution of V with other elements affects different material properties. Ti [6,7] for instance leads to a higher ductility without deteriorating strength and thermal stability, whereas Zr [8–10] leads to both, an increased ductility and strength.

Magnetron sputter deposition is a common method to synthesize HEA thin films and has been used since the early beginnings of HEA research [11–14]. By changing the deposition parameters, the structure and properties of the HEA films can be varied, where the addition of N_2 or O_2 allows the deposition of HEA nitride [3,11,15] and oxide [3] films. The chemical composition of HEAs can be easily varied by using a multi-sputter-source arrangement. Using this method, new HEAs for thin film applications can be developed. Since bulk HEAs are often more complicated to synthesize, thin films can also serve as a first step for the development of new bulk HEAs. HEA thin films are also potential candidates for future diffusion barriers for microelectronics, as it has been reported that the diffusion barrier performance of an alloy increases with increasing number of elements within the alloy [16]. Diffusion barriers are necessary because Cu, which is a common conductor and heat sink material within microelectronic systems, tends to diffuse into Si-based insulator and semiconductor materials, causing interfacial failure due to the formation of copper silicides, resulting in a failure of the electronic device [17]. For HEA diffusion barriers most of the research

is performed on AlCrRuTaTiZr and (AlCrRuTaTiZr)N based alloys [16,18–25]. Those alloys can prevent failure up to 800 °C [20] in case of the metal film and 900 °C [21] in case of the nitride film. As MoNbTaW-based films are known for their good thermal stability, they are also potential candidates for diffusion barriers [26]. The use of MoNbTaW as a diffusion barrier prevents barrier failure up to 650 °C [27,28]. In the case of MoNbTaVW only a film thickness of 1.5 nm was necessary, to prevent barrier failure up to 600 °C [29]. MoNbTaVW was not only found to be an efficient diffusion barrier between Cu and Si, but also between Mo and $MoSi_2$ [30].

Within this thesis, the diffusion barrier properties of MoNbTaW and (MoNbTaW)N based HEAs, alloyed with a fifth element, in particular Ti, V, Cr, Mn, Zr or Hf, have been investigated. All films were deposited using high power impulse magnetron sputtering (HiPIMS). As a first step, the microstructure and mechanical properties of the as-deposited single-layer MoNbTaW based films were investigated. In the case of MoNbTaWZr, a systematic deposition parameter study was performed to enable the synthesis of amorphous films, as these are expect to show a better diffusion barrier performance due to the lack of grain boundaries, which can act as fast diffusion channels [17]. The thermal stability of MoNbTaTiW, MoNbTaVW and CrMoNbTaW films was studied by annealing the films in a vacuum furnace up to 1200 °C. After each annealing step the microstructure and film stresses were investigated. After the HEA films were studied in sufficient detail, they were evaluated for their suitability as diffusion barriers. To test their suitability, 20 nm thick HEA or HEA nitride films were deposited on Si and a Cu layer was grown on top. This was done for all studied HEAs. Those bi-layers were then annealed in vacuum and subsequently examined for eventual barrier failure by X-ray diffraction (XRD), electrical resistance measurements and the evaluation of their surface topography. This thesis is a first step towards the use of MoNbTaW based diffusion barriers, where in addition new general insights on MoNbTaW based films are given.

2 THIN FILM SYNTHESIS

In thin film deposition, a distinction is made between two basic processes, physical vapor deposition (PVD) and chemical vapor deposition (CVD) [31]. In CVD, a volatile compound of the material to be deposited chemically reacts with other gases and is finally deposited on a substrate. For CVD often elevated temperatures are necessary [31]. In PVD, a distinction is made between evaporation and sputtering, where both methods can be traced back to the nineteenth century [31–33]. While for evaporation a liquid or solid material used as the source is thermally transferred to the vapor phase, in sputtering the atoms are knocked out of the target (source) due to impact of gaseous ions [31].

2.1 MAGNETRON SPUTTERING

Sputtering occurs when gas ions within a plasma are accelerated towards the target surface and knock out target atoms. In addition to these atoms, also secondary electrons escape from the target surface; those electrons are needed for the ionization of new gas atoms [31,34,35]. The ionization of the gas atoms is mostly done by impact ionization. During ionization an electron with sufficient kinetic energy knocks out an electron of the shell of an atom [35]. This process is needed to maintain the discharge, as the ions are neutralized when they hit the target surface. The newly produced ions are then again accelerated towards the target surface by an electrical field between the cathode (target) and the anode, which can be a ring around the target and the chamber wall and sometimes, if no bias voltage is used, also the substrate (Figure 1) [31,34,35]. A bias voltage is a negative voltage, often in the range of a few ten volts, used to attract ions towards the substrate to enhance film growth [36].

For magnetron sputtering, an additional magnetic field is applied using a permanent magnet [37], an electric magnet [38,39] or a combination of both [40]. A typical setup for magnetron sputtering is shown in Figure 1. In addition to the electric field force, the electrons experience the Lorentz force due to the presence of the magnetic field. The Lorentz force reaches a maximum where the magnetic field is perpendicular to the electric field. Within this region, the electrons are trapped, which leads to enhanced collisions and ionization of gas atoms; this region is marked purple in Figure 1 [31]. If a planar round-disk shaped target is used, a torus shaped ionization region is formed. As the ionization region is not homogeneously distributed throughout the whole target

surface, the target removal is also not homogeneous and a sputter erosion grove is formed [31,34,35]. The inhomogeneous target removal leads to one of the most significant disadvantages, in comparison to sputtering without a magnetic field, as only 26-45 % of the target material can be used [35,37]. This can be significantly improved by rotatable cylindrical targets, instead of planar ones, where up to 90 % of the target can be used [35,38,41]. Nevertheless, the advantages of magnetron sputtering, such as a significantly higher sputter rate, by about one magnitude, the ability to deposit films at lower gas pressures, and the reduced thermal load to the reduced bombardment of the substrate by electrons increase the applicability of this process so much that magnetron sputtering is the most widely used sputtering process and also one of the most important processes for depositing thin films [31].

The magnets can be arranged that the opposite poles of the inner and outer magnets fully close the magnetic field lines, and therefore the magnetic trap is only confined in front of the target. This arrangement is called balanced configuration [35]. Consequently, the substrate is hardly bombarded by ions, which is useful for coating of heat sensitive substrate materials [35]. As impinging ions often have a positive effect on the film growth, unbalanced magnetron sources, as developed by Window and Savvides [38,41], can be used to increase the ion flux towards the substrate. Two types can be distinguished. Type I, where the magnetic strength of the inner magnet is higher than that of the outer one. This leads to the effect that not all magnetic field lines are closed in front of the target. Therefore, the opposite pole of the inner magnet serves to close the field lines, which leads to an expansion of the magnetic field and thus the plasma towards the vacuum chamber wall [35]. In case of the Type II configuration, the magnetic strength of the outer magnet is increased compared to the inner one, leading to an expansion of the plasma towards the substrate and therefore to an increased ion flux towards the substrate [35]. This ion flux can be additionally controlled by an applied bias voltage [35].

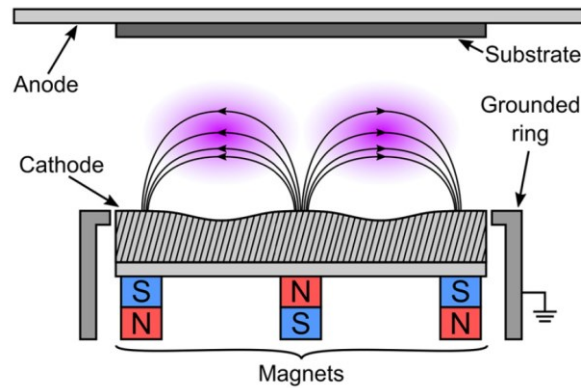

Figure 1: Typical setup for magnetron sputtering [35].

2.2 High Power Impulse Magnetron Sputtering

The ionization rate for magnetron sputtered atoms is quite low, only in the range of a few percent. As a high metal ion flux enhances the film quality, several methods to increase the metal ion flux have been developed [35,42,43]. In particular, for HiPIMS very low duty cycles (pulse on time divided by the pulse duration) are used, often in the range from 0.5-5 % (Figure 2). In comparison, for commonly used pulsed direct current magnetron sputtering, duty cycles in the range of 50-90 % are used [35]. The low duty cycles characteristic for HiPIMS lead to very high peak powers, but the time averaged power is still below the power limit of the source and the target, to prevent damage (Figure 2) [35]. As defined by Anders, only if the peak power exceeds the time averaged power by two orders of magnitude, a pulsed discharge can be considered a HiPIMS discharge [44]. The increased peak power leads to an increased electron density, which significantly decreases the electron impact ionization mean free path for a sputtered metal atom, which enhances the probability of a sputtered metal atom getting ionized [45–47].

2.2.1 The Generalized Recycling Model

The temporal current contributions of a HiPIMS discharge applied to a Ti target is shown in Figure 3a. While in this case the largest contribution to the overall current comes still from the Ar^+ ions, also the Ti^+ and Ti^{2+} ions provide a significant contribution to the total current. It is also possible that the current from the Ar^+ ions is significant lower compared to the current from the metal ions, as shown in Figure 3b. It can be seen that the contribution from the secondary electrons, which are essential for direct current magnetron sputtering (dcMS), is only minor with respect to the overall current and is therefore neglected in the generalized recycling

model (Figure 4). Thus, it can be assumed that the ion current $I_i(t)$ is equivalent to the discharge current $I_D(t)$ [48,49].

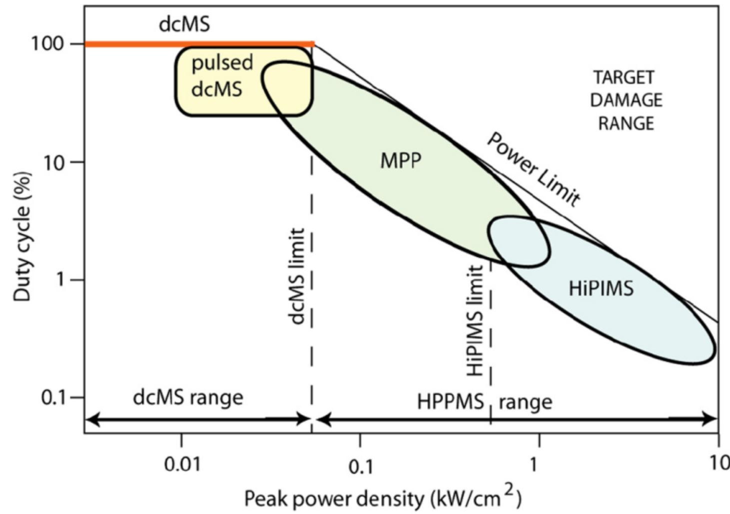

Figure 2: Peak power density of different sputtering methods, demonstrating the relation between peak power density, duty cycle and target damage. MPP stands for modulated pulse power magnetron sputtering. and HPPMS stands of high power pulsed magnetron sputtering [50].

The current I_{prim}, which is schematically visualized in Figure 4, is the current of those Ar ions which are ionized for the first time and act as a seed for the whole discharge [48]. The upper limit of I_{prim} is reached when the whole working gas (index g) reservoir is ionized and drawn towards the target; it is called I_{crit}. I_{crit} can be calculated by the equation defined by Huo et al. [51]

$$I_{crit} = e p_g S_{RT} \sqrt{\frac{1}{2\pi M_g k_B T_g}}, \quad (1)$$

where e is the elementary charge, p_g is the working gas pressure, S_{RT} is the race track area, M_g is the mass of the working gas atom, k_B is the Boltzmann's constant and T_g the gas temperature. When using a typical working gas, Ar, a typical working gas temperature of 300 K and assuming that $S_{RT} = 0.5 S_T$, where S_T is the target area, the equation can be stated as

$$J_{crit} = \frac{0.19 p_g S_T}{S_T} = 0.19 p_g, \quad (2)$$

where J_{crit} is the critical target current density stated in A/cm^2 [48]. In the case of the two discharges shown in Figure 3, this will lead to $J_{crit} = 0.1\ A/cm^2$ for the discharge with a Ti target and $J_{crit} = 0.3\ A/cm^2$ for the discharge with an Al target. The discharge current density J_D for these discharges is significantly higher compared to

J_{crit}, which suggests that the discharge cannot only be maintained by the incoming working gas. Therefore, ion recycling is needed for HiPIMS discharges, which is not the case for dcMS, as these discharges have J_D below J_{crit} [48].

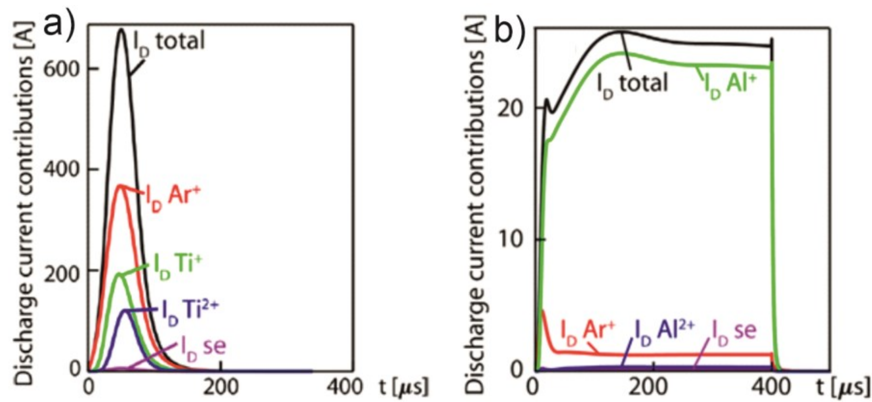

Figure 3:a) A discharge operated with 0.54 Pa Ar gas and a Ti target with a diameter of 150 mm ($J_{D,peak} \approx 3.84\ A/cm^2$) and b) a discharge operated with 1.8 Pa Ar gas, an Al target with a diameter of 50 mm ($J_{D,peak} \approx 1.32\ A/cm^2$) and a target voltage of 800 V. The temporal evolution of the total current is split up in the temporal distribution of the different currents, contributing to the total current [52].

To maintain a HiPIMS discharge, process gas recycling and self-sputter recycling can occur, as visualized in Figure 4. When the working gas ions hit the target surface, they recombine immediately [48]. A fraction ξ_{pulse} of these working gas atoms is then returning into the chamber. According to Huo et al. [51], due to bombardment of the target with ions, all embedded working gas atoms are most likely to leave the target, leading to $\xi_{\text{pulse}} = 1$. After escaping the target surface, the working gas is then again ionized with a probability of α_{g} and returns to the target with a probability of β_{g}. The remaining fraction of the working gas ions, i.e. $1 - \beta_{\text{g}}$, will not be contributing to the discharge again and leave together with the not ionized working gas atoms into the surrounding volume [48]. The recycling working gas current $I_{gas-recycle}$ combines with I_{prim} to the sum working gas current I_g towards the target [48]. Each working gas ion sputters target atoms with a sputter yield Y_{g}, which then leave the target. A part of these target atoms then also gets ionized with a probability of α_{t} [48]. A fraction of these ions is then attracted back to the target with a probability of β_{t}, or they leave towards the surrounding volume and substrate with a probability $1 - \beta_{\text{t}}$ together with the not ionized target atoms. The target ions which are drawn back towards the substrate are leading to self-sputtering with the self-sputter yield Y_{SS} [48]. The sputtered target atoms can then again be ionized and attracted back to the target or leave the discharge towards the surrounding volume and substrate. The whole process can be summarized

and visualized as a food chain: the current I_{prim} acts as a seed for the working gas recycling, which enhances the process and leads to the overall working gas current I_g. The enhanced I_g acts as the seed for the self-sputter process and the overall discharge current I_D is additionally enhanced by the recycling of the target atoms [48]. If $\pi_{SS} = \alpha_t\beta_t Y_{SS} > 1$ the discharge goes into runaway. This means that the current increases until the end of the pulse, as the whole process enhances itself [48]. Three types of discharges can be distinguished: First a self-sputter recycle dominated discharge, second a working gas recycle dominated discharge and third a mixed recycling discharge. The self-sputter yield Y_{SS} plays a key role to determine which type of ion recycling at high discharge currents occurs [48,49].

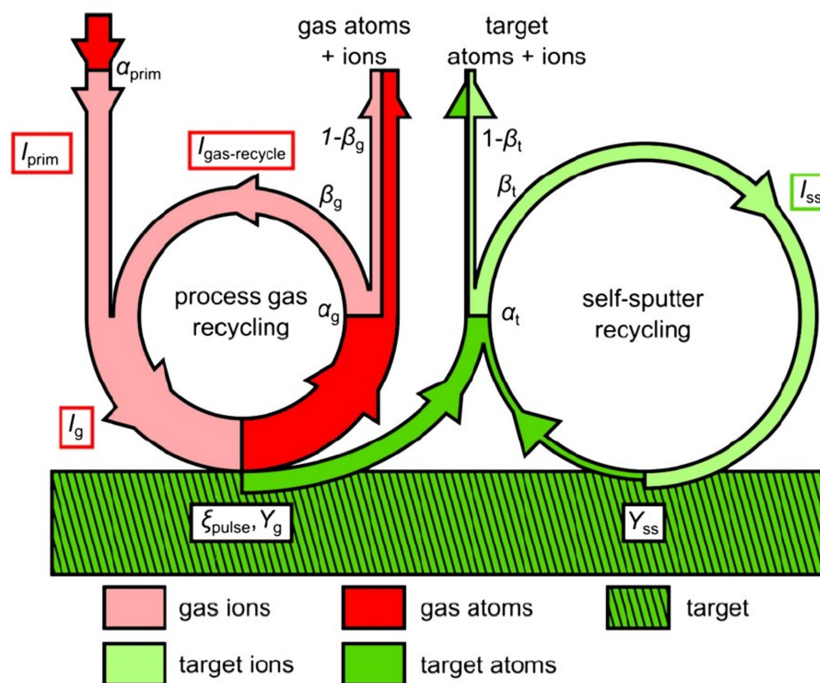

Figure 4: Schematic of the generalized recycling model. To scale with a parameter combination $\alpha_{prim} = 1$, $\xi_{pulse} = 1$, $\alpha_g = 0.7$, $\beta_g = 0.7$, $Y_g = 0.4$, $\alpha_t = 0.8$, $\beta_t = 0.7$ and $Y_{SS} = 0.5$, the width of the flow arrows is scaled according to the parameters [49].

2.2.2 The Different Types of HiPIMS Pulses

Figure 5 shows the temporal evolution of HiPIMS pulses for different contributions of process gas recycling and self-sputter recycling. The bottom two curves of HiPIMS pulses in Figure 5 represent a discharge where hardly any or even no ion recycling occurs. This mode is called working gas sputtering [53]. During this process, the working gas atoms are ionized and then sputter the target atoms and it is assumed that no ion recycling occurs. The discharge current $I_D(t)$ is dominated by the working

gas ion current. The low current in Phase 4 can be attributed to working gas rarefaction [48,50,53], which will be explained in more detail in a later stage of this work. The middle curve in Figure 5 represents a HiPIMS discharge with moderate ion recycling. This curve is characterized by working gas sustained self-sputtering [51]. There, the ionized working gas hitting the target sputters atoms out of the target. These atoms are then ionized and some of them are again attracted back to the target and sputtering atoms out of the target on their own, leading to a series of target ion recycling, which dominates the discharge. Besides the dominating target ion current I_{SS} the working gas ion current I_g also has an important contribution to the overall current $I_D(t)$ [48,51]. A HiPIMS discharge with significant ion recycling leads to a discharge current profile as exemplified by the upper two curves in Figure 5. Such a behavior can be obtained by self-sustained self-sputtering, working gas recycling or self-sputter runaway [48,50]. For the working gas recycling process, a significant fraction of the working gas, which is neutralized at the target surface, ionizes again, and part of these ions are then attracted back towards the target, starting a series of gas-recycling. A large fraction of the discharge current comes from the working gas [49]. In the case of the self-sustained self-sputtering, a large fraction of the target ions are attracted back towards the target, leading to target ion recycling. After the ignition of the discharge, the target ion recycling is sufficient to maintain the discharge and the discharge can run without working gas [48,54]. During this process the current is dominated by the recycling of the sputtered target atoms. Also in the case of the self-sputter runaway, the current is dominated by recycling of sputtered target atoms. During this process the self-sputtering is amplified by itself leading to a positive feedback, this results in an acceleration of the self-sputtering. Due to this runaway, the current increases until the end of the pulse or until the power reaches the limit of the power supply [55].

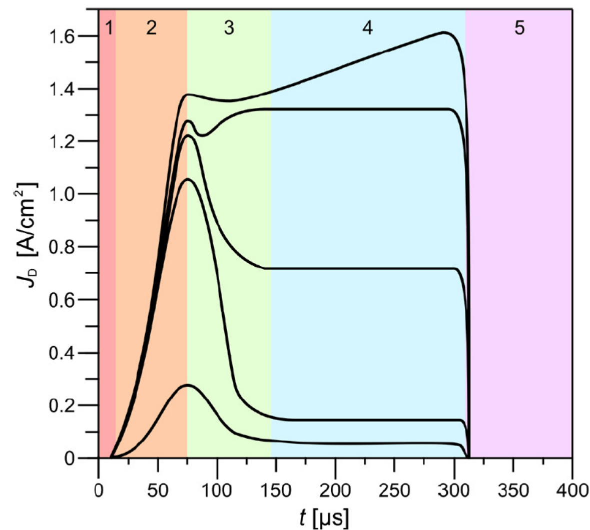

Figure 5: Different types of HiPIMS pulses are schematically shown and divided in five different phases: Phase 1: pulse ignition, Phase 2: current rise to the first maximum, Phase 3: decay/transition from the first maximum to the next phase, Phase 4: plateau or runaway, Phase 5: afterglow [50].

The **pulse ignition**, marked as phase 1 in Figure 5, is the delay time between the start of the voltage pulse and the onset of the current pulse and covers approximately the first 10 µs. It is likely that the discharge ignites near the anode ring, where the vacuum electric field is the strongest, as a localized glow discharge [48]. Experimentally it was found that the delay time depends on the working gas pressure, where Figure 6 illustrates that the delay time decreases with increasing working gas pressure [46]. Also, the composition of the working gas [56], the target material [57] and the applied voltage [58] influence the delay time. To reduce or eliminate the delay time, a DC pre-ionizer can be used. This allows also to operate the discharge at very low pressures, where the delay time would exceed the actual pulse width [59]. During this phase a significant increase of the fraction of metastable working gas atoms (Ar^m) has been reported. This occurs before a significant density of sputtered material can be found [60]. The increase can be explained by a short burst of hot electrons during the ignition phase [61]. Ar^m is then formed by electron impact excitation ($e^- + Ar \rightarrow Ar^m + e^-$) [48,61]. In contrast to charged particles (electrons and ions), Ar^m is not lost to the surrounding plasma volume and to the target (in case of the ions) during phase 1, which explains the significant increase [62].

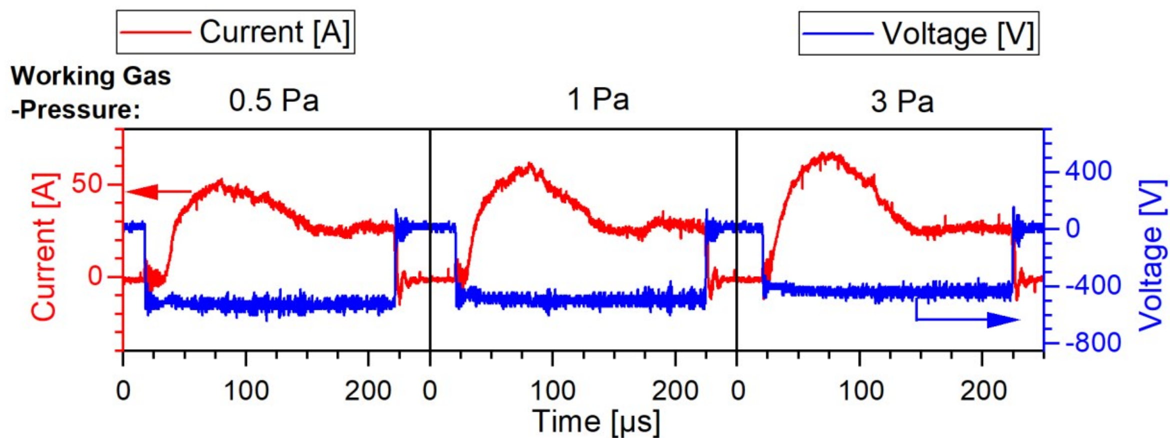

Figure 6:Current and voltage pulses of a HiPIMS discharge, operated with a MoNbTaWZr target at different working gas pressures. A reduction of the delay time between the voltage and current increase at the begin of the pulse can be seen with increasing working gas pressure. [publication II]

After the ignition phase, a **current rise** phase can be observed, which is called phase 2 in Figure 5. During this phase, secondary electrons and electrons created in the ionization region start to ionize the neutral working gas, which is then accelerated towards the target [63]. At the discharge current maximum, the highest rate of gas rarefaction dn_{Ar}/dt occurs. In case of the example shown in Figure 7, the gas density n_{Ar} reaches a minimum 40-60 µs after the discharge current reaches its maximum [64]. After the minimum is reached, the gas density increases again and stabilizes at a plateau. After the end of the pulse, the gas refills until the initial gas density is reached again. The highest rate of gas rarefaction occurs because of electron impact ionization and the sputter wind, as indicated by Figure 7 [64]. When the sputtered particles fly through the discharge, they can collide with the gas atoms and push the gas atoms into the surrounding area – this process is called sputter wind. In typical HiPIMS conditions, the mean free distance is in the order of a few cm, which means that most of the sputtered particles pass through the ionization region without any collision with a working gas atom [64,65]. The contribution of the sputter wind increases with increasing working gas pressure [65]. While in the case of dcMS the gas rarefaction is mostly due to sputter wind, this is not the case for HiPIMS, as visible in Figure 7 [66]. For HiPIMS the biggest contribution to gas rarefaction is due to electron impact ionization, which is due the significantly higher electron density compared to dcMS [64,67]. The cold Ar atoms, which are ionized, are either attracted to the target or lost to the surrounding. The Ar ions, which hit the target surface, are neutralized and return to the ionization region as hot Ar atoms. Most of these hot Ar atoms pass through the ionization region without any collision, leading to a loss flux

term which nearly balances the influx term [64,65]. Due to charge exchange ($Ar^+ + M \rightarrow Ar + M^+$) also some gas refill occurs.

During the reduction of the Ar gas density, the metal atom and ion flux increases as characterized by optical emission spectroscopy measurements of a HiPIMS discharge with a Cr target operated in N_2/Ar [56]. The authors reported that the metal ion density reaches its maximum together with the peak current.

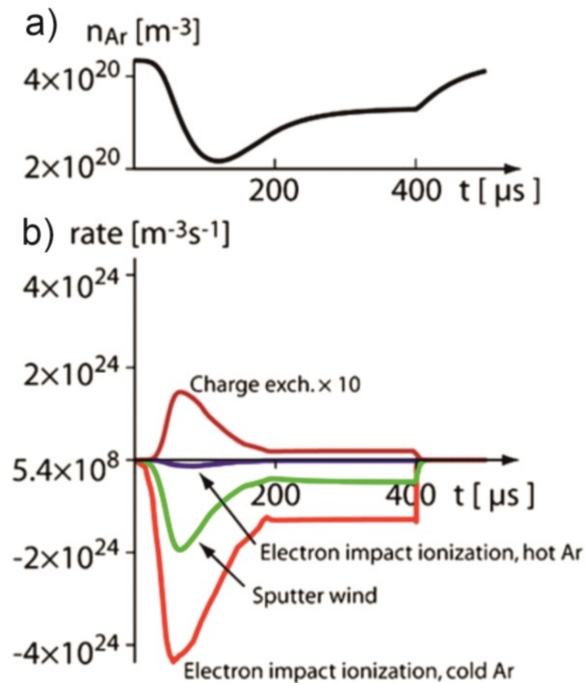

Figure 7: a) The Ar density during a 400 µs long HiPIMS discharge pulse of an Al target operated at an Ar-pressure of 1.8 Pa. b) The different contributions leading to gas rarefaction. [64,65]

Phase 3 is called **current decay or transition phase** and is also included in Figure 5. At the beginning of this phase the current first decreases, which leads to refill of the Ar gas from the surrounding gas reservoir (Figure 7). After the current decrease phase 4 begins, which can reach either a **plateau or an additional current increase phase** occurs. These two different modes were already discussed in detail in section 2.2.2.

After the end of the pulse the **afterglow** phase (phase 5) begins, which lasts until the begin of the next peak (Figure 5). When the current density peaked directly before the pulse end, a peak of the density of the sputtered species is found during the afterglow. After this peak, the metal ion density shows a slow decay [48]. If the peak was reached much earlier during the pulse, low metal ion densities are expected [48]. The electron density first shows a fast decrease, which is then followed by a much lower decay rate

[61]. Also the effective electron temperature decreases quite fast, until it reaches ~0.2 eV, from where it remains constant up to milliseconds [61]. In HiPIMS the discharge plasma can sustain up to 10 ms after the pulse is switched off [61].

2.2.3 Ion Energy Distribution Function (IEDF)

In Figure 8 the IEDF of a) a dcMS and b) a HiPIMS discharge, operated with two different pulse energies (3 and 10 J), is shown, using a Ti target and Ar as working gas [68]. The IEDF of the working gas is quite similar for all cases, as the working gas is considered to be in thermal equilibrium, due to the collisions within the gas and the chamber walls [60,65,69]. With increasing pulse energy (discharge power), the tail of the Ar^+ ions is shifted to higher energies (Figure 8b). This increase can be explained by the collision of the Ar^+ ions with the more energetic metal flux, when applying higher pulse energies [65,68]. The influence of the higher energetic metal flux is less prominent for increasing working gas pressures [70]. In the case of dcMS, the high energy tail of the Ti^+ ions is related to the energy distribution of the sputtered neutrals [71]. In comparison, the energy tail of the Ti^+ ions of the HiPIMS discharge is significantly higher, which is due to three main reasons. First, due to gas rarefaction, the sputtered particles are less likely to lose energy due to gas scattering [65,72,73]. Second, an increased energy tail results also from the reflection of ions, which return as fast neutrals into the bulk plasma. The process is additionally enhanced by the higher discharge currents used for HiPIMS [65]. Both processes are enhanced by the increase of the discharge power [72,73]. Third, the existence of plasma instabilities, such as non-stationary double-layer potential structures (i.e. potential humps), which are related to spokes (rotating dense plasma zones), accelerate ions into the ionization region near the target surface [65]. Although spokes are not only found for HiPIMS [74], but also for instance for dcMS [75], more dense spokes were reported for HiPIMS due to higher plasma densities [76–78].

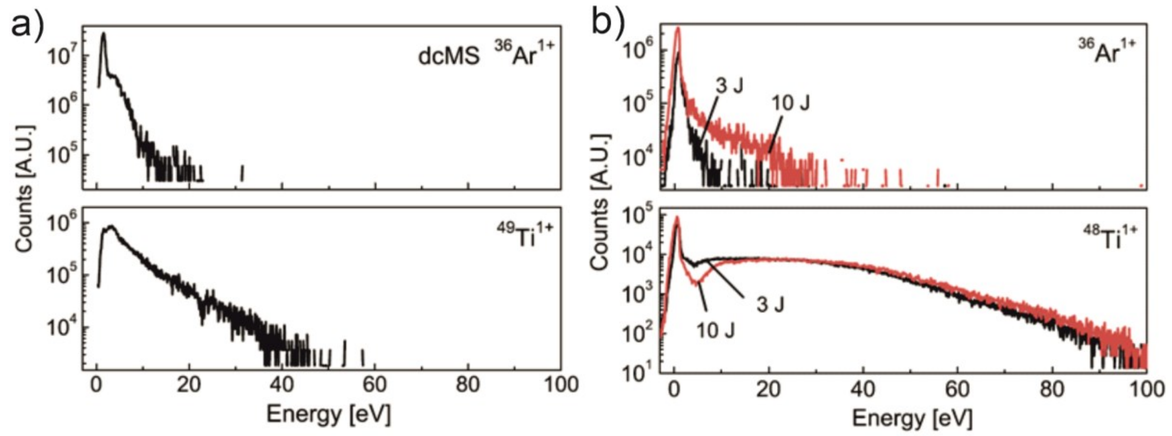

Figure 8: a) The IEDF of the Ar^+ ions and the Ti^+ ions of a dcMS discharge. b) The IEDF of the Ar^+ ions and the Ti^+ ions of a HiPIMS discharge, operated with 3 or 10 J, respectively. [68]

2.2.4 Ionized Flux Fraction

When discussing the degree of ionization, one has to keep in mind that three different definitions are distinguished: the ionized flux fraction F_{flux}, the ionized density fraction $F_{density}$, and α_t which is the fraction of sputtered metal atoms that become ionized (Figure 4) [65]. F_{flux} can be defined as

$$F_{flux}^{(s)} = \frac{\Gamma_i^{(s)}}{\Gamma_i^{(s)} + \Gamma_n^{(s)}}, \quad (3)$$

where $\Gamma_i^{(s)}$ and $\Gamma_n^{(s)}$ are the ion and neutral fluxes of the species s arriving at the substrate or detector, respectively [65,79]. In contrast, $F_{density}$ is defined using $n_i^{(s)}$ and $n_n^{(s)}$, which are the ion and neutral densities of the species s in the plasma volume, respectively [65]:

$$F_{density}^{(s)} = \frac{n_i^{(s)}}{n_i^{(s)} + n_n^{(s)}} \quad (4)$$

The last discussed parameter, α_t, is the fraction of sputtered atoms, which are ionized by the magnetron plasma [65,80]. As F_{flux} is the easiest of all three parameters to be measured, it is also the parameter which is used most often in literature [65].

Lundin et al. [81] used a grid-less quartz crystal microbalance (m-QCM) system to measure F_{flux} of a HiPIMS discharge using a Ti or Cr target with varying parameters (Figure 9). For m-QCM a quartz crystal electrode was used, which was either directly biased with +60 V to measure only the neutral mass deposition rate, R_n, or grounded

to measure the total deposition rate, R_t [82]. Using these values allows to calculate F_{flux}:

$$F_{flux} = \frac{R_t - R_n}{R_t} \tag{5}$$

It was found that the most important parameters influencing the ionized flux fraction are the gas pressure and the average pulse current density [65,81]. The average pulse current density j_D is similar to the peak current density and can be defined as

$$j_D = \frac{1}{A_{target}} \int_{t_{pulse-begin}}^{t_{pulse-end}} i_D(t)dt, \tag{6}$$

where A_{target} is the target area and $i_D(t)$ is the function of the peak current depending on the time [81]. As shown in Figure 9, F_{flux} increases significantly with increasing j_D. Lundin et al. [81] could correlate this result with measurements of the electron density and electron temperature, using Langmuir probe measurements. The authors report that both the electron density and electron temperature increase with increasing j_D, which enhances the probability for electron impact ionization [81]. In contrast, the effective electron temperature decreases with increasing working gas pressure, leading to lower probability for electron impact ionization, and therefore a lower F_{flux}.

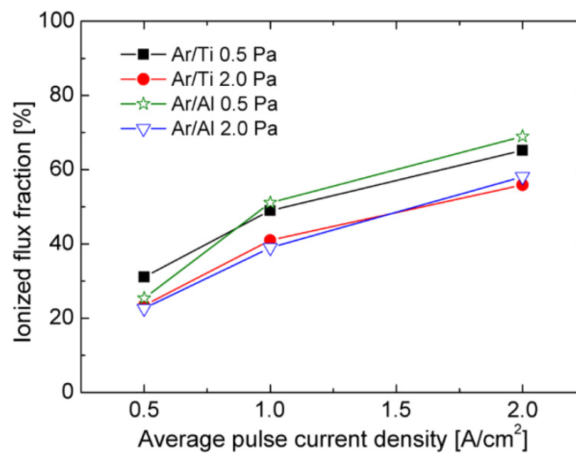

Figure 9: The measured ionized metal flux fraction of a HiPIMS discharge operated with an Al and Ti target with varying deposition parameters [65,81]

2.2.5 Deposition Rate

The biggest drawback of HiPIMS is the significantly lower deposition rate compared to dcMS. The deposition rate of HiPIMS is in the range of 30-85 % of the deposition rate of dcMS [83]. The main reason for the lower deposition rate is the back attraction of

sputtered metal ions [80]. But also the higher target voltage, and therefore the lower average current of a HiPIMS discharge, compared to a dcMS discharge when applying the same average power, leads to a decreased deposition rate for HiPIMS [84]. As working gas rarefaction results in a lower working gas density, thus, less ions available for sputtering, leading to a reduction of the deposition rate. However, this effect has not yet been experimentally proven [65]. The deposition rate also depends on the HiPIMS discharge mode, described in subsection 2.2.2, as the self-sputter yield is typically 10-15 % lower than the working gas sputter yield [85]. When applying a short pulse (t ≤ 50 µs), and therefore prevent a transformation towards significant self-sputtering, the deposition rate increases. Nevertheless, the ionized flux fraction decreases [86]. Increasing the magnetic field strength leads to a decreased deposition rate, as a higher electric field and higher plasma potential occur, leading to enhanced back attraction of the sputtered metal ions. The electric field and plasma potential are also increased for a higher applied power and during the early stage of the pulse [87]. Although a decreased magnetic field strength would lead to an increased deposition rate, this comes also with the drawback of a reduced metal ion flux [88].

2.2.6 Film Density

Due to the effect of ions with typical energies, as obtained for HiPIMS and described in subsection 2.2.3, it is possible to deposit films with a density close to the bulk density and ultra-smooth surfaces, even without providing any heating or bias voltage [44,50,83,89,90]. This differs from films grown by dcMS ($F_{flux} \approx 0$), as the adatom mobility is enhanced by the energetic bombardment with the ions [91]. Samuelson et al. [83] reported that the film density for HiPIMS is enhanced by 5-15 % compared to dcMS.

The film density is especially enhanced when depositing on complex shaped substrates. Alami et al. [92] compared the film morphology of a negatively biased substrate placed parallel to the target normal, see Figure 10. As dcMS is a line of sight process, a porous columnar structure is formed, which is due to atomic shadowing effects. The columns are also tilted from the interface normal. For HiPIMS, a dense structure with columns perpendicular to the interface normal was found, which is due to the guidance of the ions by the electric field. It is also possible to guide ions using an additional magnetic field [90]. Film deposition on complex shaped three-

dimensional substrates is especially important for microelectronics, but also for the deposition of protective coatings, as used for forming tools and turbine blades [90].

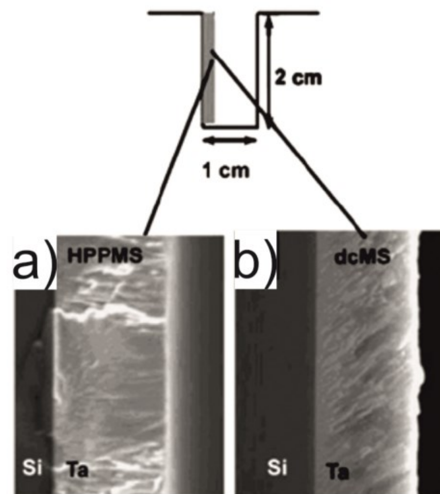

Figure 10: Film growth on a substrate placed perpendicular to the target surface, deposited using a) HiPIMS and b) dcMS with an additional negative bias voltage applied to the substrate [92].

3 THIN FILM GROWTH AND STRESS

3.1 THIN FILM GROWTH

When a sputtered metal atom with a specific kinetic energy hits the substrate surface, a fraction of its kinetic energy dissipates into lattice vibrations. Depending on the kinetic energy which is left, the atom either leaves the substrate surface again, if the remaining kinetic energy is still higher compared to the adsorption energy, or sticks to the surface and becomes an adatom, if the kinetic energy is smaller compared to the adsorption energy [90]. These adatoms can then perform a random walk on the surface. The distance of how far the adatoms can travel depends on the substrate temperature and the energy barrier an adatom has to overcome for each jump [90]. With increasing adatom density, the probability for island (atom cluster) nucleation increases. Until a specific island size is reached, thus, the islands become stable and they can either dissociate or grow in size by taking up more adatoms or by sputtered atoms impinging on the island [90,93,94]. The island nucleation process, which is typical for the formation of polycrystalline films, is schematically shown in Figure 11. The nuclei density N increases up to the point where the saturation nuclei density N_{sat} is reached. N_{sat} can be expressed as

$$N_{sat} \propto \left(\frac{F}{D}\right)^{x}, \tag{7}$$

where x is a scaling exponent, F is the adatom arrival rate, and D is the diffusivity [95]. The scaling exponent x has a value below one and depends on the dimensionality of the growth and the critical nucleus size. With increasing D, which is related to an increasing surface temperature, the adatom mean free path increases leading to a favored incorporation of adatoms into existing islands, compared to forming new ones, which results in a decreasing N_{sat} [90,95]. With increasing F the number of adatoms increases, which promotes the formation of new islands on the expense of island growth, which results in an increasing N_{sat} [90,95].

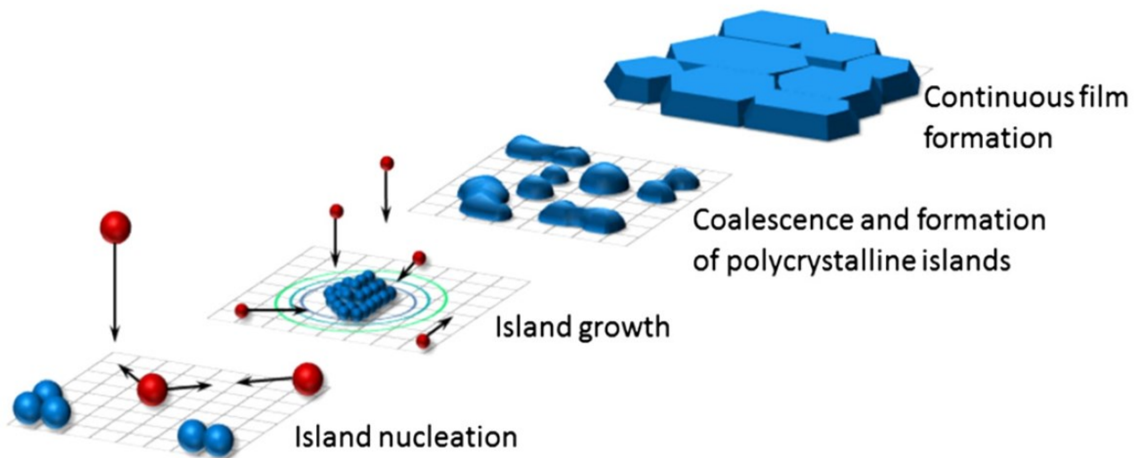

Figure 11: The nucleation and island growth process up to the formation of a continuous film. [96]

When pulsed vapor fluxes are used, like for HiPIMS, N_{sat} depends on the adatom lifetime τ_m, which is the mean time that an adatom needs to get incorporated into a stable island. Depending on τ_m three different diffusivity regimes can be distinguished, as shown in Figure 12 [97]. The first one is the slow diffusion regime ($\tau_m \gg 1/f$), where f is the pulse frequency. Within the slow diffusion regime migrating adatoms are present until the end of the next pulse (i.e. adatom density does not reach zero). The average flux F_{av} encountering the substrate can be used to calculate N_{sat}

$$F_{av} = \frac{F_i \cdot t_{on}}{f}, \tag{8}$$

$$N_{sat} \propto \left(\frac{F_{av}}{D}\right)^x, \tag{9}$$

where x is a scaling component between 0 and 1 and depends on the dimensionality of the growth (i.e. 2D or 3D growth) and F_i is the instantaneous rate [97] (Figure 12a). The second regime is the intermediated diffusivity regime ($t_{on} < \tau_m < 1/f$) [97] (Figure 12b). Within this regime N_{sat} can be calculated by:

$$N_{sat} \propto (F_i t_{on})^{\frac{x}{1-x}}. \tag{10}$$

The last one is the fast diffusion regime ($\tau_m \ll t_{on}$), where during the pulse off time the adatom density approaches zero (Figure 12c) [97]. The adatom mobility is therefore determined by the instantaneous rate F_i:

$$N_{sat} \propto \left(\frac{F_i}{D}\right)^x. \tag{11}$$

As $F_i \gg F_{av}$, the saturation nuclei density will be higher in case of the fast diffusion regime compared to the slow diffusion regime [97].

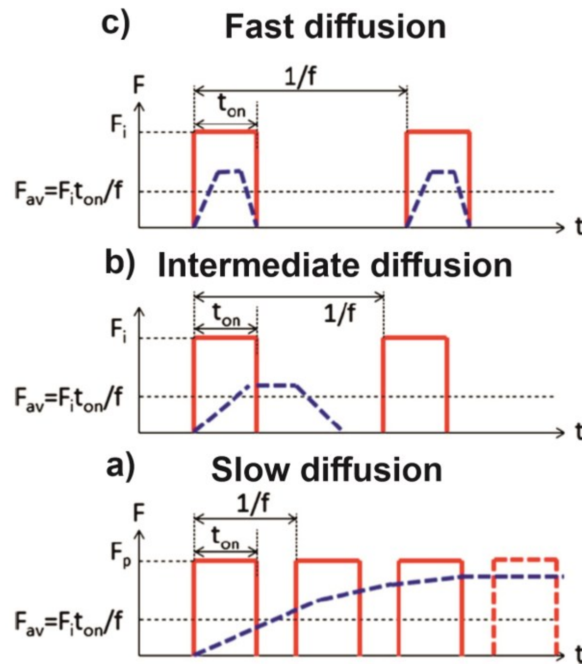

Figure 12: Depending on the mean time an adatom needs to get incorporated into an stable island, τ_m, three diffusivity regimes can be distinguished: a) slow diffusion regime ($\tau_m \gg 1/f$), b) intermediated diffusivity regime ($t_{on} < \tau_m < 1/f$) and c) fast diffusion regime ($\tau_m \ll t_{on}$).The red full line represents the instantaneous rate during the pulse and the blue dashed line the adatom density [97].

After N_{sat} is reached, island growth becomes the dominating process (Figure 11) [90]. The islands grow in size until they interfere with each other and grow together (coalescence) forming a new larger island [91]. The coalescence of different island leads to the formation of a new larger island which can either be polycrystalline or – after recrystallization – single crystalline. The coalescence continuous until a continuous film is formed (Figure 11) [91]. These processes typically only account in the beginning of a new polycrystalline film.

Possible interactions between the growing film and ions impinging on its surface depend on the ion energy. At lower ion energies (a few tens of eV), the impinging ions affect the film surface, whereas at higher ion energies (above 100 eV) they are dissipated into the film bulk [90,98]. As shown in subchapter 2.2.3, both ion energies occur in case of HiPIMS, independent of an eventually applied bias voltage.

When ions interact with the film surface the adatom mobility is enhanced, which is due to three different processes [91]. The first possibility is that the incoming ions transfer their kinetic energy to single adatoms or clusters. Second, the bombarding ions induce

a phonon when hitting the surface, where the phonons can then be coupled to an adatom. The last possibility is a shallow collision cascade, which can interact with the adatom [98]. As already discussed before, an increased adatom mobility leads to a decrease of the nucleation density. Additionally, densification, smoothening of the surface and changes of the crystallographic orientation can occur [90].

When the ions have higher ion energies and are dissipated into the film bulk, often lattice defects, such as interstitials and vacancies are formed, which leads to a densification of the film and the formation of film stresses [90,98].

3.2 Residual Stress

3.2.1 The Origin of Stresses within Thin Films

The stress distribution of a CrN film with changing film thickness is schematically shown in Figure 13a (full circles). At the beginning of film growth (region I), there is evidence for compressive stress formation, which is caused by the isolated crystallite islands, with compressive surface stresses acting on the substrate surface prior to coalescence [99]. When a continuous film is formed, the film shrinks, which leads to the development of tensile stresses (region II) [99]. The local maximum of this stress increase indicates the end of the coalescence process, where its magnitude depends on the grain boundary motion and the number of voids annihilated between the grains. The adatom mobility is also important [99], since at high mobility conditions diffusion of excess sputtered adatoms to grain boundaries occurs that gives rise to the development of compressive stresses (region III). The incorporation of surface adatoms into the grain boundaries reduces the free energy of the grain boundaries [100]. Higher substrate temperatures and ion irradiation increase this effect, as they increase the adatom mobility [99]. With increasing film thickness the grain size increases, as films often show a V-shaped morphology, which leads to a reduction of the grain boundary surface and subsequently to a reduction of the number of atoms incorporated there. Additionally, the chemical potential of atoms in the grain boundary increases due to the existing compressive stresses, which leads to a suppressed flux towards the grain boundaries. Both effects result in a reduction of the compressive stresses within the film (region IV) [99]. Organization of the disordered low density grain boundaries causes a volume shrinkage and the formation of tensile stresses (region V) [99].

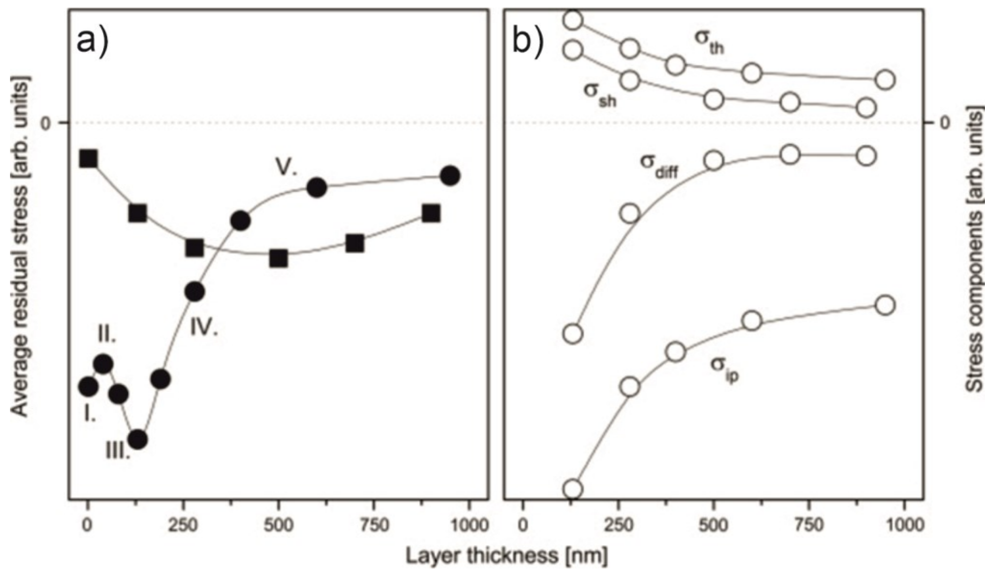

Figure 13: a) Schematic diagram of the stresses within a CrN film grown on a substrate (full circles) and a CrN film grown on a Cr layer (full squares). The different growth stages of the film lead to a different development of the stresses within the film (full circles I-V). b) The total stresses are split up into their components: the thermal stresses σ_{th} and the intrinsic stresses σ_i, which can be split up into intrinsic stresses related to ion irradiation, the tensile stresses originating from the volume shrinkage accompanying grain growth σ_{sh} and the compressive stresses due to the adatom diffusion to the grain boundaries σ_{sh}.[99]

The total stresses σ_{tot} consists of three parts

$$\sigma_{tot} = \sigma_i + \sigma_{th} + \sigma_e, \tag{12}$$

where σ_i, σ_{th} and σ_e stand for the intrinsic, thermal and extrinsic stresses, respectively [99]. Stresses caused by phase transformations, precipitation, plastic or creep deformation, structural misfit or chemical reactions are referred to σ_e and should be taken into account individually in every specific case [99].

The thermal stresses are calculated using

$$\sigma_{th} = \frac{E_f}{1-\nu_f} \cdot (\alpha_s - \alpha_f) \cdot (T - T_s), \tag{13}$$

where E_f, ν_f and α_f are the elastic modulus, Poisson's ratio and coefficient of thermal expansion (CTE) of the film, α_s is the CTE of the substrate, T_s is the substrate temperature during deposition and T is the temperature at which the stresses are measured [99]. α_f can depend on the film thickness, as the microstructure of the film changes with increasing film thickness. For instance in the case of a 500 nm thick CrN film, $\alpha_f = 9.1 \cdot 10^{-6}\ K^{-1}$ and for a 3 µm thick film $\alpha_f = 6.8 \cdot 10^{-6}\ K^{-1}$ [99]. At low film thicknesses the structure is finer grained and therefore more grain boundaries exists, leading to a higher volume expansion. Because of the changing CTE, σ_{th} decreases with increasing film thickness [99].

The intrinsic stresses depend on the growth conditions of the film, as stresses are generated during film growth, and can be expressed as

$$\sigma_i = \sigma_{sh} + \sigma_{diff} + \sigma_{ip}, \tag{14}$$

where σ_{sh} are the tensile stresses originating from the volume shrinkage accompanying grain growth and σ_{diff} for the compressive stresses due to adatom diffusion to the grain boundaries [99]. The intrinsic stresses related to ion irradiation σ_{ip} are generated by knock-on displacement of surface adatoms into interstitial or vacant lattice sites in the near surface region. When ions are dissipated into the film bulk, defects like interstitials and vacancies are formed, which also lead to an increase of the compressive stresses [90]. All of these components are shown together with σ_{th} in Figure 13b. Especially σ_{ip} leads to the formation of high compressive residual stresses within the layer [99].

3.2.2 Sin²(Ψ)-Method

Stresses within thin films can be measured using X-ray diffraction applying the sin²(Ψ)-method [101,102]. When the classical Bragg-Brentano or θ/2θ geometry is applied, the diffraction vector Q is always perpendicular to the sample surface and the 2θ diffraction angle of the different {hkl} planes can be acquired. Using Bragg's law allows to calculate the lattice spacing d using the diffraction angle θ

$$n\lambda = 2d\sin\theta, \tag{15}$$

where n is the diffraction order (typically 1) and λ is the wavelength of the used X-ray source [103]. If a tensile stress σ is applied to a material, as shown in Figure 14, the lattice spacing of a {hkl} plane varies depending on the orientation of the grain. The lattice spacing is reduced when the lattice planes are parallel to σ, due to transversal contraction, and increased, when they are perpendicular to σ [104]. The idea behind the sin²(Ψ)-method is that the lattice spacing of differently tilted grains of the same {hkl} peak are measured [102].

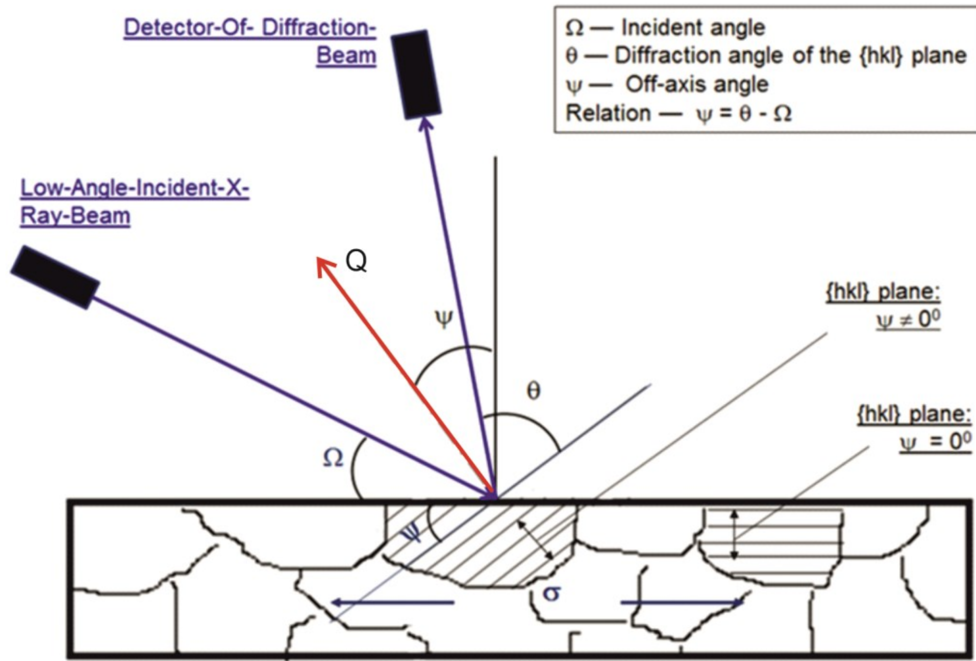

Figure 14:Schematic of an X-ray diffraction experiment performed under a specific off-axis angle Ψ of a tensile strained sample [104].

As the sin²(Ψ)-method only applies for the near surface region, the stress component of the stress tensor in its diagonal form, which is perpendicular to the surface (σ_3), is zero. If it is assumed that the stress and strain vector brought to their diagonal form coincide, only σ_1 and σ_2 are left for the stress components and ε_1, ε_2 and ε_3 are left for the strain components [102]. Using the Young's modulus E, the Poisson ratio ν and the stress components σ_1 and σ_2, the different strain components can be calculated [102]:

$$\varepsilon_1 = \frac{\sigma_1}{E} - \nu\frac{\sigma_2}{E},$$
$$\varepsilon_2 = \frac{\sigma_2}{E} - \nu\frac{\sigma_1}{E} \text{ and} \tag{16}$$
$$\varepsilon_3 = -\nu\frac{\sigma_1}{E} - \nu\frac{\sigma_2}{E}.$$

The strain in direction r can be calculated using Ψ and φ (Figure 15a) [102]:

$$\varepsilon = (sin^2\Psi cos^2\varphi)\varepsilon_1 + (sin^2\Psi sin^2\varphi)\varepsilon_1 + (cos^2\Psi)\varepsilon_3. \tag{17}$$

Using this formula $\varepsilon - \varepsilon_3$ can be obtained [102]

$$\varepsilon - \varepsilon_3 = \frac{sin^2\Psi}{E}(1+\nu)\sigma_\varphi, \tag{18}$$

where σ_φ can be calculated as follows:

$$\sigma_\varphi = \sigma_1 cos^2\varphi + \sigma_2 sin^2\varphi. \tag{19}$$

Alternatively, $\varepsilon - \varepsilon_3$ can also be calculated using the lattice spacing [102]:

$$\varepsilon - \varepsilon_3 = \frac{d_\Psi - d_0}{d} - \frac{d_0 - d}{d} = \frac{d_\Psi - d_0}{d} \approx \frac{d_\Psi - d_0}{d_0}. \tag{20}$$

Combining equation 18 and 20 leads to:

$$\frac{d_\Psi - d_0}{d_0} = \frac{sin^2\Psi}{E}(1+\nu)\sigma_\varphi. \tag{21}$$

When a graph is plotted using $\frac{d_\Psi - d_0}{d_0}$ for the y-axis and $sin^2\Psi$ for the x-axis, the obtained slope K can be used to calculate the stress σ_φ of the film (Figure 15b) [102]:

$$K = \frac{1}{E}(1+\nu)\sigma_\varphi. \tag{22}$$

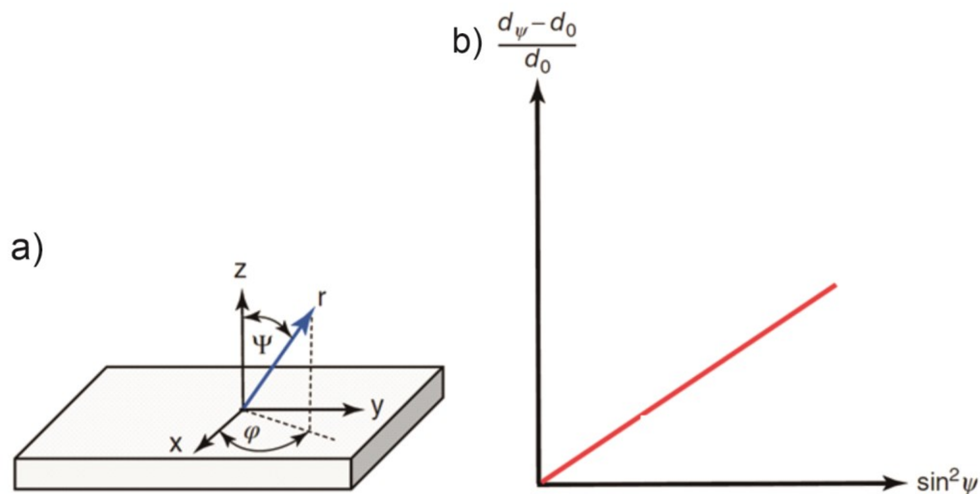

Figure 15: a) The different angles to describe r in a coordinate system. b) Schematic of the slope for a material with tensile stresses, obtained by the sin²(Ψ)-method. [102]

4 HIGH ENTROPY ALLOY FILMS

4.1 SURVEY ON HIGH ENTROPY ALLOYS

In the early 2000s a new class of materials, developed by Yeh [1,105] and Cantor [2], arose. Since then, the interest in HEAs increased every year [3]. The total mixing entropy of an alloy has four contributions, the configurational, vibrational, magnetic dipole and electronic randomness, however, the configurational entropy is the most dominant parameter [106]. The configurational entropy, ΔS_{conf}, of an alloy consisting of n elements, can be calculated using

$$\Delta S_{conf} = -R \sum_{i=1}^{n} X_i ln X_i, \tag{23}$$

where R is the gas constant and X_i is the mole fraction of the i-th element [3]. The configurational entropy of an alloy consisting of specific fractions of different elements reaches it maximum at the equiatomic composition. As an example, the formation enthalpy of NiAl and TiAl, which are two strong intermetallic compounds, divided by their respective melting temperature, leads to $1.38R$ and $2.06R$ [1]. Therefore, it seems reasonable to define the border for high entropy alloy with $\Delta S_{conf} \geq 1.5R$, as shown in Figure 16. As a mixing entropy below $1R$ is expected to be too low to compete with the strong bond strengths of intermetallic compounds, $\Delta S_{conf} \leq 1R$ is set as the border for low entropy alloys, which represent the traditional alloys (Figure 16) [105]. The alloys in between low and high entropy alloys are called medium entropy alloys.

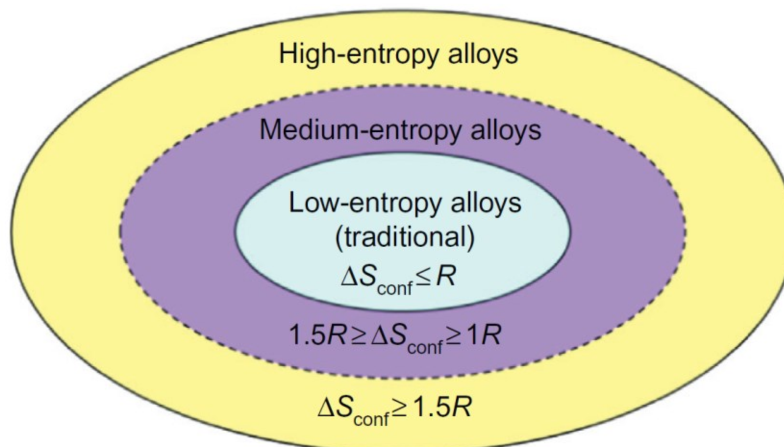

Figure 16: Visualization of the different groups of alloys, dividing them into high, medium and low entropy alloys. [3]

To rationalize the properties of HEAs, four core effects have been defined, which are the high entropy effect, the severe lattice distortion effect, the sluggish diffusion effect and the cocktail effect [105]. These effects are described in the following paragraphs.

The high entropy effect, was briefly described above and can be explained by taking a look on the Gibbs free enthalpy of mixing ΔG_{mix},

$$\Delta G_{mix} = \Delta H_{mix} - T\Delta S_{mix}, \quad (24)$$

where ΔH_{mix} is the mixing enthalpy, T is the current temperature and ΔS_{mix} is the mixing entropy [3]. The lower ΔG_{mix} is the more stable a phase is. Although intermetallic phases have a large negative ΔH_{mix}, due to their ordered nature, ΔS_{mix} is quite low. In contrast, ΔS_{mix} of a solid solution containing five or more elements in equimolar composition is significantly larger, leading to high negative ΔG_{mix} especially at high temperatures [3]. Therefore, HEAs prefer to consist of solid solutions with simple body centered cubic, face centered cubic or hexagonal crystal structures compared to intermetallic phases. While many HEAs are single phase, there are also HEAs which are composed of different phases. These can either be different solid solutions with a different structure or intermetallic precipitates within a solid solution phase, and there are also combinations of both [3].

As HEAs consists of at least five different elements, every atom is surrounded by different atoms. The surrounding atoms have a different atomic size and the bond strength between the central atom and each surrounding atom differs as well, leading to severe lattice distortion. Because HEAs consist mostly of random solid solutions, all atoms are randomly distributed within the material [107,108]. A schematic example how severe lattice distortion can look like for a bcc alloy is shown in Figure 17. Due to the significantly enhanced solid solution hardening, caused by the severe lattice distortion, hardness and strength are significantly increased within HEAs, even higher as predicted by the rule of mixture [3]. The X-ray peak determined by the average lattice of the HEA solid solution phase has a smaller peak intensity due to the increased X-ray diffuse scattering effect [107]. Due to the severe lattice distortion also the electron scattering increases, which leads to a reduction of the electrical conductivity. As the electrical conductivity is related to the electron contribution, the thermal conductivity is also reduced. Additionally, the photon scattering also increases in a distorted lattice, which leads to an additional decrease of the thermal conductivity [109]. As the lattice distortion caused by the thermal vibration of atoms is quite small

compared to the severe lattice distortion, many properties of HEAs are quite insensitive to temperature changes, like for example the resistivity [107].

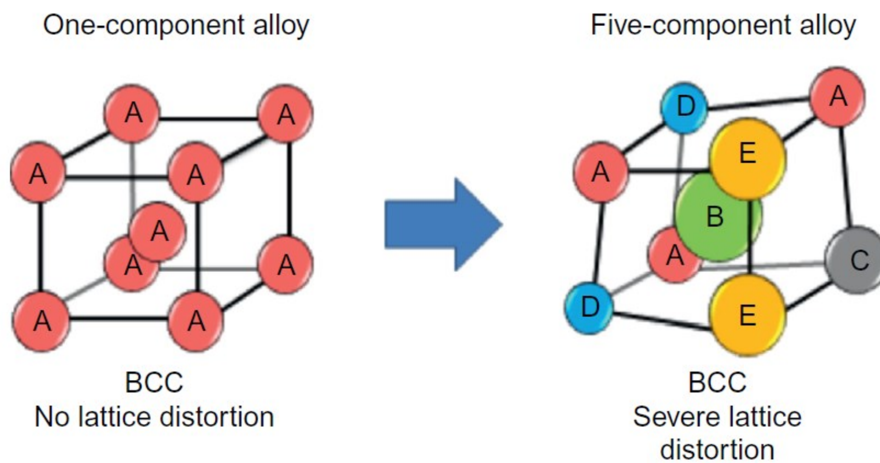

Figure 17: Comparison between the bcc lattice of a one-component bcc alloy and a five component bcc alloy. [3]

Within HEAs, each vacancy or atom is surrounded by a variety of different elements. Each atom has a different energy to overcome and a different energy benefit when occupying this vacancy, leading to large fluctuations of the lattice potential energy [108]. These large fluctuations have been found to cause a slower diffusion and higher activation energy for diffusion in HEAs, as low lattice potential energy sites could serve as traps and hinder the diffusion of atoms [108]. Tsai et al. [108] reported that with increasing number of elements the diffusion rate is lowered, representing the third core effect of HEAs, the sluggish diffusion effect. This effect was found to promote formation of super-saturated phases, to increase the recrystallization temperature, to slow down grain growth and to increase the creep resistance [3].

A HEA consists of one, two or more different phases, with a different size depending on the chemical composition and the synthesis process. To understand the overall properties of the material, the interaction of the different phases has to be known [3]. Each solid solution phase can be seen as an atomic scale composite. The overall properties of the HEA can be different to the properties predicted by the rule of mixture, due to the different interactions of all the involved elements. Therefore, it is important to understand all the interactions and related factors, when a new HEA is designed [3]. The effect described in this paragraph is the fourth core effect, the cocktail effect [105,110].

4.2 Refractory High Entropy Alloys

4.2.1 Overview on Refractory High Entropy Alloys

Refractory HEAs (RHEAs) are HEAs which consists mostly of refractory elements. As refractory metals have high melting temperatures, RHEAs are characterized by a high thermal stability, which makes them promising candidates for future high temperature applications [4]. RHEAs were first introduced by Senkov et al. [4,5], using MoNbTaW and MoNbTaVW. MoNbTaW-based alloys are still among the most important representatives of RHEAs. The effect of the different alloying elements, added to MoNbTaW, on the mechanical properties is shown in Figure 18. The data within Figure 18 has to be treated with care, as the fabrication route of the alloy, which influences its microstructure, and also the measurement procedure may affect the results. This is obvious when comparing the three different values obtained for MoNbTaW (red circle marked with 0, purple triangle marked with 0 and blue square not marked). The addition of V, which was explored since the beginning of research on RHEAs, leads to an increased yield strength [5]. In particular, MoNbTaVW is known for its good thermal stability and high yield strength at elevated temperatures. At temperatures beyond 800 °C the yield strength of MoNbTaVW is higher compared to commonly used Ni-based superalloys [5]. Similar to V also the addition of Hf leads to an increased yield strength. In contrast, alloying with Cr and Re does not have a significant impact on MoNbTaW RHEAs. Similar to commonly used W and Mo alloys, the addition of Re is expected to increase the ductility, and therefore the fracture strain of the alloy, which is in contrast to the findings obtained for MoNbTaW-based alloys [111,112]. The addition of Ti leads to an increased fracture strain and increased yield strength. The increased ductility of MoNbTaTiW compared to MoNbTaVW can be explained by the weaker interaction pairs of Ti with the other elements compared to V, which has especially strong interactions with W, Ta and Nb [113]. The addition of Zr to MoNbTaW leads to an even higher yield strength and fracture strain. The improved strength and ductility can be explained by the formation of partial Zr-Zr metallic bonds [8].

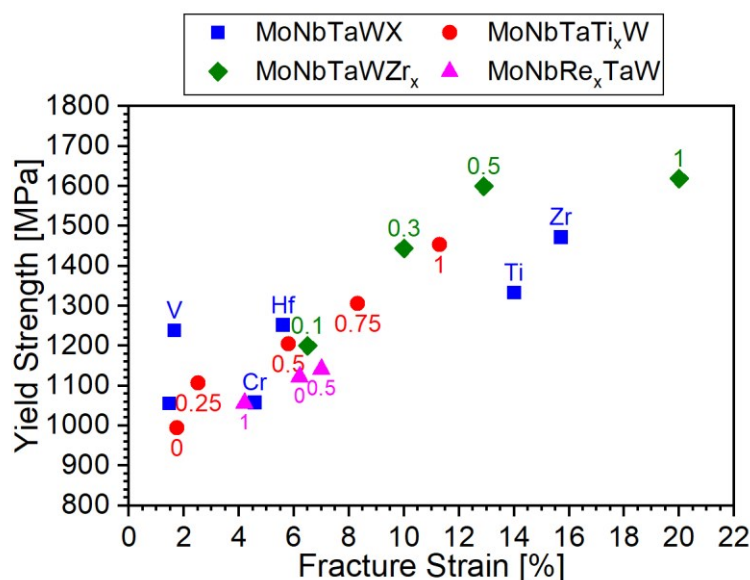

Figure 18: Yield strength and fracture strain of different MoNbTaW-based alloys, MoNbTaWX [5,6,8], MoNbTaTi$_x$W [7], MoNbTaWZr$_x$ [9], and MoNbRe$_x$TaW [114]. x = 0 or if no x is given indicates MoNbTaW. The graph is redrawn after [9].

4.2.2 Refractory High Entropy Alloy Films

One method for the synthesis of HEAs, used since the early days of HEA research, is magnetron sputtering, which can be used to deposit thin films [11–14]. By varying the process parameters, the microstructure and properties of HEA thin films can be varied. By adding N_2 or O_2 to the process, HEA nitride [3,11,15] and oxide [3] films can be deposited. Co-sputtering allows many different HEA compositions to be deposited, enabling further investigations. Beside the development of new alloys for thin film applications, thin films can also be a first step towards bulk alloy design.

Also MoNbTaW-based RHEA thin films have been studied for various applications. For nanocrystalline MoNbTaW films it was reported that with increasing annealing time at 800 °C in vacuum, the hardness increases [115]. The hardness increase was attributed to the formation of amorphous intergranular films, triggered by oxygen incorporation. The oxygen stems from the remaining oxygen in the vacuum chamber, while annealing of the films [115]. For MoNbTaVW films, deposited by cathodic arc deposition (CAD), also a hardness increase up to 1000 °C was found, however at temperatures up to 1300 °C the hardness decreases [26]. A part of this hardness decrease is related to the evaporation of V out of the film, which has a higher vapor pressure compared to the pressure in the vacuum chamber at these temperatures [26]. This was confirmed by annealing of a MoNbTaVW film in Ar at atmospheric pressure, where no evaporation of V was found, and the hardness after annealing at 1500 °C was the same after

annealing at 1100 °C in vacuum [26]. MoNbTaVW films have also been reported to show a solid solution bcc crystal structure which remains stable up to at least 1500 °C, thus indicating a high potential of these films to be used for high temperature applications [26]. Another study by Xia et al. [13] compared the dependence of different film properties on the deposition angle and for different deposition methods (dcMS, HiPIMS and CAD). They reported that independent of the deposition angle and deposition method, the films always had a solid solution bcc crystal structure, indicating its high stability. As HiPIMS and CAD are characterized by highly energetic growth conditions, the films deposited with these two methods had a denser microstructure compared to dcMS, which resulted in higher compressive stresses and higher hardness [13]. Chen et al. [116] evaluated the potential use of MoNbTaVW films for interconnects of solid oxide fuel cells and coatings for thermoelectric elements. After annealing for 1 h in air, the bcc structure has partially changed to amorphous phases, where at higher temperatures, iron containing oxide phases are formed. The iron stems from the used stainless steel substrates [116]. Although the MoNbTaVW film oxidizes, the electrical resistivity is kept significantly lower compared to the uncoated substrate, while annealing in air [116]. The influence of a varying V content on the hardness and Young's modulus of MoNbTaVW films was investigated by Li et al. [117] and their results are summarized in Figure 19. There, hardness and Young's modulus first increase up to a certain V concentration, and afterwards both decrease again. More studies are needed to illuminate the relations between these mechanical properties and the V content. MoNbTaW films also show good diffusion barrier properties, which efficiently prevent diffusion between Cu and Si [27–29] but also between Mo and $MoSi_2$ [30]. This topic is discussed in more detail in chapter 5.

Beside MoNbTaVW RHEA films, also (MoNbTaVW)N films have been investigated. Xia et al. [15] studied the influence of the nitrogen content on the microstructure of MoNbTaVW films deposited by dcMS and CAD. Depending on the used deposition method, the films show a transition from bcc to fcc between 25 to 30 at.% N. For films with a N content between 15 and 19 at.%, deposited with dcMS, an amorphous microstructure was found. The fcc, amorphous and bcc phase only occurred separately. The hardness values increased from 18 GPa for the metallic film to up to 30 GPa for the nitride films.

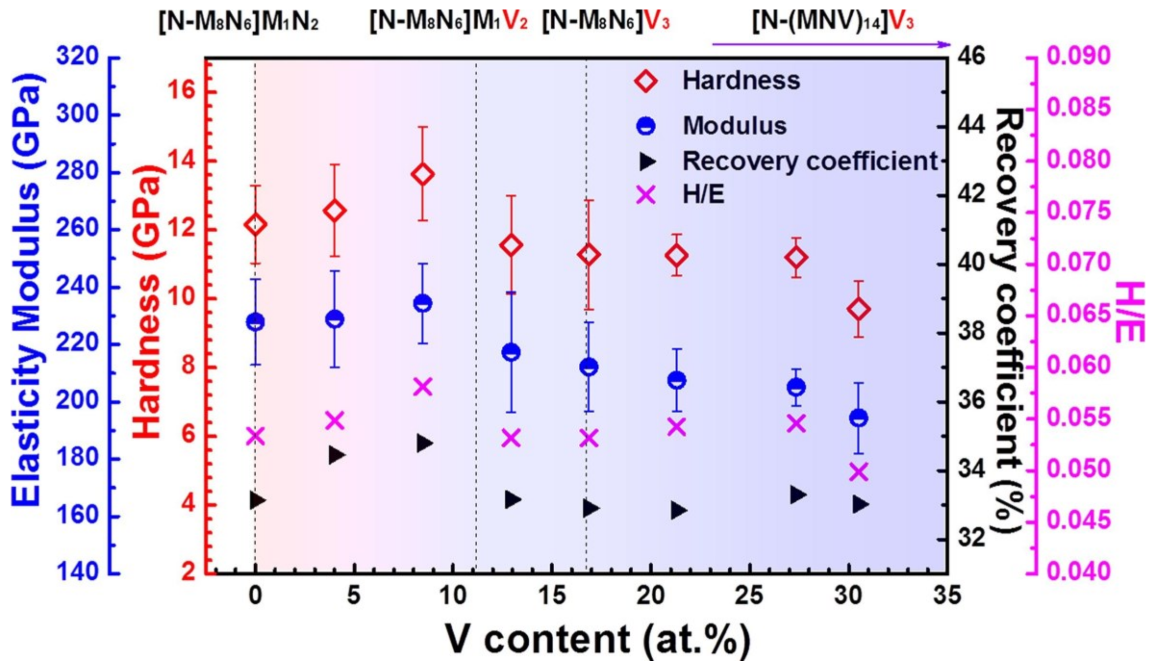

Figure 19: Influence of increasing V content on the Young's modulus (called elasticity modulus in this figure) and hardness. The recovery coefficient and H/E are not addressed in this work. [117]

5 DIFFUSION BARRIERS FOR MICROELECTRONIC SYSTEMS

5.1 GENERAL PURPOSE OF DIFFUSION BARRIERS

Whenever two materials are in contact interdiffusion may occur. Within microelectronic systems, many different materials, like semiconductors, conductors or insulators, can be in contact with each other. Intermixing of the different materials can lead to a change of the desired functional behaviors [17]. It is also possible that due to interdiffusion new phases are formed, for example Cu_3Si when Cu is in contact with Si, which can destroy the microelectronic system [17]. The flux of the diffusing species J_{Diff} can be described using Fick's first law of diffusion in one dimension

$$J_{Diff} = -D\left[\frac{\delta c(x,t)}{\delta x}\right], \tag{25}$$

where D is the diffusivity or diffusion coefficient and $\frac{\delta c(x,t)}{\delta x}$ is the concentration gradient as a function of position and time [17]. The diffusion coefficient can be calculated as:

$$D = D_0 e^{-\frac{Q}{RT}}, \tag{26}$$

where D_0 is the maximum diffusion coefficient at infinite temperature, Q is the activation energy for diffusion, R is the gas constant and T is the temperature [17]. To inhibit the interaction of two materials, a diffusion barrier layer can be put between the two materials. Depending on the materials the diffusion barrier is surrounded by, it requires certain properties: if the diffusion barrier is sandwiched between two electrically conductive layers, the diffusion barrier should also be conductive. This should also be the case, when only one of them is electrically conductive. If it is surrounded by insulator materials, the diffusion barrier should also be an insulator. Nicolet [118] has stated several characteristics of an ideal electrically conductive diffusion barrier X between A and B:

1. The material transport rate of A and B across X should be negligible
2. The material transport of X into A and B should be negligible
3. X should be thermodynamically stable against A and B
4. X should adhere strongly to A and B
5. The specific contact resistance of A to X and X to B should be small
6. X should be laterally uniform in thickness and structure
7. X should be resistant to mechanical and thermal stress

8. X should be a good electrical and thermal conductor.

As the number of transistors in a microprocessor grew, gate delays became an issue [119,120]. This could be solved by using a conductor material with a lower electrical resistivity. Therefore, Cu was introduced instead of Al, which has been used since the early beginnings of microelectronic systems [121]. A major drawback of the use of Cu is the fact that Cu tends to react with Si forming Cu-silicides (Figure 20) and it diffuses into Si based insulator materials triggering insulating failure at relatively low temperatures [17].

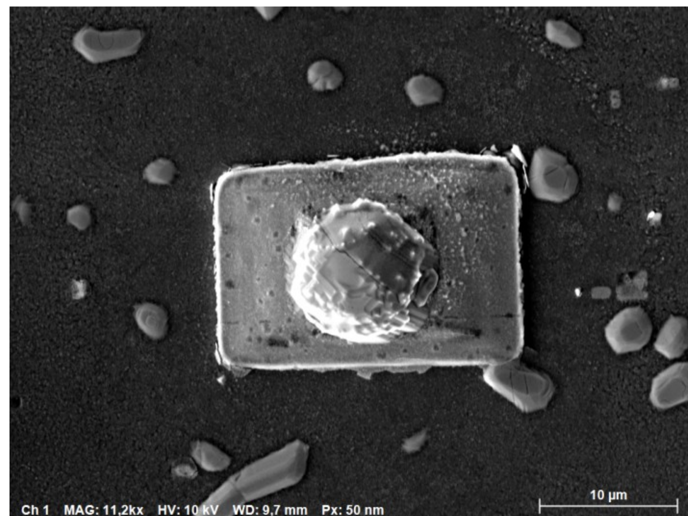

Figure 20: Secondary electron SEM picture of the surface of a Cu film deposited on top of a CrMoNbTaW diffusion barrier grown onto a Si substrate after annealing at 800 °C. The Cu_3Si crystals which are formed after the failure of the diffusion barrier are clearly visible. [own work]

The increasing transistor number in a microprocessor led to a decrease of the transistor size, which also necessitated high aspect ratio vias and trenches. These changes required to extend the characteristics of an ideal diffusion barrier [17]:

1. X should have an electrical conductivity similar to that of Cu. If this is not the case, X should be as thin as possible.
2. Deposition of X should be carried out in such a way that it coats the via/trench walls and bottoms conformably
3. If X is an insulator, it should not be thicker as a few monolayers to not contribute significantly to the capacitance of the interlayer dielectric. X should be anisotropically dry-etchable by reactive ions from the bottoms of the vias and trenches.

The microstructure of a diffusion barrier plays a vital role for the diffusion barrier performance, as grain boundaries and dislocations can act as fast diffusion paths. The activation energy to diffuse through a grain boundary is only about half of that for diffusion through the crystal lattice [17]. An approach to enhance the diffusion barrier performance is to put elements in the diffusion barrier, which segregate into the grain boundaries, leading to stuffed grain boundaries [118]. Such elements could for example be nitrogen, carbon or boron.

5.2 Overview For Used Material Systems

The activation energy of self-diffusion Q_{self} can be estimated by

$$Q_{self} = 34T_m, \tag{27}$$

where T_m is the melting temperature of the material [17]. According to this estimation, the activation energy for diffusion increases with increasing melting temperature of the used diffusion barrier. Therefore, refractory metals and alloys of these elements are most often used for classical diffusion barriers. Ono et al. [122] compared different 60 nm thick refractory metal films (Ti, Cr, Nb, Mo, Ta or W) for their applicability to serve as diffusion barrier between Cu and Si. Their resistance change with increasing annealing temperature is shown in Figure 21. Cr and Ti have the lowest resistance against barrier failure and fail already at annealing temperatures above 400 °C. Using Mo or Nb as the diffusion barrier, instead of Ti or Cr, slightly increased the failure temperature to above 500 °C. The highest failure temperature was found for Ta and W [122]. This relation agrees well with the melting temperature and the activation energy for self-diffusion [17,122]. Also the ability to form phases with Cu, which can then disrupt the multilayer structure leading to barrier failure, influences the performance of the diffusion barrier [122,123]. For example, among the metals studied in [122], Ti is known to react with Cu.

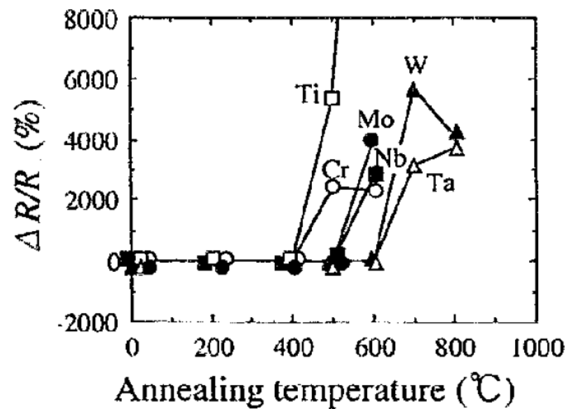

Figure 21: The resistance change of different 60 nm thick diffusion barriers (Ti, Cr, Nb, Mo, Ta or W) after annealing at elevated temperatures [122].

Often different refractory elements are alloyed with each other to form a new diffusion barrier, as for example in the case of WTi [17,124–126]. After annealing at temperatures of 600 °C and higher, Ti diffuses out of the diffusion barrier into Cu, triggering barrier failure [125]. The addition of N to WTi prevents the outdiffusion of Ti and therefore, the temperature of barrier failure could be significantly increased [125].

Another example of how the performance of a one element diffusion barrier can be improved by alloying is discussed on the basis of Ta. When Si is added to Ta ($Ta_{74}Si_{26}$) an amorphous film can be deposited, with a quite high crystallization temperature of 850 °C [17]. However, when the amorphous diffusion barrier is in contact with Cu, the crystallization temperature decreases to 650 °C. An amorphous film is known to have a better diffusion barrier performance, compared to a crystalline one, due to the missing grain boundaries, which can act as fast diffusion paths [17]. After crystallization at 650 °C, Cu diffusion along fast diffusion paths and reaction with Si is enabled, leading to barrier failure [17]. Again the addition of N increases the barrier performance significantly. For $Ta_{36}Si_{14}N_{50}$ this can be attributed to the increased crystallization temperature of 1100 °C [17].

Refractory metal nitride films are also commonly used as diffusion barriers within microelectronics. The most common representatives are TaN [127,128] and TiN [129–132]. TaN and TiN diffusion barriers are both very suitable due to their low formation enthalpy, which is below -100 kJ/mol [133]. For TiN, it was reported that films with a polycrystalline microstructure have the least resistance against Cu diffusion. A nanocrystalline microstructure was found to improve the diffusion barrier performance [129]. Mühlbacher et al. [132] reported that the diffusion barrier performance of TiN can be significantly improved by using a single-crystalline microstructure, due to the

lack of grain boundaries (fast diffusion paths). Densifying the diffusion barrier has also been investigated by bombarding of the growing TiN film with Ta ions. The Ta ions were generated from a separate Ta target operated with HiPIMS, leading to a $Ti_{0.84}Ta_{0.16}N$ film [134]. The authors found that the failure temperature increased significantly from 700 °C for TiN to 900 °C for the Ta ion bombarded $Ti_{0.84}Ta_{0.16}N$ film. However, it should be noted that using refractory metal nitrides instead of refractory metals has the disadvantage of the significantly higher electrical resistivity.

5.3 High Entropy Alloys for Diffusion Barriers

Due to the good thermal stability and the sluggish diffusion, HEAs, especially refractory HEAs due to their high melting point, are potential candidates for diffusion barriers. Chang et al. [16] found that with increasing number of elements within a diffusion barrier, the failure temperature increases. The involved elements and their content are summarized in Figure 22a. The authors could attribute the failure temperature increase to an increasing activation energy for Cu diffusion through the diffusion barrier. The increase of the activation energy can be attributed to an increase of the lattice strain energy ΔU_{strain}, the cohesive energy $\Delta\Omega_{mix}$ and the packing density S' with increasing number of elements within the diffusion barrier. The different components, besides the packing density, are visualized in Figure 22b. The activation energy for an element diffusing through the diffusion barrier can be calculated as [16]:

$$\Delta Q = (\Delta U_{strain} + \Delta\Omega_{mix})\frac{S'}{S}. \tag{28}$$

S stands for the packing density of a unitary alloy, which is for example 0.68 for a bcc metal. S' changes with changing number of elements within the lattice and can be taken from the appendix of the work of Chang et al. [16]. The different stress distribution caused by the lattice distortion affects the movement of the diffusing element through the diffusion barrier, as some sites are energetically more favorable than others, due to the different stress state. Additionally, also the vacancy formation is influenced by the local stress distribution [16]. The lattice strain energy change with varying chemical composition can be calculated using

$$\Delta U_{strain} = 4E\delta^2\overline{r^3}, \tag{29}$$

where E is the Young's modulus, δ is the lattice distortion and $\bar{r}$ is the mean atomic radius of the alloy [16]. Using

$$\delta = \sqrt{\sum_{i=1}^{n} C_i \left(1 - \frac{r_i}{\bar{r}}\right)^2} \tag{30}$$

to calculate the lattice distortion δ, where C_i is the chemical composition of the element i, and r_i is the atomic radius of the element i [135]. An increasing cohesive energy makes it more difficult to break up chemical bonds, whereas the opposite is the case for a decreasing cohesive energy. The local chemical environment defines the local cohesive energy, and therefore how easy it is to break up chemical bonds. Vacancies are favored to form in areas with low cohesive energy [16]. Therefore, the element diffusing through the diffusion barrier favors to move along areas with low cohesive energy. The cohesive energy change $\Delta\Omega_{mix}$ can be calculated by

$$\Delta\Omega_{mix} = \sum_{i=1, j\neq 1}^{n} \Delta\Omega_{ij} C_i C_j, \tag{31}$$

where C_i and C_j are the chemical composition of element i and j [16]. $\Delta\Omega_{ij}$ can be calculated by using

$$\Delta\Omega_{ij} = \frac{\Omega_{ii} + \Omega_{jj}}{2} - \Delta H_{ij}^{mix}, \tag{32}$$

where H_{ij}^{mix} is the mixing enthalpy and Ω_{ii}, Ω_{jj} is the fusion enthalpy of the different elements [16]. Following the approach by Chang et al. [16] allows for the selection of the elements within the diffusion barrier, and can be used in addition to other selection methods for HEAs regarding for example the structure (crystalline vs. amorphous, solid solution vs. intermetallic phases and crystal structure) of HEAs [136–138].

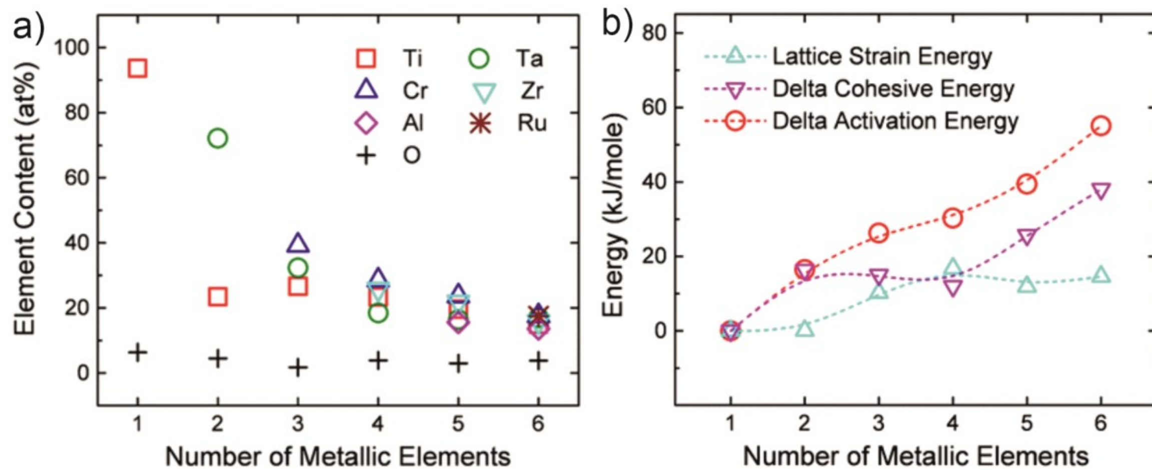

Figure 22: a) The chemical composition of the different alloys used by Chang et al. [16]. b) The change of the strain energy, cohesive energy and activation energy for an element diffusing through the diffusion barrier consisting of a different number of metallic elements. [16]

The state of the art of the different HEA diffusion barriers is summarized in Table 1. Reported investigations on HEA diffusion barriers focus mainly on six different base alloys: AlCrTaTiZr, AlCrNbTaTi, CrHfTiVZr, AlMoNbSiTaTiVZr, NbSiTaTiZr and MoNbTaW. Most of the research reported up to now deals with AlCrTaTiZr based diffusion barriers. In case of metal HEA diffusion barriers, AlCrRuTaTiZr [19] and NbSiTaTiZr [139] were reported to yield with 800 °C the highest temperature where the film can prevent the system from failing. Nevertheless, the achievable failure temperatures of some nitride films are even higher. For example, (AlCrTaTiZr)N [21] films can prevent failing of the system up to 900 °C. It is also incredible that an only 1.5 nm thick MoNbTaVW film [29] can inhibit system failure up to 600 °C. When comparing this result to the data presented in Figure 21, 60 nm thick (i.e. 40 times thicker) Ta or W films are needed to obtain a similar performance.

Table 1: Summary of state of the art HEAs explored as diffusion barriers. T_{max} is the highest temperature where failure of the system could be prevented.

HEA	Thickness [nm]	Structure	T_{max} [°C]	Annealing Time [h]	Source
		AlCrTaTiZr			
AlCrTaTiZr	50	amorphous	< 700	0.5	[19]
AlCrRuTaTiZr	5	amorphous	800	0.5	[19]
(AlCrTaTiZr)N	40	nanocrystals in an amorphous matrix	900	0.5	[21]
AlCrTaTiZr/ (AlCrTaTiZr)N	10	Metal (amorphous)/ nitride (fcc)	900	1	[25]
(AlCrMoTaTiZr)N	10	amorphous	800	1	[24]
(AlCrMoTaTiZr)N	300	amorphous	800	>7	[23]
$(AlCrRuTaTiZr)N_{0.5}$	5	mostly amorphous	700	0.5	[20]
$(AlCrRuTaTiZr)N_{0.5}$/ AlCrRuTaTiZr	1/1/1/1	-	800	0.5	[18]
$(AlCrRuTaTiZr)N_{0.7}$/ AlCrRuTaTiZr	7.5/7.5	mostly amorphous	800	0.5	[22]
		AlCrNbTaTi			
$(AlCrNbTaTi)_xN_yO_{1-x-y}$	15-30	amorphous	800	0.5	[140]
		CrHfTiVZr			
CrHfTiVZr	10	amorphous	600	0.5	[141]
$(CrHfTiVZr)N_{0.4}$	10	amorphous	600	1	[142]
(CrHfTiVZr)N	10	amorphous	800	1	[142]
		AlMoNbSiTaTiVZr			
AlMoNbSiTaTiVZr	100	amorphous	700	0.5	[143]
(AlMoNbSiTaTiVZr)N	70	amorphous	850	0.5	[144]
		NbSiTaTiZr			
NbSiTaTiZr	20	amorphous	800	0.5	[139]
		MoNbTaW			
MoNbTaW	40	amorphous	650	0.5	[27]
MoNbTaW	15	amorphous	500	0.5	[28]
CrTiV/MoNbTaW	3/3/3/3/3	amorphous	750	0.5	[28]
MoNbTaVW	1.5	-	600	1	[29]

6 SUMMARY AND CONCLUSION

Within this thesis, the suitability of MoNbTaW films, alloyed with a fifth element, i.e. Ti, V, Cr, Mn, Zr or Hf, for their use as diffusion barriers was investigated. As a first step, the microstructure and mechanical properties of these films deposited using HiPIMS were investigated. All films consist of a single phased bcc solid solution. The microstructure is characterized by a stress gradient, most probably along the film thickness. The highest hardness of about 17 GPa was found for CrMoNbTaW and MnMoNbTaW films. For the Young's modulus a value of 295 GPa was obtained for the MnMoNbTaW film, which is the highest value of all films studied within this thesis. For MoNbTaWZr, a deposition parameter study (duty-cycle, Ar pressure and pulse frequency) was performed, to investigate the influence of those parameters on the film microstructure. Depending on the deposition parameters, films can either be crystalline, partly amorphous or fully amorphous. Film growth parameter sets yielding high particle energies enable to deposit dense amorphous films, whereas low particle energies lead to crystalline microstructure.

The bcc phase of MoNbTaTiW, MoNbTaVW and CrMoNbTaW films remains stable up to 1200 °C when annealed in vacuum. Stress relaxation covers a low temperature regime up to about 400 °C and a high temperature regime, which starts between 800 and 1000 °C, depending on the HEA film. While for the MoNbTaTiW and MoNbTaVW films severe grain growth was observed after annealing at 1200 °C, the grain growth was less pronounced in the case of the CrMoNbTaW film.

In a last step, six different MoNbTaW and (MoNbTaW)N based alloys were evaluated for their suitability to serve as diffusion barriers. The nitride films showed a significantly higher failure temperature compared to the metal films. While all metal films show after annealing at 700 °C at least small fractions of Cu_3Si, after annealing at 800 °C of the nitride films no Cu_3Si was observed, independent of the HEA nitride film. The barrier failure mechanism of the HEA nitride films depends strongly on the formation enthalpy of the nitride of the fifth element (Ti, V, Cr, Mn, Zr or Hf). For those barriers with a fifth alloying element with a high nitride formation enthalpy, hardly any Cu_3Si formation occurs, even after annealing at 950 °C; however, dewetting of the Cu layer starts at 900 °C. For the other HEA nitride barriers, Cu_3Si formation was observed after annealing at 850 °C. For the HEA metal barrier films, the barrier failure temperature depends on the mixing enthalpy of the elements within the diffusion barrier and Cu. If

the mixing enthalpy of one element with Cu is negative, the barrier failure temperature decreases. It is expected that this element tends to diffuse into the Cu film, leaving defects within the diffusion barrier, which triggers the barrier failure. From the results of the diffusion barrier investigations, one rule each can be derived for metal and nitride HEA diffusion barriers, i.e. for metals **“The mixing enthalpy between Cu and all elements within the HEA diffusion barrier should be positive”** as stated in publication IV of this thesis and for nitrides **“The nitride formation enthalpy of all elements within the HEA diffusion barrier, should be as high as possible”** as stated in publication V of this thesis.

In summary, this work not only represents a first step towards the development of MoNbTaW based diffusion barriers, but also provides rules which can be used for the development of new HEA diffusion barriers. In addition, the knowledge about MoNbTaW films was expanded, which can also be important for the further development of the HEA films for other applications

7 REFERENCES

[1] J.-W. Yeh, S.-K. Chen, S.-J. Lin, J.-Y. Gan, T.-S. Chin, T.-T. Shun, C.-H. Tsau, S.-Y. Chang, Nanostructured High-Entropy Alloys with Multiple Principal Elements: Novel Alloy Design Concepts and Outcomes, Advanced Engineering Materials 6 (2004) 299–303. https://doi.org/10.1002/adem.200300578.

[2] B. Cantor, I. Chang, P. Knight, A. Vincent, Microstructural development in equiatomic multicomponent alloys, Materials Science and Engineering: A 375-377 (2004) 213–218. https://doi.org/10.1016/j.msea.2003.10.257.

[3] B.S. Murty, J.-W. Yeh, S. Ranganathan, High-entropy alloys, Butterworth-Heinemann an imprint of Elsevier, London, Oxford, Amsterdam, San Diego, 2014.

[4] O.N. Senkov, G.B. Wilks, D.B. Miracle, C.P. Chuang, P.K. Liaw, Refractory high-entropy alloys, Intermetallics 18 (2010) 1758–1765. https://doi.org/10.1016/j.intermet.2010.05.014.

[5] O.N. Senkov, G.B. Wilks, J.M. Scott, D.B. Miracle, Mechanical properties of Nb25Mo25Ta25W25 and V20Nb20Mo20Ta20W20 refractory high entropy alloys, Intermetallics 19 (2011) 698–706. https://doi.org/10.1016/j.intermet.2011.01.004.

[6] Z.D. Han, N. Chen, S.F. Zhao, L.W. Fan, G.N. Yang, Y. Shao, K.F. Yao, Effect of Ti additions on mechanical properties of NbMoTaW and VNbMoTaW refractory high entropy alloys, Intermetallics 84 (2017) 153–157. https://doi.org/10.1016/j.intermet.2017.01.007.

[7] Z.D. Han, H.W. Luan, X. Liu, N. Chen, X.Y. Li, Y. Shao, K.F. Yao, Microstructures and mechanical properties of Ti NbMoTaW refractory high-entropy alloys, Materials Science and Engineering: A 712 (2018) 380–385. https://doi.org/10.1016/j.msea.2017.12.004.

[8] Y. Tong, L. Bai, X. Liang, Y. Chen, Z. Zhang, J. Liu, Y. Li, Y. Hu, Influence of alloying elements on mechanical and electronic properties of NbMoTaWX (X = Cr, Zr, V, Hf and Re) refractory high entropy alloys, Intermetallics 126 (2020) 106928. https://doi.org/10.1016/j.intermet.2020.106928.

[9] S.H. Chen, J.S. Zhang, S. Guan, T. Li, J.Q. Liu, F.F. Wu, Y.C. Wu, Microstructure and mechanical properties of WNbMoTaZrx (x = 0.1, 0.3, 0.5, 1.0) refractory high entropy alloys, Materials Science and Engineering: A 835 (2022) 142701. https://doi.org/10.1016/j.msea.2022.142701.

[10] M. Xia, Y. Chen, K. Chen, Y. Tong, X. Liang, B. Shen, Synthesis of WTaMoNbZr refractory high-entropy alloy powder by plasma spheroidization process for additive manufacturing, Journal of Alloys and Compounds 917 (2022) 165501. https://doi.org/10.1016/j.jallcom.2022.165501.

[11] T.-K. Chen, M.-S. Wong, T.-T. Shun, J.-W. Yeh, Nanostructured nitride films of multi-element high-entropy alloys by reactive DC sputtering, Surface and Coatings Technology 200 (2005) 1361–1365. https://doi.org/10.1016/j.surfcoat.2005.08.081.

[12] M.C. Gao, J.-W. Yeh, P.K. Liaw, Y. Zhang, High-Entropy Alloys, Springer International Publishing, Cham, 2016.

[13] A. Xia, A. Togni, S. Hirn, G. Bolelli, L. Lusvarghi, R. Franz, Angular-dependent deposition of MoNbTaVW HEA thin films by three different physical vapor deposition methods, Surface and Coatings Technology 385 (2020) 125356. https://doi.org/10.1016/j.surfcoat.2020.125356.

[14] N.I. Muhammad Nadzri, D.S.C. Halin, M.M. Al Bakri Abdullah, S. Joseph, M.A.A. Mohd Salleh, P. Vizureanu, D.-P. Burduhos-Nergis, A.V. Sandu, High-Entropy Alloy for Thin Film Application: A Review, Coatings 12 (2022) 1842. https://doi.org/10.3390/coatings12121842.

[15] A. Xia, R. Dedoncker, O. Glushko, M.J. Cordill, D. Depla, R. Franz, Influence of the nitrogen content on the structure and properties of MoNbTaVW high entropy alloy thin films, Journal of Alloys and Compounds 850 (2021) 156740. https://doi.org/10.1016/j.jallcom.2020.156740.

[16] S.-Y. Chang, C.-E. Li, Y.-C. Huang, H.-F. Hsu, J.-W. Yeh, S.-J. Lin, Structural and thermodynamic factors of suppressed interdiffusion kinetics in multi-component high-entropy materials, Sci. Rep. 4 (2014) 4162. https://doi.org/10.1038/srep04162.

[17] D. Gupta, Diffusion processes in advanced technological materials, William Andrew Pub, Norwich N.Y., 2005.

[18] S.-Y. Chang, C.-E. Li, S.-C. Chiang, Y.-C. Huang, 4-nm thick multilayer structure of multi-component (AlCrRuTaTiZr)N as robust diffusion barrier for Cu interconnects, Journal of Alloys and Compounds 515 (2012) 4–7. https://doi.org/10.1016/j.jallcom.2011.11.082.

[19] S.-Y. Chang, C.-Y. Wang, M.-K. Chen, C.-E. Li, Ru incorporation on marked enhancement of diffusion resistance of multi-component alloy barrier layers, Journal of Alloys and Compounds 509 (2011) L85-L89. https://doi.org/10.1016/j.jallcom.2010.11.124.

[20] S.-Y. Chang, C.-Y. Wang, C.-E. Li, Y.-C. Huang, 5 nm-Thick $(AlCrTaTiZrRu)N_{0.5}$ Multi-Component Barrier Layer with High Diffusion Resistance for Cu Interconnects, Nanosci Nanotechnol Lett 3 (2011) 289–293. https://doi.org/10.1166/nnl.2011.1155.

[21] D.-S. Chen, M.-K. Chen, S.-Y. Chang, Multiprincipal-Element AlCrTaTiZr-Nitride Nanocomposite Film of Extremely High Thermal Stability as Diffusion Barrier for Cu Metallization, ECS Trans. 19 (2009) 751–762. https://doi.org/10.1149/1.3122130.

[22] R. Li, T. Chen, C. Jiang, J. Zhang, Y. Zhang, P.K. Liaw, Applications of High Diffusion Resistance Multi-component AlCrTaTiZrRu/(AlCrTaTiZrRu)N 0.7 Film in Cu Interconnects, Adv. Eng. Mater. 22 (2020) 2000557. https://doi.org/10.1002/adem.202000557.

[23] R. Li, M. Li, C. Jiang, B. Qiao, W. Zhang, J. Xu, Thermal stability of AlCrTaTiZrMo-nitride high entropy film as a diffusion barrier for Cu metallization, Journal of Alloys and Compounds 773 (2019) 482–489. https://doi.org/10.1016/j.jallcom.2018.09.283.

[24] R. Li, B. Qiao, H. Shang, J. Zhang, C. Jiang, W. Zhang, Multi-component AlCrTaTiZrMo-nitride film with high diffusion resistance in copper metallization, Journal of Alloys and Compounds 748 (2018) 258–264. https://doi.org/10.1016/j.jallcom.2018.03.084.

[25] C. Jiang, R. Li, X. Wang, H. Shang, Y. Zhang, P.K. Liaw, Diffusion Barrier Performance of AlCrTaTiZr/AlCrTaTiZr-N High-Entropy Alloy Films for Cu/Si Connect System, Entropy (Basel) 22 (2020). https://doi.org/10.3390/e22020234.

[26] A. Xia, R. Franz, Thermal Stability of MoNbTaVW High Entropy Alloy Thin Films, Coatings 10 (2020) 941. https://doi.org/10.3390/coatings10100941.

[27] K. Hu, Q.F. Hu, X. Xu, S.H. Chen, J. Ma, W.W. Dong, Excellent diffusion barrier property of amorphous NbMoTaW medium entropy alloy thin films used in Cu/Si Connect System, Vacuum 202 (2022) 111195. https://doi.org/10.1016/j.vacuum.2022.111195.

[28] P.F. Li, Y.J. Ma, H. Ma, S.W. Ta, Z. Yang, X.T. Han, M.J. Kai, J.H. Chen, Z.H. Cao, Enhanced diffusion barrier property of nanolayered NbMoTaW/TiVCr high entropy alloy for copper metallization, Journal of Alloys and Compounds 895 (2022) 162574. https://doi.org/10.1016/j.jallcom.2021.162574.

[29] Y.-T. Hsiao, C.-H. Tung, S.-J. Lin, J.-W. Yeh, S.-Y. Chang, Thermodynamic route for self-forming 1.5 nm V-Nb-Mo-Ta-W high-entropy alloy barrier layer: Roles of enthalpy and mixing entropy, Acta Materialia 199 (2020) 107–115. https://doi.org/10.1016/j.actamat.2020.08.029.

[30] J. Yan, Y.Z. Lin, Y. Wang, J. Qiu, F. Wan, C. Song, Refractory WMoNbVTa high-entropy alloy as a diffusion barrier between a molybdenum substrate and MoSi2 ceramic coating, Ceramics International 48 (2022) 11410–11418. https://doi.org/10.1016/j.ceramint.2021.12.364.

[31] M. Ohring, The Materials Science of Thin Films.

[32] VII. On the electro-chemical polarity of gases, Phil. Trans. R. Soc. 142 (1852) 87–101. https://doi.org/10.1098/rstl.1852.0008.

[33] X. The Bakerian Lecture. —Experimental relations of gold (and other metals) to light, Phil. Trans. R. Soc. 147 (1857) 145–181. https://doi.org/10.1098/rstl.1857.0011.

[34] D.M. Mattox, Handbook of physical vapor deposition (PVD) processing, second. ed., William Andrew; Elsevier William Andrew, Oxford, Amsterdam, Heidelberg, 2010.

[35] J.T. Gudmundsson, D. Lundin, Introduction to magnetron sputtering, in: High Power Impulse Magnetron Sputtering, Elsevier, 2020, pp. 1–48.

[36] K.S.S. Harsha, Principles of Vapor Deposition of Thin Films, firstst ed., Elsevier, Burlington, 2006.

[37] R.K. Waits, Planar magnetron sputtering, Journal of Vacuum Science and Technology 15 (1978) 179–187. https://doi.org/10.1116/1.569451.

[38] B. Window, N. Savvides, Charged particle fluxes from planar magnetron sputtering sources, Journal of Vacuum Science & Technology A: Vacuum, Surfaces, and Films 4 (1986) 196–202. https://doi.org/10.1116/1.573470.

[39] A.E. Wendt, M.A. Lieberman, Spatial structure of a planar magnetron discharge, Journal of Vacuum Science & Technology A: Vacuum, Surfaces, and Films 8 (1990) 902–907. https://doi.org/10.1116/1.576894.

[40] A.A. Solov'ev, N.S. Sochugov, K.V. Oskomov, S.V. Rabotkin, Investigation of plasma characteristics in an unbalanced magnetron sputtering system, Plasma Phys. Rep. 35 (2009) 399–408. https://doi.org/10.1134/S1063780X09050055.

[41] B. Window, N. Savvides, Unbalanced dc magnetrons as sources of high ion fluxes, Journal of Vacuum Science & Technology A: Vacuum, Surfaces, and Films 4 (1986) 453–456. https://doi.org/10.1116/1.573904.

[42] V. Kouznetsov, K. Macák, J.M. Schneider, U. Helmersson, I. Petrov, A novel pulsed magnetron sputter technique utilizing very high target power densities, Surface and Coatings Technology 122 (1999) 290–293. https://doi.org/10.1016/S0257-8972(99)00292-3.

[43] K. Macák, V. Kouznetsov, J. Schneider, U. Helmersson, I. Petrov, Ionized sputter deposition using an extremely high plasma density pulsed magnetron discharge, Journal of Vacuum Science & Technology A: Vacuum, Surfaces, and Films 18 (2000) 1533–1537. https://doi.org/10.1116/1.582380.

[44] A. Anders, Discharge physics of high power impulse magnetron sputtering, Surface and Coatings Technology 205 (2011) S1-S9. https://doi.org/10.1016/j.surfcoat.2011.03.081.

[45] J.T. Gudmundsson, J. Alami, U. Helmersson, Evolution of the electron energy distribution and plasma parameters in a pulsed magnetron discharge, Appl. Phys. Lett. 78 (2001) 3427–3429. https://doi.org/10.1063/1.1376150.

[46] J.T. Gudmundsson, J. Alami, U. Helmersson, Spatial and temporal behavior of the plasma parameters in a pulsed magnetron discharge, Surface and Coatings Technology 161 (2002) 249–256. https://doi.org/10.1016/S0257-8972(02)00518-2.

[47] J.T. Gudmundsson, The high power impulse magnetron sputtering discharge as an ionized physical vapor deposition tool, Vacuum 84 (2010) 1360–1364. https://doi.org/10.1016/j.vacuum.2009.12.022.

[48] D. Lundin, A. Hecimovic, T. Minea, A. Anders, N. Brenning, J.T. Gudmundsson, Physics of high power impulse magnetron sputtering discharges, in: High Power Impulse Magnetron Sputtering, Elsevier, 2020, pp. 265–332.

[49] N. Brenning, J.T. Gudmundsson, M.A. Raadu, T.J. Petty, T. Minea, D. Lundin, A unified treatment of self-sputtering, process gas recycling, and runaway for high power impulse sputtering magnetrons, Plasma Sources Sci. Technol. 26 (2017) 125003. https://doi.org/10.1088/1361-6595/aa959b.

[50] J.T. Gudmundsson, N. Brenning, D. Lundin, U. Helmersson, High power impulse magnetron sputtering discharge, Journal of Vacuum Science & Technology A: Vacuum, Surfaces, and Films 30 (2012) 30801. https://doi.org/10.1116/1.3691832.

[51] C. Huo, D. Lundin, M.A. Raadu, A. Anders, J.T. Gudmundsson, N. Brenning, On the road to self-sputtering in high power impulse magnetron sputtering: particle balance and discharge characteristics, Plasma Sources Science and Technology 23 (2014) 25017. https://doi.org/10.1088/0963-0252/23/2/025017.

[52] C. Huo, D. Lundin, J.T. Gudmundsson, M.A. Raadu, J.W. Bradley, N. Brenning, Particle-balance models for pulsed sputtering magnetrons, J. Phys. D: Appl. Phys. 50 (2017) 354003. https://doi.org/10.1088/1361-6463/aa7d35.

[53] D. Lundin, N. Brenning, D. Jädernäs, P. Larsson, E. Wallin, M. Lattemann, M.A. Raadu, U. Helmersson, Transition between the discharge regimes of high power impulse magnetron sputtering and conventional direct current magnetron sputtering, Plasma Sources Sci. Technol. 18 (2009) 45008. https://doi.org/10.1088/0963-0252/18/4/045008.

[54] A. Anders, J. Andersson, A. Ehiasarian, High power impulse magnetron sputtering: Current-voltage-time characteristics indicate the onset of sustained self-sputtering, Journal of Applied Physics 102 (2007) 113303. https://doi.org/10.1063/1.2817812.

[55] A. Anders, Self-sputtering runaway in high power impulse magnetron sputtering: The role of secondary electrons and multiply charged metal ions, Appl. Phys. Lett. 92 (2008) 201501. https://doi.org/10.1063/1.2936307.

[56] M. Hala, N. Viau, O. Zabeida, J.E. Klemberg-Sapieha, L. Martinu, Dynamics of reactive high-power impulse magnetron sputtering discharge studied by time- and space-resolved optical emission spectroscopy and fast imaging, Journal of Applied Physics 107 (2010) 43305. https://doi.org/10.1063/1.3305319.

[57] A. Hecimovic, A.P. Ehiasarian, Temporal Evolution of the Ion Fluxes for Various Elements in HIPIMS Plasma Discharge, IEEE Transactions on Plasma Science 39 (2011) 1154–1164. https://doi.org/10.1109/TPS.2011.2106516.

[58] G.Y. Yushkov, A. Anders, Origin of the Delayed Current Onset in High-Power Impulse Magnetron Sputtering, IEEE Transactions on Plasma Science 38 (2010) 3028–3034. https://doi.org/10.1109/TPS.2010.2063041.

[59] P. Poolcharuansin, B. Liebig, J. Bradley, Plasma Parameters in a Pre-Ionized HiPIMS Discharge Operating at Low Pressure, IEEE Transactions on Plasma Science 38 (2010) 3007–3015. https://doi.org/10.1109/TPS.2010.2069572.

[60] C. Vitelaru, D. Lundin, G.D. Stancu, N. Brenning, J. Bretagne, T. Minea, Argon metastables in HiPIMS: time-resolved tunable diode-laser diagnostics, Plasma Sources Sci. Technol. 21 (2012) 25010. https://doi.org/10.1088/0963-0252/21/2/025010.

[61] P. Poolcharuansin, J.W. Bradley, Short- and long-term plasma phenomena in a HiPIMS discharge, Plasma Sources Sci. Technol. 19 (2010) 25010. https://doi.org/10.1088/0963-0252/19/2/025010.

[62] G.D. Stancu, N. Brenning, C. Vitelaru, D. Lundin, T. Minea, Argon metastables in HiPIMS: validation of the ionization region model by direct comparison to time resolved tunable diode-laser diagnostics, Plasma Sources Sci. Technol. 24 (2015) 45011. https://doi.org/10.1088/0963-0252/24/4/045011.

[63] D. Lundin, S.A. Sahab, N. Brenning, C. Huo, U. Helmersson, Internal current measurements in high power impulse magnetron sputtering, Plasma Sources Sci. Technol. 20 (2011) 45003. https://doi.org/10.1088/0963-0252/20/4/045003.

[64] C. Huo, M.A. Raadu, D. Lundin, J.T. Gudmundsson, A. Anders, N. Brenning, Gas rarefaction and the time evolution of long high-power impulse magnetron sputtering pulses, Plasma Sources Sci. Technol. 21 (2012) 45004. https://doi.org/10.1088/0963-0252/21/4/045004.

[65] M. Čada, N. Britun, A. Hecimovic, J.T. Gudmundsson, D. Lundin, Heavy species dynamics in high power impulse magnetron sputtering discharges, in: High Power Impulse Magnetron Sputtering, Elsevier, 2020, pp. 111–158.

[66] D.W. Hoffman, A sputtering wind, Journal of Vacuum Science & Technology A: Vacuum, Surfaces, and Films 3 (1985) 561–566. https://doi.org/10.1116/1.572994.

[67] M.A. Raadu, I. Axnäs, J.T. Gudmundsson, C. Huo, N. Brenning, An ionization region model for high-power impulse magnetron sputtering discharges, Plasma Sources Sci. Technol. 20 (2011) 65007. https://doi.org/10.1088/0963-0252/20/6/065007.

[68] J. Bohlmark, M. Lattemann, J.T. Gudmundsson, A.P. Ehiasarian, Y. Aranda Gonzalvo, N. Brenning, U. Helmersson, The ion energy distributions and ion flux composition from a high power impulse magnetron sputtering discharge, Thin Solid Films 515 (2006) 1522–1526. https://doi.org/10.1016/j.tsf.2006.04.051.

[69] A. Kanitz, A. Hecimovic, M. Böke, J. Winter, Two dimensional spatial Argon metastable dynamics in HiPIMS discharges, J. Phys. D: Appl. Phys. 49 (2016) 125203. https://doi.org/10.1088/0022-3727/49/12/125203.

[70] K. Burcalova, A. Hecimovic, A.P. Ehiasarian, Ion energy distributions and efficiency of sputtering process in HIPIMS system, J. Phys. D: Appl. Phys. 41 (2008) 115306. https://doi.org/10.1088/0022-3727/41/11/115306.

[71] S. Kadlec, C. Quaeyhaegens, G. Knuyt, L.M. Stals, Energy distribution of ions in an unbalanced magnetron plasma measured with energy-resolved mass spectrometry, Surface and Coatings Technology 89 (1997) 177–184. https://doi.org/10.1016/S0257-8972(96)03088-5.

[72] A.P. Ehiasarian, A. Vetushka, A. Hecimovic, S. Konstantinidis, Ion composition produced by high power impulse magnetron sputtering discharges near the substrate, Journal of Applied Physics 104 (2008) 83305. https://doi.org/10.1063/1.3000446.

[73] A. Hecimovic, K. Burcalova, A.P. Ehiasarian, Origins of ion energy distribution function (IEDF) in high power impulse magnetron sputtering (HIPIMS) plasma discharge, J. Phys. D: Appl. Phys. 41 (2008) 95203. https://doi.org/10.1088/0022-3727/41/9/095203.

[74] A.V. Kozyrev, N.S. Sochugov, K.V. Oskomov, A.N. Zakharov, A.N. Odivanova, Optical studies of plasma inhomogeneities in a high-current pulsed magnetron discharge, Plasma Phys. Rep. 37 (2011) 621–627. https://doi.org/10.1134/S1063780X11060122.

[75] M. Panjan, A. Anders, Plasma potential of a moving ionization zone in DC magnetron sputtering, Journal of Applied Physics 121 (2017) 63302. https://doi.org/10.1063/1.4974944.

[76] C. Maszl, W. Breilmann, J. Benedikt, A. von Keudell, Origin of the energetic ions at the substrate generated during high power pulsed magnetron sputtering of titanium, J. Phys. D: Appl. Phys. 47 (2014) 224002. https://doi.org/10.1088/0022-3727/47/22/224002.

[77] Y. Yang, K. Tanaka, J. Liu, A. Anders, Ion energies in high power impulse magnetron sputtering with and without localized ionization zones, Appl. Phys. Lett. 106 (2015) 124102. https://doi.org/10.1063/1.4916233.

[78] M. Panjan, R. Franz, A. Anders, Asymmetric particle fluxes from drifting ionization zones in sputtering magnetrons, Plasma Sources Sci. Technol. 23 (2014) 25007. https://doi.org/10.1088/0963-0252/23/2/025007.

[79] J. Hopwood, Ionized physical vapor deposition of integrated circuit interconnects, Physics of Plasmas 5 (1998) 1624–1631. https://doi.org/10.1063/1.872829.

[80] D.J. Christie, Target material pathways model for high power pulsed magnetron sputtering, Journal of Vacuum Science & Technology A: Vacuum, Surfaces, and Films 23 (2005) 330–335. https://doi.org/10.1116/1.1865133.

[81] D. Lundin, M. Čada, Z. Hubička, Ionization of sputtered Ti, Al, and C coupled with plasma characterization in HiPIMS, Plasma Sources Sci. Technol. 24 (2015) 35018. https://doi.org/10.1088/0963-0252/24/3/035018.

[82] T. Kubart, M. Čada, D. Lundin, Z. Hubička, Investigation of ionized metal flux fraction in HiPIMS discharges with Ti and Ni targets, Surface and Coatings Technology 238 (2014) 152–157. https://doi.org/10.1016/j.surfcoat.2013.10.064.

[83] M. Samuelsson, D. Lundin, J. Jensen, M.A. Raadu, J.T. Gudmundsson, U. Helmersson, On the film density using high power impulse magnetron sputtering, Surface and Coatings Technology 205 (2010) 591–596. https://doi.org/10.1016/j.surfcoat.2010.07.041.

[84] J. Emmerlich, S. Mráz, R. Snyders, K. Jiang, J.M. Schneider, The physical reason for the apparently low deposition rate during high-power pulsed magnetron sputtering, Vacuum 82 (2008) 867–870. https://doi.org/10.1016/j.vacuum.2007.10.011.

[85] A. Anders, Deposition rates of high power impulse magnetron sputtering: Physics and economics, Journal of Vacuum Science & Technology A: Vacuum, Surfaces, and Films 28 (2010) 783–790. https://doi.org/10.1116/1.3299267.

[86] S. Konstantinidis, J.P. Dauchot, M. Ganciu, A. Ricard, M. Hecq, Influence of pulse duration on the plasma characteristics in high-power pulsed magnetron discharges, Journal of Applied Physics 99 (2006) 13307. https://doi.org/10.1063/1.2159555.

[87] A. Mishra, P.J. Kelly, J.W. Bradley, The evolution of the plasma potential in a HiPIMS discharge and its relationship to deposition rate, Plasma Sources Sci. Technol. 19 (2010) 45014. https://doi.org/10.1088/0963-0252/19/4/045014.

[88] J.W. Bradley, A. Mishra, P.J. Kelly, The effect of changing the magnetic field strength on HiPIMS deposition rates, J. Phys. D: Appl. Phys. 48 (2015) 215202. https://doi.org/10.1088/0022-3727/48/21/215202.

[89] U. Helmersson, M. Lattemann, J. Bohlmark, A.P. Ehiasarian, J.T. Gudmundsson, Ionized physical vapor deposition (IPVD): A review of technology and applications, Thin Solid Films 513 (2006) 1–24. https://doi.org/10.1016/j.tsf.2006.03.033.

[90] K. Sarakinos, L. Martinu, Synthesis of thin films and coatings by high power impulse magnetron sputtering, in: High Power Impulse Magnetron Sputtering, Elsevier, 2020, pp. 333–374.

[91] I. Petrov, P.B. Barna, L. Hultman, J.E. Greene, Microstructural evolution during film growth, Journal of Vacuum Science & Technology A: Vacuum, Surfaces, and Films 21 (2003) S117-S128. https://doi.org/10.1116/1.1601610.

[92] J. Alami, P.O.Å. Persson, D. Music, J.T. Gudmundsson, J. Bohlmark, U. Helmersson, Ion-assisted physical vapor deposition for enhanced film properties on nonflat surfaces, Journal of Vacuum Science & Technology A: Vacuum, Surfaces, and Films 23 (2005) 278–280. https://doi.org/10.1116/1.1861049.

[93] J. Frenkel, Theorie der Adsorption und verwandter Erscheinungen, Z. Physik 26 (1924) 117–138. https://doi.org/10.1007/BF01327320.

[94] G. Zinsmeister, A contribution to Frenkel's theory of condensation, Vacuum 16 (1966) 529–535. https://doi.org/10.1016/0042-207X(66)90349-6.

[95] Y.A. Kryukov, J.G. Amar, Scaling of the island density and island-size distribution in irreversible submonolayer growth of three-dimensional islands, Phys. Rev. B 81 (2010) 165435. https://doi.org/10.1103/PhysRevB.81.165435.

[96] Iris Pilch, Kostas Sarakinos, Pulsed Plasmas: Nanoparticles and Thin Film Synthesis, in: J.L. Shohet (Ed.), Encyclopedia of plasma technology, CRC Press, Boca Raton, 2017, pp. 1201–1215.

[97] K. Sarakinos, D. Magnfält, V. Elofsson, B. Lü, Atomistic view on thin film nucleation and growth by using highly ionized and pulsed vapour fluxes, Surface and Coatings Technology 257 (2014) 326–332. https://doi.org/10.1016/j.surfcoat.2014.04.015.

[98] W. Ensinger, Low energy ion assist during deposition — an effective tool for controlling thin film microstructure, Nuclear Instruments and Methods in Physics Research Section B: Beam Interactions with Materials and Atoms 127-128 (1997) 796–808. https://doi.org/10.1016/S0168-583X(97)00010-4.

[99] R. Daniel, K.J. Martinschitz, J. Keckes, C. Mitterer, The origin of stresses in magnetron-sputtered thin films with zone T structures, Acta Materialia 58 (2010) 2621–2633. https://doi.org/10.1016/j.actamat.2009.12.048.

[100] PII: 0040-6090(76)90453-3.

[101] I.C. Noyan, J.B. Cohen, Residual Stress: Measurement by Diffraction and Interpretation, Springer New York; Imprint; Springer, New York, NY, 1987.

[102] E. Zolotoyabko, Basic concepts of crystallography: An outcome from crystal symmetry, Wiley-VCH, Weinheim Germany, 2011.

[103] M. Lee, X-ray diffraction for materials research: From fundamentals to applications, Apple Academic Press; Exclusive worldwide distribution by CRC Press Taylor & Francis Group, Oakville ON Canada, Waretown NJ USA, New York, 2016.

[104] Q. Luo, S. Yang, Uncertainty of the X-ray Diffraction (XRD) sin2 ψ Technique in Measuring Residual Stresses of Physical Vapor Deposition (PVD) Hard Coatings, Coatings 7 (2017) 128. https://doi.org/10.3390/coatings7080128.

[105] J.-W. Yeh, Alloy Design Strategies and Future Trends in High-Entropy Alloys, JOM 65 (2013) 1759–1771. https://doi.org/10.1007/s11837-013-0761-6.

[106] B. Fultz, Vibrational thermodynamics of materials, Progress in Materials Science 55 (2010) 247–352. https://doi.org/10.1016/j.pmatsci.2009.05.002.

[107] J.-W. Yeh, S.-Y. Chang, Y.-D. Hong, S.-K. Chen, S.-J. Lin, Anomalous decrease in X-ray diffraction intensities of Cu–Ni–Al–Co–Cr–Fe–Si alloy systems with multi-principal elements, Materials Chemistry and Physics 103 (2007) 41–46. https://doi.org/10.1016/j.matchemphys.2007.01.003.

[108] K.-Y. Tsai, M.-H. Tsai, J.-W. Yeh, Sluggish diffusion in Co–Cr–Fe–Mn–Ni high-entropy alloys, Acta Materialia 61 (2013) 4887–4897. https://doi.org/10.1016/j.actamat.2013.04.058.

[109] Y.-F. Kao, S.-K. Chen, T.-J. Chen, P.-C. Chu, J.-W. Yeh, S.-J. Lin, Electrical, magnetic, and Hall properties of AlxCoCrFeNi high-entropy alloys, Journal of Alloys and Compounds 509 (2011) 1607–1614. https://doi.org/10.1016/j.jallcom.2010.10.210.

[110] S. Ranganathan, Alloyed pleasures: Multimetallic cocktails (2003).

[111] N.I. Medvedeva, Y.N. Gornostyrev, A.J. Freeman, Solid solution softening and hardening in the group-V and group-VI bcc transition metals alloys: First principles calculations and atomistic modeling, Phys. Rev. B 76 (2007). https://doi.org/10.1103/PhysRevB.76.212104.

[112] T. Jörg, D. Music, F. Hauser, M.J. Cordill, R. Franz, H. Köstenbauer, J. Winkler, J.M. Schneider, C. Mitterer, Deformation behavior of Re alloyed Mo thin films on flexible substrates: In situ fragmentation analysis supported by first-principles calculations, Sci Rep 7 (2017) 7374. https://doi.org/10.1038/s41598-017-07825-1.

[113] X. Liu, J. Zhang, J. Yin, S. Bi, M. Eisenbach, Y. Wang, Monte Carlo simulation of order-disorder transition in refractory high entropy alloys: A data-driven approach, Computational Materials Science 187 (2021) 110135. https://doi.org/10.1016/j.commatsci.2020.110135.

[114] J. Zhang, Y. Hu, Q. Wei, Y. Xiao, P. Chen, G. Luo, Q. Shen, Microstructure and mechanical properties of RexNbMoTaW high-entropy alloys prepared by arc melting using metal powders, Journal of Alloys and Compounds 827 (2020) 154301. https://doi.org/10.1016/j.jallcom.2020.154301.

[115] X. Feng, J. Utama Surjadi, Y. Lu, Annealing-induced abnormal hardening in nanocrystalline NbMoTaW high-entropy alloy thin films, Materials Letters 275 (2020) 128097. https://doi.org/10.1016/j.matlet.2020.128097.

[116] Y.-Y. Chen, S.-B. Hung, C.-J. Wang, W.-C. Wei, J.-W. Lee, High temperature electrical properties and oxidation resistance of V-Nb-Mo-Ta-W high entropy alloy thin films, Surface and Coatings Technology 375 (2019) 854–863. https://doi.org/10.1016/j.surfcoat.2019.07.080.

[117] L. Bi, X. Li, Y. Hu, J. Zhang, X. Wang, X. Cai, T. Shen, R. Liu, Q. Wang, C. Dong, P.K. Liaw, Weak enthalpy-interaction-element-modulated NbMoTaW high-entropy alloy thin films, Applied Surface Science 565 (2021) 150462. https://doi.org/10.1016/j.apsusc.2021.150462.

[118] M.-A. Nicolet, Diffusion barriers in thin films, Thin Solid Films 52 (1978) 415–443. https://doi.org/10.1016/0040-6090(78)90184-0.

[119] Dang R.L.M., Shigyo N., Coupling Capacitances for Two-Dimensonal Wires, IEEE Electron Device Letters (1981) 196–197.

[120] IEEE, Proceedings of the IEEE 1998 International Interconnect Technology Conference, Hyatt Regency Hotel, San Francisco, CA, June 1-3,1998, IEEE, Piscataway New Jersey, 1998.

[121] P.C. Andricacos, Copper On-Chip Interconnections: A Breakthrough in Electrodeposition to Make Better Chips, Electrochem. Soc. Interface 8 (1999) 32–37. https://doi.org/10.1149/2.F06991IF.

[122] H. Ono, T. Nakano, T. Ohta, Diffusion barrier effects of transition metals for Cu/M/Si multilayers (M=Cr, Ti, Nb, Mo, Ta, W), Appl. Phys. Lett. 64 (1994) 1511–1513. https://doi.org/10.1063/1.111875.

[123] J. Li, J.W. Strane, S.W. Russell, S.Q. Hong, J.W. Mayer, T.K. Marais, C.C. Theron, R. Pretorius, Observation and prediction of first phase formation in binary Cu-metal thin films, Journal of Applied Physics 72 (1992) 2810–2816. https://doi.org/10.1063/1.351533.

[124] Q. Wang, Z. Fan, S. Liang, Thermal stability of nanocrystalline W-Ti diffusion barrier thin films, Sci. China Technol. Sci. 53 (2010) 1049–1055. https://doi.org/10.1007/s11431-009-0402-z.

[125] M. Fugger, M. Plappert, C. Schäffer, O. Humbel, H. Hutter, H. Danninger, M. Nowottnick, Comparison of WTi and WTi(N) as diffusion barriers for Al and Cu metallization on Si with respect to thermal stability and diffusion behavior of Ti, Microelectronics Reliability 54 (2014) 2487–2493. https://doi.org/10.1016/j.microrel.2014.04.016.

[126] I. Souli, V.L. Terziyska, J. Keckes, W. Robl, J. Zechner, C. Mitterer, Effect of growth conditions on interface stability and thermophysical properties of sputtered Cu films on Si with and without WTi barrier layers, Journal of Vacuum Science & Technology B, Nanotechnology and Microelectronics: Materials, Processing, Measurement, and Phenomena 35 (2017) 22201. https://doi.org/10.1116/1.4975805.

[127] T. Oku, E. Kawakami, M. Uekubo, K. Takahiro, S. Yamaguchi, M. Murakami, Diffusion barrier property of TaN between Si and Cu, Applied Surface Science 99 (1996) 265–272. https://doi.org/10.1016/0169-4332(96)00464-3.

[128] N. Fréty, F. Bernard, J. Nazon, J. Sarradin, J.C. Tedenac, Copper Diffusion Into Silicon Substrates Through TaN and Ta/TaN Multilayer Barriers, Journal of Phase Equilibria & Diffusion 27 (2006) 590–597. https://doi.org/10.1361/154770306X153602.

[129] A. Gupta, H. Wang, A. Kvit, G. Duscher, J. Narayan, Effect of microstructure on diffusion of copper in TiN films, Journal of Applied Physics 93 (2003) 5210–5214. https://doi.org/10.1063/1.1566472.

[130] M.B. Chamberlain, Diffusion of copper in thin TiN films, Thin Solid Films 91 (1982) 155–162. https://doi.org/10.1016/0040-6090(82)90429-1.

[131] M. Mühlbacher, G. Greczynski, B. Sartory, F. Mendez-Martin, N. Schalk, J. Lu, L. Hultman, C. Mitterer, TiN diffusion barrier failure by the formation of Cu 3 Si investigated by electron microscopy and atom probe tomography, Journal of Vacuum Science & Technology B, Nanotechnology and Microelectronics: Materials, Processing, Measurement, and Phenomena 34 (2016) 22202. https://doi.org/10.1116/1.4942003.

[132] M. Mühlbacher, A.S. Bochkarev, F. Mendez-Martin, B. Sartory, L. Chitu, M.N. Popov, P. Puschnig, J. Spitaler, H. Ding, N. Schalk, J. Lu, L. Hultman, C. Mitterer, Cu diffusion in single-crystal and polycrystalline TiN barrier layers: A high-resolution experimental study supported by first-principles calculations, Journal of Applied Physics 118 (2015) 85307. https://doi.org/10.1063/1.4929446.

[133] H. Aghajani, M.S. Motlagh, Effect of temperature on surface characteristics of nitrogen ion implanted biocompatible titanium, J. Mater. Sci. Mater. Med. 28 (2017) 29. https://doi.org/10.1007/s10856-016-5843-x.

[134] M. Mühlbacher, G. Greczynski, B. Sartory, N. Schalk, J. Lu, I. Petrov, J.E. Greene, L. Hultman, C. Mitterer, Enhanced Ti0.84Ta0.16N diffusion barriers, grown by a hybrid sputtering technique with no substrate heating, between Si(001) wafers and Cu overlayers, Sci. Rep. 8 (2018) 5360. https://doi.org/10.1038/s41598-018-23782-9.

[135] S. Guo, C.T. Liu, Phase stability in high entropy alloys: Formation of solid-solution phase or amorphous phase, Progress in Natural Science: Materials International 21 (2011) 433–446. https://doi.org/10.1016/S1002-0071(12)60080-X.

[136] S. Guo, Q. Hu, C. Ng, C.T. Liu, More than entropy in high-entropy alloys: Forming solid solutions or amorphous phase, Intermetallics 41 (2013) 96–103. https://doi.org/10.1016/j.intermet.2013.05.002.

[137] Y. Zhang, X. Yang, P.K. Liaw, Alloy Design and Properties Optimization of High-Entropy Alloys, JOM 64 (2012) 830–838. https://doi.org/10.1007/s11837-012-0366-5.

[138] S. Guo, C. Ng, J. Lu, C.T. Liu, Effect of valence electron concentration on stability of fcc or bcc phase in high entropy alloys, Journal of Applied Physics 109 (2011) 103505. https://doi.org/10.1063/1.3587228.

[139] M.-H. Tsai, C.-W. Wang, C.-W. Tsai, W.-J. Shen, J.-W. Yeh, J.-Y. Gan, W.-W. Wu, Thermal Stability and Performance of NbSiTaTiZr High-Entropy Alloy Barrier for Copper Metallization, J. Electrochem. Soc. 158 (2011) H1161. https://doi.org/10.1149/2.056111jes.

[140] A. Kretschmer, F. Bohrn, H. Hutter, E. Pitthan, T.T. Tran, D. Primetzhofer, P.H. Mayrhofer, Analysis of (Al,Cr,Nb,Ta,Ti)-nitride and -oxynitride diffusion barriers in Cu-Si interconnects by 3D-Secondary Ion Mass Spectrometry, 2023.

[141] X. Peng, L. Chen, Effect of high entropy alloys TiVCrZrHf barrier layer on microstructure and texture of Cu thin films, Materials Letters 230 (2018) 5–8. https://doi.org/10.1016/j.matlet.2018.07.080.

[142] S.-C. Liang, D.-C. Tsai, Z.-C. Chang, T.-N. Lin, M.-H. Shiao, F.-S. Shieu, Thermally Stable TiVCrZrHf Nitride Films as Diffusion Barriers in Copper Metallization, Electrochem. Solid-State Lett. 15 (2012) H5. https://doi.org/10.1149/2.012201esl.

[143] M.-H. Tsai, J.-W. Yeh, J.-Y. Gan, Diffusion barrier properties of AlMoNbSiTaTiVZr high-entropy alloy layer between copper and silicon, Thin Solid Films 516 (2008) 5527–5530. https://doi.org/10.1016/j.tsf.2007.07.109.

[144] M.-H. Tsai, C.-W. Wang, C.-H. Lai, J.-W. Yeh, J.-Y. Gan, Thermally stable amorphous (AlMoNbSiTaTiVZr)50N50 nitride film as diffusion barrier in copper metallization, Appl. Phys. Lett. 92 (2008) 52109. https://doi.org/10.1063/1.2841810.

8 PUBLICATIONS

8.1 LIST OF INCLUDED PUBLICATIONS

I. **Synthesis and structure of refractory high entropy alloy thin films based on the MoNbTaW system**
Georg C. Gruber, Alice Lassnig, Stanislav Zak, Christoph Gammer, Megan J. Cordill and Robert Franz.
Surface and Coatings Technology 439 (2022) 128446

II. **Tuning microstructure and properties of MoNbTaWZr high entropy alloy films by adjusting the HiPIMS parameters**
Georg C. Gruber, Alice Lassnig, Stefan Wurster, Christoph Gammer, Megan J. Cordill and Robert Franz.
Thin Solid Films (submitted)

III. **Thermal Stability of MoNbTaTiW, MoNbTaVW and CrMoNbTaW thin films deposited by high power impulse magnetron sputtering**
Georg C. Gruber, Alice Lassnig, Stanislav Zak, Christoph Gammer, Megan J. Cordill and Robert Franz.
Surface and Coatings Technology 454 (2023) 129189

IV. **A new design rule for high entropy alloy diffusion barriers for microelectronics**
Georg C. Gruber, Magdalena Kirchmair, Stefan Wurster, Megan J. Cordill and Robert Franz.
Journal of Alloys and Compounds 953 (2023) 170166

V. **Refractory high entropy alloy nitride thin films as diffusion barriers in Cu metallizations**
Georg C. Gruber, Stefan Wurster, Megan J. Cordill and Robert Franz.
Surface and Coatings Technology (under review)

Publication I

Synthesis and structure of refractory high entropy alloy thin films based on the MoNbTaW system

Georg C. Gruber, Alice Lassnig, Stanislav Zak, Christoph Gammer, Megan J. Cordill and Robert Franz

Surface and Coatings Technology 439 (2022) 128446

Synthesis and structure of refractory high entropy alloy thin films based on the MoNbTaW system

Georg C. Gruber[1†*], **Alice Lassnig**[2], **Stanislav Zak**[2], **Christoph Gammer**[2], **Megan J. Cordill**[1,2] **and Robert Franz**[1]

[1]*Department of Materials Science, Montanuniversität Leoben, Franz-Josef-Strasse 18, 8700 Leoben, Austria*

[2]*Erich Schmid Institute of Materials Science, Austrian Academy of Sciences, Jahnstrasse 12, 8700 Leoben, Austria*

[†]*corresponding author (georg.gruber@unileoben.ac.at)*

Keywords:

High Entropy Alloy, Refractory Metal, MoNbTaW, MoNbTaTiW, MoNbTaVW, CrMoNbTaW, MnMoNbTaW, HfMoNbTaW, Thin Film, High Power Impulse Magnetron Sputtering, Nanoindentation

Abstract

To explore structure and properties of refractory high entropy alloy (HEA) thin films, targets with five different equimolar compositions based on the MoNbTaW system and alloyed with Ti, V, Cr, Mn or Hf were used for the synthesis of films by high power impulse magnetron sputtering. All HEA films showed a body-centered cubic structure and a dense, columnar morphology as revealed by X-ray diffraction and transmission electron microscopy, respectively. Alloying of the additional element affects the film stress and the mechanical properties. The overall compressive stress state present in the films was distributed inhomogeneously with an expected gradient along the film growth direction. Hardness and Young's modulus values ranging from 14 to 17 GPa and 230 to 295 GPa, respectively, were measured by nanoindentation.

1 INTRODUCTION

Since their introduction in the early 2000s by Yeh [1] and Cantor [2], the scientific interest for high entropy alloys (HEAs) has been increasing each year. HEAs, which are also known as multi-principal element alloys, multi-component alloys or complex concentrated alloys, are alloys with a configurational entropy of at least $1.5R$ [3], where R is the gas constant. Due to these high entropy values the formation of simple solid solution phases with face-centered cubic, body-centered cubic (bcc) or hexagonal close-packed (hcp) structure is usually preferred over the formation of intermetallic phases [3]. Based on the elements incorporated, different groups of HEAs are typically distinguished [4], where the refractory HEAs, comprising mainly refractory metals, are promising candidates for future high temperature applications due to their high thermal stability. Within the refractory HEAs, MoNbTaVW, introduced by Senkov et al. [5,6], is studied most in literature and known for its good thermal stability and high strength at elevated temperatures, which exceeds the performance of Ni-based superalloys [6]. The addition of Ti instead of V to MoNbTaW leads to a higher ductility of the material, especially at room temperature, with a similar strength and thermal stability [7,8].

Among the different methods used to synthesize HEAs, physical vapor deposition has been employed since the introduction of HEA thin films [9–12]. Most of the research on HEA thin films focused on wear and corrosion protective properties of these films [3]. However, HEA thin films are also potential candidates for future diffusion barriers within microelectronic applications based on their good thermal stability and sluggish diffusion [13,14]. As it was the case for bulk HEAs, as mentioned above, also in the case of thin films the alloy MoNbTaVW is most widely studied, showing a high hardness [9,15] and a good thermal stability [15]. Further, this alloy is also a potential candidate for interconnects of solid oxide fuel cells and coatings for thermoelectric elements due to its high temperature electrical conductivity [16].

MoNbTaVW thin films show quite promising properties and are already studied within literature. Nevertheless, beside this alloy, to the best of the authors knowledge, no other MoNbTaW based thin films are studied within literature. Therefore, within this study, equimolar MoNbTaTiW, MoNbTaVW, CrMoNbTaW, MnMoNbTaW and HfMoNbTaW thin films were deposited using high power impulse magnetron sputtering (HiPIMS). HiPIMS was chosen over conventional DC magnetron sputtering due to the fact that the higher degree of ionization of the sputtered metal atoms in HiPIMS

plasmas enables the deposition of denser coatings [17], a beneficial feature for the intended use of these films as diffusion barriers. The elements were chosen to compare different room temperature crystal structures of the fifth alloying element, Ti and Zr have a hcp microstructure, V and Cr have a bcc microstructure and Mn has an alpha manganese microstructure. The synthesized HEA films were characterized as to their microstructure, residual stress state and mechanical properties to study the influence of the additional element, namely Ti, V, Cr, Mn and Hf, on the base alloy MoNbTaW.

2 METHODS

For the synthesis of the refractory HEA films equimolar MoNbTaTiW, MoNbTaVW, CrMoNbTaW, MnMoNbTaW and HfMoNbTaW targets with a diameter of 76 mm were used, which were manufactured by powder metallurgical methods by Plansee Composite Materials GmbH (Lechbruck, Germany). The films were deposited on polished 325 µm thick B-doped (100) Si substrates (21 mm × 7 mm) and polyvinyl alcohol (PVA) foils (150 mm x 50 mm) using a lab-scale deposition system equipped with an unbalanced magnetron source. The substrates were carefully cleaned with acetone and afterwards ethanol in an ultrasonic bath before deposition and then placed in front of the magnetron source at a distance of 150 mm. Subsequently, the chamber was evacuated to a base pressure of $9 \cdot 10^{-4}$ Pa or below, before Ar was introduced to establish the deposition pressure of 1 Pa. The deposition in high power impulse magnetron sputtering (HiPIMS) mode was carried out with an average power of 400 W, a frequency of 100 Hz and a duty cycle of 2 %. Here, the duty cycle is defined as the ratio between the pulse on-time (200 µs) and the pulse duration (10000 µs). The discharge voltage and current were monitored by an oscilloscope during the deposition. No external heating was applied and the substrate holder was on ground potential. The substrate temperature due to heating from the plasma reached a maximum value of around 100 °C as measured by a thermocouple placed next to the Si substrates. After deposition, the PVA foils were dissolved in cold distilled water while stirring to ensure that only the film material remained as a solid. The solid film material was then filtered from the solution and ground to a fine-grained powder with a mortar.

The chemical composition of the as-deposited films was measured by energy-dispersive X-ray (EDX) spectroscopy using a Bruker Type XFlash 6-60 detector which

was attached to a Tescan Magna scanning electron microscope (SEM). The microstructure of the film and the powder was analyzed by X-Ray diffraction (XRD) using a Bruker-AXS D8 Advance diffractometer equipped with Cu-K_α radiation and parallel optics. The measurements were performed in Bragg-Brentano geometry. The residual stresses of the film were measured using the wafer curvature method with a custom-built device with two parallel laser beams [18] and with a Bruker-AXS D8 Advance DaVinci diffractometer using the $\sin^2\Psi$ method [19].

The cross-sectional film microstructures of the different compositions were characterized by means of transmission electron microscopy (TEM) using a JEOL 2200 FS operating at 200 kV. Therefore, the TEM samples were prepared by a mechanical wedge polishing technique followed by ion polishing in a Gatan PIPS II system.

Nanoindentation was performed on a TS77 Select Nanoindenter from Bruker-Hysitron using a well-calibrated Berkovich tip. The area function and frame compliance calibrations were made using 100 open loop indents into fused silica with quasi-static indents at maximum loads between 100 µN and 10 mN. Quasi-static indents into the HEA films as well as into the Si substrate were performed to obtain the thin film material properties as a direct result and substrate data for a reference and to distinguish indentation depths in the films with substrate effects. Indents into each HEA film and Si were made using the load range between 100 µN and 2.5 mN with a constant loading time of 10 s. The maximum loads corresponded to contact depths between 15 nm and 75 nm. A total of 50 indents were made into each film in several subsequent indentation runs. All of the load-displacement curves were analyzed using the Oliver and Pharr method [20] and proper area function. The Young's modulus, E, was evaluated from the reduced elastic modulus, E_r, values:

$$\frac{1}{E_r} = \frac{1-\nu_t}{E_t} + \frac{1-\nu}{E}, \tag{1}$$

with the Young's modulus of the tip, $E_t = 1170\ \mathrm{GPa}$, and its Poisson's ratio, $\nu_t = 0.17$. The Poisson's ratio of the film, ν, was assumed to $\nu = 0.3$. To obtain correct Young's moduli of the films without influence of the substrate, the respective indentation sets were analyzed as a function of the contact depth, h_c, and fitted with a full cubic function where its constant term was used to obtain E at $h_c = 0$ (Figure 1a). The statistical analysis of the fit with the Python code was used to obtain the standard deviation of

the results. For the evaluation of the film hardness, deeper indents need to be used. Therefore, the mean values and standard deviations were calculated from the plateau area of the $H(h_c)$ function (Figure 1b). The area function was checked midway through the experiments to ensure correct indentation results.

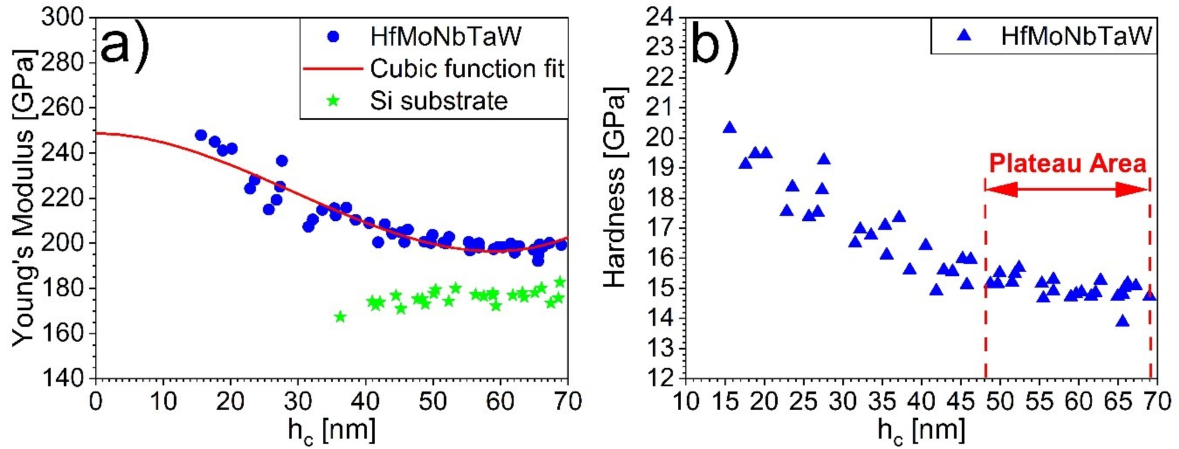

Figure 1: a) Example of the Young's modulus from all indentations for the HfMoNbTaW film and the Si substrate. The indentation data were fitted with a cubic function (red line). This fit was used to derive the real Young's modulus of the film, without influence of the substrate, by calculating the fit function value for h_c = 0. b) Example of the hardness values from all indentations for the HfMoNbTaW film. The plateau area indicates the results used for the evaluation of the correct hardness.

3 Results and Discussion

3.1 Phase Stability Considerations

For HEAs, a set of criteria have been established to estimate if stable single-phase solid solutions exist for a certain alloy and if this phase has a bcc or fcc microstructure. The analysis is limited to cubic systems. Based on these criteria, phase stability considerations are presented in the following for the five different alloys synthesized within the current work together with the base alloy MoNbTaW, all in equimolar chemical composition.

First, the configurational entropy,

$$\Delta S_{conf} = -R\sum_{i=1}^{n} C_i lnC_i \geq 1.5R, \quad (2)$$

was calculated to check if the criterion of HEAs is fulfilled. Here, C_i is the concentration of an element present in the alloy. With $1.39R$, the configurational entropy of MoNbTaW was in the range of medium entropy alloys. All other alloys fulfilled this criterion with $\Delta S_{conf} = 1.61R$ [21].

Further criteria concern the mixing enthalpy,

$$\Delta H_{mix} = \sum_{i=1,j\neq 1}^{n} 4\Delta H_{ij}^{mix} C_i C_j,$$
$$-11.6 \leq \Delta H_{mix} \leq 3.2\ kJ/mol, \tag{3}$$

and the atomic size difference,

$$\delta = 100 \times \sqrt{\sum_{i=1}^{n} C_i \left(1 - \frac{r_i}{\bar{r}}\right)^2},$$
$$\delta \leq 6.6, \tag{4}$$

as defined by Guo et al. [22]. They predict the formation of a crystalline solid solution over an amorphous phase for a certain alloy. Here, ΔH_{ij}^{mix} denotes the mixing enthalpy of the binary interaction between atoms i and j and r_i and $\bar{r}$ the metallic radius of the i-th atom and the mean radius of the alloy, respectively. Based on data obtained from refs. [23,24], Figure 2a shows the mixing enthalpy and atomic size difference for the different alloys. The lowest mixing enthalpy was found for MoNbTaW followed by CrMoNbTaW, which has also the highest atomic size difference, and the highest mixing enthalpy was found for MnMoNbTaW. The lowest atomic size difference was found for MoNbTaTiW, which has a value close to that of MoNbTaW. However, all studied alloys fulfill both criteria and a crystalline solid solution should be preferred.

Another criterion includes the melting temperature,

$$T_m = \sum_{i=1}^{n} C_i (T_m)_i, \tag{5}$$

which is used to calculate the Omega value,

$$\Omega = \frac{T_m \Delta S_{conf}}{|\Delta H_{mix}|} \geq 1.1\ . \tag{6}$$

Zhang et al. [25] claimed that when criteria (4) and (6) are fulfilled, the HEA should consist of a single-phase solid solution, without the formation of additional intermetallic phases, while with increasing Ω the formation of intermetallic phases becomes more and more unlikely. Figure 2b shows that the lowest value of Ω was found for MoNbTaW, which can be explained by the low configurational entropy and the low mixing enthalpy of this alloy. CrMoNbTaW has the second lowest value, which can also be attributed to the low mixing enthalpy. The highest Ω value was found for MnMoNbTaW and can be attributed to the high mixing enthalpy. Even though the Ω values differ significantly, all values exceed the threshold of 1.1 and, therefore, for all

studied HEAs single-phase solid solutions can be expected. Additionally, Figure 2b also shows the melting temperatures of the alloys which were calculated using a rule of mixture calculation (equation (5)). Such calculation are used to estimate the melting temperatures of alloys with solid solution microstructure [5]. However, this is just a simple calculation and does not consider all the factors influencing the melting temperature. The highest melting temperature was found for MoNbTaW and the lowest for MnMoNbTaW while all others are around 2700 °C.

Another criterion, frequently discussed in literature, was introduced by Guo et al. [26] who stated that the valence electron concentration (VEC) of high entropy alloys is an indication for the microstructure of the formed solid solution:

$$\begin{gathered} VEC < 6.87 \rightarrow bcc, \\ VEC > 8 \rightarrow fcc. \end{gathered} \tag{7}$$

As can be seen in Figure 2c, the lowest VEC is found for MoNbTaTiW and HfMoNbTaW and the highest for MnMoNbTaW. Since only one element is changed from alloy to alloy, the differences in VEC are minor. All studied HEAs have a VEC well below 6.87 which means that a bcc microstructure should form. In general, taking all criteria into consideration, a single-phase solid solution with bcc microstructure can be expected for all HEAs studied in this work.

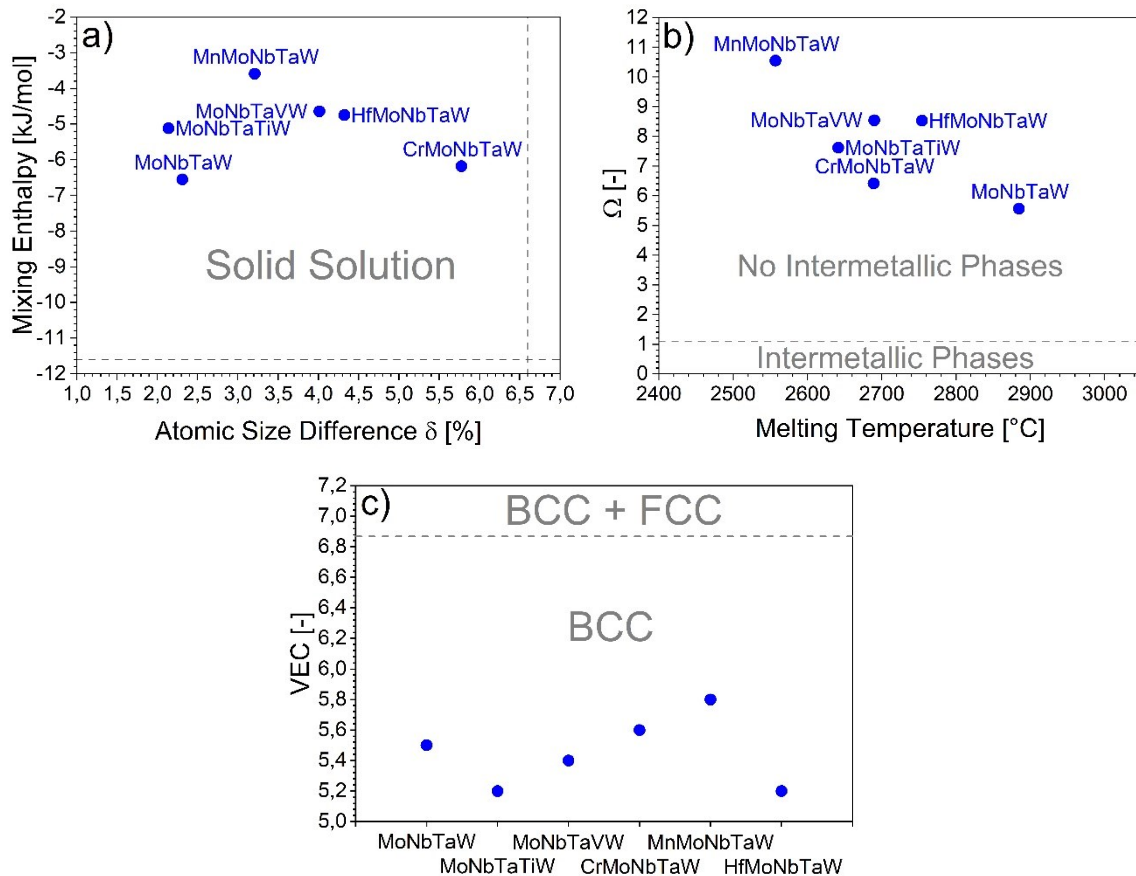

Figure 2: a) Mixing enthalpy and atomic size difference, b) Omega value and melting temperature and c) valence electron concentration of the different alloys studied within this work.

3.2 HiPIMS Discharge

The voltage and current characteristics of the HiPIMS pulse from the different HEA targets are shown in Figure 3a-e. The voltage peak has a rectangular shape and reaches a plateau. The current pulses show a short delay of a few µs before they increase. This is a typical feature of HiPIMS pulses, where the extent of the time delay depends on the working gas pressure, the target material and the applied voltage [27]. After reaching its maximum value within the first 50 µs, the current decreases to a lower steady-state value which remains constant until the end of the peak. According to literature such a profile can be related to working gas sustained self-sputtering [28]. This means that during the discharge the current is dominated by ionized target atoms which return to the cathode (target) causing self-sputtering. However, the working gas ion current still provides an important contribution to the overall current [27,29].

The discharge voltage increases with increasing group number of the fifth alloying element: Ti and Hf – group 4, V – group 5, Cr – group 6 and Mn – group 7 (see Figure 3f). Since the discharge power was kept constant during deposition, the discharge current needs to decrease as the voltage rises. The latter applies to the integrated value of the current, but is also true for the peak value as can be seen in see Figure 3f. As discussed before, working gas sustained self-sputtering occurred during the applied HiPIMS process, which means that most of the current is carried by metal ions. A major factor influencing the discharge current is the ionization energy of the metals as it determines how easily metal ions can be provided for carrying the current. Since only one element was changed between the individual HEAs, the ionization energy of this element should be decisive for the differences in the current. Elements with a similar ionization energy like Ti – 6.83 eV, V – 6.75 eV, Cr – 6.77 eV and Hf – 6.83 eV [30] have a similar discharge voltage. The highest discharge voltage was found for the HEA containing Mn, as it has also the highest ionization energy of 7.43 eV [30].

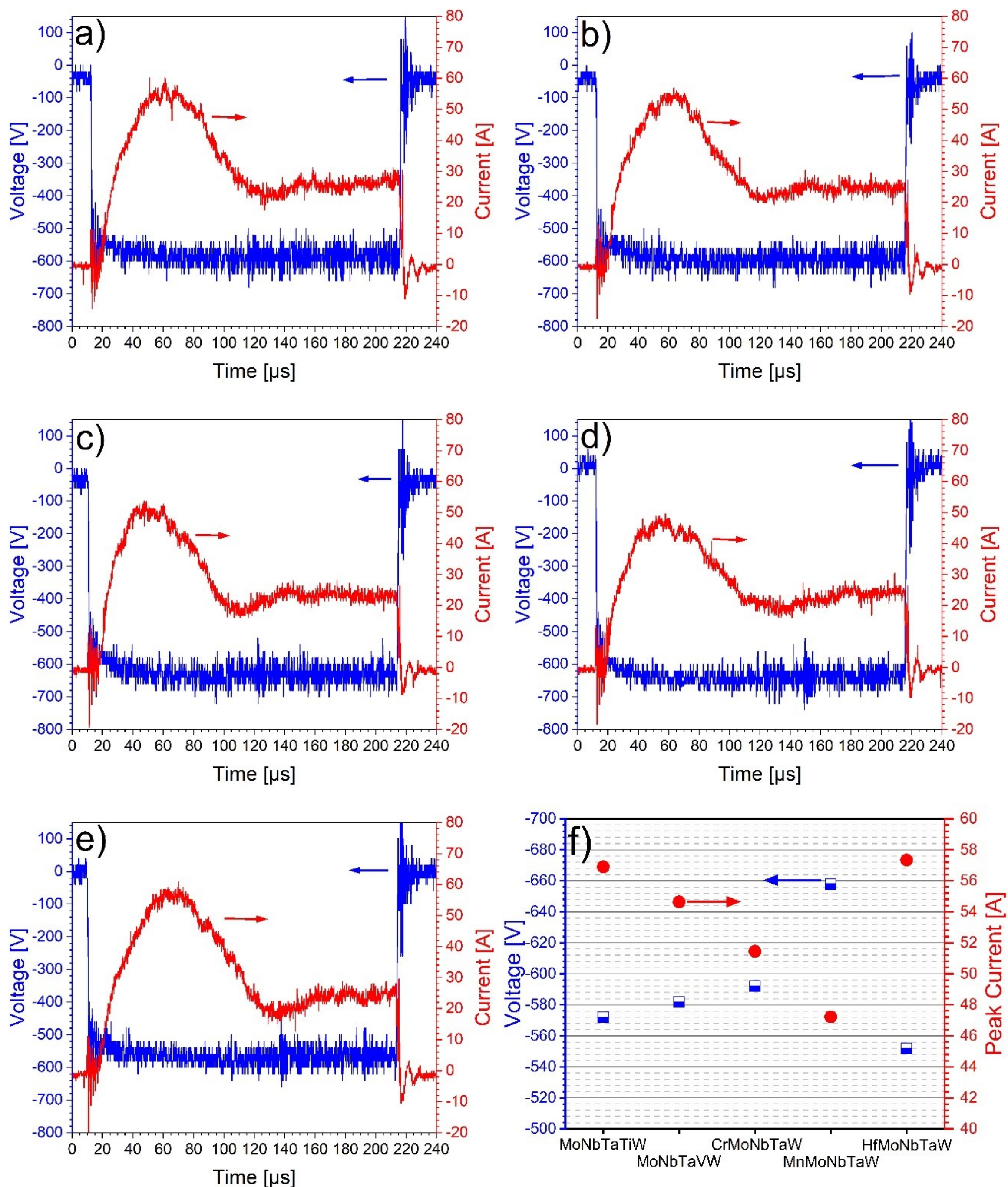

Figure 3: *Voltage and current characteristics of the HiPIMS pulse from the a) MoNbTaTiW, b) MoNbTaVW, c) CrMoNbTaW, d) MnMoNbTaW and e) HfMoNbTaW target. f) Summary of voltage and peak current of the different targets.*

3.3 Chemical Composition

The deposited films have a film thickness between 300 and 400 nm and a chemical composition as shown in Table 1**.** In the current case, the composition of the HEA films containing Ti, V and Cr can still be considered equimolar taking into account an error of about 1 at.% of the EDX measurements. Only the Mn and Hf concentration in their

corresponding alloy is slightly lower, compared to the equimolar targets used for the deposition. However, considering the measured chemical composition of the HEA films, minor changes of the values calculated for the criteria (2)-(7) will occur but the classification of the films as HEAs with a single-phase bcc solid solution microstructure still remains.

Table 1: Chemical composition of the HEA thin films as measured by EDX. All values are in at.%.

	Nb	Mo	Ta	W	Ti	V	Cr	Mn	Hf
MoNbTaTiW	20.7	20.7	18.7	19.7	20.2	-	-	-	-
MoNbTaVW	20.2	20.4	18.3	19.4	-	21.7	-	-	-
CrMoNbTaW	21.3	20.5	19.1	20.0	-	-	19.1	-	-
MnMoNbTaW	20.8	21.2	19.9	20.6	-	-	-	17.5	-
HfMoNbTaW	20.9	21.4	20.7	21.3	-	-	-	-	15.7

3.4 Microstructure

In Figure 4a the X-ray diffractograms of the different HEA films are shown which reveal that all films show a bcc microstructure with a preferred (110) orientation. Additionally, the (211) peak is visible but overlaps with the Si substrate peak. All peaks are shifted towards lower 2θ-angles, in comparison to the unstrained value calculated using Vegard's rule [31] which is indicated in Figure 4a for all alloys. Such a shift is generally a sign for the presence of compressive stresses within the films. HfMoNbTaW and MnMoNbTaW show the smallest deviation from the unstrained value indicating a low level of compressive stress within those films. The other three alloys show a similar shift from their unstrained value. Regarding the peak shape, all (110) peaks show a more or less pronounced shoulder towards higher 2θ-angles. It is least pronounced in the case of MnMoNbTaW. Possible reasons for such a shoulder are the existence of a second bcc phase, with a slightly different chemical composition, and regions of different stress states within the film. To reveal the origin of the peak shoulder, XRD measurements of stress-free CrMoNbTaW film powder were performed as shown in Figure 4b. The absence of the shoulder in the (110) peak of the CrMoNbTaW film powder confirms that stress inhomogeneities exist in the as-deposited films rather than the presence of a second bcc phase with different chemical composition. Further, the existence of a single-phase bcc solid solution is in good agreement with the

calculations mentioned above and with reports in literature for MoNbTaTiW and MoNbTaVW [7,9].

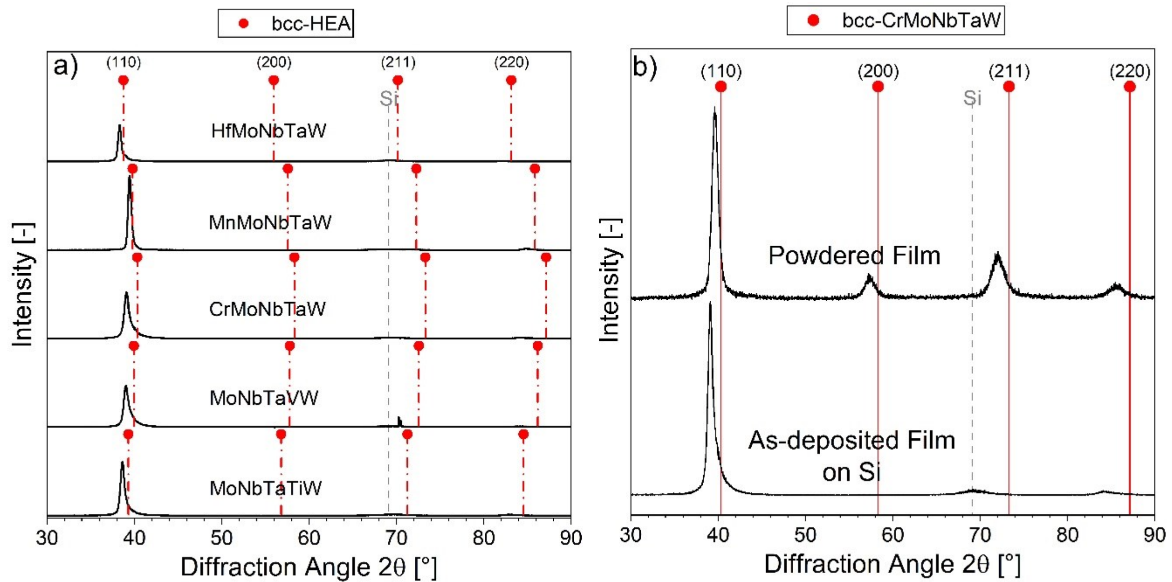

Figure 4: a) X-ray diffractograms of the as-deposited HEA thin films. b) Comparison of the X-ray diffractograms of the as-deposited CrMoNbTaW film and prepared CrMoNbTaW film powder.

Using the X-ray diffractograms also the lattice constant of the different studied HEAs were calculated and compared to the values calculated using Vegard's rule [31]. The results are shown in Table 2. The lattice constant was calculated by fitting the (110) peak using a Pseudo-Voight function. The measured lattice constant is always higher compared to the calculated one. The reason for this could be compressive stresses within the film. Do measure a more accurate lattice constant of the alloy, it would be necessary to prepare a film powder of the different HEAs and anneal this powder, to have a fully relaxed material. Additional the calculation using Vegard's rule is just a very simple calculation and does not consider everything influencing the lattice constant.

Table 2: The calculated lattice constant, $a_{calc.}$, calculated using Vegard's rule and the lattice constant calculated from the X-ray diffractograms, a_{XRD}, of the different studied HEAs are shown. All values are given in Å.

	MoNbTaTiW	MoNbTaVW	CrMoNbTaW	MnMoNbTaW	HfMoNbTaW
$a_{calc.}$	3.238	3.189	3.161	3.199	3.283
a_{XRD}	3.295	3.262	3.257	3.229	3.321

Further details about morphology and microstructure of the films were revealed by TEM. Figure 5a and b show the brightfield (BF) and darkfield (DF) scanning TEM (STEM) cross sectional images of the MoNbTaTiW film. The MoNbTaTiW film shows a dense columnar morphology with a column width of about 30 nm. According to the STEM and high-resolution TEM (HRTEM) images (Figure 5c), the MoNbTaTiW film has a homogenous morphology. The selected area electron diffraction (SAED) pattern, obtained from the cross section and shown in Figure 5d, reveals the presence a single-phase bcc microstructure in the MoNbTaTiW film. The fact that also in the TEM investigations no additional phase was noticed supports the conclusion that a stress gradient in the films is responsible for the shoulder in the (110) peaks in the X-ray diffractograms as stresses present in the as-deposited films can relax during preparation of the TEM lamella.

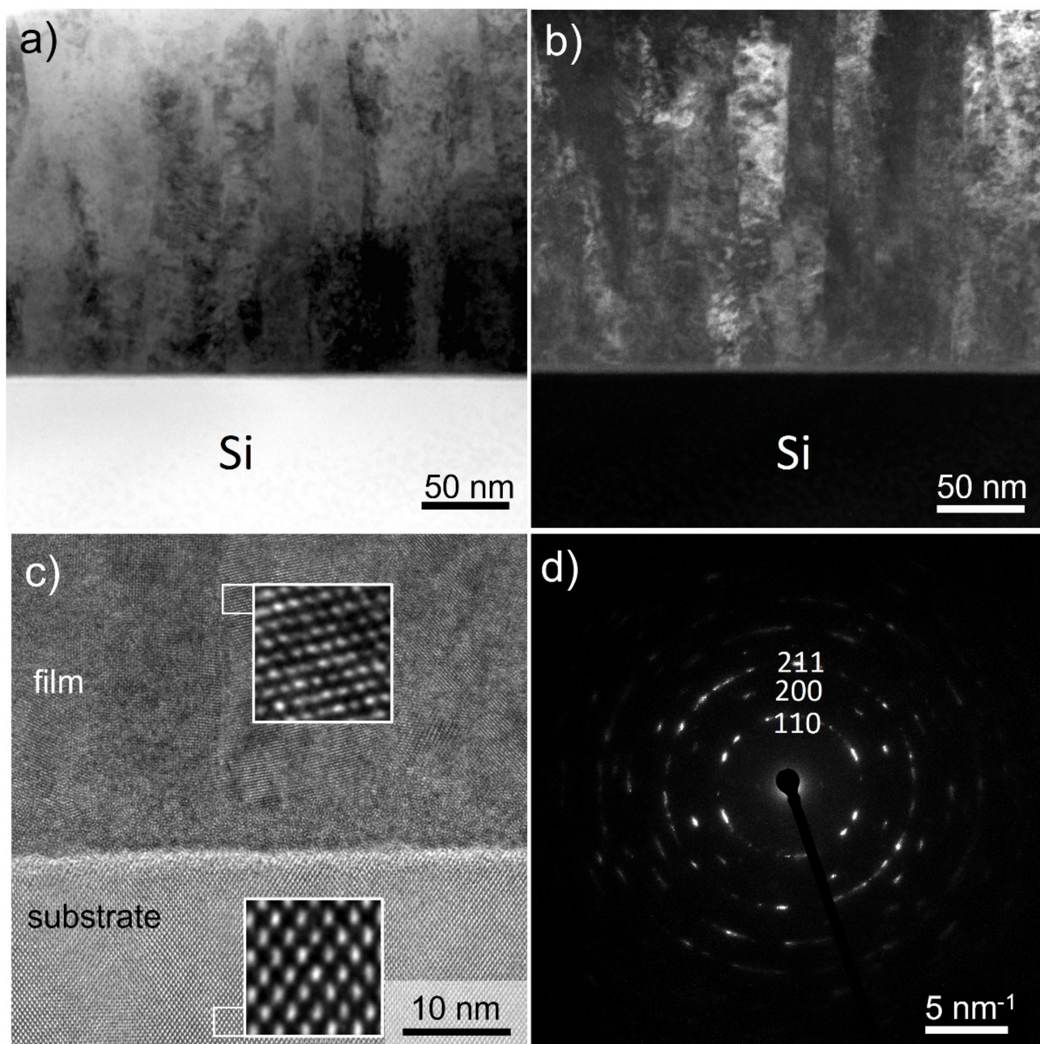

Figure 5: TEM analysis of the as-deposited MoNbTaTiW film: a) BF-STEM and b) DF-STEM of the film cross-section, c) HRTEM of the interface between film and Si substrate and d) SAED pattern of the film showing a bcc crystal structure.

In Figure 6a-e BF-STEM cross sectional images of all studied HEA films are shown where an amorphous nucleation layer on the substrate of varying thickness can be noticed. A dependence of the thickness and the atomic size difference is found. MoNbTaTiW, which has the lowest atomic size difference, shows hardly any amorphous nucleation layer and CrMoNbTaW, which has the highest atomic size difference, has an amorphous nucleation layer of a few 10 nm. Nevertheless, also other parameters, like the condition of the substrate surface can influence the thickness of the amorphous nucleation layer. Apart from this, all films show a dense and homogeneous columnar morphology. Further, the elemental distribution is homogenous over the film thickness as shown in Figure 6f where EDX line profiles from the CrMoNbTaW film are presented.

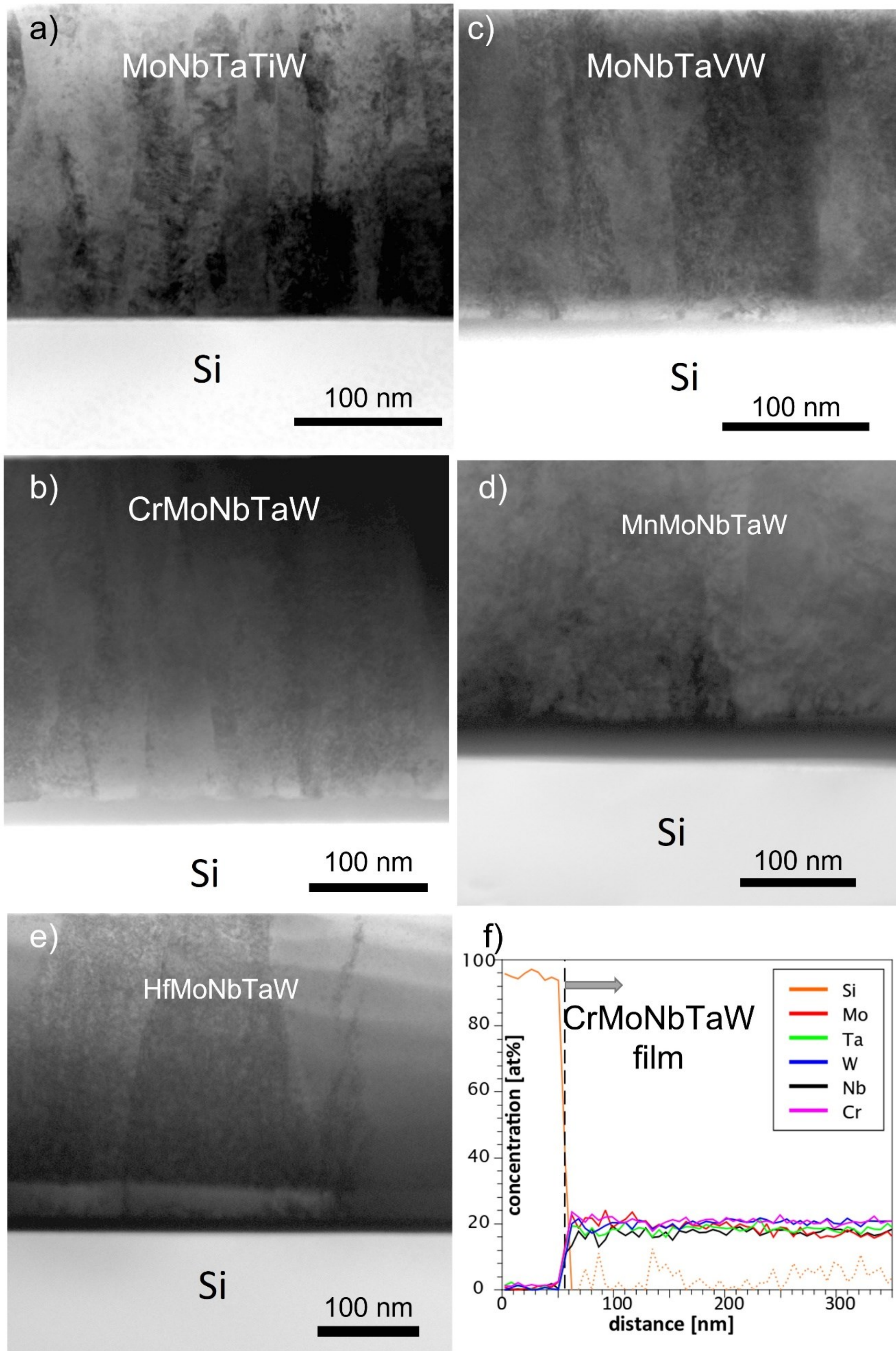

Figure 6: Cross sectional BF-STEM images of the as-deposited HEA films containing (a) Ti, (b) Hf, (c) V, (d) Mn and (e) Cr. f) EDX line profiles across the as-deposited HEA film containing Cr (dashed line indicates location of interface).

3.5 Residual Stress and Mechanical Properties

The residual stress of the films was measured using two different methods, the wafer curvature and the $\sin^2\Psi$ method. As shown in Figure 7, there is a significant, non-constant difference in the stress values obtained by the two methods, where the values measured by the wafer curvature method always show a lower compressive stress. The magnitude in the difference between both stress values correlates well with the observed shoulder in the (110) peaks in the X-ray diffractograms (see Figure 4). The more pronounced the peak shoulder in the diffractogram, the larger the difference between the stress values measured by the two methods. A large difference in the stress values was noticed for MoNbTaTiW, MoNbTaVW and CrMoNbTaW. This behavior can be understood by the fact that the wafer curvature method measures the average stress state of the entire film, whereas in the $\sin^2\Psi$ method only regions contributing to the (110) peak with maximum intensity are taken into account. This excludes regions contributing to the shoulder of the (110) peak, crystallites with orientations of the (110) planes not parallel to the surface of the film and grain boundaries. In other words, the observed difference between the stress values from the two different methods is an indication for the existence of a stress gradient, most likely along the thickness of the films [32]. Köstenbauer et al. [32] explained the stress gradient along the film thickness with a decreasing point defect density with increasing film thickness. The transformation of an amorphous interlayer to a crystalline structure is an indication that also the films studied in this study show a decreasing point defect density with increasing film thickness. This is a further confirmation of the already discussed inhomogeneous stress distribution within the films.

The general compressive stress state is lower for the MnMoNbTaW and HfMoNbTaW films than compared to the stress state of the other three films. From TEM we know that the grain size of MnMoNbTaW and HfMoNbTaW is also higher compared the other three films. This can be a sign for a higher ad-atom mobility during film growth, which would lead to less stresses within the film. Xia et al. reported stress values of about 1 GPa compressive stress for MoNbTaVW films deposited with HiPIMS using the wafer curvature method [9]. The higher stress values observed within the current work can be understood by the shorter distance between target and substrate during deposition leading to higher energetic growth conditions and higher film stress [33].

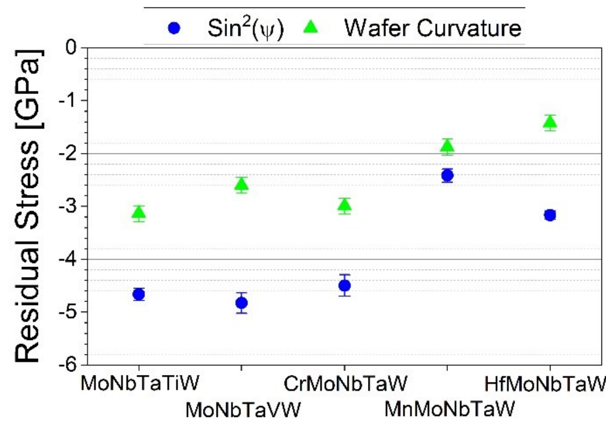

Figure 7: Residual stress state of the different HEA films measured by wafer curvature and $sin^2\Psi$ method.

Hardness and Young's modulus of the films as obtained by nanoindentation, are shown in Figure 8. The maximum hardness with 17.4 GPa was found for CrMoNbTaW. The MnMoNbTaW film has a slightly lower hardness. The lowest hardness of about 14 GPa was found for MoNbTaTiW and MoNbTaVW. Xia et al. reported a hardness of 15 GPa for their MoNbTaVW films deposited using HiPIMS, which is only slightly higher than the hardness values observed in this study [9]. MoNbTaVW films deposited using DC-magnetron sputtering, as reported by Hung et al [34], have a slightly lower hardness of 11.2 GPa. This can be explained by the most likely reduced film density compared to films deposited using HiPIMS [17]. The hardness of the HfMoNbTaW films lies in the middle of the highest and the lowest hardness values. According to the Hall-Petch relation [35,36] the MnMoNbTaW and HfMoNbTaW films should have the lowest hardness, as they have the highest grain sizes according to the TEM investigations. As this is not the case within these films, it can be stated that the grain size has not a significant influence of the hardness of these films and other factors seem to be more important. One of these factors is for example the atomic size difference, as the highest hardness is found for the CrMoNbTaW film, which has also the highest atomic size difference and the lowest hardness was found for the MoNbTaTiW film, which has the lowest atomic size difference. Nevertheless, the MoNbTaVW film has a similar hardness as the MoNbTaTiW film, but the atomic size difference is in between the one of MoNbTaTiW and CrMoNbTaW. This means also the atomic size mismatch alone cannot describe the hardness trends within the different alloys.

The measured Young's modulus values are shown in Figure 8b, together with values calculated by the rule of mixture and Young's modulus values obtained from literature. For the rule of mixture calculation, the Young's moduli were taken from [37] and the measured chemical composition of the films (see Table 1) were used. The MoNbTaTiW film shows the lowest Young's modulus, but the measured value of 230 GPa is significantly higher than the ones calculated by Bhandari et al. and Liu et al. [39]. The MoNbTaVW film shows a similar value for the Young's modulus. The values measured by Xia et al. [9] and Hung et al. [34] and the calculated values by Zheng et al. [40] are slightly lower, but still in good agreement, whereas the value calculated by Liu et al. [39] is again significantly lower. The CrMoNbTaW film shows the second highest Young's modulus of 274 GPa, which, in this case, matches the value calculated by Liu et al. [39]. The highest Young's Modulus was measured for the MnMoNbTaW film. The Young's Modulus of the HfMoNbTaW is much higher than expected from the calculations by Liu et al. [39].

With the exception of MnMoNbTaW, all values for the Young's modulus calculated from the rule of mixture match closely the measured values. A detailed comparison of both values reveals that the alloying element has a significant influence on the Young's modulus. However, the rule of mixture is just a simple calculation where parameters like bond length and crystal orientation, which can also influence the measured Young's modulus, are not considered. For calculating the Young's modulus of each element the value at room temperature was used. This causes another uncertainty due to the fact that for some elements (Ti, Mn and Hf) the bcc crystal structure is not stable at room temperature and the Young's modulus is influenced by the crystal structure. All these reasons can contribute to the for some alloys observed difference in the measured and by the rule of mixture calculated Young's modulus values.

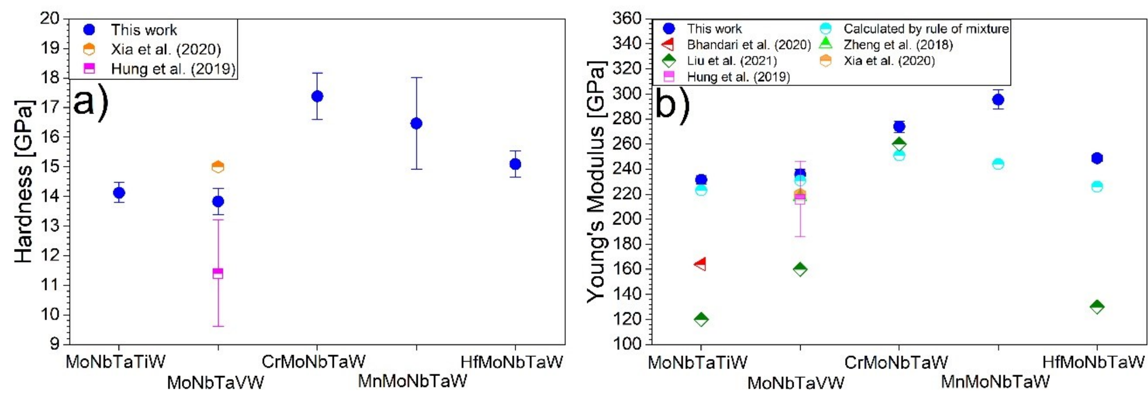

Figure 8: a) Hardness and b) Young's modulus of the as-deposited HEA films. Values obtained from literature are given for comparison.

4 Conclusions

Within this study five different refractory HEA films based on the MoNbTaW system have been deposited by HiPIMS. All films present a single-phase bcc solid solution microstructure which is in agreement with the predictions based on phase stability criteria. According to the TEM investigations all films show a dense columnar morphology, which is a typical feature of films synthesized by HiPIMS deposition processes like the one applied within this work. The analysis of the stress state in the films by different methods revealed generally high compressive stresses with an inhomogeneous distribution within the films where the latter was least pronounced in the case of MnMoNbTaW. The values obtained for hardness and Young's modulus were in the range from 14 to 17 GPa and from 230 to 295 GPa, respectively. In general, the current study contributes to the understanding of the relations between synthesis, structure and properties of refractory HEA films and exemplifies how changing one element in the alloy can affect these relations. The obtained results may also contribute to the further development of such films for specific applications.

Acknowledgements

The authors acknowledge the financial support by the Austrian Research Promotion Agency (FFG, project number: 871687). A. Lassnig acknowledges funding from the Austrian Science Fund (FWF, project number: T891-N36). The authors are grateful to S. Wurster (Austrian Academy of Sciences, Austria) for the SEM investigations and G.C. Gruber wishes to thank S. Hirn (Montanuniversität Leoben, Austria) for the help

with the depositions and M. Golizadeh (now at Oerlikon Balzers, Liechtenstein) for the inspiring discussions.

REFERENCES

[1] J.-W. Yeh, S.-K. Chen, S.-J. Lin, J.-Y. Gan, T.-S. Chin, T.-T. Shun, C.-H. Tsau, S.-Y. Chang, Nanostructured High-Entropy Alloys with Multiple Principal Elements: Novel Alloy Design Concepts and Outcomes, Advanced Engineering Materials 6 (2004) 299–303. https://doi.org/10.1002/adem.200300578.

[2] B. Cantor, I. Chang, P. Knight, A. Vincent, Microstructural development in equiatomic multicomponent alloys, Materials Science and Engineering: A 375-377 (2004) 213–218. https://doi.org/10.1016/j.msea.2003.10.257.

[3] B.S. Murty, J.-W. Yeh, S. Ranganathan, High-entropy alloys, Butterworth-Heinemann an imprint of Elsevier, London, Oxford, Amsterdam, San Diego, 2014.

[4] D.B. Miracle, O.N. Senkov, A critical review of high entropy alloys and related concepts, Acta Materialia 122 (2017) 448–511. https://doi.org/10.1016/j.actamat.2016.08.081.

[5] O.N. Senkov, G.B. Wilks, D.B. Miracle, C.P. Chuang, P.K. Liaw, Refractory high-entropy alloys, Intermetallics 18 (2010) 1758–1765. https://doi.org/10.1016/j.intermet.2010.05.014.

[6] O.N. Senkov, G.B. Wilks, J.M. Scott, D.B. Miracle, Mechanical properties of Nb25Mo25Ta25W25 and V20Nb20Mo20Ta20W20 refractory high entropy alloys, Intermetallics 19 (2011) 698–706. https://doi.org/10.1016/j.intermet.2011.01.004.

[7] Z.D. Han, N. Chen, S.F. Zhao, L.W. Fan, G.N. Yang, Y. Shao, K.F. Yao, Effect of Ti additions on mechanical properties of NbMoTaW and VNbMoTaW refractory high entropy alloys, Intermetallics 84 (2017) 153–157. https://doi.org/10.1016/j.intermet.2017.01.007.

[8] Z.D. Han, H.W. Luan, X. Liu, N. Chen, X.Y. Li, Y. Shao, K.F. Yao, Microstructures and mechanical properties of Ti NbMoTaW refractory high-entropy alloys, Materials Science and Engineering: A 712 (2018) 380–385. https://doi.org/10.1016/j.msea.2017.12.004.

[9] A. Xia, A. Togni, S. Hirn, G. Bolelli, L. Lusvarghi, R. Franz, Angular-dependent deposition of MoNbTaVW HEA thin films by three different physical vapor deposition methods, Surface and Coatings Technology 385 (2020) 125356. https://doi.org/10.1016/j.surfcoat.2020.125356.

[10] T.-K. Chen, M.-S. Wong, T.-T. Shun, J.-W. Yeh, Nanostructured nitride films of multi-element high-entropy alloys by reactive DC sputtering, Surface and Coatings Technology 200 (2005) 1361–1365. https://doi.org/10.1016/j.surfcoat.2005.08.081.

[11] Y. Zhang, C.C. Koch, S.G. Ma, H. Zhang, Y. Pan, Fabrication Routes, in: M.C. Gao, J.-W. Yeh, P.K. Liaw, Y. Zhang (Eds.), High-Entropy Alloys, Springer International Publishing, Cham, 2016, pp. 151–179.

[12] A. Xia, R. Dedoncker, O. Glushko, M.J. Cordill, D. Depla, R. Franz, Influence of the nitrogen content on the structure and properties of MoNbTaVW high entropy alloy thin films, Journal of Alloys and Compounds 850 (2021) 156740. https://doi.org/10.1016/j.jallcom.2020.156740.

[13] Z. Li, Y. Tian, C. Teng, H. Cao, Recent Advances in Barrier Layer of Cu Interconnects, Materials (Basel) 13 (2020) 5049. https://doi.org/10.3390/ma13215049.

[14] S.-Y. Chang, C.-E. Li, Y.-C. Huang, H.-F. Hsu, J.-W. Yeh, S.-J. Lin, Structural and thermodynamic factors of suppressed interdiffusion kinetics in multi-component high-entropy materials, Sci. Rep. 4 (2014) 4162. https://doi.org/10.1038/srep04162.

[15] A. Xia, R. Franz, Thermal Stability of MoNbTaVW High Entropy Alloy Thin Films, Coatings 10 (2020) 941. https://doi.org/10.3390/coatings10100941.

[16] Y.-Y. Chen, S.-B. Hung, C.-J. Wang, W.-C. Wei, J.-W. Lee, High temperature electrical properties and oxidation resistance of V-Nb-Mo-Ta-W high entropy alloy thin films, Surface and Coatings Technology 375 (2019) 854–863. https://doi.org/10.1016/j.surfcoat.2019.07.080.

[17] K. Sarakinos, L. Martinu, Synthesis of thin films and coatings by high power impulse magnetron sputtering, in: High Power Impulse Magnetron Sputtering, Elsevier, 2020, pp. 333–374.

[18] C. Saringer, M. Tkadletz, C. Mitterer, Restrictions of stress measurements using the curvature method by thermally induced plastic deformation of silicon substrates, Surface and Coatings Technology 274 (2015) 68–75. https://doi.org/10.1016/j.surfcoat.2015.04.038.

[19] E. Zolotoyabko, Basic concepts of crystallography: An outcome from crystal symmetry, Wiley-VCH, Weinheim Germany, 2011.

[20] W.C. Oliver, G.M. Pharr, An improved technique for determining hardness and elastic modulus using load and displacement sensing indentation experiments, Journal of Materials Research 7 (1992) 1564–1583. https://doi.org/10.1557/JMR.1992.1564.

[21] J.-W. Yeh, Alloy Design Strategies and Future Trends in High-Entropy Alloys, JOM 65 (2013) 1759–1771. https://doi.org/10.1007/s11837-013-0761-6.

[22] S. Guo, Q. Hu, C. Ng, C.T. Liu, More than entropy in high-entropy alloys: Forming solid solutions or amorphous phase, Intermetallics 41 (2013) 96–103. https://doi.org/10.1016/j.intermet.2013.05.002.

[23] A. Debski, R. Debski, W. Gasior, New Features of Entall Database: Comparison of Experimental and Model Formation Enthalpies/ Nowe Funkcje Bazy Danych Entall: Porównanie Doświadczalnych I Modelowych Entalpii Tworzenia, Archives of Metallurgy and Materials 59 (2014) 1337–1343. https://doi.org/10.2478/amm-2014-0228.

[24] S. Guo, C.T. Liu, Phase stability in high entropy alloys: Formation of solid-solution phase or amorphous phase, Progress in Natural Science: Materials International 21 (2011) 433–446. https://doi.org/10.1016/S1002-0071(12)60080-X.

[25] Y. Zhang, X. Yang, P.K. Liaw, Alloy Design and Properties Optimization of High-Entropy Alloys, JOM 64 (2012) 830–838. https://doi.org/10.1007/s11837-012-0366-5.

[26] S. Guo, C. Ng, J. Lu, C.T. Liu, Effect of valence electron concentration on stability of fcc or bcc phase in high entropy alloys, Journal of Applied Physics 109 (2011) 103505. https://doi.org/10.1063/1.3587228.

[27] D. Lundin, A. Hecimovic, T. Minea, A. Anders, N. Brenning, J.T. Gudmundsson, Physics of high power impulse magnetron sputtering discharges, in: High Power Impulse Magnetron Sputtering, Elsevier, 2020, pp. 265–332.

[28] J.T. Gudmundsson, N. Brenning, D. Lundin, U. Helmersson, High power impulse magnetron sputtering discharge, Journal of Vacuum Science & Technology A: Vacuum, Surfaces, and Films 30 (2012) 30801. https://doi.org/10.1116/1.3691832.

[29] C. Huo, D. Lundin, M.A. Raadu, A. Anders, J.T. Gudmundsson, N. Brenning, On the road to self-sputtering in high power impulse magnetron sputtering: particle balance and discharge characteristics, Plasma Sources Science and Technology 23 (2014) 25017. https://doi.org/10.1088/0963-0252/23/2/025017.

[30] A. Kramida, Y. Ralchenko, NIST Atomic Spectra Database, NIST Standard Reference Database 78, 2021. https://physics.nist.gov/asd (accessed 24 February 2022).

[31] L. Vegard, VI. Results of crystal analysis, The London, Edinburgh, and Dublin Philosophical Magazine and Journal of Science 32 (1916) 65–96.

[32] H. Köstenbauer, G.A. Fontalvo, M. Kapp, J. Keckes, C. Mitterer, Annealing of intrinsic stresses in sputtered TiN films: The role of thickness-dependent gradients of point defect density, Surface and Coatings Technology 201 (2007) 4777–4780. https://doi.org/10.1016/j.surfcoat.2006.10.017.

[33] M. Ohring, Materials science of thin films: Deposition and structure, second ed., Academic Press, San Diego, CA, 2002.

[34] S.-B. Hung, C.-J. Wang, Y.-Y. Chen, J.-W. Lee, C.-L. Li, Thermal and corrosion properties of V-Nb-Mo-Ta-W and V-Nb-Mo-Ta-W-Cr-B high entropy alloy coatings, Surface and Coatings Technology 375 (2019) 802–809. https://doi.org/10.1016/j.surfcoat.2019.07.079.

[35] N. Petch, The Cleavage Strength Of Polycrystals, The Journal of the Iron and Steel Institute 173 (1953) 25.

[36] E.O. Hall, The deformation and ageing of mild steel: III discussion of results, Proceedings of the Physical Society: Section B 64 (1951) 747.

[37] G.V. Samsonov, Handbook of the Physicochemical Properties of the Elements, Springer US, Boston, MA, 1968.

[38] U. Bhandari, C. Zhang, S. Guo, S. Yang, First-principles study on the mechanical and thermodynamic properties of MoNbTaTiW, International Journal of Minerals, Metallurgy and Materials 27 (2020) 1398–1404. https://doi.org/10.1007/s12613-020-2077-1.

[39] H. Liu, L. Liu, C. Xin, Effect of alloying elements on the structure and mechanical properties of NbMoTaWX (X = Cr, V, Ti, Zr, and Hf) refractory high-entropy alloys, AIP Advances 11 (2021) 25044. https://doi.org/10.1063/5.0038405.

[40] S. Zheng, S. Wang, First-Principles Design of Refractory High Entropy Alloy VMoNbTaW, Entropy (Basel) 20 (2018) 965. https://doi.org/10.3390/e20120965.

Publication II

Tuning microstructure and properties of MoNbTaWZr high entropy alloy films by adjusting the HiPIMS parameters

Georg C. Gruber, Alice Lassnig, Stefan Wurster, Christoph Gammer, Megan J. Cordill and Robert Franz

Thin Solid Films (submitted)

Tuning microstructure and properties of MoNbTaWZr high entropy alloy films by adjusting the HiPIMS parameters

GEORG C. GRUBER[1†*], ALICE LASSNIG[2], STEFAN WURSTER[2], CHRISTOPH GAMMER[2], MEGAN J. CORDILL[1,2] AND ROBERT FRANZ[1]

[1]*Department of Materials Science, Montanuniversität Leoben, Franz-Josef-Straße 18, 8700 Leoben, Austria*

[2]*Erich Schmid Institute of Materials Science, Austrian Academy of Sciences, Jahnstrasse 12, 8700 Leoben, Austria*

[†]*corresponding author (georg.gruber@unileoben.ac.at)*

KEYWORDS

High Entropy Alloy, Refractory Metal, MoNbTaW, Thin Film, Amorphous Film, High Power Impulse Magnetron Sputtering,

ABSTRACT

Within this study a series of MoNbTaWZr thin films were synthesized using high power impulse magnetron sputtering (HiPIMS) with varying the deposition parameters: duty cycle from 0.5 to 100 % (i.e. DC magnetron sputtering (DCMS)), Ar pressure from 0.5 to 3 Pa and pulse frequency from 25 to 200 Hz. The structure of the deposited films was analyzed by X-ray diffraction and scanning and transmission electron microscopy. In addition, the electrical resistivity and the residual stress of the films was determined. The influence of the deposition parameter variation on structure and properties of the MoNbTaWZr films is discussed on the established framework of film growth conditions achievable with HiPIMS and DCMS and how they can be influenced by adapting the deposition parameters. The performed work is intended to contribute to a comprehensive understanding about synthesis-structure-property relations for refractory high entropy alloy thin films while using MoNbTaWZr films as a model system.

1 INTRODUCTION

Since their introduction in the early 2000s by Yeh [1] and Cantor [2], the scientific interest in high entropy alloys (HEAs) has been increasing each year. HEAs are alloys with a configurational entropy of at least $1.5R$ [3], where R is the gas constant. Due to these high entropy values the formation of simple solid solution phases with face-centered cubic, body-centered cubic (bcc) or hexagonal close-packed (hcp) structure is usually preferred over the formation of intermetallic phases [3]. HEAs consisting of mainly refractory elements are called refractory HEAs [4] and are promising candidates for future high temperature applications due to their high thermal stability. Within the refractory HEAs, MoNbTaVW, introduced by Senkov et al. [5,6], is studied most in literature and known for its good thermal stability and high strength at elevated temperatures [6]. To further improve the yield strength and the ductility, V was substituted by different elements, for example by Ti, which indeed improves the desired properties especially at room temperature [7,8]. However, substituting V by Zr resulted in an even more pronounced improvement on those properties [9,10]. This means of all studied MoNbTaW-based HEAs the equimolar MoNbTaWZr alloy has the highest yield strength and highest ductility [9,10].

Among the different methods used to synthesize HEAs, physical vapor deposition has been employed since the introduction of HEA thin films [11–15]. Similar to the bulk refractory HEAs, also in the case of thin films, MoNbTaW-based refractory HEAs are most studied within literature. MoNbTaW-based films are known for their good thermal stability [16,17]. Films based on MoNbTaW are potential candidate to serve as diffusion barrier within microelectronic systems [18–20]. For diffusion barriers, an amorphous microstructure is superior to a polycrystalline one, because of the missing grain boundaries, which act as fast diffusion channels [21,22]. The microstructure of thin films depends strongly on the growth conditions, and therefore the deposition parameters [23]. High power impulse magnetron sputtering (HiPIMS), which is a variant of magnetron sputtering, allows for a wide variety of parameters to be tuned [24]. During deposition the pulse frequency and duty cycle (ratio between the pulse on-time and the total pulse duration including pulse off-time) can be varied for HiPIMS in addition to the target power, working gas pressure, substrate temperature, bias voltage and working distance which are the most common parameters for DC-magnetron sputtering (DCMS).

To study the correlation between deposition parameters and film growth conditions in HiPIMS processes with the formation of the film's microstructure and evolution of relevant properties, a comprehensive investigation on the synthesis of MoNbTaWZr films deposited by HiPIMS and DCMS was carried out. MoNbTaWZr was chosen as a model system as frequently amorphous microstructures were observed in Zr-containing metal films [25,26]. Within the current work, the deposition parameters Ar pressure, duty cycle and pulse frequency were varied and correlated with the obtained microstructure of the synthesized MoNbTaWZr films. Further, the properties of the deposited films are evaluated in terms of electrical resistivity and residual stresses.

2 EXPERIMENTAL DETAILS

For the synthesis of the refractory HEA films an equimolar MoNbTaWZr target with a diameter of 76 mm was used, which was manufactured by powder metallurgical methods by Plansee Composite Materials GmbH (Lechbruck, Germany). The films were deposited on polished 325 µm thick B-doped (100) Si substrates (21 mm × 7 mm) using a lab-scale deposition system equipped with an unbalanced magnetron source. The substrates were carefully cleaned with acetone and afterwards ethanol in an ultrasonic bath before deposition and then placed in front of the magnetron source at a distance of 150 mm. Subsequently, the chamber was evacuated to a base pressure of $9 \cdot 10^{-4}$ Pa or below, before Ar was introduced to establish the deposition pressure of 0.5, 0.7, 1, 2 or 3 Pa. The deposition was carried out with a power of 400 W which was averaged over the pulses in the case of HiPIMS. Here, duty cycles of 0.5, 1, 2 or 4 % as well as 100 % (DCMS deposition) were used. All these parameter variations were carried out with a constant pulse frequency of 100 Hz. An additional second set of experiments had the pulse frequency varied for the duty cycle values of 0.5 % and 1 % applying 25, 50 or 200 Hz and 50 or 200 Hz, respectively. The Ar pressure in these cases was kept constant at 2 Pa. During the deposition processes the discharge voltage and current were monitored by an oscilloscope. No external heating was applied and the substrate holder was on ground potential. The substrate temperature due to heating from the plasma reached a maximum value of around 100 °C as measured by a thermocouple placed next to the Si substrates.

The thickness of the deposited films was analyzed using a Keyence VK-X1100 Series 3D confocal laser scanning microscope. The deposition rate was calculated by dividing the measured film thickness by the corresponding deposition time, which was 35 min in the case of the films deposited using HiPIMS and 20 min in the case of the films deposited using DCMS. The chemical composition of the as-deposited films was measured by energy-dispersive X-ray (EDX) spectroscopy using a Bruker Type XFlash 6-60 detector which was attached to a Tescan Magna scanning electron microscope (SEM). From each film analyzed, 40 spectra were recorded and the mean value and the standard deviation were calculated. In addition, surface images were taken using the SEM with a back scatter electron detector. The microstructure of the films was analyzed by X-Ray diffraction (XRD) using a Bruker-AXS D8 Advance diffractometer equipped with Cu-K_α radiation and parallel optics. The measurements were performed in Bragg-Brentano geometry. The resistivity of the films was measured by a Jandel Model RM2 cylindrical four-point probe using three measurement points on each sample. The residual stresses of the film were measured using the wafer curvature method with a custom-built device with two parallel laser beams [27]. The cross-sectional film microstructures were characterized by means of transmission electron microscopy (TEM) using a JEOL 2200 FS operating at 200 kV. For this purpose, TEM specimens were prepared by a mechanical wedge polishing technique followed by ion polishing in a Gatan PIPS II system.

3 RESULTS

3.1 DEPOSITION PROCESS

In Figure 1, the dependence of the discharge voltage on the deposition parameters Ar pressure, duty cycle and pulse frequency is shown. Although the target material and deposition device were kept constant, these deposition parameter changes are influencing the discharge voltage significantly, which shows an overall variation from -260 V to -760 V. With increasing duty cycle as well as with increasing Ar pressure, the discharge voltage decreases. Furthermore, when applying a low duty cycle of 0.5 %, an increase in the frequency, which is equivalent to a reduction in pulse length, results in an increase of the discharge voltage. In contrast, no influence of the pulse frequency was noticed for a duty cycle of 1 %.

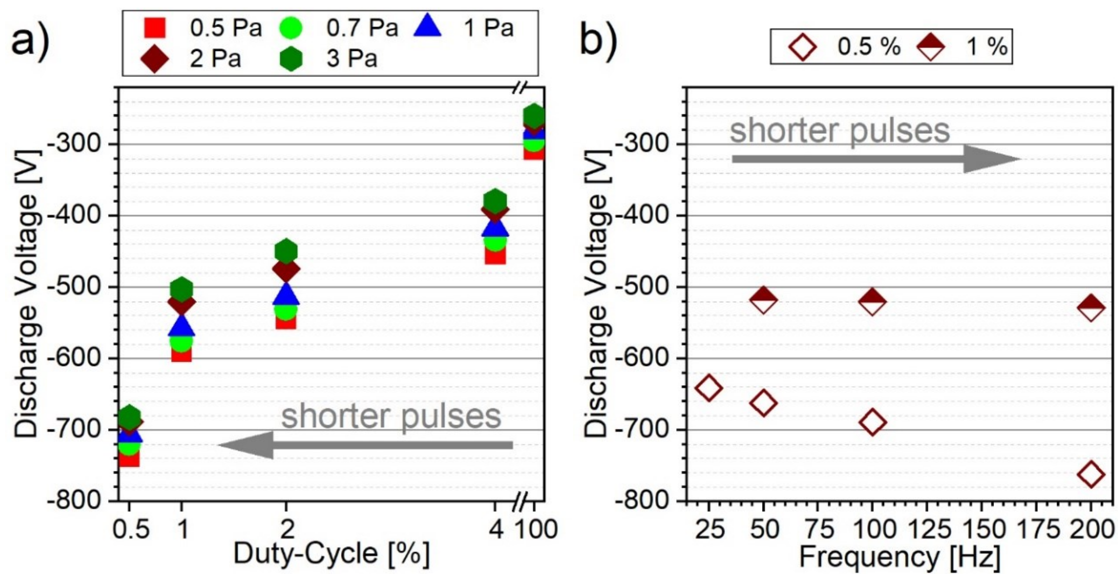

Figure 1: Discharge voltage as a function of (a) the duty cycle for different Ar pressures at a constant pulse frequency of 100 Hz and (b) the pulse frequency for duty cycles of 0.5 and 1 % at constant Ar pressure of 2 Pa.

Further details about the discharge can be derived from the current pulses that are displayed in Figure 2 in conjunction with the corresponding voltage pulses for the variation of duty cycle and Ar pressure. The voltage pulses show a rectangular shape regardless of the pulse length and only change in their height, which is already summarized in Figure 1 where the average values of voltage pulse heights are compared for the different discharge parameters. However, the current pulses reveal some distinct changes when varying duty cycle and Ar pressure. With increasing duty cycle, which corresponds to an increase in pulse length, the peak current decreases significantly from up to 170 A to around 30 A. When applying an Ar pressure of 1 Pa and a duty cycle of 0.5 % the current reaches a plateau after about half of the pulse length and the current stays constant until the end of the peak. When applying a duty cycle of 1 %, with the same Ar pressure of 1 Pa, the current peak also reaches a maximum value after about half of the pulse length but then decreases slightly. In the case of 2 % duty cycle, the current reaches its maximum value early in the pulse and then decreases before stabilizing at a lower level for the second half of the pulse. At the highest duty cycle of 4 % the current hardly reaches a maximum but mainly stays constant during the entire pulse. Similar observations for the current pulses with varying duty cycle can be made for the other Ar pressure values within this work. However, minor differences do exist. For example, with decreasing Ar pressure the delay time between the voltage pulse onset and the current pulse onset increases. Such a delay has been described in literature in detail and it depends on the working

gas pressure and the applied voltage [24]. While for the duty cycles of 2 and 4 % this change in delay time is basically the only influence of the Ar pressure, further changes in the current peak shape can be observed for the duty cycles of 0.5 and 1 %. In the case of 0.5 % duty cycle, the length of the current plateau increases with increasing Ar pressure. A similar observation is also true for 1 % duty cycle but in this case a reduction of the current occurs after the peak value where the reduction is more pronounced with decreasing Ar pressure.

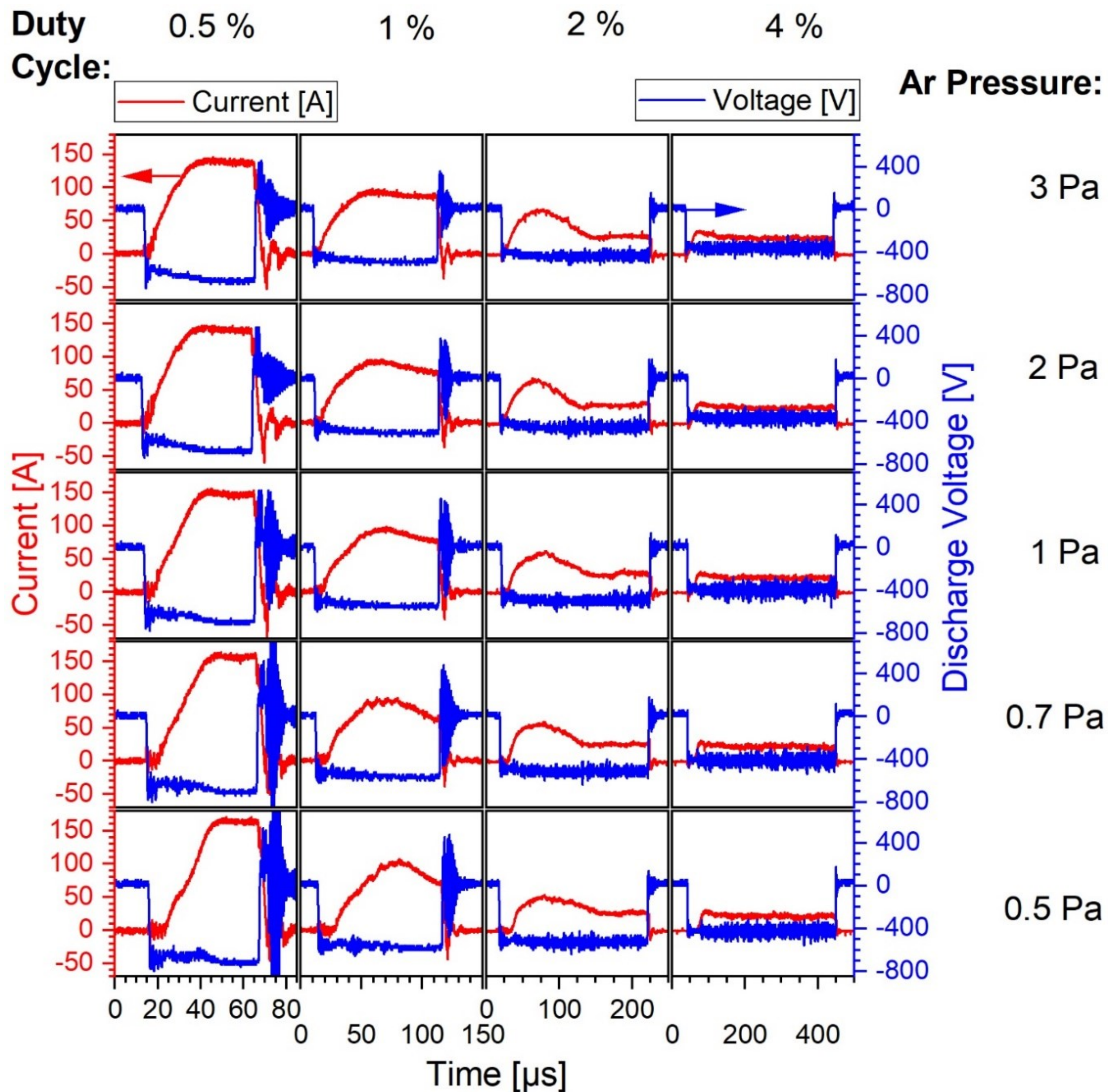

Figure 2: The evolution of discharge current and discharge voltage during pulse on-time for varying duty cycles and Ar pressures (pulse frequency: 100 Hz).

Besides the duty cycle and the Ar pressure also the pulse frequency was varied at a constant Ar pressure of 2 Pa for two different duty cycles of 0.5 and 1 %. The current pulses for the variation of the pulse frequency are shown in Figure 3. It should be noted that a pulse at a duty cycle of 0.5 % and a frequency of 25 Hz has the same pulse on-

time as a pulse at a duty cycle of 1 % and 50 Hz pulse frequency. In these cases, the current peak shapes are similar, only the peak current is significantly lower for the discharges at the higher duty cycle. The peaks with the highest pulse on-time show a first maximum early in the pulse and a second maximum with a lower peak current in the second half of the pulse. For the second longest pulse on-time of 100 µs, the current increases first to a maximum value and then decreases again towards the end of the pulse. Further, in the case of the pulse on-time of 50 µs, the current increases to a maximum and then remains constant at this value for the lower duty cycle of 0.5 % or slightly decreases for the higher duty cycle of 1 %. The shortest pulse on-time of 25 µs was only used for a duty cycle of 0.5 %. Here, the current is continuously increasing through the entire pulse and reaches its maximum value at the end of the peak. The peak current of about 170 A is the highest one within this work.

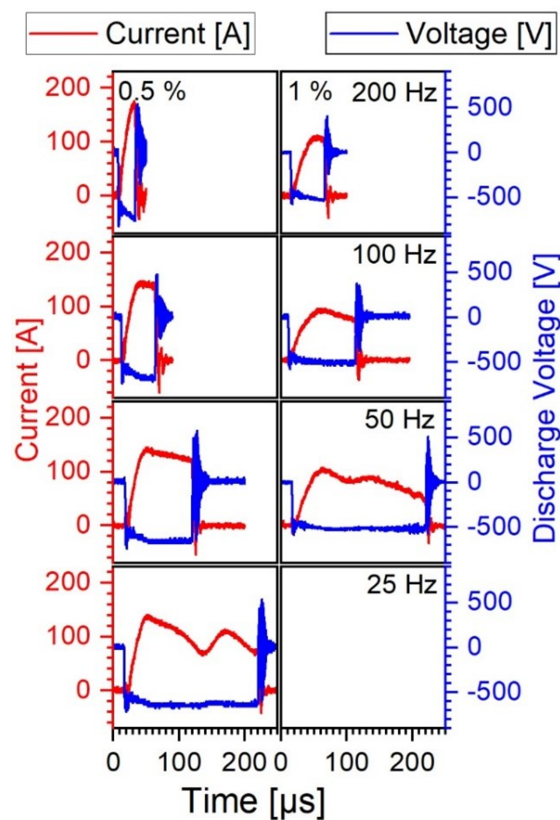

Figure 3: The evolution of discharge current and discharge voltage during pulse on-time for two different duty cycles and varying pulse frequencies (Ar pressure: 2 Pa).

The deposition rate determined for the variation of the discharge parameters is shown in Figure 4. The highest deposition rates were found for films deposited using the highest duty cycle 100 % (see Figure 4a), i.e. DCMS. Among them, the maximum deposition rate was recorded for the films deposited with the maximum Ar pressure of 3 Pa within this work. The films deposited with a duty-cycle of 100 % and 2 Pa did not

adhere to the substrate, thus, no deposition rate could be determined. For the films deposited using HiPIMS at a pulse frequency of 100 Hz, the highest deposition rate was found for the films deposited with the lowest duty cycle of 0.5 % (see Figure 4a). Increasing the duty-cycle to 1 % resulted in a pronounced reduction of the deposition rate, whereas with a further increase to 2 % a slight increase was noticed. The deposition rate remained largely constant with further raising the duty cycle to 4 % but it showed a distinct dependence on the Ar pressure, where a higher deposition rate was obtained with increasing Ar pressure. Such a dependence is absent for the other duty cycles studied. As shown in Figure 4b, the deposition rate generally decreases with decreasing pulse frequency. However, also in this case the dependence is not strict and other effects occurring during the deposition process may be superimposed.

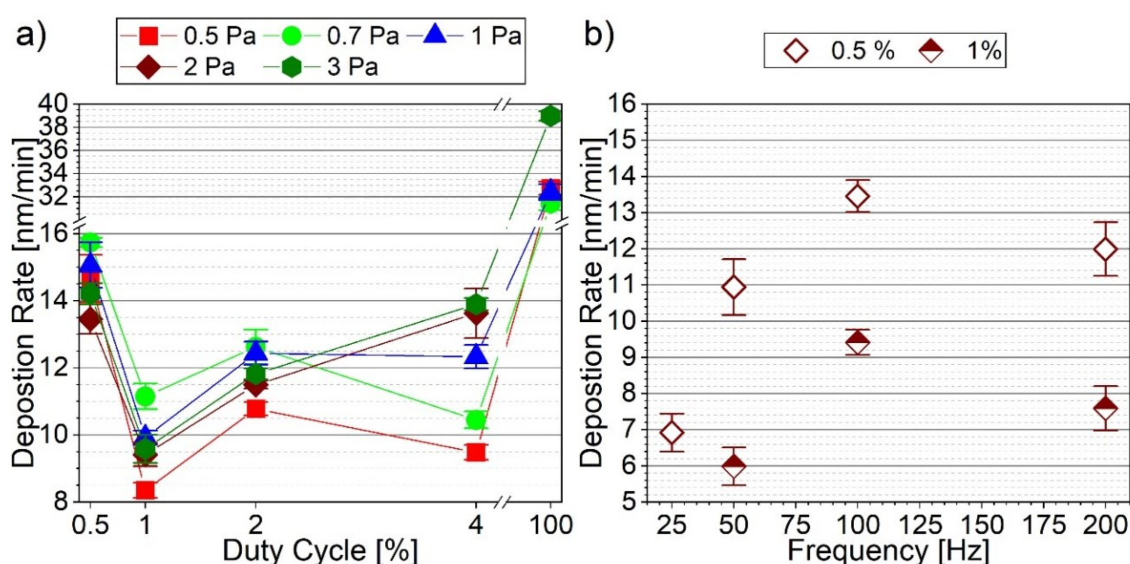

Figure 4: Deposition rate as a function of (a) the duty cycle for different Ar pressures at a constant pulse frquency of 100 Hz and (b) the pulse frequency for duty cycles of 0.5 and 1 % at constant Ar pressure of 2 Pa. Lines are a guide for the eye.

3.2 Chemical Composition

The chemical composition of selected films was measured to study the influence of duty cycle and Ar pressure. As seen in Figure 5a, the Zr content decreases with increasing duty cycle for both Ar pressures, 0.7 and 2 Pa. However, the fractions of the other elements remain largely constant regardless of variations in the duty cycle of the depositions by HiPIMS. The fractions of Nb and Mo are typically slightly above 20 at.% which represents an equimolar chemical composition, while Ta and W are typically slightly below this value. An exception is encountered for the DCMS deposition (100 % duty cycle) where a tendency of enrichment in the heavier elements Ta and W

was noticed for an Ar pressure of 0.7 Pa. As mentioned above, the films for 2 Pa Ar pressure did not adhere to the substrate impeding the determination of the chemical composition.

With increasing Ar pressure the Zr content generally increases, as shown in Figure 5b. For the discharges operated with a higher duty cycle of 4 %, the content of Mo and Nb slightly decreases to compensate the increase in Zr content. The fraction of Ta and W remain constant regardless of the change in Ar pressure. The films deposited with a lower duty cycle of 0.5 % show a similar trend. However, in this case the content of the heavier elements (Ta and W) decrease with increasing Ar pressure, especially above 0.7 Pa.

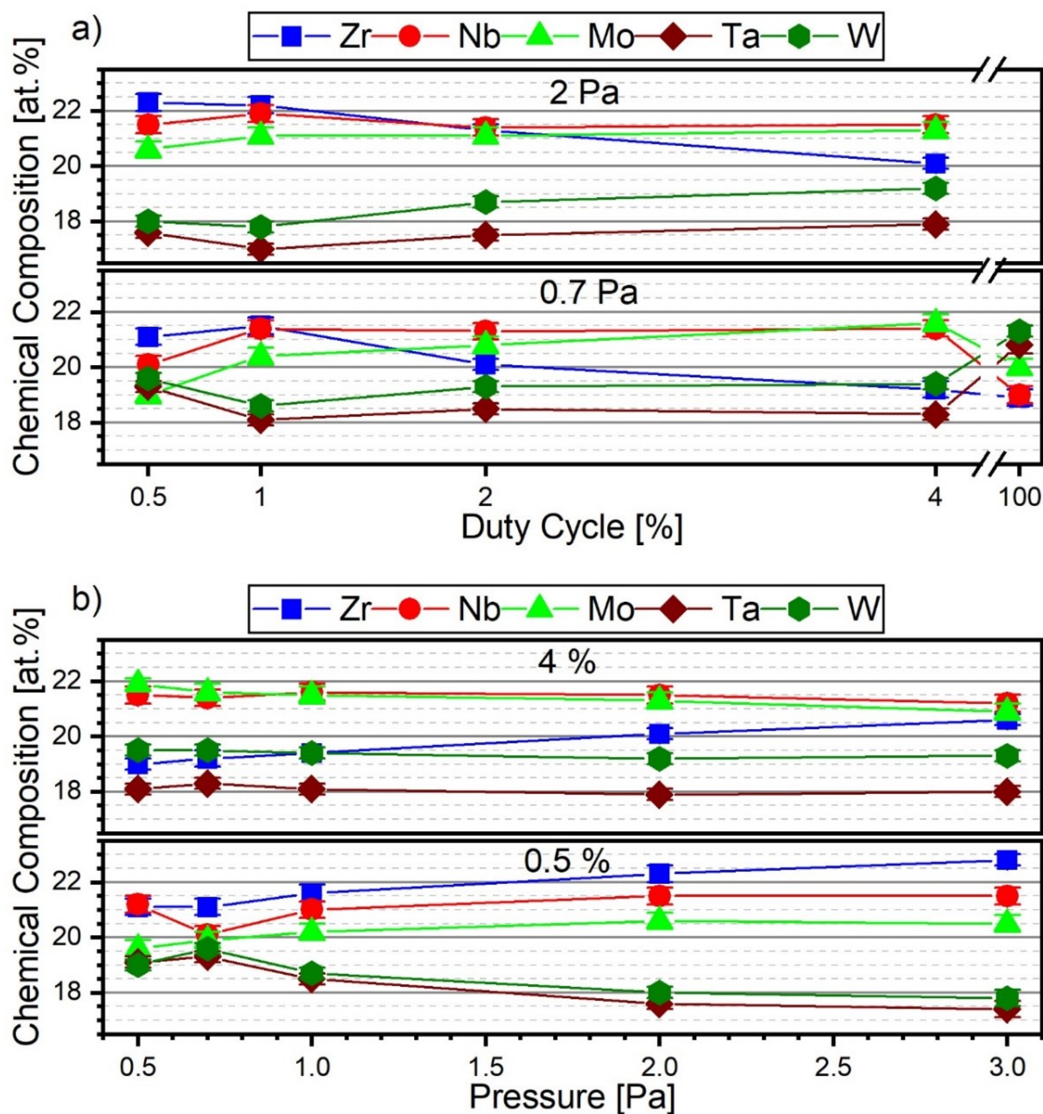

Figure 5: The chemical composition with (a) varying duty cycle for 0.7 and 2 Pa Ar pressure and (b) varying Ar pressure for 0.5 and 4 % duty cycle. The pulse frequency was 100 Hz in all cases. Lines are a guide for the eye and have no mathematical meaning.

3.3 MICROSTRUCTURE AND MORPHOLOGY

Information about the microstructure of the different films was derived from X-ray diffractograms shown in Figure 6. The expected peak position was calculated based on Vegard's rule using an equimolar chemical composition [28]. The observed microstructures can be divided into three types, an amorphous microstructure, a crystalline bcc microstructure and a mixed microstructure, consisting of a crystalline bcc microstructure with a pronounced fraction of an amorphous phase. The amorphous microstructure is indicated by a broad peak, while the crystalline bcc microstructure is indicated by the appearance of a sharp peak. The mixed microstructure has features of both other phases (crystalline and amorphous), a broad peak in combination with a small, sharp peak due to the bcc fraction in the film. The amorphous microstructure is mainly found for films deposited with a duty cycle of 1 % and low Ar-pressures, 0.5 or 0.7 Pa. A mixed microstructure is found for films deposited with a duty cycle of 0.5 % as well as 1 % at higher Ar pressures of 2 and 3 Pa. The films deposited with a duty cycle of 2 % and an Ar-pressure of 0.5 or 1 Pa also revealed a mixed microstructure. In summary, amorphous or mixed microstructures are preferentially found for films deposited with lower duty cycles. In contrast, crystalline films are found for films deposited with high duty cycle, in particular 4 and 100 %. In the case of 1 % duty cycle only the film deposited at an Ar pressure of 1 Pa shows a crystalline microstructure as well as for a duty-cycle of 2 % the films deposited at Ar pressures of 0.7, 2 or 3 Pa. Crystalline peaks, especially those deposited at low Ar pressures, show a pronounced shoulder towards higher diffraction angles similar to the ones reported in [15]. The films deposited with a duty cycle of 100 % and an Ar pressure of 2 Pa were not measured due to poor adhesion to the substrate.

Figure 7 shows the X-ray diffractograms of the films deposited with varying pulse frequency. The microstructure of the films deposited with a duty cycle of 0.5 % is amorphous regardless of the pulse frequency. In a similar way, the films deposited with a duty cycle of 1 % all revealed a mixed microstructure. However, the intensity of the crystalline peak in this case increases with decreasing pulse frequency.

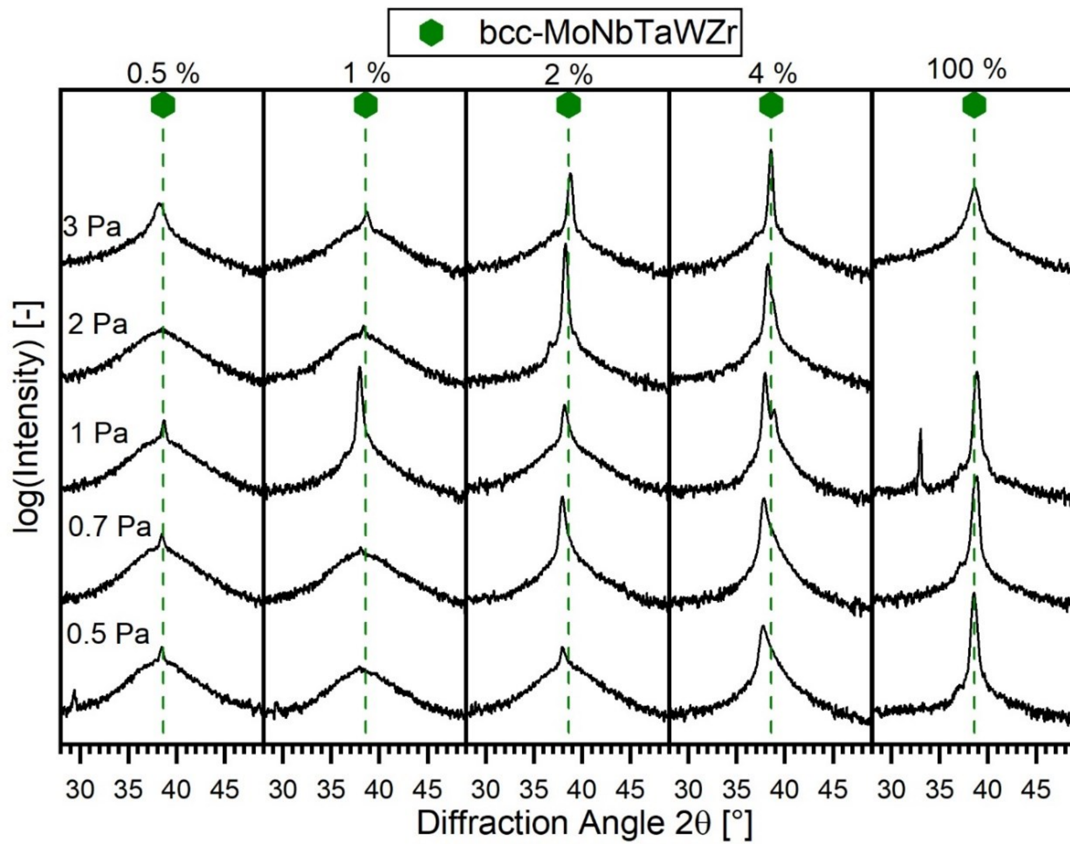

Figure 6: X-ray diffractograms of films deposited with varying duty cycle and Ar pressure. The pulse frequency was 100 Hz in all cases.

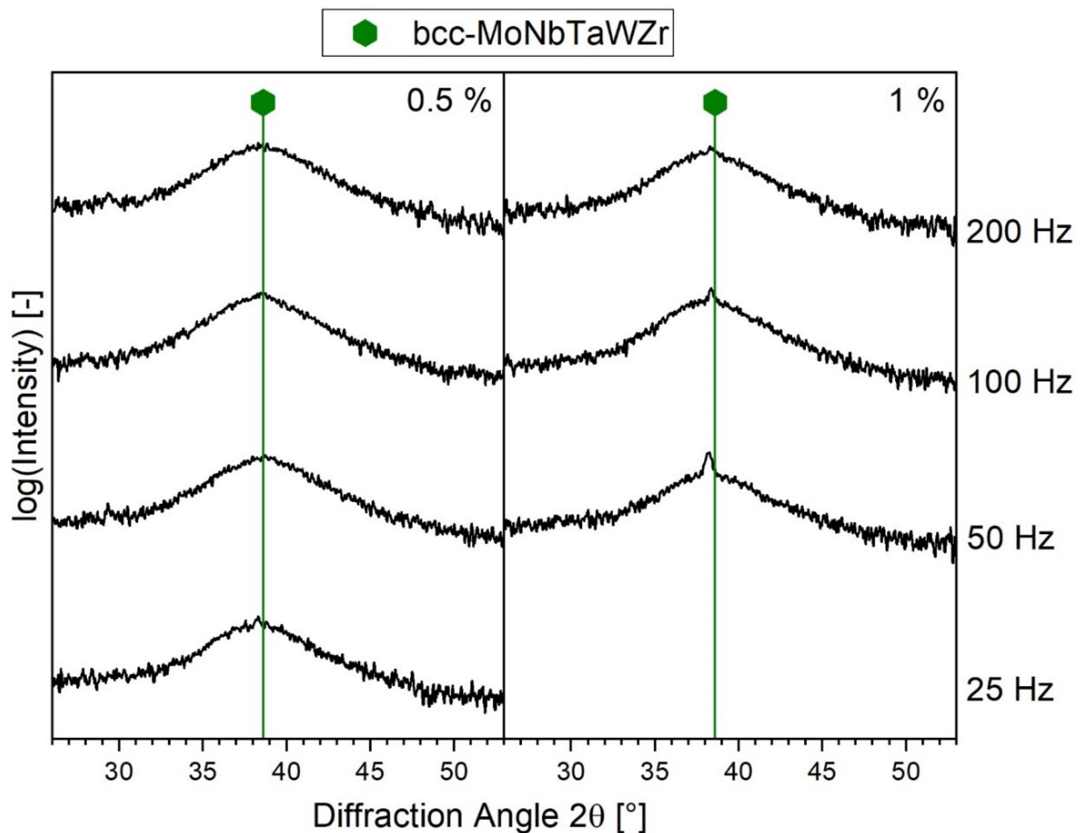

Figure 7: X-ray diffractograms of films deposited with varying pulse frequency at duty cycles of 0.5 and 1 %. The Ar pressure was 2 Pa in all cases.

The surface morphology of the MoNbTaWZr films was evaluated from SEM images recorded with a backscattered electron detector as shown in Figure 8. According to the film surface, the films can be divided into three groups, those with a smooth and patterned surface, those with a smooth and featureless surface and those with featured surfaces. The films with a smooth and pattered surface are deposited with a duty cycle of 2 % or higher. Films with a smooth and featureless surface are mostly deposited with a duty cycle of 1 %, but also with a duty cycle of 0.5 % and an Ar pressure of 0.7 Pa and lower. Films deposited with a duty cycle of 0.5 % and an Ar pressure higher than 0.7 Pa show a featured surface.

To complement the observations on the surface morphology and microstructure observed by XRD, cross-sections of the two films deposited with a duty cycle of 0.5 % and two different Ar pressures (0.7 and 2 Pa) were investigated using TEM. The bright-field scanning TEM (Figure 9a) shows a not fully dense morphology, which is visible by the brighter elongated areas, indicating open boundaries, for the film deposited with an Ar pressure of 2 Pa. The high-resolution TEM image (Figure 9b) and the select area electron diffraction (SAED) pattern (Figure 9c) suggest that the film is amorphous which agrees with XRD analysis shown in Figure 6. The film deposited with a lower Ar pressure of 0.7 Pa shows two types of microstructures depending on the distance to the substrate. While the film is fully amorphous near the substrate (Figure 9e), some parts of the film are crystalline near the film surface (Figure 9d). This agrees to the SAED pattern (Figure 9f) and the X-ray diffractogram (Figure 6), which also suggest a mixture of an amorphous and a crystalline part.

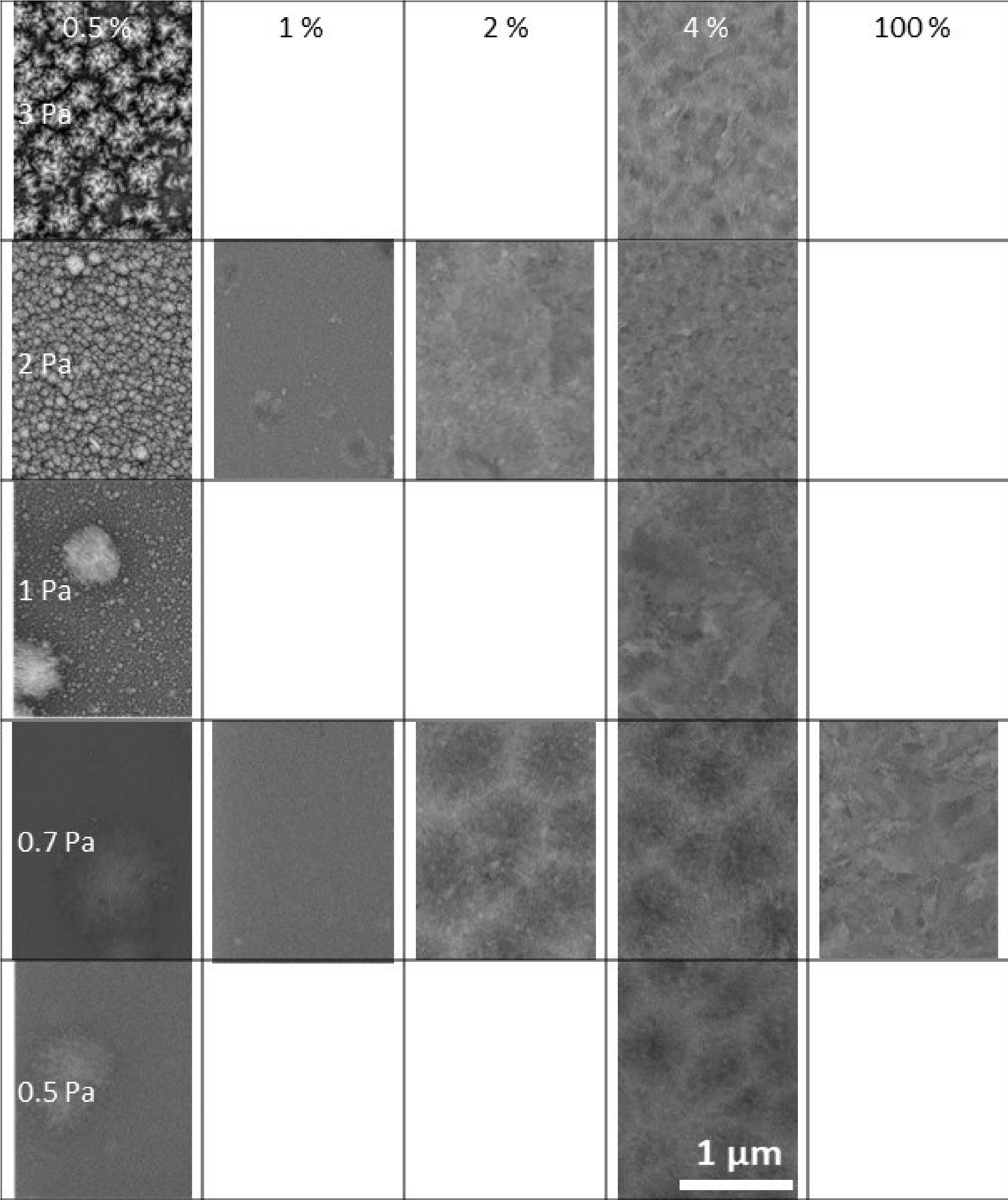

Figure 8: SEM images of the surfaces of different films taken with a backscattered electron detector.

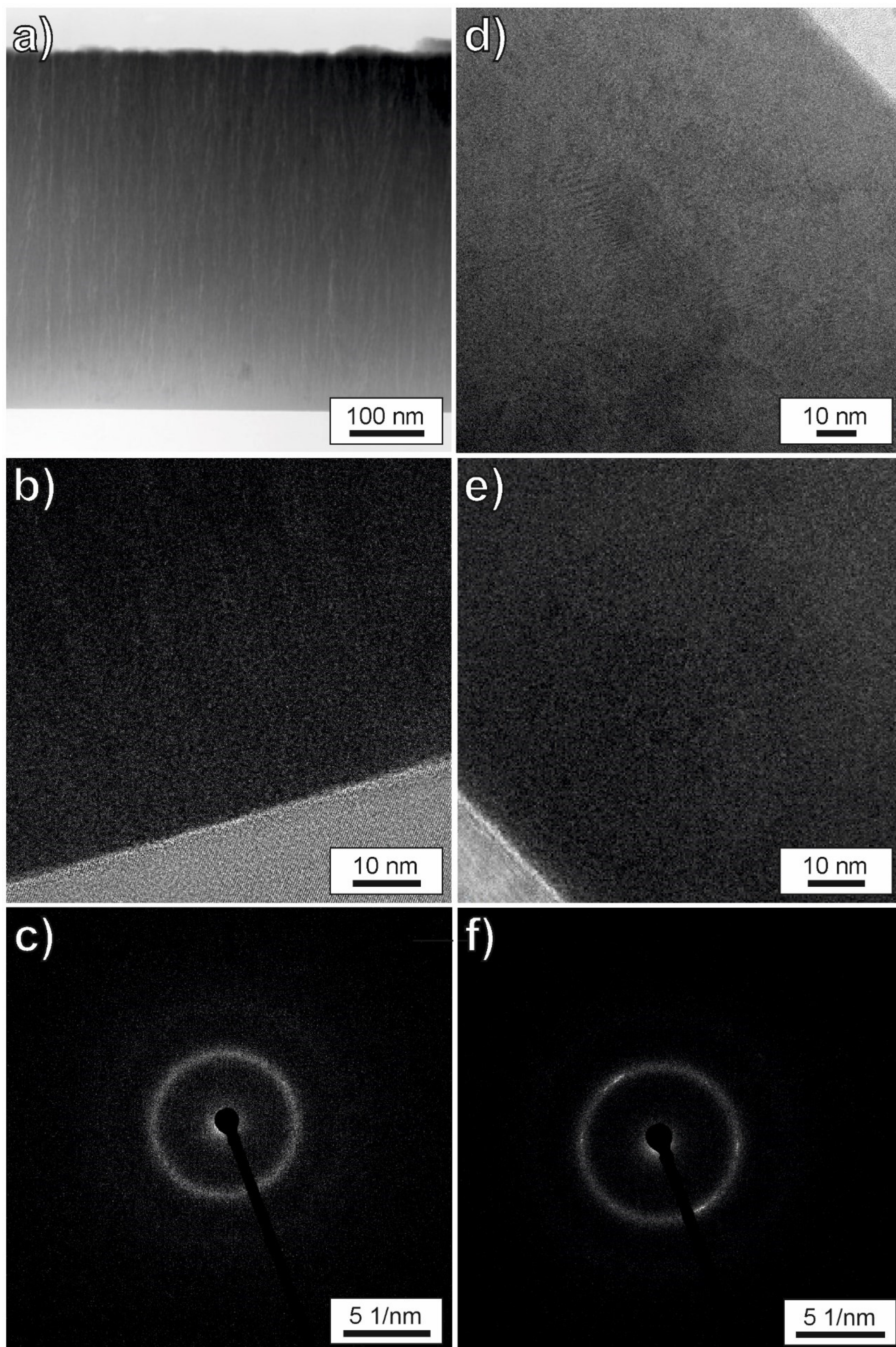

Figure 9: TEM investigation of films deposited with a duty cycle of 0.5 % and different Ar pressures: a)-c) 2 Pa and d)-f) 0.7 Pa. a) shows a bright-field scanning TEM image, b), d) and e) show high resolution TEM images taken near the substrate (b and e) and near the film surface (d). c) and f) show SAED patterns of the two different films.

3.4 Resistivity and Residual Stress

The synthesized MoNbTaWZr films were further analyzed as to their resistivity and residual stress. According to the values obtained for resistivity shown in Figure 10, the films can be divided into three groups: (i) a resistivity below 115 µΩcm, (ii) between 115 and 215 µΩcm and (iii) above 215 µΩcm. The films belonging to the first group were mostly deposited with duty cycles of 4 and 100 %, while some films deposited with lower duty cycles of 1 and 2 % also belong to this group. The most noticeable exception is the film deposited with a duty cycle of 100 % and 3 Pa which showed a significantly higher resistivity.

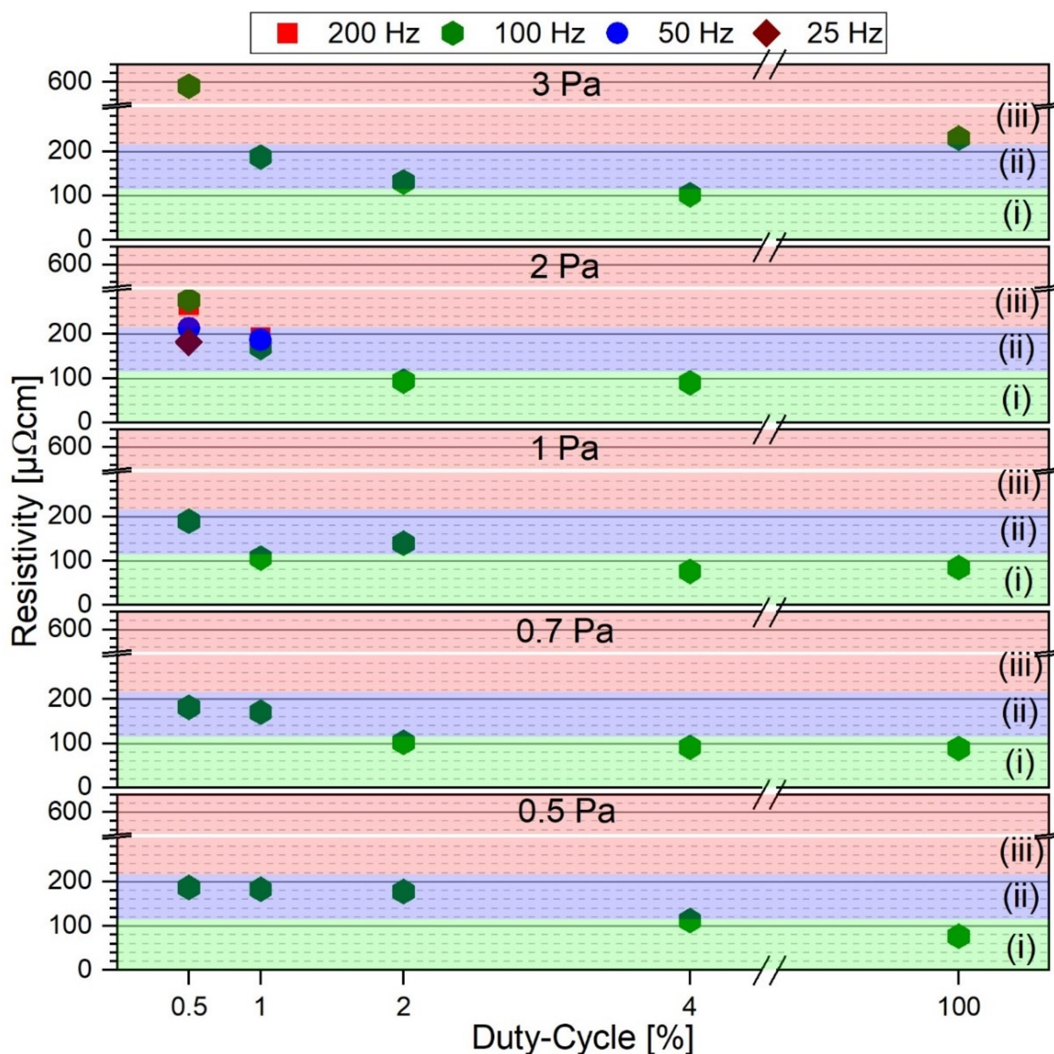

Figure 10: Resistivity values of the different MoNbTaWZr films deposited with varying duty cycle, Ar pressure and pulse frequency.

The films with medium resistivity (second group) were mostly deposited with low duty cycles of 0.5 and 1 %. This includes also the films deposited with varying pulse frequencies except for the cases of duty cycle 0.5 % and pulse frequencies of 100 and

200 Hz. The third group comprises mainly films deposited with a duty cycle of 0.5 % and high Ar pressures. As a general trend, an increase in duty cycle results in a decrease of the resistivity.

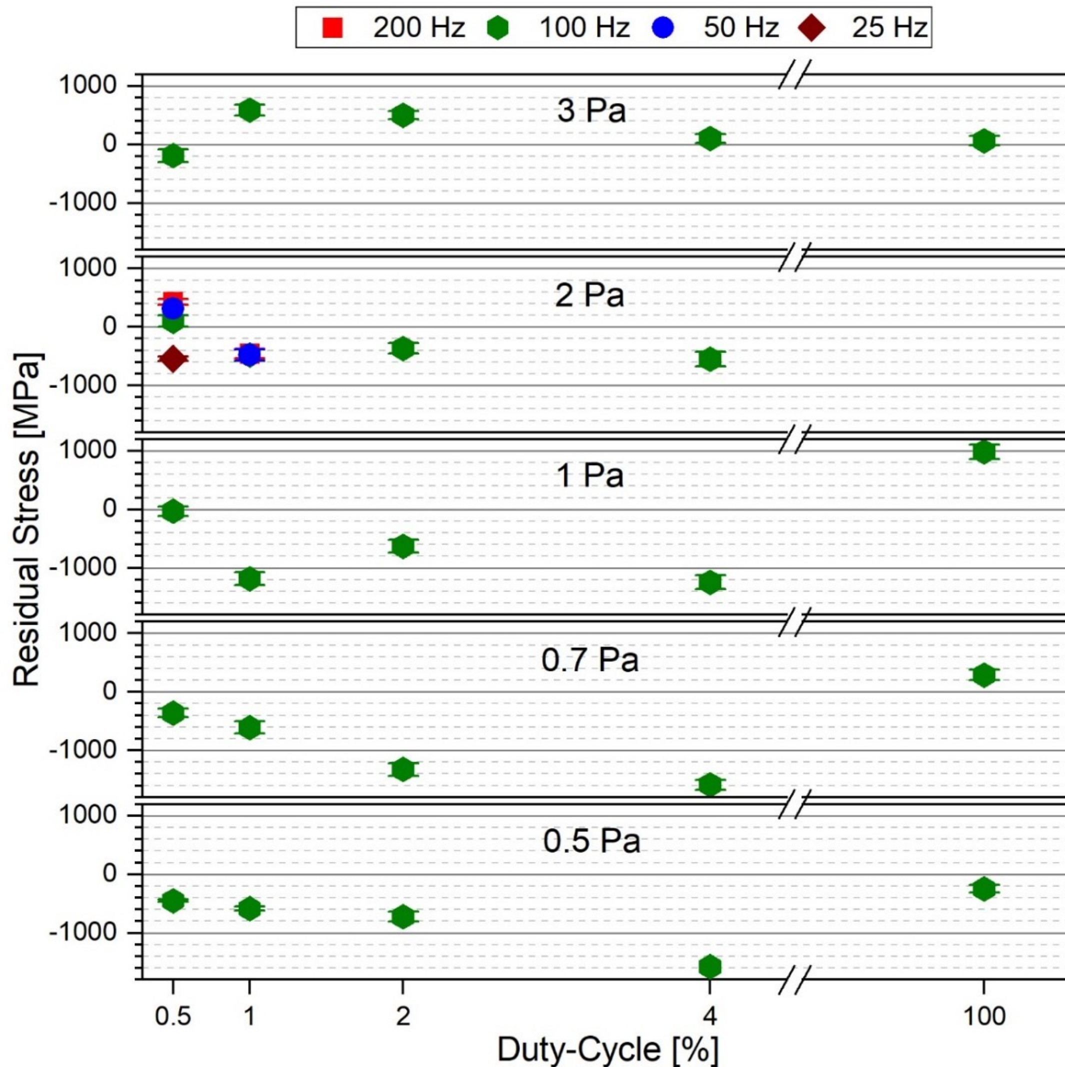

Figure 11: Residual stress values of the MoNbTaWZr films deposited with different duty cycles, Ar pressures and pulse frequencies.

Another important aspect in terms of film properties is the residual stress which is displayed in Figure 11. For Ar pressures up to 1 Pa, the compressive residual stress generally increases with increasing duty cycle up to 4 %. For the films deposited with a duty cycle of 100 %, i.e. DCMS, a transition from compressive to tensile residual stresses with increasing Ar pressure was observed. All films deposited with an Ar pressure of 2 Pa and a duty cycle of 1 % or above show a compressive stress of about -500 MPa. Only in the case of the duty cycle of 0.5 % a transition from about 500 MPa tensile stress to about -500 MPa compressive was noticed with decreasing pulse frequency. No clear trend is present in the evolution of the residual stress of the films

deposited with an Ar pressure of 3 Pa. The films are either in a stress-free state or revealed a tensile stress of about 500 MPa

4 DISCUSSION

4.1 HIPIMS DISCHARGE

While varying the deposition parameters within this work, the average power $\bar{P}$ was always kept constant. Nevertheless, as the pulse length varied for the different duty cycles used (at constant frequency), the average pulse power density also varied, as shown in Figure 12 for a discharge operated with a pulse frequency of 100 Hz and an Ar pressure of 1 Pa. In general, the average pulse power density, $\bar{p}_{pulse}$, is calculated according to:

$$\bar{p}_{pulse} = \frac{1}{A_{target} \cdot t_{pulse}} \int_{t_{pulse-start}}^{t_{pulse-end}} i(t) \cdot u(t) dt, \qquad (1)$$

where A_{target} is the target area, t_{pulse} is the pulse length, $t_{pulse-begin}$ and $t_{pulse-end}$ are the start and end time of the pulse, $i(t)$ is the current and $u(t)$ is the voltage. In the actual case $\bar{p}_{pulse}$ only depends on the duty cycle or rather the pulse on-time as $\bar{P}$ is constant. Variations in other parameters like Ar pressure or pulse frequency causing a change in the discharge voltage will be balanced by altering the current to keep $\bar{P}$ constant. As shown in Figure 12, $\bar{p}_{pulse}$ increases significantly with decreasing duty cycle. Here, both discharge voltage and current increase, which has been frequently reported in literature for a decrease in pulse on-time [24].

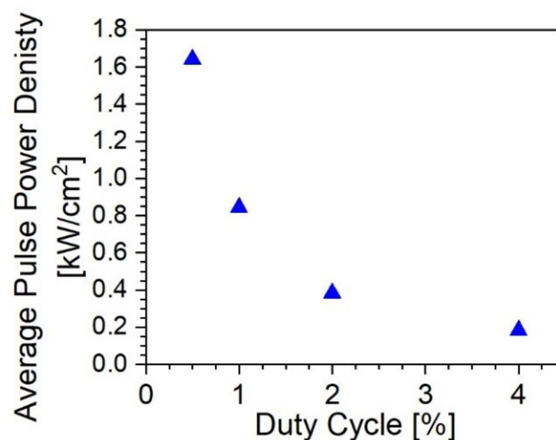

Figure 12: Average pulse power density as a function of duty cycle for discharges operated at a pulse frequency of 100 Hz and an Ar pressure of 1 Pa.

For the discharges operated with constant duty cycle (0.5 or 1 %) by varying the frequency, $\bar{p}_{pulse}$ remains constant. The 1 % duty cycle results also in a constant discharge voltage when varying the frequency, while a slight increase in voltage was observed for 0.5 % duty cycle with increasing frequency. A possible explanation for the latter may be the longer off-time for the discharges with a lower frequency leading to a reduced concentration of ions during the after-glow, which is the end of the pulse off-time or the beginning of the new pulse [29]. When the voltage pulse is turned on, the remaining ions are accelerated towards the target and help initiate the next pulse which can be noticed by a reduction in the discharge voltages. However, further studies including a detailed analysis of the plasma, the change in gas and metal ion fractions during the pulse, i.e. the transition to self-sputtering [24,30], are required to clarify this effect unambiguously.

The influence of the Ar pressure on the discharge voltage is clearly noticeable in Figure 1 as the voltage decreases with increasing Ar pressure. In general, a higher number of Ar atoms present in the discharge region facilitates ionization collisions and lower voltages to accelerate the electrons are needed. This situation is independent of the applied duty cycle. Additionally, an increased Ar pressure leads to more ions present in the after-glow, which, as mentioned above, is beneficial for the ignition of a new pulse [29]. As the plasma ignition is facilitated in this way, the delay time between voltage and current peak is decreased as seen in Figure 2. The same effect can be observed when increasing the frequency (see Figure 3), as the pulse off-time is reduced with increasing frequency.

Considering the shape of the current pulses shown in Figure 2, discharge mode present in the HiPIMS pulses can be attributed to working gas sustained self-sputtering [24,31]. This mode can be seen best for the discharges using a duty cycle of 2 %. Typically, such current peaks increase to a maximum in the initial part of the pulse, but then decrease until they reach a steady state for the remaining time of the pulse. Even though the plateau values for the pulses with 2 % and 4 % duty cycle are similar at constant Ar pressure, the current maximum at 4 % duty cycle is significantly lower than the maximum at 2 %. In the case of 1 % duty cycle no steady state is reached but the current decrease after reaching the current maximum is a sign that also these discharges can be assigned to working gas sustained self-sputtering [24,31]. In general, the decrease in current after a certain time in the pulse is typically explained

by gas rarefaction effects [32,33]. For the lowest duty cycle used in this work, the pulse length is too short to unambiguously classify the pulses. However, it can be expected that for such short pulse lengths the discharge does not have sufficient time to transform to a self-sputtering mode according to refs. [24,30].

A similar situation is encountered for the variation of the pulse frequency, where the shape of the current pulses also suggests the occurrence of working gas sustained self-sputtering [24,31]. Again, short pulses, in this case down to 25 μs, are cut off before the steady-state plateau is reached. However, this variation includes long pulses at low duty cycle and low pulse frequency (50 and 25 Hz) that show a distinct second maximum during the pulse. Such a second maximum is seen as an indication for working gas refill during the first current decrease [32].

The deposition rates of the films deposited with a duty cycle of 100 %, i.e. DCMS, are two to three times higher compared to the rates of the films deposited using HiPIMS. Such a difference is in agreement with frequent reports in literature, e.g. [24,34], which is explained by a significant back attraction of the sputtered metal ions not contributing to the film growth [24,35]. Of the films deposited using HiPIMS, the highest deposition rate was found for the films deposited using a duty-cycle of 0.5 %. As already discussed earlier, for such short pulse lengths, the metal ionization rate is lower and, therefore, a lower part of the sputtered material is attracted back towards the target [24,30]. When the pulse length increases but the duty cycle is kept constant at 0.5 %, the deposition rate decreases, which supports this assumption that with increasing pulse length the discharge has enough time to transition from pronounced gas sputtering to a significant fraction of self-sputtering which in turn causes a reduction of the deposition rate due to the back attraction of sputtered metal ions [30]. A similar trend is found for the films deposited with a duty cycle of 1 %. However, a minor reduction in the deposition rate is present when increasing the pulse frequency to 200 Hz for both duty cycles which is most likely unrelated to the metal ion recycling. The deposition rate of the MoNbTaWZr films deposited with duty cycles of 2 and 4 % is generally similar and slightly higher compared to the one in the case of a duty cycle of 1 %.

In terms of Ar pressure, only the films deposited using a duty cycle of 4 % show a clear dependency of the deposition rate on the Ar pressure. Reports in literature suggest an increase in deposition rate with increasing Ar pressure due to a reduction in the fraction

of metal ions [33,36]. It appears that other effects are superimposed to the influence of the Ar pressure, like angular distribution, sticking of atoms/ions on the growing film, re-sputtering or film density, which are not in the focus of the current work, rendering the influence of the Ar pressure less significant.

4.2 FILM PROPERTIES

The obtained chemical composition of the MoNbTaWZr films generally reflects the target composition regardless of the deposition parameters. This means that the use of powder-metallurgically produced targets is a promising approach to synthesize high entropy alloy thin films. The minor deficiency in the heavy elements Ta and W in several films, shown in Figure 5, is most likely related to slight differences in the angular emission of the elements as a function of their mass similar to [11].

As mentioned in section 3.3, the films can be divided into three groups, according to their resistivity (Figure 10). Group (i) includes the films with a resistivity below 115 µΩcm, group (ii) those with a resistivity between 115 and 215 µΩcm and group (iii) those with a resistivity higher than 215 µΩcm. Films belonging to group (i) have a crystalline bcc microstructure according to XRD and a smooth and patterned surface according to the surface images. Crystalline films with high compressive stresses (see Figure 11) show a shoulder towards higher 2Θ diffraction angles in their X-ray diffractograms (see Figure 6). This shoulder is an indication for an inhomogeneous stress distribution within the films, as it was also found for other MoNbTaW-based refractory HEA films deposited by HiPIMS [15]. The lowest measured resistivity values are around 80 µΩcm and are obtained for the crystalline films deposited with duty cycles of 4 % and 100 %. In comparison, for pure Mo films deposited by DCMS a resistivity in the range from 10 to 20 µΩcm was measured where a larger grain size yielded a lower resistivity [37,38]. The reason for the generally higher resistivity of the MoNbTaWZr films is the distorted lattice of HEAs, which leads to more electron scattering and an increase in resistivity [39,40]. Other factors contributing to an increased resistivity include crystal defects, like vacancies, interstitials and dislocations.

The microstructure of the films within group (ii) is amorphous or a mixture between amorphous and crystalline and their surface morphology is smooth and patterned or featureless (see Figure 8). This is corroborated by the cross-sectional TEM investigations of a film from this group (see Figure 9 d-f) which show that in the region

near the substrate the film is fully amorphous, while in the region near the surface amorphous and crystalline parts exist. A possible explanation for the transition from amorphous to partly crystalline microstructure is the decrease in defect density with increasing film thickness [41]. The resistivity of the fully amorphous films is about 180 µΩcm, while with increasing fraction of the crystalline part in the films it reduces down to 130 µΩcm. The latter can again be understood by reduced electron scattering in crystalline parts as compared to amorphous or grain boundary regions.

The films of group (iii) have the highest resistivity within this work. According to the X-ray diffractograms (see Figure 6), these films can have a crystalline or amorphous microstructure. The main reason for their high resistivity is the less dense morphology as indicated by the SEM surface pictures (see Figure 8) and confirmed by the cross-sectional TEM investigation (see Figure 9a-c). All these films were deposited at high Ar pressures where the frequent collisions of the sputtered metal atoms and ions results in a pronounced reduction of their kinetic energy and, hence, in low energetic film growth conditions. The fact that a nearly stress-free state is present in these films agrees with such film growth conditions. A change in the pulse frequency in the case of a duty cycle of 0.5 % does not result in a change of the microstructure (see Figure 7), but with lower pulse frequency a reduction in resistivity is observed as well as a shift towards compressive stresses in the films. This change can be understood by the increased pulse length at lower pulse frequency which is associated to a shift from Ar gas ionization towards ionization of the sputtered metal atoms and gas rarefaction effects [24,30] leading to slightly higher energetic growth conditions and a film densification.

While the microstructure of the MoNbTaWZr films within this work ranges from amorphous to a crystalline bcc microstructure, MoNbTaW-based films in literature show a single phase bcc microstructure [11,15,42]. Since in these publications, no extensive variation of the deposition parameters was performed, the possibility to deposit other MoNbTaW-based films with an amorphous microstructure still remains. In the case of bulk MoNbTaWZr alloy the formation of a crystalline microstructure consisting of two slightly different bcc phases was reported [9,10]. A similar result was obtained for a powder of the material [43]. The existence of a bcc solid solution microstructure is in agreement with phase stability calculations that also suggest the formation of this microstructure for MoNbTaW-based alloys [44]. However, for WZr_x films deposited by DCMS formation of an amorphous microstructure was observed

[25,26]. In this work an amorphous microstructure was only obtained in films deposited by HiPIMS while all films deposited by DCMS (duty cycle of 100 %) were crystalline with a bcc microstructure.

In general, an amorphous microstructure is a microstructure with a high level of disorder, which can be caused by the incorporated defects [45]. As known from literature, with increasing film thickness the defect density is decreasing [41] which can cause a transition from amorphous to crystalline microstructure during film growth. This phenomenon can be observed in Figure 9d-f, where the film near the substrate is fully amorphous and only near the film surface (film thickness of about 550 nm) a partly crystalline microstructure is observed. A similar behavior was also found for other MoNbTaW-based films, where the amorphous layer near the substrate had a thickness of up to a few 10 nm [15]. On the one hand, this means that care needs to be taken when comparing the microstructure of different MoNbTaWZr films as their film thickness plays a significant role in determining which microstructure is formed even when all deposition parameters are kept constant. On the other hand, the deposition parameters can be tuned to increase the defect density in the films by increasing the energy of the incoming particles [46], where, as mentioned above, an increasing defect densities enhances the tendency to form an amorphous microstructure. Ways to increase the energy of the incoming particle include a reduction of the Ar pressure [23], increasing the target voltage [23] or increasing the peak power [47]. As shown by Magnfält et al. [47] the particle energy increases with increasing peak power, which is the case when reducing the duty cycle as discussed above. This means that the highest particle energies within this work can be expected at low Ar pressure and low duty cycle, and indeed this is the parameter set region where films with an amorphous microstructure were obtained. When the particle energy is slightly reduced by increasing the duty cycle or the Ar pressure competing microstructures, amorphous and crystalline bcc, are encountered. This region comprises films deposited with a duty cycle of 1 % and Ar pressures of 1 Pa or above as well as films deposited with a duty cycle of 2 % regardless of the Ar pressures. It is hypothesized that this region can be seen as a transition region, where small changes in the film growth conditions, including the state of substrate surface, can result in the formation of either amorphous or crystalline microstructure or a mixture of both.

5 CONCLUSIONS

Within this study the HiPIMS deposition parameters Ar pressure, duty cycle and pulse frequency were systematically varied to tune microstructure and properties of the synthesized MoNbTaWZr HEA films. Here, high energetic film growth conditions achieved at low Ar pressure and short pulses, for example, low duty cycle or high pulse frequency, yielded films with fully amorphous microstructure or a mixture of amorphous and crystalline bcc microstructure. These films are characterized by medium values of electrical resistivity ranging from 115 to 215 µΩcm and residual stresses ranging from stress-free to medium levels of compressive stress. A transition to lower energetic film growth conditions by increasing Ar pressure and duty cycle resulted in an increase of the fraction of bcc microstructure in the films up to fully crystalline films. This transition was associated with a decrease in electrical resistivity, if a dense film morphology was preserved, due to a reduced electron scattering in the crystalline microstructure. Exceptions to this rule were observed at high Ar pressures, where underdense film morphologies were obtained causing a significant increase in electrical resistivity as a result of enhanced electron scattering at underdense grain boundaries. The residual stress in the mainly crystalline films varied from compressive with up to -1.5 GPa to tensile with up to 500 GPa depending on the film morphology, i.e. the density of the grain boundaries.

ACKNOWLEDGEMENTS

The authors acknowledge the funding from the Austrian Research Promotion Agency (FFG) (project number: 871687). A. Lassnig acknowledges funding from the Austrian Science Fund (FWF) (project number T891-N36).

REFERENCES

[1] J.-W. Yeh, S.-K. Chen, S.-J. Lin, J.-Y. Gan, T.-S. Chin, T.-T. Shun, C.-H. Tsau, S.-Y. Chang, Nanostructured High-Entropy Alloys with Multiple Principal Elements: Novel Alloy Design Concepts and Outcomes, Advanced Engineering Materials 6 (2004) 299–303. https://doi.org/10.1002/adem.200300578.

[2] B. Cantor, I. Chang, P. Knight, A. Vincent, Microstructural development in equiatomic multicomponent alloys, Materials Science and Engineering: A 375-377 (2004) 213–218. https://doi.org/10.1016/j.msea.2003.10.257.

[3] B.S. Murty, J.-W. Yeh, S. Ranganathan, High-entropy alloys, Butterworth-Heinemann an imprint of Elsevier, London, Oxford, Amsterdam, San Diego, 2014.

[4] D.B. Miracle, O.N. Senkov, A critical review of high entropy alloys and related concepts, Acta Materialia 122 (2017) 448–511. https://doi.org/10.1016/j.actamat.2016.08.081.

[5] O.N. Senkov, G.B. Wilks, D.B. Miracle, C.P. Chuang, P.K. Liaw, Refractory high-entropy alloys, Intermetallics 18 (2010) 1758–1765. https://doi.org/10.1016/j.intermet.2010.05.014.

[6] O.N. Senkov, G.B. Wilks, J.M. Scott, D.B. Miracle, Mechanical properties of Nb25Mo25Ta25W25 and V20Nb20Mo20Ta20W20 refractory high entropy alloys, Intermetallics 19 (2011) 698–706. https://doi.org/10.1016/j.intermet.2011.01.004.

[7] Z.D. Han, N. Chen, S.F. Zhao, L.W. Fan, G.N. Yang, Y. Shao, K.F. Yao, Effect of Ti additions on mechanical properties of NbMoTaW and VNbMoTaW refractory high entropy alloys, Intermetallics 84 (2017) 153–157. https://doi.org/10.1016/j.intermet.2017.01.007.

[8] Z.D. Han, H.W. Luan, X. Liu, N. Chen, X.Y. Li, Y. Shao, K.F. Yao, Microstructures and mechanical properties of Ti NbMoTaW refractory high-entropy alloys, Materials Science and Engineering: A 712 (2018) 380–385. https://doi.org/10.1016/j.msea.2017.12.004.

[9] T. Li, W. Jiao, J. Miao, Y. Lu, E. Guo, T. Wang, T. Li, P.K. Liaw, A novel ZrNbMoTaW refractory high-entropy alloy with in-situ forming heterogeneous structure, Materials Science and Engineering: A 827 (2021) 142061. https://doi.org/10.1016/j.msea.2021.142061.

[10] S.H. Chen, J.S. Zhang, S. Guan, T. Li, J.Q. Liu, F.F. Wu, Y.C. Wu, Microstructure and mechanical properties of WNbMoTaZrx (x = 0.1, 0.3, 0.5, 1.0) refractory high entropy alloys, Materials Science and Engineering: A 835 (2022) 142701. https://doi.org/10.1016/j.msea.2022.142701.

[11] A. Xia, A. Togni, S. Hirn, G. Bolelli, L. Lusvarghi, R. Franz, Angular-dependent deposition of MoNbTaVW HEA thin films by three different physical vapor deposition methods, Surface and Coatings Technology 385 (2020) 125356. https://doi.org/10.1016/j.surfcoat.2020.125356.

[12] T.-K. Chen, M.-S. Wong, T.-T. Shun, J.-W. Yeh, Nanostructured nitride films of multi-element high-entropy alloys by reactive DC sputtering, Surface and Coatings Technology 200 (2005) 1361–1365. https://doi.org/10.1016/j.surfcoat.2005.08.081.

[13] Y. Zhang, C.C. Koch, S.G. Ma, H. Zhang, Y. Pan, Fabrication Routes, in: M.C. Gao, J.-W. Yeh, P.K. Liaw, Y. Zhang (Eds.), High-Entropy Alloys, Springer International Publishing, Cham, 2016, pp. 151–179.

[14] A. Xia, R. Dedoncker, O. Glushko, M.J. Cordill, D. Depla, R. Franz, Influence of the nitrogen content on the structure and properties of MoNbTaVW high entropy alloy thin films, Journal of Alloys and Compounds 850 (2021) 156740. https://doi.org/10.1016/j.jallcom.2020.156740.

[15] G.C. Gruber, A. Lassnig, S. Zak, C. Gammer, M.J. Cordill, R. Franz, Synthesis and structure of refractory high entropy alloy thin films based on the MoNbTaW system, Surface and Coatings Technology 439 (2022) 128446. https://doi.org/10.1016/j.surfcoat.2022.128446.

[16] A. Xia, R. Franz, Thermal Stability of MoNbTaVW High Entropy Alloy Thin Films, Coatings 10 (2020) 941. https://doi.org/10.3390/coatings10100941.

[17] G.C. Gruber, A. Lassnig, S. Zak, C. Gammer, M.J. Cordill, R. Franz, Thermal stability of MoNbTaTiW, MoNbTaVW and CrMoNbTaW thin films deposited by high power impulse magnetron sputtering, Surface and Coatings Technology 454 (2023) 129189. https://doi.org/10.1016/j.surfcoat.2022.129189.

[18] Y.-T. Hsiao, C.-H. Tung, S.-J. Lin, J.-W. Yeh, S.-Y. Chang, Thermodynamic route for self-forming 1.5 nm V-Nb-Mo-Ta-W high-entropy alloy barrier layer: Roles of enthalpy and mixing entropy, Acta Materialia 199 (2020) 107–115. https://doi.org/10.1016/j.actamat.2020.08.029.

[19] K. Hu, Q.F. Hu, X. Xu, S.H. Chen, J. Ma, W.W. Dong, Excellent diffusion barrier property of amorphous NbMoTaW medium entropy alloy thin films used in Cu/Si Connect System, Vacuum 202 (2022) 111195. https://doi.org/10.1016/j.vacuum.2022.111195.

[20] P.F. Li, Y.J. Ma, H. Ma, S.W. Ta, Z. Yang, X.T. Han, M.J. Kai, J.H. Chen, Z.H. Cao, Enhanced diffusion barrier property of nanolayered NbMoTaW/TiVCr high entropy alloy for copper metallization, Journal of Alloys and Compounds 895 (2022) 162574. https://doi.org/10.1016/j.jallcom.2021.162574.

[21] D. Gupta, Diffusion processes in advanced technological materials, William Andrew Pub, Norwich N.Y., 2005.

[22] Z. Li, Y. Tian, C. Teng, H. Cao, Recent Advances in Barrier Layer of Cu Interconnects, Materials (Basel) 13 (2020) 5049. https://doi.org/10.3390/ma13215049.

[23] M. Ohring, Materials science of thin films: Deposition and structure, second ed., Academic Press, San Diego, CA, 2002.

[24] D. Lundin, A. Hecimovic, T. Minea, A. Anders, N. Brenning, J.T. Gudmundsson, Physics of high power impulse magnetron sputtering discharges, in: High Power Impulse Magnetron Sputtering, Elsevier, 2020, pp. 265–332.

[25] J. Bhattarai, E. Akiyama, H. Habazaki, A. Kawashima, K. Asami, K. Hashimoto, Electrochemical and xps studies of the corrosion behavior of sputter-deposited amorphous W-Zr alloys in 6 and 12 M HCl solutions, Corrosion Science 39 (1997) 355–375. https://doi.org/10.1016/S0010-938X(97)83351-3.

[26] M. Červená, R. Čerstvý, T. Dvořák, J. Rezek, P. Zeman, Metastable structures in magnetron sputtered W–Zr thin-film alloys, Journal of Alloys and Compounds 888 (2021) 161558. https://doi.org/10.1016/j.jallcom.2021.161558.

[27] C. Saringer, M. Tkadletz, C. Mitterer, Restrictions of stress measurements using the curvature method by thermally induced plastic deformation of silicon substrates, Surface and Coatings Technology 274 (2015) 68–75. https://doi.org/10.1016/j.surfcoat.2015.04.038.

[28] L. Vegard, VI. Results of crystal analysis, The London, Edinburgh, and Dublin Philosophical Magazine and Journal of Science 32 (1916) 65–96.

[29] N. Britun, M. Palmucci, S. Konstantinidis, R. Snyders, Particle visualization in high-power impulse magnetron sputtering. I. 2D density mapping, Journal of Applied Physics 117 (2015) 163302. https://doi.org/10.1063/1.4919006.

[30] S. Konstantinidis, J.P. Dauchot, M. Ganciu, A. Ricard, M. Hecq, Influence of pulse duration on the plasma characteristics in high-power pulsed magnetron discharges, Journal of Applied Physics 99 (2006) 13307. https://doi.org/10.1063/1.2159555.

[31] J.T. Gudmundsson, N. Brenning, D. Lundin, U. Helmersson, High power impulse magnetron sputtering discharge, Journal of Vacuum Science & Technology A: Vacuum, Surfaces, and Films 30 (2012) 30801. https://doi.org/10.1116/1.3691832.

[32] C. Huo, M.A. Raadu, D. Lundin, J.T. Gudmundsson, A. Anders, N. Brenning, Gas rarefaction and the time evolution of long high-power impulse magnetron sputtering pulses, Plasma Sources Sci. Technol. 21 (2012) 45004. https://doi.org/10.1088/0963-0252/21/4/045004.

[33] M. Čada, N. Britun, A. Hecimovic, J.T. Gudmundsson, D. Lundin, Heavy species dynamics in high power impulse magnetron sputtering discharges, in: High Power Impulse Magnetron Sputtering, Elsevier, 2020, pp. 111–158.

[34] M. Samuelsson, D. Lundin, J. Jensen, M.A. Raadu, J.T. Gudmundsson, U. Helmersson, On the film density using high power impulse magnetron sputtering, Surface and Coatings Technology 205 (2010) 591–596. https://doi.org/10.1016/j.surfcoat.2010.07.041.

[35] D.J. Christie, Target material pathways model for high power pulsed magnetron sputtering, Journal of Vacuum Science & Technology A: Vacuum, Surfaces, and Films 23 (2005) 330–335. https://doi.org/10.1116/1.1865133.

[36] D. Lundin, M. Čada, Z. Hubička, Ionization of sputtered Ti, Al, and C coupled with plasma characterization in HiPIMS, Plasma Sources Sci. Technol. 24 (2015) 35018. https://doi.org/10.1088/0963-0252/24/3/035018.

[37] M. Rausch, A. Sabag, K.-H. Pichler, G.C. Gruber, J. Köstenbauer, H. Köstenbauer, P. Kreiml, M.J. Cordill, J. Winkler, C. Mitterer, The sputter performance of an industrial-scale planar Mo-target over its lifetime: Target erosion and film properties, Surface and Coatings Technology 381 (2020) 125174. https://doi.org/10.1016/j.surfcoat.2019.125174.

[38] T. Jörg, M.J. Cordill, R. Franz, O. Glushko, J. Winkler, C. Mitterer, The electro-mechanical behavior of sputter-deposited Mo thin films on flexible substrates, Thin Solid Films 606 (2016) 45–50. https://doi.org/10.1016/j.tsf.2016.03.032.

[39] A. Matthiessen, C. Vogt, Ueber den Einfluss der Temperatur auf die elektrische Leitungsfähigkeit der Legirungen, Annalen der Physik 198 (1864) 19–78. https://doi.org/10.1002/andp.18641980504.

[40] R.E. Hummel, Electronic Properties of Materials, Springer New York, New York, NY, 2011.

[41] H. Köstenbauer, G.A. Fontalvo, M. Kapp, J. Keckes, C. Mitterer, Annealing of intrinsic stresses in sputtered TiN films: The role of thickness-dependent gradients of point defect density, Surface and Coatings Technology 201 (2007) 4777–4780. https://doi.org/10.1016/j.surfcoat.2006.10.017.

[42] Y.-Y. Chen, S.-B. Hung, C.-J. Wang, W.-C. Wei, J.-W. Lee, High temperature electrical properties and oxidation resistance of V-Nb-Mo-Ta-W high entropy alloy thin films, Surface and Coatings Technology 375 (2019) 854–863. https://doi.org/10.1016/j.surfcoat.2019.07.080.

[43] M. Xia, Y. Chen, K. Chen, Y. Tong, X. Liang, B. Shen, Synthesis of WTaMoNbZr refractory high-entropy alloy powder by plasma spheroidization process for additive manufacturing, Journal of Alloys and Compounds 917 (2022) 165501. https://doi.org/10.1016/j.jallcom.2022.165501.

[44] H. Liu, L. Liu, C. Xin, Effect of alloying elements on the structure and mechanical properties of NbMoTaWX (X = Cr, V, Ti, Zr, and Hf) refractory high-entropy alloys, AIP Advances 11 (2021) 25044. https://doi.org/10.1063/5.0038405.

[45] M.R. Bennett, J.G. Wright, Amorphous films of the transition elements, Phys. Stat. Sol. (a) 13 (1972) 135–144. https://doi.org/10.1002/pssa.2210130114.

[46] K. Sarakinos, L. Martinu, Synthesis of thin films and coatings by high power impulse magnetron sputtering, in: High Power Impulse Magnetron Sputtering, Elsevier, 2020, pp. 333–374.

[47] D. Magnfält, G. Abadias, K. Sarakinos, Atom insertion into grain boundaries and stress generation in physically vapor deposited films, Appl. Phys. Lett. 103 (2013) 51910. https://doi.org/10.1063/1.4817669.

Publication III

Thermal Stability of MoNbTaTiW, MoNbTaVW and CrMoNbTaW thin films deposited by high power impulse magnetron sputtering

Georg C. Gruber, Alice Lassnig, Stanislav Zak, Christoph Gammer, Megan J. Cordill and Robert Franz

Surface and Coatings Technology 454 (2023) 129189

Thermal Stability of MoNbTaTiW, MoNbTaVW and CrMoNbTaW thin films deposited by high power impulse magnetron sputtering

GEORG C. GRUBER[1†*], ALICE LASSNIG[2], STANISLAV ZAK[2], CHRISTOPH GAMMER[2], MEGAN J. CORDILL[1,2] AND ROBERT FRANZ[1]

[1]*Department of Materials Science, Montanuniversität Leoben, Franz-Josef-Strasse 18, 8700 Leoben, Austria*

[2]*Erich Schmid Institute of Materials Science, Austrian Academy of Sciences, Jahnstrasse 12, 8700 Leoben, Austria*

[†]*corresponding author (georg.gruber@unileoben.ac.at)*

KEYWORDS:

High Entropy Alloy, Refractory Metal, MoNbTaW based, Thin Film, High Power Impulse Magnetron Sputtering, Thermal Stability

ABSTRACT

With the envisioned use as high-temperature materials, the thermal stability of three high entropy alloy thin films, based on the system MoNbTaW with additional Cr, Ti or V, was studied. All films were deposited by high power impulse magnetron sputtering and subsequently annealed in vacuum up to a temperature of 1200 °C and analyzed by X-ray diffraction. The obtained body-centered cubic structure in the as-deposited state remained stable up to the maximum annealing temperature. Measurements of the residual stress by wafer curvature and $\sin^2\Psi$ method revealed a general reduction of the stress with annealing temperature due to defect annihilation.

1 INTRODUCTION

The scientific interest for high entropy alloys (HEAs), introduced by Yeh et al. [1] and Cantor et al. [2] in the early 2000s, is increasing each year. HEAs, are alloys with a configurational entropy of at least $1.5R$ [3], where R is the gas constant. Refractory HEAs, which consist mostly of refractory elements, are of interest for high temperature applications, since refractory elements are known for their high thermal stability. Such alloys were first introduced by Senkov et al. [4,5], who studied MoNbTaW and

MoNbTaVW. They found that these alloys have a good thermal stability and high strength at elevated temperature, exceeding the performance of Ni-based superalloys in vacuum atmosphere. A ductility increase, especially at room temperature (RT), with a similar strength and thermal stability was found when adding Ti to form MoNbTaTiW and MoNbTaTiVW [6,7].

One method to synthesize HEA thin films is magnetron sputtering which has been used since the early days of HEAs [8–10]. Sputtering is a convenient method to synthesize HEAs and study their structure and properties as the microstructure can readily be varied by altering the process parameters and HEA nitride [3,8,11] and oxide [3] films can be deposited by adding N_2 or O_2 to the process gas. Additionally, a multi-source arrangement allows the variation of the chemical composition. A potential application for HEA films is their use as diffusion barriers [12]. Chang et al. showed that with increasing number of elements within a diffusion barrier between Si and Cu, as used within microelectronic systems, the barrier efficacy increases [13]. This makes them interesting candidates for future diffusion barriers. Further, the good thermal stability of refractory HEAs may also enable their use in electronic systems with high thermal loads, e.g. in power electronics. Xia and Franz [14] reported a phase stability of MoNbTaVW films deposited by cathodic arc deposition of up to 1500 °C.

Within the current work, MoNbTaTiW, MoNbTaVW and CrMoNbTaW films have been deposited using high power impulse magnetron sputtering (HiPIMS) and form a body-centered cubic (bcc) structure as reported in our previous work [15]. HiPIMS was used for the synthesis as it enables the deposition of dense films [16], a beneficial feature for the intended use as diffusion barriers. After annealing the films in vacuum up to 1200 °C, their microstructure was analyzed using X-ray diffraction (XRD) to study the thermal stability. In addition, the stresses of the films before and after annealing were measured using the wafer curvature method and the $\sin^2\Psi$ method.

2 Experimental Details

For the synthesis of the refractory HEA films, equimolar MoNbTaTiW, MoNbTaVW, CrMoNbTaW targets with a diameter of 76 mm were used, which were manufactured by powder metallurgical methods by Plansee Composite Materials GmbH (Lechbruck, Germany). The films were deposited on polished 325 µm thick B-doped (100) Si substrates (21 mm × 7 mm), polished 500 µm thick (0001) sapphire substrates

(10 mm x 10 mm) and polyvinyl alcohol (PVA) foils (150 mm x 50 mm) using a lab-scale deposition system equipped with an unbalanced magnetron source. The Si and sapphire substrates were carefully cleaned with acetone and afterwards ethanol in an ultrasonic bath before deposition and then placed in front of the magnetron source at a distance of 150 mm. Subsequently, the chamber was evacuated to a base pressure of $9\cdot10^{-4}$ Pa or below, before Ar was introduced to establish the deposition pressure of 1 Pa. The deposition in HiPIMS mode was carried out with an average power of 400 W, a frequency of 100 Hz and a duty cycle of 2 % leading to a peak power density of 0.7 kW/cm^2. Here, the duty cycle is defined as the ratio between the pulse on-time (200 µs) and the pulse duration (10000 µs). Further details, e.g. voltage and current pulse shapes, can be found in our previous work where the identical deposition process was used [15]. No external heating was applied and the substrate holder was on ground potential. The substrate temperature due to heating from the plasma reached a maximum value of around 100 °C as measured by a thermocouple placed next to the Si substrates. After deposition, the PVA foils were dissolved in cold distilled water while stirring to ensure that only the film material remained as a solid. The solid film material was then filtered from the solution and ground to a fine-grained powder by a mortar.

The chemical composition of the films was measured by energy-dispersive X-ray (EDX) spectroscopy using a Bruker Type XFlash 6-60 detector which was attached to a Tescan Magna scanning electron microscope (SEM). The microstructure of the films and the powders was analyzed by XRD using a Bruker-AXS D8 Advance diffractometer equipped with Cu-K_α radiation and parallel optics. The measurements were performed in Bragg-Brentano geometry. From the diffractograms the full width at half maximum (FWHM) and the lattice constant were determined by fitting the peaks with a pseudo-Voigt function. The residual stresses of the films were measured using the wafer curvature method with a custom-built device with two parallel laser beams [17]. For the evaluation of the stresses the modified Stoney equation [18,19] was used. Additionally, the stresses were measured using a Bruker-AXS D8 Advance DaVinci diffractometer using the $\sin^2\Psi$ method [20]. To measure the stresses using XRD a Euler cradle was used and the (110) peak was measured at Ψ angles of 0.00, 18.44, 26.56, 33.22, 39.24, 45.00, 50.76, 56.78, 63.44 and 71.56°. The peaks were fitted using a Pearson VII function. The stresses were then evaluated by using the Young's modulus measured in our previous paper [15], and the Poisson's ratio was assumed to be 0.3.

The evaluation of the stresses, determined by the $\sin^2\Psi$ method, was done by using the Bruker Leptos 7.10 software.

The annealing experiments in vacuum comprised a temperature from 100 to 1200 °C in 100 °C steps. Before the annealing of the films the furnace was evacuated to a pressure of $5\cdot10^{-4}$ Pa. For each annealing step a different sample was used. Up to an annealing temperature of 700 °C films deposited on Si were used, at higher temperatures the substrate was changed to sapphire. For the annealing of the samples annealed at 100 and 200 °C the heated substrate stage in a custom-built deposition system was employed. For all other annealing temperatures, a HTM Retz vacuum furnace was used. In the first step this vacuum furnace was heated up to 250 °C with a heating rate of 20 K/min. To allow the temperature to stabilize, a waiting period of 30 minutes was introduced. Afterwards, the vacuum furnace was heated up to the desired annealing temperature with the same heating rate. The annealing temperature was kept constant for 15 minutes before cooling down to RT in vacuum. In addition to the films on the substrates, a sample of each powdered film was annealed in the sequence 400, 600, 800 and 1000 °C using the vacuum furnace.

3 Results and Discussion

3.1 Chemical Composition

The deposited films have a film thickness between 300 and 400 nm and Table 1 shows the chemical composition of the different films in their as-deposited state and after annealing at 800, 1000 and 1200 °C. All films showed a slight O content which remains similar up to an annealing temperature of 1000 °C. The metal ratio of the different HEA films before and after annealing is shown in Figure 1. Taking into account a typical error of ±1 at.% for the EDX measurements, most of the elements revealed a content of around 20 at.% in the as-deposited films, which would be expected for an equimolar alloy. Even though the Ta concentration is generally slightly lower, the films can still be considered near equimolar. Up to an annealing temperature of 1000 °C the metal ratios of the different elements in the films remains constant (Figure 1). However, after annealing at 1200 °C, the Mo and W contents in the films decrease, slightly in the case of MoNbTaTiW or pronounced as in the case of MoNbTaVW and CrMoNbTaW. Additionally, as shown in Table 1, the O content

within the films increases significantly. The strongest change in Mo and W as well as O content was found for MoNbTaVW. The decrease of the Mo and W content cannot be explained by evaporation of these elements directly out of the film due to their low vapor pressure in this temperature range [21], but by the volatility of their oxides. Hung et al. [22] observed a decreasing Mo and W content within the films after annealing MoNbTaVW films at 800 °C in air. In the present case the residual O in the vacuum chamber causes a slight oxidation during annealing, especially above 1000 °C. As a consequence of the loss in Mo and W, the fraction of the other metals increases in the metal ratio presented in Figure 1. Further, as parts of the film evaporate, film thickness and density of the film may decrease. This can result in a stronger signal from the substrate in the EDX measurements, which in turn may be a contributing factor to the increased O content.

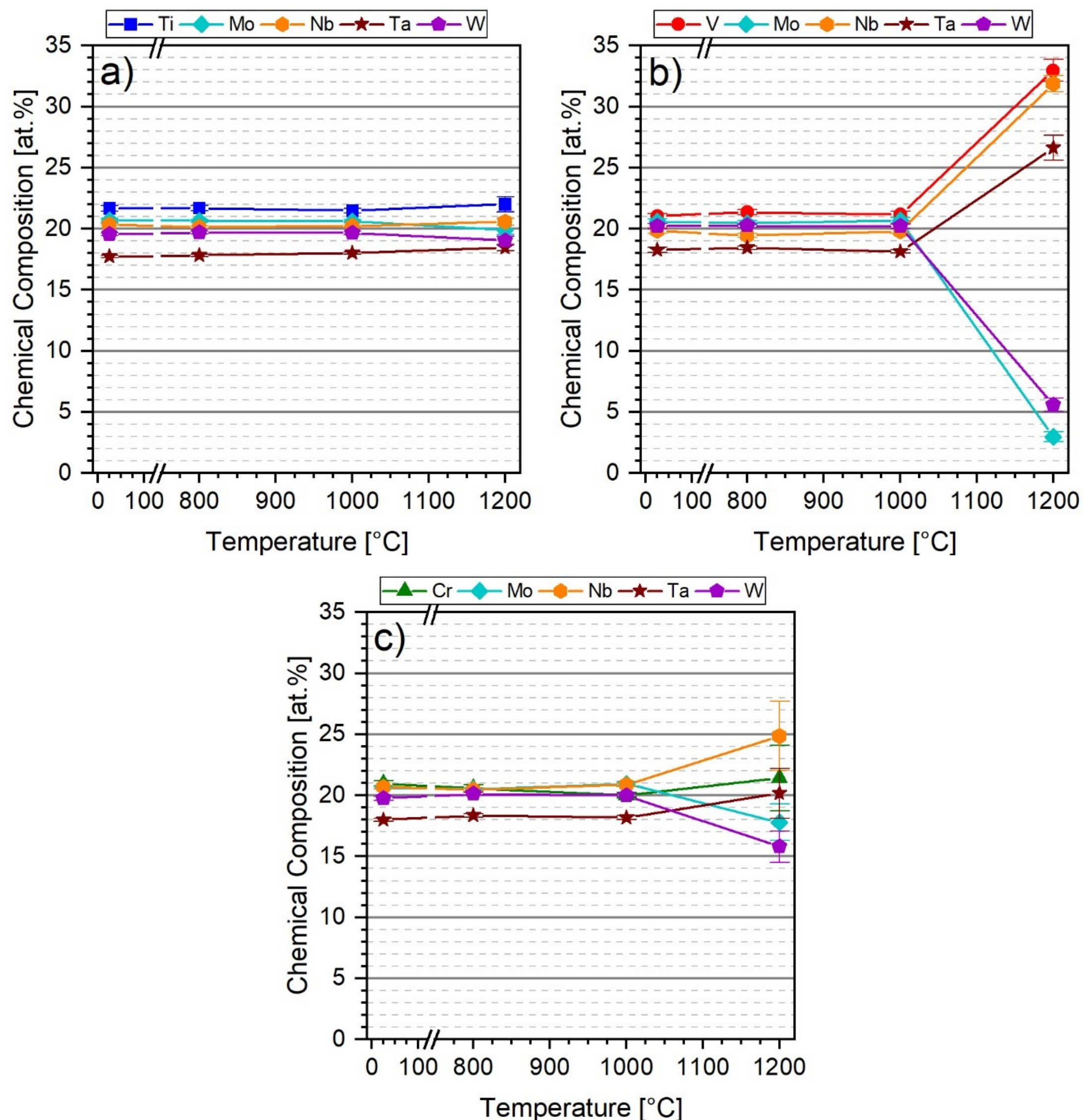

Figure 1: The metal ratio of the different HEA films as measured by EDX: (a) MoNbTaTiW, (b) MoNbTaVW and (c) CrMoNbTaW. The values shown are an average of twenty spectra.

Table 1: Chemical composition of the HEA thin films, deposited on sapphire, as measured by EDX. The values shown are an average of twenty spectra. The O signal originating from the sapphire substrate was deducted based on the measured Al signal for each sample and considering an Al_2O_3 stoichiometry. All values are in at.%.

	Temperature	Mo	Nb	Ta	W	Ti	V	Cr	O
MoNbTaTiW	As deposited	19.9 ±0.2	19.5 ±0.1	17.0 ±0.1	18.7 ±0.1	20.8 ±0.2	-	-	4.1 ±0.4
	800 °C	19.3 ±0.1	18.9 ±0.1	16.7 ±0.1	18.4 ±0.1	20.3 ±0.2	-	-	6.4 ±0.4
	1000 °C	19.5 ±0.2	19.2 ±0.1	17.1 ±0.1	18.6 ±0.1	20.4 ±0.2	-	-	5.2 ±0.4
	1200 °C	16.2 ±0.3	16.8 ±0.3	15.0 ±0.2	15.5 ±0.3	17.9 ±0.6	-	-	18.4 ±0.8
MoNbTaVW	As deposited	19.5 ±0.2	18.8 ±0.2	17.3 ±0.2	19.1 ±0.2	-	19.9 ±0.2	-	5.4 ±0.9
	800 °C	19.9 ±0.2	18.9 ±0.2	17.9 ±0.2	19.7 ±0.1	-	20.8 ±0.2	-	2.8 ±0.6
	1000 °C	19.8 ±0.2	19.0 ±0.2	17.4 ±0.1	19.3 ±0.2	-	20.3 ±0.3	-	4.3 ±0.6
	1200 °C	1.3 ±0.4	14.5 ±0.7	12.1 ±1.0	2.5 ±0.5	-	14.9 ±0.9	-	54.7 ±2.5
CrMoNbTaW	As deposited	20.2 ±0.1	20.3 ±0.1	17.6 ±0.1	19.4 ±0.2	-	-	20.5 ±0.2	2.0 ±0.3
	800 °C	19.9 ±0.2	19.9 ±0.1	17.8 ±0.1	19.6 ±0.1	-	-	20.0 ±0.3	2.7 ±0.4
	1000 °C	20.2 ±0.2	20.2 ±0.1	17.6 ±0.2	19.3 ±0.2	-	-	19.3 ±0.3	3.4 ±0.7
	1200 °C	14.1 ±1.8	19.8 ±2.8	16.0 ±2.0	12.5 ±1.3	-	-	17.0 ±2.7	20.5 ±7.4

3.2 THERMAL STABILITY

In the as-deposited state all three HEA films reveal a single-phase bcc structure according to the diffractograms shown in Figure 2. Here, only the (110) peak is presented since the films have a pronounced preferred orientation. The peak is shifted towards lower 2Θ-angles indicating the presence of compressive stresses in the films, while the shoulder on the right-hand side of the peaks is related to an inhomogeneous stress distribution.

Up to 400 °C the shoulder of the (110) peak of the bcc-MoNbTaTiW solid solution phase increases in intensity, which results in apparent broadening of the peak. In addition, the peak shifts slightly to higher 2Θ angles indicating a stress relaxation within the film. From 400 to 700 °C the peak remains largely unchanged.

A generally similar development was observed for MoNbTaVW where from RT to 500 °C the shoulder of the (110) peak increases in intensity. At temperatures above 500 °C only one symmetrical peak is recorded. During this reshaping process of the peak, the peak shifts slightly to higher 2Θ angles, again indicating stress relaxation. Additionally, a seeming peak broadening occurs which is caused by the growth of the shoulder in the (110) peak. From 500 to 700 °C the peak remains unchanged.

In the case of CrMoNbTaW, the changes in the shape of the (110) peak upon annealing up to 700 °C are most pronounced from all three thin film materials and can be related to the evolution of the peak shoulder including a seeming peak broadening.

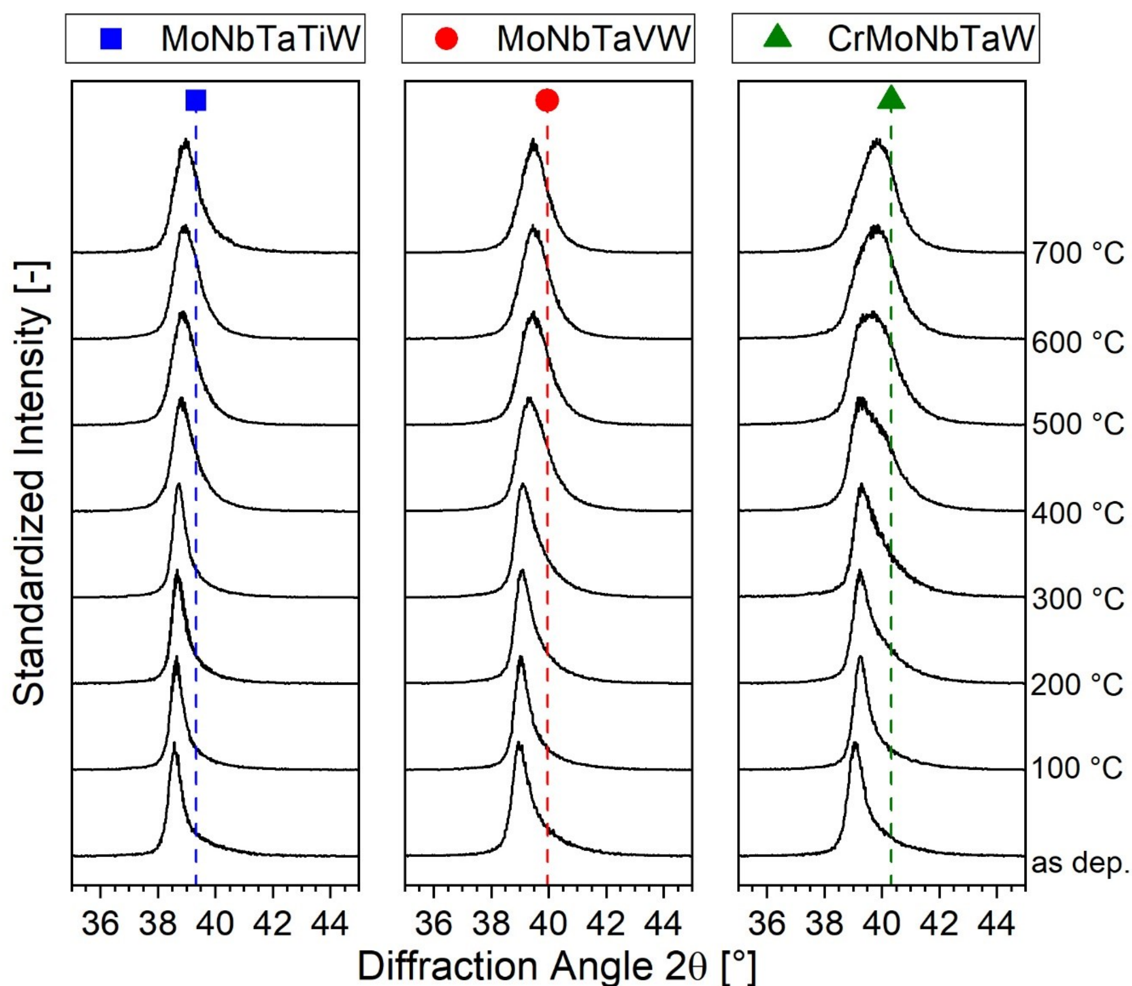

Figure 2: X-ray diffractograms of the three HEA films, deposited on Si, after annealing up to 700 °C.

In our previous work we showed that the asymmetry of the (110) peak of the HEA films in as-deposited state stems from an inhomogeneous stress distribution in the films rather than a different phase [15]. This was concluded from analyzing powdered films where macroscopic stresses are relieved and transmission electron microscopy of the film cross-sections. To confirm the absence of phase changes during annealing of the HEA films up to 1000 °C, powdered films were also annealed using the same conditions as used for the films deposited on Si and sapphire. According to the X-ray diffractograms shown in Figure 3, all three powdered HEA films show no signs of a shoulder in the (110) peak in their as-deposited state, confirming the absence of a second bcc-phase. Further, also after annealing up to the maximum temperature no signs for the presence or formation of a second phase can be noticed. This means that all changes in the peak shapes after annealing of the films deposited on Si or sapphire can be related to changes in the stresses within the HEA films. Similar to the diffractograms shown in Figure 2, there is also a slight peak shift to higher 2Θ angles noticeable for the (110) peaks in Figure 3 of all three HEAs. Even after removing the substrate and preparation of the film powder, not all stresses of the film are relaxed. Those contributions originating from stresses between different grains and defects within the grains remain and the observed slight peak shift can be explained by the relaxation of such stresses.

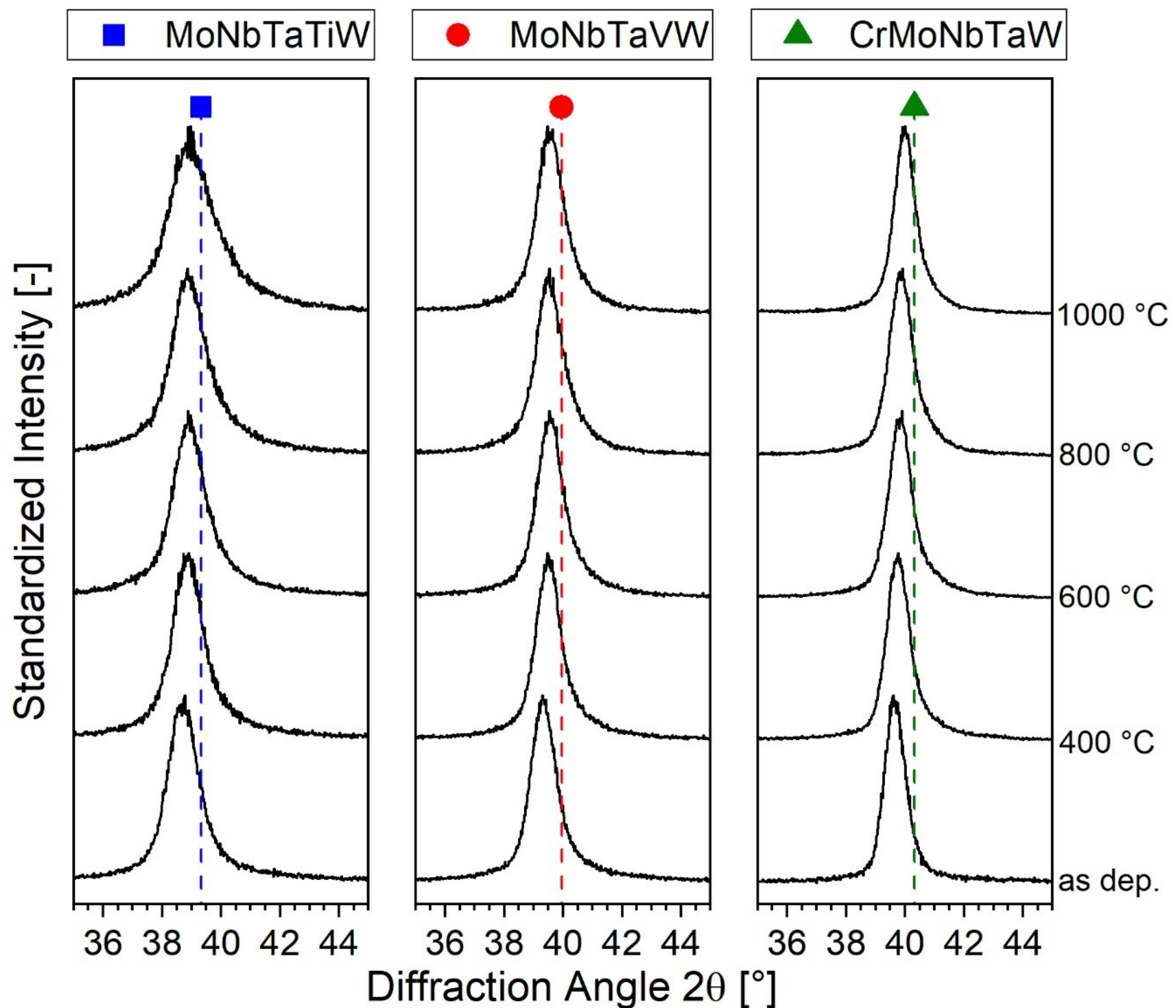

Figure 3: X-ray diffractograms of the three powdered HEA films annealed up to 1000°C.

As shown by Xia and Franz, the bcc-phase of MoNbTaVW films synthesized by cathodic arc deposition remained stable up to 1500 °C [14] and, hence, the phase stability of the MoNbTaVW, MoNbTaTiW and CrMoNbTaW films deposited by HiPIMS within this work was studied at temperatures exceeding 700 °C. After annealing at 800 °C the shoulder of the (110) MoNbTaTiW peak is still slightly visible. Only when further increasing the temperature, the (110) peak becomes symmetrical (Figure 4a). From 800 to 1000 °C a slight decrease of the lattice constant occurs (Figure 4b). After annealing at 1100 °C the lattice constant drops significantly in comparison to the films annealed at 1000 °C. The pronounced lattice constant decrease is a sign for stress relaxation. Additionally, also the FWHM, shown in Figure 4c, drops after annealing at 1100 °C. The decrease of the FWHM of the peak is a sign for defect annihilation and grain growth. Although the peak changes quite abruptly, the occurrence of recrystallization is unlikely as during recrystallization new grains are formed [23] which would result in a change of texture. Here, no significant changes in the ratio of peak

intensities was noticed. After annealing at 1200 °C the FWHM of the peak decreases slightly compared to the film annealed at 1100 °C, indicating further grain growth and defect annihilation, while the lattice constant stays constant. The bcc phase remains stable up to the highest annealing temperature.

The lattice constant obtained for MoNbTaVW are similar as the one that can be found in literature [10,24]. The lattice constant (Figure 4b) decreases slightly up to 900 °C, while at higher annealing temperatures the decrease is accelerated. This is a sign, that starting from 1000 °C, a pronounced stress relaxation occurs. From 800 to 1100 °C the FWHM (Figure 4c) decreases slightly, indicating grain growth and defect annihilation. After annealing at 1200 °C the FWHM drops significantly to the lowest observed value. However, also in this case the bcc phase remains stable up to the highest annealing temperature of 1200 °C (Figure 4a).

In contrast to the other two films, the CrMoNbTaW film did not show a pronounced drop of the lattice constant or the FWHM at a certain temperature step, as shown in Figure 4b and c. The lattice constant shows a continuous decrease throughout the entire temperature range which can be associated to a continuous stress relaxation. Further, also the FWHM decreases continuously up to 1100 °C, an indication of grain growth and defect annihilation, while at 1200 °C, the FWHM remains constant in comparison to 1100 °C. As it was the case for the other two alloys, also the bcc structure of the CrMoNbTaW film remains stable up to the highest annealing temperature (Figure 4a).

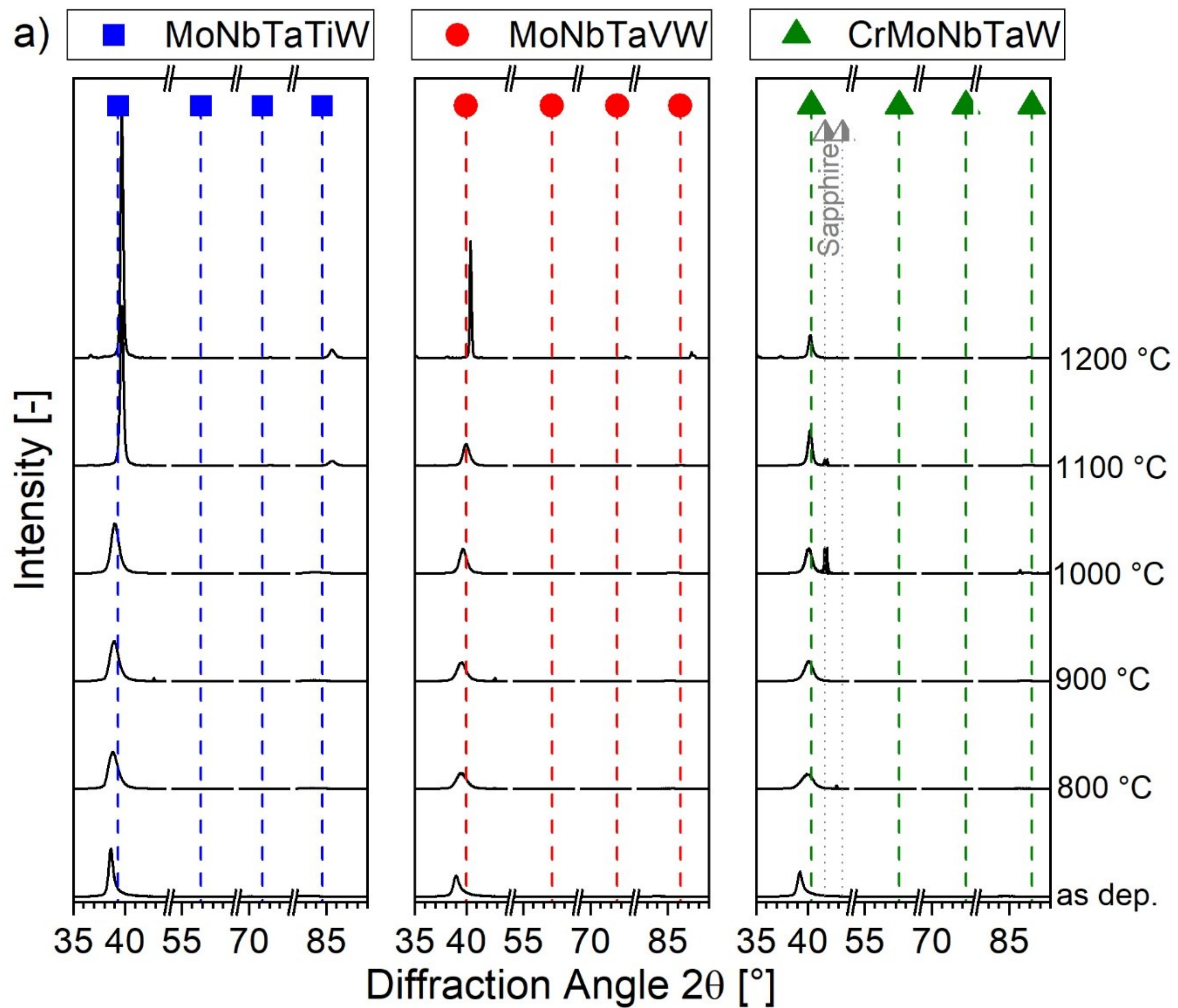

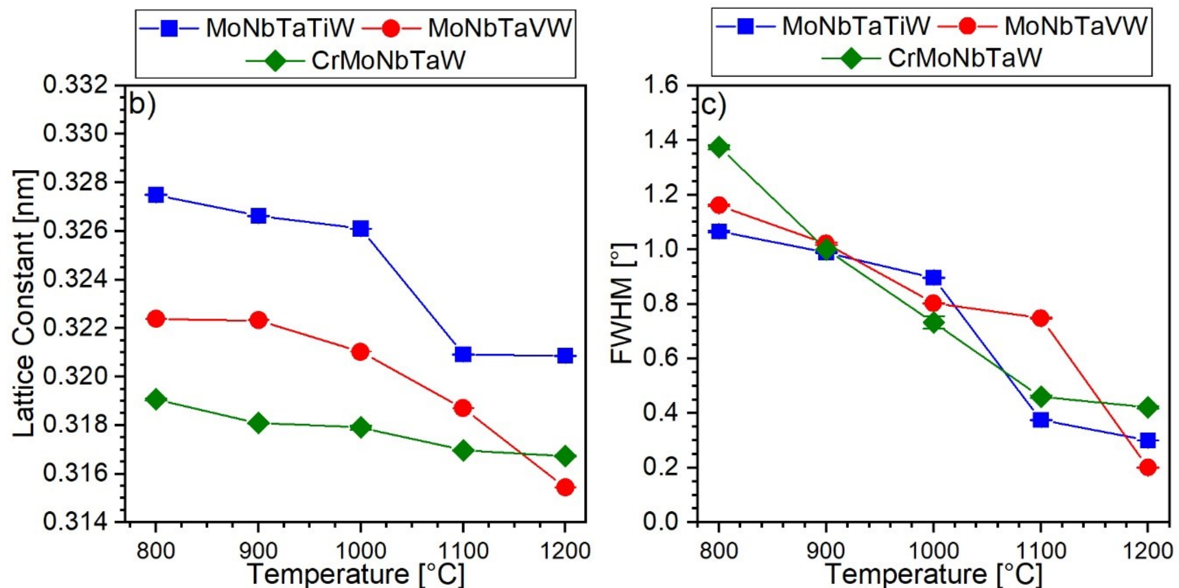

Figure 4: a) X-ray diffractograms of the three HEA films, deposited on sapphire and annealed up to 1200 °C. b) The lattice constant obtained from the (110) diffraction peak of the HEAs, after anneling at elevated temperatures, are shown. c) The FWHM of the the (110) diffraction peak for all HEA films deposited on sappire after annealing at eleveated temperatures is shown.

3.3 Evolution of Film Stress

Since most of the changes observed in the X-ray diffractograms of the films after annealing indicate changes in the stress states of the films, the evolution of the residual stresses with annealing temperature has been studied in detail. In Figure 5a results from wafer curvature measurements before and after annealing are shown. After annealing of the MoNbTaTiW film at 400 °C, the compressive stress of the film relaxed by about 1 GPa, as compared to the stress of the as-deposited film. However, further annealing of this film up to 700 °C revealed no further changes in the stress state which remained constant at about -2 GPa. The first stress reduction up to 400 °C can be understood by the low deposition temperature of about 100 °C without external heating. Annealing above this temperature will cause the annihilation of defects with low activation energy. However, it is apparent that also defects with high activation energy for annihilation are present in the film as even after annealing to 700 °C a compressive stress state of -2 GPa is observed. A stress-free film at annealing temperature would cause the observation of tensile stresses at room temperature due to the higher CTE of the MoNbTaTiW alloy film as compared to the CTE of Si. The MoNbTaVW and CrMoNbTaW films show a similar behavior. The reduction in stress in case of the CrMoNbTaW film is more pronounced, from about -3 GPa in the as-deposited state to about -1.5 GPa after annealing at temperatures ranging from 400 to 700 °C. In contrast, the stress reduction of MoNbTaVW is the lowest of all three films, from about -2.6 to about -2 GPa.

At annealing temperatures above 700 °C, sapphire was used as substrate material to be comparable to the results obtained from the XRD measurements. In addition, the stresses were measured by the $\sin^2\Psi$ method as the change in sample geometry impeded wafer curvature measurements. To ensure the comparability of the results of the stress measurements up to 700 °C with the ones above, the films deposited on Si were measured by both techniques after annealing at 700 °C as shown in Figure 5b). Similar to the as-deposited films described in a previous work [15], also the films annealed at 700 °C show different values for the stress when analyzed by the two different techniques. This difference was mainly attributed to a stress gradient along the film thickness. However, the difference observed for the annealed films is lower than the one for the as-deposited films. This can be understood by stress reduction and homogenization within the films which is expected to already have happened at the lowest annealing temperature of 400 °C. Further, comparing the obtained stress

values of the films on Si after annealing at 700 °C to the ones on sapphire annealed at 800 °C, a good agreement is noticed for MoNbTaVW and CrMoNbTaW, whereas a larger deviation exists for MoNbTaTiW. To confirm the existence of the deviation in stresses of MoNbTaTiW deposited on the two different substrates, a MoNbTaTiW film deposited on sapphire was also annealed at 700 °C which revealed a compressive stress of about -3.8 GPa. This is significantly lower than the values obtained for the film on Si at this temperature (see Figure 5b). Also, a slight variation of the lattice constants of the film deposited on Si and sapphire and annealed at 700 °C was found. The MoNbTaTiW film deposited on Si has a lower lattice constant of 0.3263 nm, compared to 0.3271 nm when deposited on sapphire. A different substrate can, on the one hand, influence the stress state in the film during film growth and, on the other hand, influence the stress evolution during annealing due to a different mismatch of the coefficient of thermal expansion (CTE) causing thermal stresses [25]. The CTE of the HEA films was calculated using the rule of mixture:

$$CTE = \sum_{i=1}^{n} f_i \times CTE_i, \quad (1)$$

where f_i is the mole fraction of element i and CTE_i the CTE of the element i at 227 °C. While the CTE of Si ($2.8 \cdot 10^{-6}$ [1/K] [26]) is lower compared to the ones of the HEA films, shown in Table 2 and calculated by the rule of mixture, the one of sapphire ($7.2 \cdot 10^{-6}$ [1/K] [27]) is in the range of the CTE values of the HEA films.

Table 2: Coefficient of thermal expansion as calculated by the rule of mixture, with the values for the single metals at 227 °C, taken from [28–30].

	MoNbTaTiW	MoNbTaVW	CrMoNbTaW
CTE [1/K]	$6.8 \cdot 10^{-6}$	$6.8 \cdot 10^{-6}$	$6.6 \cdot 10^{-6}$

At temperatures exceeding 800 °C, the compressive stresses of the MoNbTaTiW film slightly decrease up to 1000 °C before the film becomes stress-free at 1100 and 1200 °C. The stresses of the MoNbTaVW film deposited on sapphire remain constant up to 900 °C before decreasing linearly to a stress-free state after annealing at 1200 °C. In case of the CrMoNbTaW film, the compressive stresses in the film decrease continuously from 700 to 1000 °C and reach the tensile region after annealing at 1100 and 1200 °C.

In summary, it can be stated that the fifth element (Ti, V or Cr) used to alloy MoNbTaW has a significant effect on the stress relaxation of the films, especially at temperatures above 700 °C. The addition of V leads to the highest onset temperature for the second stress relaxation, which is 200 °C higher than in the case of the Cr-containing HEA.

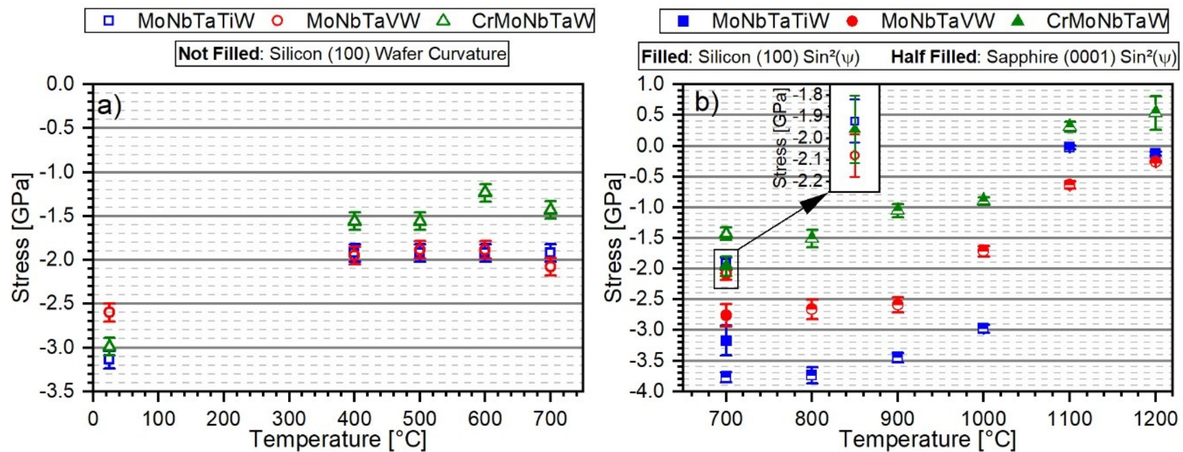

Figure 5: a) The residual stresses of the films deposited on Si before and after annealing, measured using the wafer curvature method. b) The residual stresses of the films deposited on sapphire after annealing at 800 °C and above measured using the $sin^2\Psi$ method are visualized. The stresses of films deposited on Si after annealing at 700 °C and measured by $sin^2\Psi$ and wafer curvature method are shown for comparison.

4 CONCLUSIONS

The thermal stability of three different refractory HEAs, MoNbTaTiW, MoNbTaVW and CrMoNbTaW, deposited by HiPIMS has been studied up to an annealing temperature of 1200 °C. Regardless of the chemical composition of the alloy films, the observed bcc structure of the films was stable over the entire temperature range within this study. Differences were noticed in the evolution of the residual stress state, where the stresses of the MoNbTaTiW films show a sudden drop to the stress-free state after annealing at 1100 °C and above. The high compressive stress measured up to 1000 °C in this case acts as a driving force for the observed strong recovery and grain growth. In contrast, a rather steady decrease in film stress during annealing was observed for MoNbTaVW and CrMoNbTaW. In the case of MoNbTaVW pronounced grain growth was noticed after annealing to 1200 °C, whereas grain growth was less pronounced in the case of CrMoNbTaW within the tested temperature range. In general, the obtained results show that refractory HEA thin films based on the system MoNbTaW are promising materials for high temperature applications where a high thermal stability is a prerequisite.

ACKNOWLEDGEMENTS

The authors acknowledge the funding from the Austrian Research Promotion Agency (FFG) (project number: 871687). A. Lassnig acknowledges funding from the Austrian Science Fund (FWF) (project number T891-N36). The authors are grateful to S. Wurster (Austrian Academy of Sciences, Austria) for the SEM investigations. G.C. Gruber thanks S. Hirn (Montanuniversität Leoben, Austria) for the help with the depositions.

REFERENCES

[1] J.-W. Yeh, S.-K. Chen, S.-J. Lin, J.-Y. Gan, T.-S. Chin, T.-T. Shun, C.-H. Tsau, S.-Y. Chang, Nanostructured High-Entropy Alloys with Multiple Principal Elements: Novel Alloy Design Concepts and Outcomes, Advanced Engineering Materials 6 (2004) 299–303. https://doi.org/10.1002/adem.200300578.

[2] B. Cantor, I. Chang, P. Knight, A. Vincent, Microstructural development in equiatomic multicomponent alloys, Materials Science and Engineering: A 375-377 (2004) 213–218. https://doi.org/10.1016/j.msea.2003.10.257.

[3] B.S. Murty, J.-W. Yeh, S. Ranganathan, High-entropy alloys, Butterworth-Heinemann an imprint of Elsevier, London, Oxford, Amsterdam, San Diego, 2014.

[4] O.N. Senkov, G.B. Wilks, D.B. Miracle, C.P. Chuang, P.K. Liaw, Refractory high-entropy alloys, Intermetallics 18 (2010) 1758–1765. https://doi.org/10.1016/j.intermet.2010.05.014.

[5] O.N. Senkov, G.B. Wilks, J.M. Scott, D.B. Miracle, Mechanical properties of Nb25Mo25Ta25W25 and V20Nb20Mo20Ta20W20 refractory high entropy alloys, Intermetallics 19 (2011) 698–706. https://doi.org/10.1016/j.intermet.2011.01.004.

[6] Z.D. Han, N. Chen, S.F. Zhao, L.W. Fan, G.N. Yang, Y. Shao, K.F. Yao, Effect of Ti additions on mechanical properties of NbMoTaW and VNbMoTaW refractory high entropy alloys, Intermetallics 84 (2017) 153–157. https://doi.org/10.1016/j.intermet.2017.01.007.

[7] Z.D. Han, H.W. Luan, X. Liu, N. Chen, X.Y. Li, Y. Shao, K.F. Yao, Microstructures and mechanical properties of Ti NbMoTaW refractory high-entropy alloys, Materials Science and Engineering: A 712 (2018) 380–385. https://doi.org/10.1016/j.msea.2017.12.004.

[8] T.-K. Chen, M.-S. Wong, T.-T. Shun, J.-W. Yeh, Nanostructured nitride films of multi-element high-entropy alloys by reactive DC sputtering, Surface and Coatings Technology 200 (2005) 1361–1365. https://doi.org/10.1016/j.surfcoat.2005.08.081.

[9] M.C. Gao, J.-W. Yeh, P.K. Liaw, Y. Zhang, High-Entropy Alloys, Springer International Publishing, Cham, 2016.

[10] A. Xia, A. Togni, S. Hirn, G. Bolelli, L. Lusvarghi, R. Franz, Angular-dependent deposition of MoNbTaVW HEA thin films by three different physical vapor deposition methods, Surface and Coatings Technology 385 (2020) 125356. https://doi.org/10.1016/j.surfcoat.2020.125356.

[11] A. Xia, R. Dedoncker, O. Glushko, M.J. Cordill, D. Depla, R. Franz, Influence of the nitrogen content on the structure and properties of MoNbTaVW high entropy alloy thin films, Journal of Alloys and Compounds 850 (2021) 156740. https://doi.org/10.1016/j.jallcom.2020.156740.

[12] Z. Li, Y. Tian, C. Teng, H. Cao, Recent Advances in Barrier Layer of Cu Interconnects, Materials (Basel) 13 (2020) 5049. https://doi.org/10.3390/ma13215049.

[13] S.-Y. Chang, C.-E. Li, Y.-C. Huang, H.-F. Hsu, J.-W. Yeh, S.-J. Lin, Structural and thermodynamic factors of suppressed interdiffusion kinetics in multi-component high-entropy materials, Sci. Rep. 4 (2014) 4162. https://doi.org/10.1038/srep04162.

[14] A. Xia, R. Franz, Thermal Stability of MoNbTaVW High Entropy Alloy Thin Films, Coatings 10 (2020) 941. https://doi.org/10.3390/coatings10100941.

[15] G.C. Gruber, A. Lassnig, S. Zak, C. Gammer, M.J. Cordill, R. Franz, Synthesis and structure of refractory high entropy alloy thin films based on the MoNbTaW system, Surface and Coatings Technology 439 (2022) 128446. https://doi.org/10.1016/j.surfcoat.2022.128446.

[16] K. Sarakinos, L. Martinu, Synthesis of thin films and coatings by high power impulse magnetron sputtering, in: High Power Impulse Magnetron Sputtering, Elsevier, 2020, pp. 333–374.

[17] C. Saringer, M. Tkadletz, C. Mitterer, Restrictions of stress measurements using the curvature method by thermally induced plastic deformation of silicon substrates, Surface and Coatings Technology 274 (2015) 68–75. https://doi.org/10.1016/j.surfcoat.2015.04.038.

[18] G. G. Stoney, The tension of metallic films deposited by electrolysis, Proc. R. Soc. Lond. A 82 (1909) 172–175. https://doi.org/10.1098/rspa.1909.0021.

[19] W.D. Nix, Mechanical properties of thin films, Metall Mater Trans A 20 (1989) 2217–2245. https://doi.org/10.1007/BF02666659.

[20] E. Zolotoyabko, Basic concepts of crystallography: An outcome from crystal symmetry, Wiley-VCH, Weinheim Germany, 2011.

[21] Vapor Pressure Calculator [IAP/TU Wien], 2019. https://www.iap.tuwien.ac.at/www/surface/vapor_pressure (accessed 17 February 2022).

[22] S.-B. Hung, C.-J. Wang, Y.-Y. Chen, J.-W. Lee, C.-L. Li, Thermal and corrosion properties of V-Nb-Mo-Ta-W and V-Nb-Mo-Ta-W-Cr-B high entropy alloy coatings, Surface and Coatings Technology 375 (2019) 802–809. https://doi.org/10.1016/j.surfcoat.2019.07.079.

[23] P.H. Mayrhofer, C. Mitterer, L. Hultman, H. Clemens, Microstructural design of hard coatings, Progress in Materials Science 51 (2006) 1032–1114. https://doi.org/10.1016/j.pmatsci.2006.02.002.

[24] L. Bi, X. Li, Y. Hu, J. Zhang, X. Wang, X. Cai, T. Shen, R. Liu, Q. Wang, C. Dong, P.K. Liaw, Weak enthalpy-interaction-element-modulated NbMoTaW high-entropy alloy thin films, Applied Surface Science 565 (2021) 150462. https://doi.org/10.1016/j.apsusc.2021.150462.

[25] R. Daniel, K.J. Martinschitz, J. Keckes, C. Mitterer, The origin of stresses in magnetron-sputtered thin films with zone T structures, Acta Materialia 58 (2010) 2621–2633. https://doi.org/10.1016/j.actamat.2009.12.048.

[26] X. Tang, J. Dong, P. Hutchins, O. Shebanova, J. Gryko, P. Barnes, J.K. Cockcroft, M. Vickers, P.F. McMillan, Thermal properties of Si136 Theoretical and experimental study of the type-II clathrate polymorph of Si, Phys. Rev. B 74 (2006). https://doi.org/10.1103/PhysRevB.74.014109.

[27] G.K. White, R.B. Roberts, Thermal expansion of reference materials: tungsten and α-Al2O3, High Temperatures - High Pressures 15 (1983) 321–328.

[28] G.K. White, C. Andrikidis, Thermal expansion of chromium at high temperature, Phys. Rev. B 53 (1996) 8145–8147. https://doi.org/10.1103/PhysRevB.53.8145.

[29] R.A. MacDonald, R.C. Shukla, Thermodynamic properties of bcc crystals at high temperatures: The transition metals, Phys. Rev. B 32 (1985) 4961–4968. https://doi.org/10.1103/PhysRevB.32.4961.

[30] R.J. Gambino, P.E. Seiden, Correlation of the Superconducting Transition Temperature with an Empirical Pseudopotential Determined from Atomic Spectra, Phys. Rev. B 2 (1970) 3571–3577. https://doi.org/10.1103/PhysRevB.2.3571.

Publication IV

A new design rule for high entropy alloy diffusion barriers in Cu metallization

Georg C. Gruber, Magdalena Kirchmair, Stefan Wurster, Megan J. Cordill and Robert Franz

Journal of Alloys and Compounds 953 (2023) 170166

A new design rule for high entropy alloy diffusion barriers in Cu metallization

GEORG C. GRUBER[a†*], MAGDALENA KIRCHMAIR[a], STEFAN WURSTER[b], MEGAN J. CORDILL[a,b] AND ROBERT FRANZ[a]

[a]*Department of Materials Science, Montanuniversität Leoben, Franz-Josef-Strasse 18, 8700 Leoben, Austria*

[b]*Erich Schmid Institute of Materials Science, Austrian Academy of Sciences, Jahnstrasse 12, 8700 Leoben, Austria*

[†]*corresponding author (georg.gruber@unileoben.ac.at)*

KEWORDS

High Entropy Alloy, Refractory Metal, MoNbTaW, Thin Film, Diffusion Barrier

ABSTRACT

High entropy alloy (HEA) thin films are potential candidates to act as diffusion barrier between Cu and Si in microelectronics. To evaluate the suitability of refractory HEAs, six different HEA thin films based on the MoNbTaW system and alloyed with Ti, V, Cr, Mn, Zr or Hf have been deposited by high power impulse magnetron sputtering with a thickness of 20 nm on Si substrates. The bi-layer architecture was completed by a 150 nm thick top-layer of Cu. The microstructure of the bi-layers before and after annealing in vacuum up to 800 °C was investigated by X-ray diffraction to observe possible phase changes or formations. In addition, resistance measurements and confocal laser scanning microscopy were employed to check for potential barrier failure. The lowest onset temperature for barrier failure of 600 °C was found for MoNbTaWZr, whereas the highest of 700 °C was observed for CrMoNbTaW. The obtained results for the failure temperature are discussed in terms of microstructure, strain and cohesive energy of the HEA films as well as the enthalpy of mixing between the elements in the HEA and Cu. A direct correlation between the mixing enthalpy of the fifth alloying element with Cu and the barrier failure temperature was observed.

1 INTRODUCTION

When integrated circuits were developed 60 years ago, Al was used as a conductor material and SiO_2 as dielectric material [1]. As the number of transistors in a microprocessor grew, this material choice resulted in gate delays [2,3]. The solution

was to use a conductor material with a lower resistivity, which was Cu. Although the use of Cu has many advantages, it brought the disadvantage that Cu diffuses into Si where it forms copper-silicides, and into Si-based insulating materials, triggering insulating failure at relative low temperatures [4]. To overcome this problem, various diffusion barriers have been developed. Typical state-of-the-art diffusion barriers are often refractory metals, such as Ti, Mo, Ta or W [5,6]. Alloys consisting of those elements are also used, for example WTi [7,8]. Another possibility is to use nitride based on Ti or Ta: TaN [6,9], TiN [10] or TiTaN [11]. To further improve the performance of diffusion barriers, several new approaches were developed, such as the use of high entropy alloys (HEAs). HEAs are alloys with a configurational entropy of at least 1.5*R* [12], where *R* is the gas constant. HEAs are known for their good thermal stability [13–15], excellent mechanical properties [14,16–19], good wear resistance [20,21] and also good irradiation resistance [22,23], which makes them interesting materials for many different applications. Chang et al. [24] showed that the diffusion barrier performance of an alloy increases with the number of elements in it and underlined the suitability of HEAs as diffusion barriers. Most of the research on HEA diffusion barriers focuses on AlCrRuTaTiZr and (AlCrRuTaTiZr)N based diffusion barriers [24–32], where the highest failure temperature of a 5 nm thick metal film was found to be 800 °C [27]; the failure temperature of the nitride films was found for a 40 nm thick film, which was 900 °C [28]. Also, diffusion barriers based on TiVCZrHf have been studied which showed a maximum failure temperature of 600 °C for the metal films and 800 °C for the nitride films [33,34]. AlMoNbSiTaTiVZr films showed a failure temperature of 700 °C for the metal films and 850 °C for the nitride films. The alloys NbSiTaTiZr has been studied as well. Using this HEA could prevent barrier failure up to 800 °C. Another candidate for diffusion barriers are films based on the MoNbTaW [35,36] system, as those films are known for their good thermal stability [15,37]. It was found that these HEAs could prevent barrier failure up to 650 °C [35]. When alloyed with V only 1.5 nm of this HEA are necessary to prevent barrier failure up to 600 °C [38]. MoNbTaVW was also found to be a good diffusion barrier between Mo and $MoSi_2$ [39].

Within this study the influence of the fifth element of the base alloy MoNbTaW, alloyed with Ti, V, Cr, Mn, Zr or Hf, on the diffusion barrier performance has been investigated. These elements were added to the base alloy to vary different parameters, such as different crystal structures of the alloying elements as pure metals, and different atomic

sizes, leading to a different lattice distortion within the HEA. As known from literature an amorphous microstructure is preferred over a crystalline one, as grain boundaries provide fast diffusion channels [29,35]. Therefore, all studied HEA diffusion barriers in literature also have this microstructure. According to our previous study, the alloys analyzed in this work have a bcc microstructure, but many of them showed an amorphous interlayer up to a few 10 nm next to the Si substrate [40]. To investigate the diffusion barrier performance of these HEAs, a 20 nm thick diffusion barrier layer was deposited on Si substrates, with a 150 nm thick Cu layer on top of it. The depositions were carried out using high power impulse magnetron sputtering (HiPIMS). Afterwards, the films were annealed at elevated temperatures and then evaluated for barrier failure. The barrier failure was investigated by X-ray diffraction (XRD) measurement, resistance measurements and scanning laser microscopy.

2 Experimental Details

For the synthesis of the refractory HEA diffusion barrier films, equimolar MoNbTaTiW, MoNbTaVW, CrMoNbTaW, MnMoNbTaW, MoNbTaWZr and HfMoNbTaW targets with a diameter of 76 mm were used, which were manufactured by powder metallurgical methods by Plansee Composite Materials GmbH (Lechbruck, Germany). The contents of O, C, Fe and H in the targets were below 9300 µg/g, 1200 µg/g, 140 µg/g and 850 µg/g respectively. For the Cu films a Cu Target with a purity of 99.99 %, with the same diameter was used. The films were deposited on polished 325 µm thick B-doped (100) Si substrates (21 mm × 7 mm) using a lab-scale deposition system equipped with an unbalanced magnetron source. The substrates were carefully cleaned with acetone and afterwards ethanol in an ultrasonic bath before deposition and then placed in front of the magnetron source at a distance of 150 mm. Subsequently, the chamber was evacuated to a base pressure of $9\cdot10^{-4}$ Pa or below, before Ar was introduced to establish a pressure of 3 Pa for the plasma etching. First, the samples were plasma etched for 10 min applying a voltage of 800 V, a pulse frequency of 100 kHz and a pulse on-time of 1 µs. After the etching procedure the Ar flow was reduced to establish the deposition pressure of 1 Pa. The HEA films were deposited using HiPIMS, with an average power of 400 W, a frequency of 100 Hz, and a duty cycle of 1 %. Here, the duty cycle is defined as the ratio between the pulse on-time (100 µs) and the pulse duration (10000 µs). The deposition time was 2 min to achieve a film thickness of about 20 nm. The Cu deposition was performed at the same Ar pressure without breaking

vacuum and about 3 min after the HEA deposition was finished. For the Cu deposition also HiPIMS was used, with an average power of 400 W, a frequency of 100 Hz and a duty cycle of 2 % was used. As a reference film, to study the Cu self-annealing effect, a Cu film without a HEA diffusion barrier layer was deposited using the same deposition parameters.

Within the first hour after deposition, the resistivity of the films was measured using a Jandel Model RM2 cylindrical four-point probe using three measurement points on each sample. The measurements were repeated a few times until at least 260 h had passed after the deposition process. After this point further investigations were performed. The samples were annealed in a HTM Retz vacuum furnace. Prior to annealing of the films, the furnace was evacuated to a pressure of $5 \cdot 10^{-4}$ Pa. In the first step, the vacuum furnace was heated up to 250 °C with a heating rate of 20 K/min. To allow the temperature to stabilize, a waiting period of 30 min was introduced. Afterwards, the vacuum furnace was heated up to the desired annealing temperature with the same heating rate and held at this temperature for 30 min. The bi-layers using MoNbTaTiW, MoNbTaVW, CrMoNbTaW, MnMoNbTaW or HfMoNbTaW as diffusion barrier, were annealed at 600, 650, 700, 750 and 800 °C while the bi-layer using MoNbTaWZr as diffusion barrier were annealed at 550, 600, 650, 700 and 750 °C. The different annealing temperature of the Cu/MoNbTaWZr bi-layer was necessary due to the earlier diffusion barrier failure of MoNbTaWZr. For every annealing step a different sample was used.

To investigate the microstructure of the bi-layers before and after annealing, XRD measurements were performed using a Bruker-AXS D8 Advance diffractometer equipped with Cu-K_α radiation and parallel optics. The measurements were performed in Bragg-Brentano geometry with the diffraction angle 2Θ ranging from 20 to 90°. The XRD measurements were performed to check for new phases arising after annealing, which could be a sign for barrier failure, for example Cu_3Si. The resistance after annealing was also measured using the same four-point probe to check for changes in the resistance due to barrier failure. Additionally, surface images were recorded using a Keyence 3D confocal laser scanning microscope, VK-X1100 Series, to monitor changes in the surface appearance of the bi-layer films. The chemical composition of the occurring phases after barrier failure, was measured by energy-dispersive X-ray (EDX) spectroscopy using a Bruker Type XFlash 6-60 detector which was attached to a Tescan Magna scanning electron microscope (SEM).

3 Results

3.1 As-Deposited Films

To investigate the self-annealing of the Cu films the resistivity of all of the bi-layers with a MoNbTaW based diffusion barrier and one Cu single layer film was measured up to at least 260 h after deposition (Figure 1). The bi-layer structures were investigated as well, since the diffusion barrier could have an influence on the growth behavior of the Cu films. The resistivity of the Cu films deposited on top of the diffusion barriers are mostly within the error bars of the single Cu film deposited on Si used as reference, only the resistivity of the Cu film deposited on top of MnMoNbTaW is slightly higher. For all studied Cu films, the resistivity remains constant from the first to the last measurement. No self-annealing of the Cu during the measured time frame was observed.

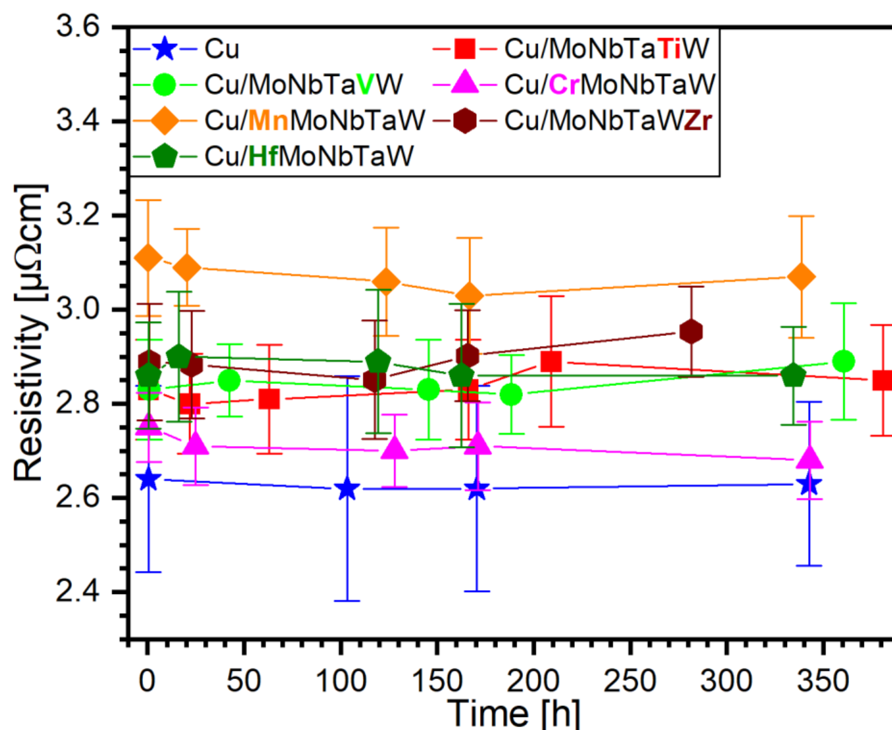

Figure 1: The resistivity as a function of time elapsed since deposition is shown.

After ensuring that the Cu film microstructure remained constant, the as-deposited microstructure of the films was investigated by XRD as shown in Figure 2. The intensity of the (111) Cu peak of the Cu films deposited on top of a diffusion barrier is higher compared to the intensity of the Cu film deposited directly on the (100) Si substrate. In contrast to that, the intensity of the (200) Cu peak is similar. This suggests that the Cu

film shows a more preferred (111) orientation when deposited on MoNbTaW based films instead of directly on (100) Si. Additionally, a small peak most probably related to Cu_4O_3 indicates a slight surface oxidation. For most of the MoNbTaW based films no peak can be noticed, suggesting an amorphous microstructure. Only for the MoNbTaTiW and MoNbTaVW diffusion barrier layer a clear peak can be observed, which suggests that these films have a body centered cubic (bcc) microstructure.

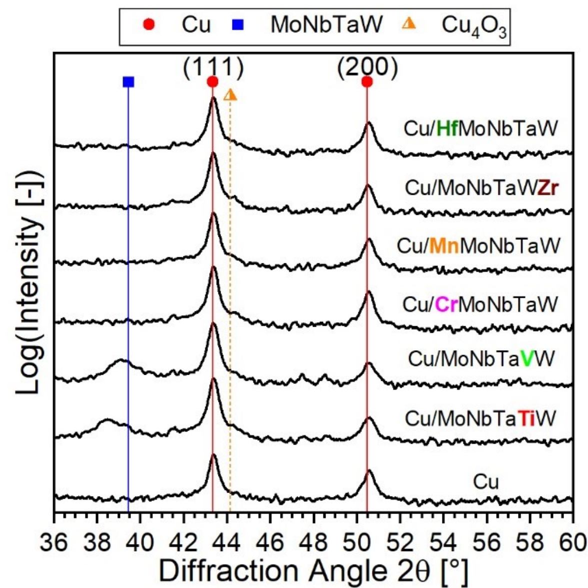

Figure 2: X-ray diffractograms of the as-deposited films showing the microstructure of the MoNbTaW based diffusion barriers and the Cu top layer. The diffractogram of the Cu film deposited directly on a (100) Si substrate is shown for comparison.

3.2 Diffusion Barrier Performance

The electrical resistance, shown in Figure 3, of all as-deposited bi-layers is similar, and does not depend on the used MoNbTaW-based diffusion barrier. After annealing at moderate temperature, the resistance of the bi-layers decreases. This can be attributed to grain growth and defect annihilation. The dotted line within Figure 3 represents the resistance value of the as-deposited bi-layer. An increase of the resistance above this value indicates a damaged Cu layer and is a sign for the failure of the diffusion barrier. The higher the resistance, the more the Cu layer is damaged. The MoNbTaWZr diffusion barrier fails already at 600 °C and shows a quite sharp failure characteristic. At 550 °C, this bi-layer shows a resistance even lower than in as-deposited state and, hence, an intact diffusion barrier can be assumed. After annealing at 600 °C the resistance increases by two orders of magnitude and it remains constant up to the highest studied temperature. Such an increase in resistance can be associated to a complete diffusion barrier failure. The MoNbTaTiW diffusion barrier is

the next film showing an increase in resistance, in this case at 650 °C. In contrast to MoNbTaWZr, the resistance of the MoNbTaTiW bi-layer rises only slightly above the value in as-deposited state. A similar behavior can be noticed for all other bi-layers, but their resistance values at 650 °C still not exceed the value measured for the as-deposited films. However, this slight increase could already be a sign for an early stage of diffusion barrier failure. After annealing at 700 °C the resistance of the HfMoNbTaW film reaches its maximum value indicating complete failure of the diffusion barrier. The failure characteristic is as sharp as that of the MoNbTaWZr bi-layer. The resistance of the bi-layer using MoNbTaTiW also increases significantly, whereas only a slight increase over the value in as-deposited state is noticed for MoNbTaVW and MnMoNbTaW. The only bi-layer not exceeding the initial resistance value after annealing at 700 °C was CrMoNbTaW. A further rise in annealing temperature to 750 °C results in maximum resistance values for all bi-layers, with the exceptions of CrMoNbTaW and MnMoNbTaW. However, the resistance of these two bi-layers is also significantly above the value of the as-deposited bi-layers indicating a progressing diffusion barrier failure. After annealing at 800 °C all bi-layers reached their maximum resistance.

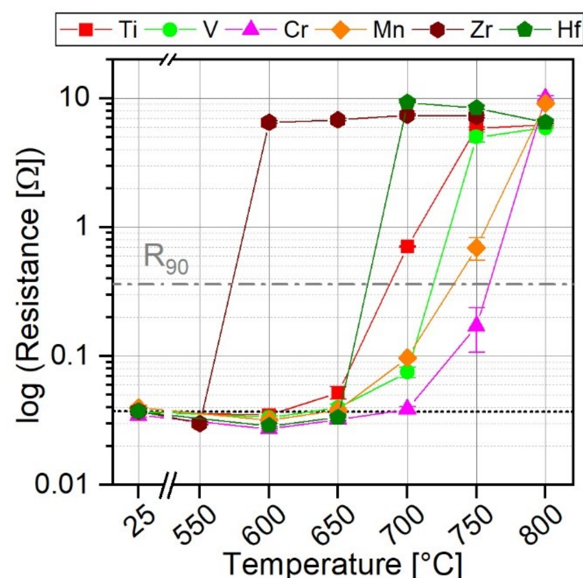

Figure 3: The electrical resistance of the bi-layers as a function of annealing temperature. The doted line represents the resistance of the as-deposited bi-layers. For the definition of R_{90} please see the discussion on the diffusion barrier performance in Section 4.2.

In addition to the as-deposited microstructure, the evolution of phases of the annealed bi-layers was investigated using XRD. The Cu peaks of the bi-layer with MoNbTaTiW, shown in Figure 4a are visible up to 700 °C, above this temperature no Cu peaks are

visible, which is a sign for barrier failure. Instead of the Cu peaks, peaks attributed to a Cu_3Si phase are visible. First indications for the presence of this phase can already be observed at annealing temperatures of 700 °C. The shoulder visible on the right hand side of the (111) Cu peak below 700 °C is most likely related to the surface oxide and not to Cu_3Si, since the shoulder is already visible in the diffractogram of the as-deposited bi-layer. The peak attributed to the MoNbTaTiW phase is shifted towards lower diffraction angles compared to the peak position calculated by the rule of mixture which indicates compressive residual stresses within the diffusion barrier layer. These results are in good agreement with our previous findings, where compressive residual stresses within MoNbTaTiW films were observed [40]. Up to 650 °C no changes related to the MoNbTaTiW phase could be noticed. Starting with 700 °C the peak intensity is reduced and the peak completely disappears after annealing at 750 °C. Instead, a $(MoNbTaTiW)Si_2$ peak emerges which is represented by $MoSi_2$ in Figure 4a and b. The occurrence of this silicide phase is another indication for the failure of the barrier layer.

The intensity of the Cu peaks of the Cu/CrMoNbTaW bi-layer, shown in Figure 4b, remains similar up to 750 °C, but after annealing at 800 °C the peaks vanished. Starting with 750 °C peaks which can be attributed to the Cu_3Si phase are found. Below 750 °C the peak on the right of the (111) Cu peak can again be attributed to the surface oxide phase. Up to the highest annealing temperature no CrMoNbTaW peak can be seen, indicating an amorphous microstructure throughout the entire range of annealing temperatures within this work. After annealing at 750 °C a small $(CrMoNbTaW)Si_2$ peak is visible, which increases in size after annealing at 800 °C.

The phase evolution with annealing temperature is summarized in Figure 4c for all studied Cu/HEA bi-layers. Only the Cu/MoNbTaTiW and Cu/MoNbTaVW bi-layers show peaks for the MoNbTaW-based diffusion barrier, for the other bi-layers such peaks cannot be seen up to the highest annealing temperature. Nevertheless, all bi-layers show the formation of a HEA silicide phase, but the formation temperature where this phase first occur varies. For Cu/MoNbTaWZr this phase already occurs after annealing at 600 °C, whereas for Cu/CrMoNbTaW it only occurs after annealing at 800 °C. For MoNbTaW-based single layers, such a silicide phase was not found, indicating that the formation of this silizide phase is related to the formation of the Cu_3Si phase, as the $(MoNbTaW)Si_2$ never forms before Cu_3Si [15]. Besides Cu/MoNbTaWZr

and Cu/MoNbTaWHf, all bi-layers show a gradual transition from Cu to Cu_3Si. The lowest annealing temperature of 600 °C, after which Cu_3Si can be found, was found for the MoNbTaWZr containing bi-layer. For the MoNbTaTiW, MoNbTaVW, MnMoNbTaW or HfMoNbTaW containing bi-layer, the Cu_3Si formation starts at 700 °C. The highest Cu_3Si formation temperature of 750 °C was found for CrMoNbTaW.

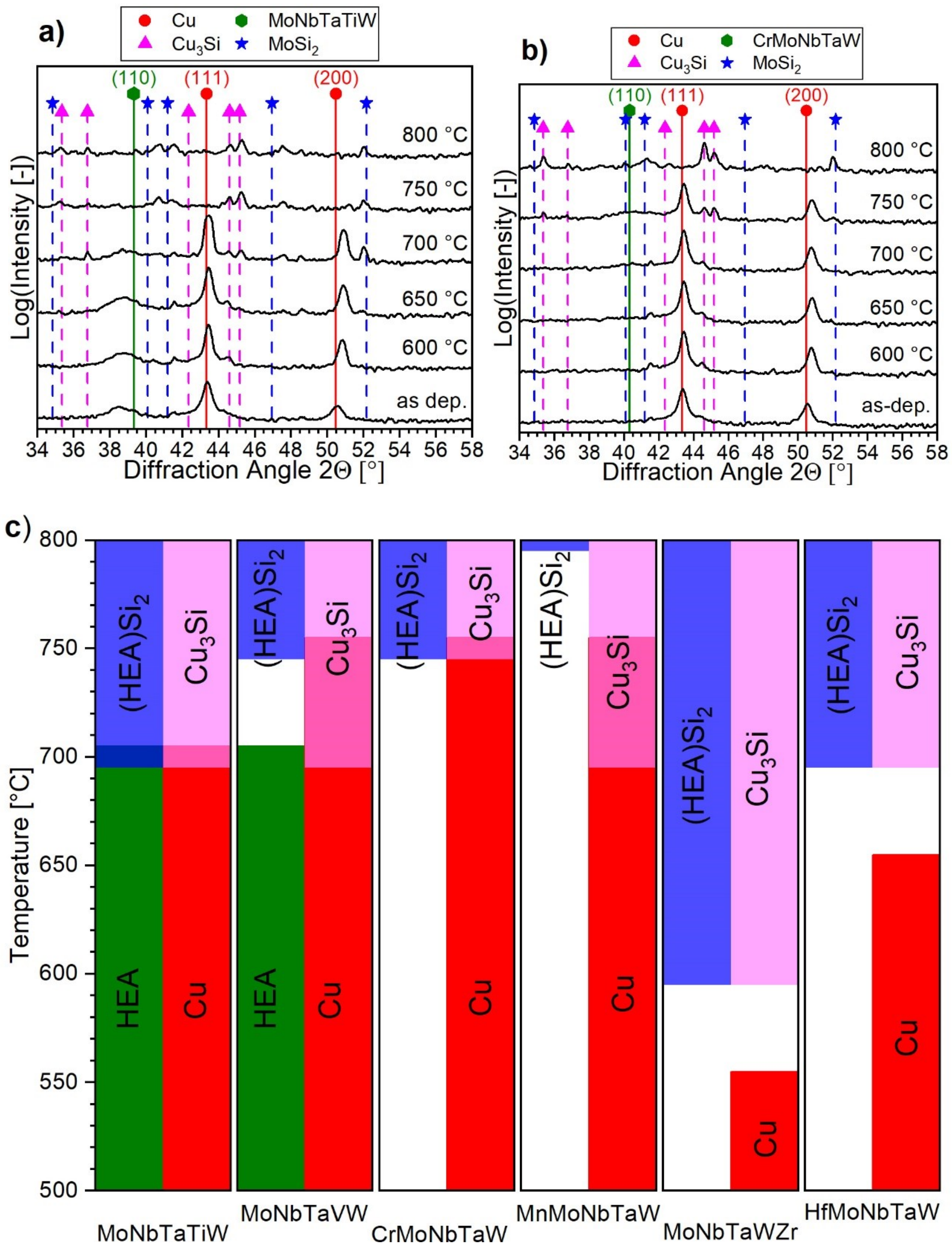

Figure 4: X-ray diffractograms of the bi-layers using a) MoNbTaTiW and b) CrMoNbTaW. c) Schematic overview of the phase evolution with annealing temperature derived from XRD measurements for all studied bi-layers.

The surface of the bi-layers was also investigated using a confocal laser-scanning-microscope (Figure 5). The surface images are a combination of an optical and a laser intensity image. The Cu/MoNbTaTiW bi-layer, shown in Figure 5a-c, shows some circular defects after annealing at 600 °C (Figure 5a). After annealing at 700 °C the circular defects grow in number and size (Figure 5b) until no Cu seems to be left after annealing at 800 °C (Figure 5c). Within the light gray circles black spots are visible. The Cu/MoNbTaVW also has circular defects after annealing at 600 °C (Figure 5d), but not as many as the bi-layer using MoNbTaTiW as diffusion barrier (Figure 5a-c). Also, after annealing at 700 °C (Figure 5e) the defect number of the Cu/MoNbTaVW film is lower. After annealing at 800 °C the surface images look similar (compare Figure 5c with Figure 5f). Annealing the Cu/CrMoNbTaW bi-layer to 600 °C (Figure 5g) revealed that the Cu layer is still intact. Only after annealing at 700 °C small circular defects can be seen (Figure 5h). After annealing at 800 °C (Figure 5g) the surface appearance is similar to other bi-layer after annealing at 800 °C (see Figure 5c,f). The bi-layer using MnMoNbTaW as diffusion barrier already illustrates defects after annealing at 600 °C (Figure 5j). After annealing at 700 °C (Figure 5k) the defects mostly grow in size but not in number, which is in contrast to the Cu/MoNbTaTiW (Figure 5b) and Cu/MoNbTaVW (Figure 5e) bi-layers, where the circular defects grow in number and size with increased annealing temperatures. Still, after annealing at 800 °C (Figure 5l) the surface images look similar to the bi-layers in Figures 5c,f, and i. After annealing at 550 °C (Figure 5m) no defects are observed for the Cu/MoNbTaWZr bi-layer, but after annealing at 650 °C (Figure 5n) the barrier has fully failed and no Cu is visible. In comparison to Cu/MoNbTaTiW, Cu/MoNbTaVW, Cu/CrMoNbTaW and Cu/MnMoNbTaW the density of the black spots is higher at similar annealing temperatures. After annealing at 750 °C (Figure 5o) the density of the black spots increases further. The bi-layer using HfMoNbTaW as diffusion barrier shows a similar behavior as MoNbTaWZr, but the temperatures are 50 °C higher (Figure 5p-r).

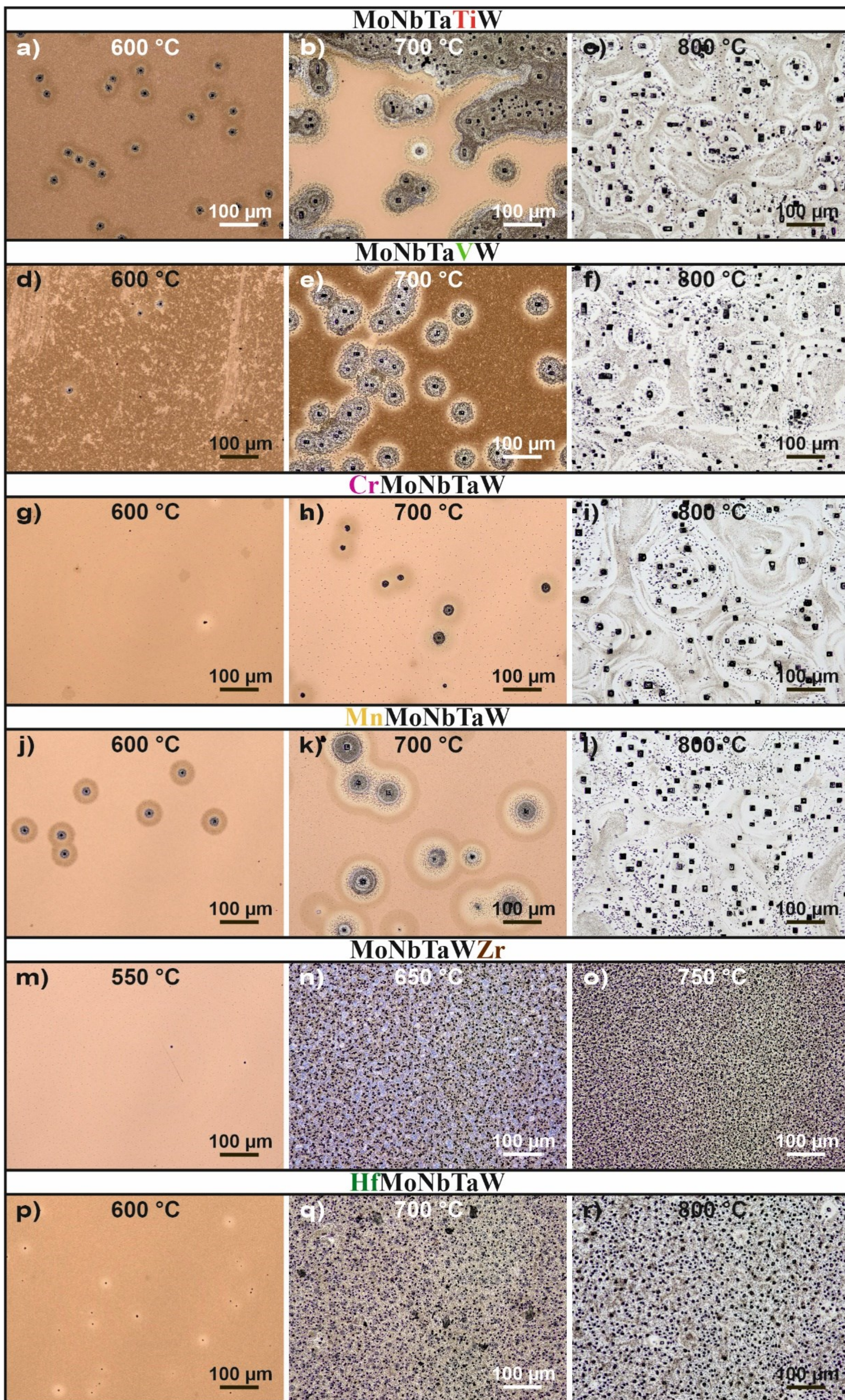

Figure 5 : The combination of an optical and a laser image for all bi-layers after annealing at elevated temperature is shown.

To reveal further details about the defects observed in Figure 5 EDX measurements were performed. The SEM surface micrographs shown in Figure 6 provide a detailed view of the circular defects formed during annealing. Here, the Cu/MoNbTaTiW and Cu/CrMoNbTaW bi-layers after annealing at 700 °C are shown as representative for all bi-layers. The large crystals, called black spots in Figure 5, show a composition according to Cu_3Si crystals where some Cu is replaced by O, i.e. $(Cu_xO_{1-x})_3Si$. The smaller crystals show also a composition according to Cu_3Si without pronounced incorporation of O. For simplicity reasons, both phases are summarized as Cu_3Si phase within this work. The light gray areas visible in Figure 6a are remnants of the Cu and MoNbTaTiW bi-layer according to the EDX measurements but with reduced thickness as compared to the fully intact film, due to Cu migration. The dark gray areas seen in both micrographs of Figure 6 are regions with unchanged bi-layers on top of the Si substrate. While in Figure 6a the unchanged bi-layer is found as remnant in a largely damaged region, the unchanged bi-layer in Figure 6b is mainly present surrounding the circular defect. A phase with a composition according to a $(MoNbTaW)Si_2$-based phase was not found in any of the films investigated by EDX.

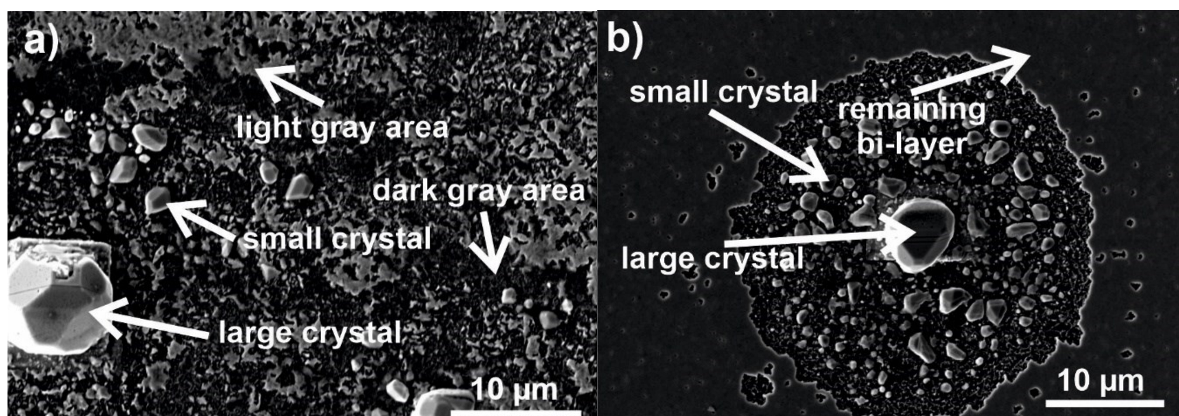

Figure 6: Secondary electron SEM picture of the surface of a) Cu/MoNbTaTiW and b) Cu/CrMoNbTaW after annealing at 700 °C.

4 DISCUSSION

4.1 AS-DEPOSITED FILMS

Cu is known to show room-temperature recrystallization or self-annealing [9,31], which leads to abnormal grain growth which happens within hours or days after deposition. During self-annealing the defect density decreases which can also lead to stress relaxation [41–43]. Grain growth and defect annihilation will influence the measured

electrical resistance of the film, which makes resistance measurements a tool to monitor Cu self-annealing. The resistance of all investigated bi-layers remained constant within the measured error bar, regardless of time when the deposition was performed. Within the investigated time no Cu self-annealing was observed, however, it cannot be excluded that it occurred prior to the first measurement, since 0.5 to 1 h have elapsed after the deposition and the first measurement. It is not expected to occur after the measured time frame, as according to literature it should already occur within the first 100 h [41–43].

In comparison to the single Cu layer, the Cu film on top of a MoNbTaW-based diffusion barrier shows a slightly more preferred (111) orientation suggesting a minor influence on the Cu growth behavior of the diffusion barriers. Among the different diffusion barriers, no significant influence on the Cu growth could be found. Most of the diffusion barrier layers show an amorphous microstructure, with only MoNbTaTiW and MoNbTaVW having a crystalline bcc microstructure. This is in agreement with our previous work, where it was found that these two alloys form only thin amorphous layers during early stages of film deposition [40].

4.2 Diffusion Barrier Performance

While bi-layers that show a sharp failure characteristic, such as Cu/MoNbTaWZr and Cu/HfMoNbTaW, the failure temperature observed by the different analysis techniques, namely XRD, resistivity, and surface imaging, align well, the same is not true for the other investigated bi-layers. The Hf and Zr containing barrier layers are either fully intact or have fully failed, within the annealing temperature steps applied in the current work, while the other bi-layers show a localized failure mode in the initial stage. The localized failure behavior, in the form of circular defects with black spots (Figure 5), suggests that growth defects within the diffusion barrier trigger barrier failure locally in the film. In principle, such a mechanism allows to further increase the failure temperature of the diffusion barriers by identifying and reducing or even omitting those defects with optimized film growth conditions. However, the mechanism also suggests that the failure of the bi-layer is statistically distributed and depends locally on the quality of the diffusion barrier as well as the incorporated growth defects within the diffusion barrier layer.

As the bi-layers in this work show a statistical behavior, it is convenient to evaluate the failure in a statistical manner. For this reason, the failure temperature T_{90}, where 90 %

of the film has failed, is introduced. This failure temperature can best be determined by the resistance measurements, as they provide good statistics over large parts of the surface. Here, the resistance value R_{90} where 90 % of the film has failed is calculated according to:

$$R_{90} = \frac{1}{\frac{0.1}{R_1} + \frac{0.9}{R_2}}, \quad (1)$$

where R_1 is the average resistance of all as-deposited bi-layers (0.038 Ω) and R_2 is the average resistance of all bi-layers after full failure (7.2 Ω). This gives a value of R_{90} = 0.36 Ω. The T_{90} temperature is now the temperature where the resistance is higher than R_{90} and can be derived from Figure 4 and is listed in Table 1.

Table 2: The T_{90} value of the different diffusion barriers MoNbTaW+X is summarized.

X	Ti	V	Cr	Mn	Zr	Hf
T_{90} [°C]	700	750	800	750	600	700

Diffusion barriers with an amorphous microstructure are expected to have a good barrier efficiency, due to the lack of grain boundaries which can act as fast diffusion channels [35]. Therefore, an amorphous microstructure is preferred over a polycrystalline microstructure. Within this study no clear influence of the microstructure was observed, as the bi-layers using MoNbTaWZr had an amorphous microstructure and showed the lowest T_{90} temperature of 600 °C, whereas the bilayers with a diffusion barrier with a crystalline bcc microstructure, Cu/MoNbTaTiW and Cu/MoNbTaVW showed significantly higher T_{90} temperatures of 700 and 750 °C, respectively. This suggests that besides the microstructure other parameters influence the barrier performance of the studied HEA-based diffusion barriers. According to literature such parameters could be the lattice distortion, cohesive energy and the packing density [24]. The lattice distortion leads to a different stress distribution in different directions, which influences the vacancy formation and the direction of the movement of the diffusing element [24]. According to Chang et al. [24], the change of the activation energy for diffusion ΔQ can be calculated using:

$$\Delta Q = (\Delta U_{strain} + \Delta \Omega_{mix}) \frac{S'}{S}, \quad (2)$$

where ΔU_{strain} is the change in strain energy, $\Delta \Omega_{mix}$ the change in cohesive energy and S' is the packing density of the HEA. The values of S' can be taken from the

appendix of their work [24] and S is the packing density of a unitary bcc alloy, which is 0.68. Further, the change in strain energy can be calculated using [24]:

$$\Delta U_{strain} = 4E\delta^2\overline{r^3}, \tag{3}$$

where E is the Young's modulus, calculated by rule of mixture [40], $\bar{r}$ is the mean atom radius using the values from [44], and δ is the lattice distortion calculated according to:

$$\delta = \sqrt{\sum_{i=1}^{n} C_i \left(1 - \frac{r_i}{\bar{r}}\right)^2}, \tag{4}$$

as defined by Guo et al. [45]. Here, C_i is the chemical composition of the element in at.% and r_i is the atom radius taken from [44]. The change in cohesive energy makes it easier or more difficult to break the bonds as well as to form vacancies. Since the cohesive energy depends on the local chemical environment, more vacancies will form in areas with low cohesive energy compared to areas with high cohesive energy. As a result, atoms are more likely to migrate along areas with low cohesive energy [24]. Thus, the $\Delta\Omega_{mix}$ can be calculated as:

$$\Delta\Omega_{mix} = \sum_{i=1, j\neq 1}^{n} \Delta\Omega_{ij} C_i C_j, \tag{5}$$

using

$$\Delta\Omega_{ij} = \frac{\Omega_{ii} + \Omega_{jj}}{2} - \Delta H_{ij}^{mix}, \tag{6}$$

where Ω_{ii}, Ω_{jj} is the fusion enthalpy of the different elements and ΔH_{ij}^{mix} is the mixing enthalpy [24]. The data is based on the references [46,47]. The calculated values for the change in strain energy, cohesive energy and activation energy for Cu diffusion are shown in Figure 7. The highest activation energy increase for Cu diffusion and, therefore, the highest diffusion barrier performance is expected for CrMoNbTaW, which is in good agreement with the obtained results. The second highest activation energy for Cu diffusion increase is predicted for the MoNbTaWZr and HfMoNbTaW diffusion barrier. This is in contrast to the obtained results where those two alloys have the lowest and second lowest T_{90} failure temperature. According to this analysis the influence of the fifth element can not only be explained by the changing strain energy

and cohesive energy. However, the analysis can be used to explain why the MoNbTaW-based alloys (with additional elements Ti, V, Cr, Mn, Zr or Hf) show a similar failure temperature as the base alloy of MoNbTaW, which fails between 600 [36] and 750 °C [35].

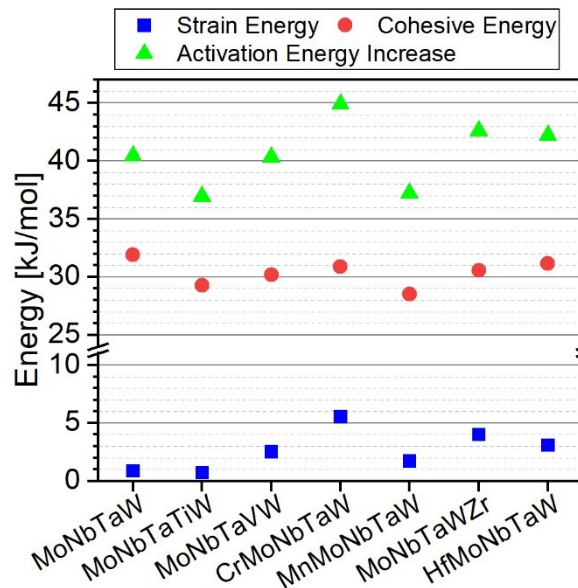

Figure 7: The strain energy increase, cohesive energy increase and the resulting activation energy increase of Cu diffusion for MoNbTaW-based diffusion barriers is shown. A high activation energy increase is typically associated to good Cu diffusion barrier performance.

From evaluating the performance of WTi-based diffusion barriers, it was found that Ti diffuses into Cu where it is dissolved, leading to defects within the diffusion barrier that are responsible for barrier failure [7]. To check if elements from the diffusion barrier studied in the current work show the tendency to be dissolved in Cu, the mixing enthalpy between Cu and the different elements within the HEA are compared, as shown in Figure 8a. The more negative the mixing enthalpy, the more the element is prone to be dissolved within Cu. Positive mixing enthalpies indicate less mixing. As Mo, Nb, W and Ta always have a positive mixing enthalpy when mixed with Cu, and their concentrations are constant within all studied diffusion barriers, the mixing enthalpy of the fifth alloying element is compared. As shown in Figure 8b, a linear correlation between the mixing enthalpy, between Cu and the respective element, and the failure temperature T_{90} exists. The coefficient of determination R^2 is 0.95, which can be interpreted, that the linear fit corelates well with the data points. The good agreement with our results points out the importance of the mixing enthalpy of the alloying elements within a HEA diffusion barrier and Cu. This leads to a new design

rule for HEA diffusion barriers: **The mixing enthalpy between Cu and all elements within the HEA diffusion barrier should be positive.**

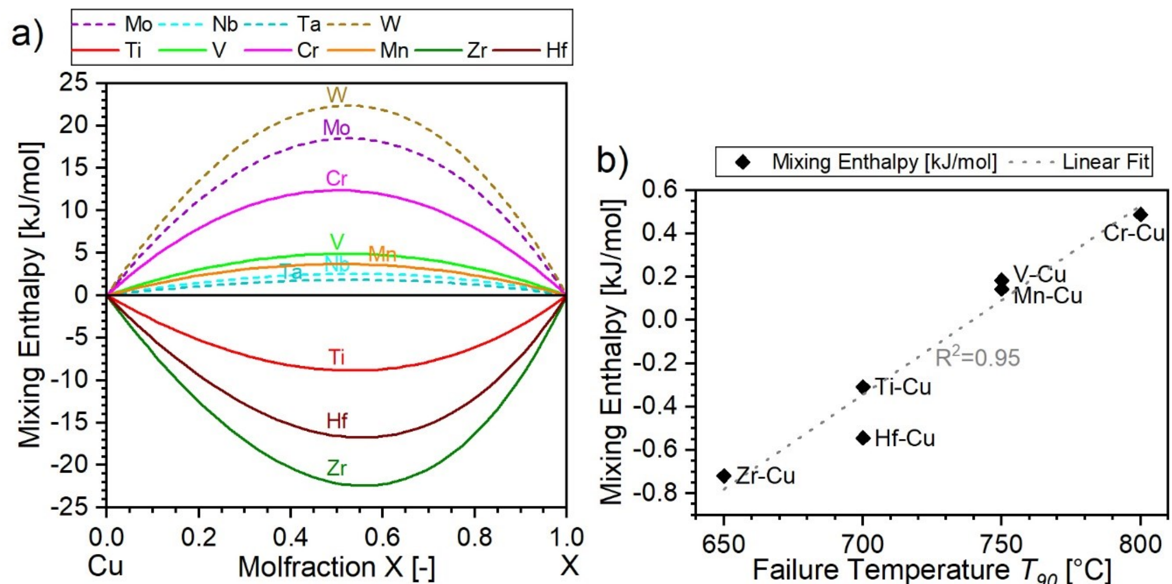

Figure 8: a) The mixing enthalpies between the different alloying elements used within the MoNbTaW based diffusion barrier and Cu are shown [46]. Elements with negative mixing enthalpies will mix more with Cu, while elements with positive values will mix less. b) Linear regression between the mixing enthalpy and the failure temperature T_{90}. The values for the mixing enthalpy are taken for a nearly pure Cu film (99 at.%) mixed with 1 at.% of the resprective element as shown in (a).

5 Conclusions

Six different HEA thin films based on MoNbTaW and alloyed with Ti, V, Cr, Mn, Zr or Hf have been investigated for their applicability to serve as diffusion barriers between Cu and Si. Most of the diffusion barriers showed an amorphous microstructure, only MoNbTaTiW and MoNbTaVW showed a crystalline bcc microstructure. The lowest failure temperatures of 600 and 700 °C were observed for MoNbTaWZr and HfMoNbTaW, respectively, and the highest one of 800 °C for CrMoNbTaW, where all these HEA barriers showed an amorphous microstructure. This indicates that the barrier performance of the studied HEA films is not or only weakly correlated to the microstructure being amorphous or bcc. Further, the cohesion energy and strain energy increase, which results in an increase of the activation energy of Cu diffusion within the HEA diffusion barrier and is used to explain the barrier performance, did not show a correlation to the failure temperature of the HEA barriers as well. However, a direct relation was found for the mixing enthalpy of the elements present in the HEA barrier and Cu which leads to a new design rule for HEA diffusion barriers: **The mixing**

enthalpy between Cu and all elements within the HEA diffusion barrier should be positive.

ACKNOWLEDGEMENTS

The authors acknowledge the funding from the Austrian Research Promotion Agency (FFG) (project number: 871687, PowerHEA). G.C. Gruber wishes to thank Prof. C. Mitterer (Montanuniversität Leoben, Austria) for the inspiring discussions.

REFERENCES

[1] P.C. Andricacos, Copper On-Chip Interconnections: A Breakthrough in Electrodeposition to Make Better Chips, Electrochem. Soc. Interface 8 (1999) 32–37. https://doi.org/10.1149/2.F06991IF.

[2] IEEE, Proceedings of the IEEE 1998 International Interconnect Technology Conference, Hyatt Regency Hotel, San Francisco, CA, June 1-3,1998, IEEE, Piscataway New Jersey, 1998.

[3] Dang R.L.M., Shigyo N., Coupling Capacitances for Two-Dimensonal Wires, IEEE Electron Device Letters (1981) 196–197.

[4] D. Gupta, Diffusion processes in advanced technological materials, William Andrew Pub, Norwich N.Y., 2005.

[5] H. Ono, T. Nakano, T. Ohta, Diffusion barrier effects of transition metals for Cu/M/Si multilayers (M=Cr, Ti, Nb, Mo, Ta, W), Appl. Phys. Lett. 64 (1994) 1511–1513. https://doi.org/10.1063/1.111875.

[6] N. Fréty, F. Bernard, J. Nazon, J. Sarradin, J.C. Tedenac, Copper Diffusion Into Silicon Substrates Through TaN and Ta/TaN Multilayer Barriers, Journal of Phase Equilibria & Diffusion 27 (2006) 590–597. https://doi.org/10.1361/154770306X153602.

[7] M. Fugger, M. Plappert, C. Schäffer, O. Humbel, H. Hutter, H. Danninger, M. Nowottnick, Comparison of WTi and WTi(N) as diffusion barriers for Al and Cu metallization on Si with respect to thermal stability and diffusion behavior of Ti, Microelectronics Reliability 54 (2014) 2487–2493. https://doi.org/10.1016/j.microrel.2014.04.016.

[8] I. Souli, V.L. Terziyska, J. Keckes, W. Robl, J. Zechner, C. Mitterer, Effect of growth conditions on interface stability and thermophysical properties of sputtered Cu films on Si with and without WTi barrier layers, Journal of Vacuum Science & Technology B, Nanotechnology and Microelectronics: Materials, Processing, Measurement, and Phenomena 35 (2017) 22201. https://doi.org/10.1116/1.4975805.

[9] T. Oku, E. Kawakami, M. Uekubo, K. Takahiro, S. Yamaguchi, M. Murakami, Diffusion barrier property of TaN between Si and Cu, Applied Surface Science 99 (1996) 265–272. https://doi.org/10.1016/0169-4332(96)00464-3.

[10] M. Mühlbacher, A.S. Bochkarev, F. Mendez-Martin, B. Sartory, L. Chitu, M.N. Popov, P. Puschnig, J. Spitaler, H. Ding, N. Schalk, J. Lu, L. Hultman, C. Mitterer, Cu diffusion in single-crystal and polycrystalline TiN barrier layers: A high-resolution experimental study supported by first-principles calculations, Journal of Applied Physics 118 (2015) 85307. https://doi.org/10.1063/1.4929446.

[11] M. Mühlbacher, G. Greczynski, B. Sartory, N. Schalk, J. Lu, I. Petrov, J.E. Greene, L. Hultman, C. Mitterer, Enhanced Ti0.84Ta0.16N diffusion barriers, grown by a hybrid sputtering technique with no substrate heating, between Si(001) wafers and Cu overlayers, Scientific reports 8 (2018) 5360. https://doi.org/10.1038/s41598-018-23782-9.

[12] B.S. Murty, J.-W. Yeh, S. Ranganathan, High-entropy alloys, Butterworth-Heinemann an imprint of Elsevier, London, Oxford, Amsterdam, San Diego, 2014.

[13] A. Xia, R. Franz, Thermal Stability of MoNbTaVW High Entropy Alloy Thin Films, Coatings 10 (2020) 941. https://doi.org/10.3390/coatings10100941.

[14] O.N. Senkov, G.B. Wilks, J.M. Scott, D.B. Miracle, Mechanical properties of Nb25Mo25Ta25W25 and V20Nb20Mo20Ta20W20 refractory high entropy alloys, Intermetallics 19 (2011) 698–706. https://doi.org/10.1016/j.intermet.2011.01.004.

[15] G.C. Gruber, A. Lassnig, S. Zak, C. Gammer, M.J. Cordill, R. Franz, Thermal stability of MoNbTaTiW, MoNbTaVW and CrMoNbTaW thin films deposited by high power impulse magnetron sputtering, Surface and Coatings Technology 454 (2023) 129189. https://doi.org/10.1016/j.surfcoat.2022.129189.

[16] Y. Tong, L. Bai, X. Liang, Y. Chen, Z. Zhang, J. Liu, Y. Li, Y. Hu, Influence of alloying elements on mechanical and electronic properties of NbMoTaWX (X = Cr, Zr, V, Hf and Re) refractory high entropy alloys, Intermetallics 126 (2020) 106928. https://doi.org/10.1016/j.intermet.2020.106928.

[17] Z.D. Han, N. Chen, S.F. Zhao, L.W. Fan, G.N. Yang, Y. Shao, K.F. Yao, Effect of Ti additions on mechanical properties of NbMoTaW and VNbMoTaW refractory high entropy alloys, Intermetallics 84 (2017) 153–157. https://doi.org/10.1016/j.intermet.2017.01.007.

[18] S.H. Chen, J.S. Zhang, S. Guan, T. Li, J.Q. Liu, F.F. Wu, Y.C. Wu, Microstructure and mechanical properties of WNbMoTaZrx (x = 0.1, 0.3, 0.5, 1.0) refractory high entropy alloys, Materials Science and Engineering: A 835 (2022) 142701. https://doi.org/10.1016/j.msea.2022.142701.

[19] Y. Li, W.-B. Liao, H. Chen, J. Brechtl, W. Song, W. Yin, Z. He, P.K. Liaw, Y. Zhang, A low-density high-entropy dual-phase alloy with hierarchical structure and exceptional specific yield strength, Sci. China Mater. 66 (2023) 780–792. https://doi.org/10.1007/s40843-022-2178-x.

[20] O. Samoilova, N. Shaburova, A. Ostovari Moghaddam, E. Trofimov, Al0.25CoCrFeNiSi0.6 high entropy alloy with high hardness and improved wear resistance, Materials Letters 328 (2022) 133190. https://doi.org/10.1016/j.matlet.2022.133190.

[21] C. Feng, X. Wang, L. Yang, Y. Guo, Y. Wang, High Hardness and Wear Resistance in AlCrFeNiV High-Entropy Alloy Induced by Dual-Phase Body-Centered Cubic Coupling Effects, Materials (Basel, Switzerland) 15 (2022). https://doi.org/10.3390/ma15196896.

[22] Y. Guo, P. Zhang, X. Zhang, Y. Cui, X. Mei, X. Li, H. Fan, D. Liu, Y. Wang, Study on the microstructural evolution in NbMoTaW series refractory multi-principal element alloy films by low-energy and high-flux He ions irradiation, Surface and Coatings Technology 452 (2023) 129140. https://doi.org/10.1016/j.surfcoat.2022.129140.

[23] Y. Zong, N. Hashimoto, H. Oka, Study on irradiation effects of refractory bcc high-entropy alloy, Nuclear Materials and Energy 31 (2022) 101158. https://doi.org/10.1016/j.nme.2022.101158.

[24] S.-Y. Chang, C.-E. Li, Y.-C. Huang, H.-F. Hsu, J.-W. Yeh, S.-J. Lin, Structural and thermodynamic factors of suppressed interdiffusion kinetics in multi-component high-entropy materials, Scientific reports 4 (2014) 4162. https://doi.org/10.1038/srep04162.

[25] S.-Y. Chang, C.-E. Li, S.-C. Chiang, Y.-C. Huang, 4-nm thick multilayer structure of multi-component (AlCrRuTaTiZr)N as robust diffusion barrier for Cu interconnects, Journal of Alloys and Compounds 515 (2012) 4–7. https://doi.org/10.1016/j.jallcom.2011.11.082.

[26] S.-Y. Chang, C.-Y. Wang, M.-K. Chen, C.-E. Li, Ru incorporation on marked enhancement of diffusion resistance of multi-component alloy barrier layers, Journal of Alloys and Compounds 509 (2011) L85-L89. https://doi.org/10.1016/j.jallcom.2010.11.124.

[27] S.-Y. Chang, C.-Y. Wang, C.-E. Li, Y.-C. Huang, 5 nm-Thick $(AlCrTaTiZrRu)N_{0.5}$ Multi-Component Barrier Layer with High Diffusion Resistance for Cu Interconnects, Nanosci Nanotechnol Lett 3 (2011) 289–293. https://doi.org/10.1166/nnl.2011.1155.

[28] D.-S. Chen, M.-K. Chen, S.-Y. Chang, Multiprincipal-Element AlCrTaTiZr-Nitride Nanocomposite Film of Extremely High Thermal Stability as Diffusion Barrier for Cu Metallization, ECS Trans. 19 (2009) 751–762. https://doi.org/10.1149/1.3122130.

[29] R. Li, T. Chen, C. Jiang, J. Zhang, Y. Zhang, P.K. Liaw, Applications of High Diffusion Resistance Multi- component AlCrTaTiZrRu/(AlCrTaTiZrRu)N 0.7 Film in Cu Interconnects, Adv. Eng. Mater. 22 (2020) 2000557. https://doi.org/10.1002/adem.202000557.

[30] R. Li, M. Li, C. Jiang, B. Qiao, W. Zhang, J. Xu, Thermal stability of AlCrTaTiZrMo-nitride high entropy film as a diffusion barrier for Cu metallization, Journal of Alloys and Compounds 773 (2019) 482–489. https://doi.org/10.1016/j.jallcom.2018.09.283.

[31] R. Li, B. Qiao, H. Shang, J. Zhang, C. Jiang, W. Zhang, Multi-component AlCrTaTiZrMo-nitride film with high diffusion resistance in copper metallization, Journal of Alloys and Compounds 748 (2018) 258–264. https://doi.org/10.1016/j.jallcom.2018.03.084.

[32] C. Jiang, R. Li, X. Wang, H. Shang, Y. Zhang, P.K. Liaw, Diffusion Barrier Performance of AlCrTaTiZr/AlCrTaTiZr-N High-Entropy Alloy Films for Cu/Si Connect System, Entropy (Basel, Switzerland) 22 (2020). https://doi.org/10.3390/e22020234.

[33] X. Peng, L. Chen, Effect of high entropy alloys TiVCrZrHf barrier layer on microstructure and texture of Cu thin films, Materials Letters 230 (2018) 5–8. https://doi.org/10.1016/j.matlet.2018.07.080.

[34] S.-C. Liang, D.-C. Tsai, Z.-C. Chang, T.-N. Lin, M.-H. Shiao, F.-S. Shieu, Thermally Stable TiVCrZrHf Nitride Films as Diffusion Barriers in Copper Metallization, Electrochem. Solid-State Lett. 15 (2012) H5. https://doi.org/10.1149/2.012201esl.

[35] K. Hu, Q.F. Hu, X. Xu, S.H. Chen, J. Ma, W.W. Dong, Excellent diffusion barrier property of amorphous NbMoTaW medium entropy alloy thin films used in Cu/Si Connect System, Vacuum 202 (2022) 111195. https://doi.org/10.1016/j.vacuum.2022.111195.

[36] P.F. Li, Y.J. Ma, H. Ma, S.W. Ta, Z. Yang, X.T. Han, M.J. Kai, J.H. Chen, Z.H. Cao, Enhanced diffusion barrier property of nanolayered NbMoTaW/TiVCr high entropy alloy for copper metallization, Journal of Alloys and Compounds 895 (2022) 162574. https://doi.org/10.1016/j.jallcom.2021.162574.

[37] A. Xia, R. Franz, Thermal Stability of MoNbTaVW High Entropy Alloy Thin Films, Coatings 10 (2020) 941. https://doi.org/10.3390/coatings10100941.

[38] Y.-T. Hsiao, C.-H. Tung, S.-J. Lin, J.-W. Yeh, S.-Y. Chang, Thermodynamic route for self-forming 1.5 nm V-Nb-Mo-Ta-W high-entropy alloy barrier layer: Roles of enthalpy and mixing entropy, Acta Materialia 199 (2020) 107–115. https://doi.org/10.1016/j.actamat.2020.08.029.

[39] J. Yan, Y.Z. Lin, Y. Wang, J. Qiu, F. Wan, C. Song, Refractory WMoNbVTa high-entropy alloy as a diffusion barrier between a molybdenum substrate and MoSi2 ceramic coating, Ceramics International 48 (2022) 11410–11418. https://doi.org/10.1016/j.ceramint.2021.12.364.

[40] G.C. Gruber, A. Lassnig, S. Zak, C. Gammer, M.J. Cordill, R. Franz, Synthesis and structure of refractory high entropy alloy thin films based on the MoNbTaW system, Surface and Coatings Technology 439 (2022) 128446. https://doi.org/10.1016/j.surfcoat.2022.128446.

[41] N. Alshwawreh, M. Militzer, D. Bizzotto, J.C. Kuo, Resistivity-microstructure correlation of self-annealed electrodeposited copper thin films, Microelectronic Engineering 95 (2012) 26–33. https://doi.org/10.1016/j.mee.2012.02.035.

[42] G. Brunoldi, S. Guerrieri, S.G. Alberici, E. Ravizza, G. Tallarida, C. Wiemer, T. Marangon, Self-annealing and aging effect characterization on copper seed thin films, Microelectronic Engineering 82 (2005) 289–295. https://doi.org/10.1016/j.mee.2005.07.037.

[43] I. Souli, V.L. Terziyska, J. Zechner, C. Mitterer, Microstructure and physical properties of sputter-deposited Cu-Mo thin films, Thin Solid Films 653 (2018) 301–308. https://doi.org/10.1016/j.tsf.2018.03.039.

[44] Charles Kittel, Introduction to solid state physics, 8th ed., John Wiley & Sons, Ltd, New Jersey, 2005.

[45] S. Guo, C.T. Liu, Phase stability in high entropy alloys: Formation of solid-solution phase or amorphous phase, Progress in Natural Science: Materials International 21 (2011) 433–446. https://doi.org/10.1016/S1002-0071(12)60080-X.

[46] A. Debski, R. Debski, W. Gasior, New Features of Entall Database: Comparison of Experimental and Model Formation Enthalpies/ Nowe Funkcje Bazy Danych Entall: Porównanie Doświadczalnych I Modelowych Entalpii Tworzenia, Archives of Metallurgy and Materials 59 (2014) 1337–1343. https://doi.org/10.2478/amm-2014-0228.

[47] P. Patnaik, Handbook of inorganic chemicals, McGraw-Hill, New York, NY, 2003.

Publication V

Refractory high entropy alloy nitride thin films as diffusion barriers in Cu metallizations

Georg C. Gruber, Stefan Wurster, Megan J. Cordill and Robert Franz

Surface and Coatings Technology (under review)

Refractory high entropy alloy nitride thin films as diffusion barriers in Cu metallizations

GEORG C. GRUBER[a†*], STEFAN WURSTER[b], MEGAN J. CORDILL[a,b] AND ROBERT FRANZ[a]

[a]Department of Materials Science, Montanuniversität Leoben, Franz-Josef-Strasse 18, 8700 Leoben, Austria

[b]Erich Schmid Institute of Materials Science, Austrian Academy of Sciences, Jahnstrasse 12, 8700 Leoben, Austria

[†]corresponding author (georg.gruber@unileoben.ac.at)

KEYWORDS

High Entropy Alloy, Refractory Metal, Transition Metal Nitride, MoNbTaW, Thin Film, Diffusion Barrier

ABSTRACT

The suitability of refractory high entropy alloy nitride (HEAN) thin films to act as diffusion barrier between Cu and Si was evaluated. For this purpose, bi-layers comprising a 150 nm thick Cu layer and a 20 nm thick layer based on (MoNbTaW)N and alloyed with either Ti, V, Cr, Mn, Zr or Hf have been deposited onto Si substrates using high power impulse magnetron sputtering. Subsequently, the bi-layers were annealed up to 950 °C in vacuum and analyzed by X-ray diffraction, confocal laser scanning microscopy and resistance measurements to check for barrier failure. Depending on the elements present in the HEAN layer, two failure modes were identified: (1) interdiffusion of Cu and Si leading to the formation of Cu_3Si starting at 850 °C and (2) dewetting of the Cu layer starting at 900 °C. A better barrier performance could be correlated to a lower formation enthalpy of the binary nitride of metals present in the HEAN layer leading to the conclusion that more stable metal-nitrogen bonds in the HEAN phase are beneficial for its diffusion barrier performance.

1 INTRODUCTION

As the number of transistors in microcontrollers increased, Al was replaced in the metallization by the more conductive Cu [1,2]. Besides the many advantages, Cu also poses a few challenges: it reacts with Si to form copper silicides and it can diffuse into insulating layers, especially Si-based layers [3]. In both cases, device failure may be

the consequence and therefore, diffusion barriers are introduced to prevent the detrimental effects associated to Cu. Besides stopping material transport between Cu and the insulator material or Si, a diffusion barrier must also fulfil several other requirements [4]. The diffusion barrier needs to adhere strongly to all materials it is in contact with and it needs to be resistant against mechanical and thermal stresses [4]. Furthermore, the diffusion barrier should be thermodynamically stable against all materials in its vicinity [4] and it needs to be a good electrical conductor when it is applied in the conduction path of the device. Many diffusion barrier materials cannot match the electrical conductivity of Cu and are applied as thin as possible to limit their influence on the overall electrical conductivity of the metal stack. If the diffusion barrier is only in contact with insulator materials, it should also be an insulator [3]. Apart from the requirements on the electrical conductivity, a diffusion barrier always needs to be a good thermal conductor [4].

It can be estimated that the activation energy for diffusion increases with increasing melting temperature. Thus, refractory metals like Ti, Cr, Nb, Mo, Ta or W and alloys based on these elements are often used as diffusion barriers [3,5]. An alloy that is frequently applied is WTi, but the out-diffusion of Ti into Cu can cause an early failure of the diffusion barrier and the device [6–8]. The out-diffusion of Ti could be prevented by the addition of N and the formation of a nitride layer, which led to a significant improvement of the diffusion barrier [7]. In general, refractory metal nitrides are well suited for diffusion barriers and frequently used materials are based on TiN [9–13] and TaN [14,15]. For TiN, different microstructures were compared for their barrier effectiveness. A polycrystalline TiN microstructure had the least resistance against Cu diffusion, and the highest resistance against Cu diffusion was found for a single crystalline TiN microstructure [9,12]. The improved diffusion barrier properties are due to the missing grain boundaries of a single crystalline film, as grain boundaries can act as fast diffusion paths [3,12]. Since it is not always possible to apply a single crystalline film in actual devices often amorphous films, which also lack grain boundaries, are used for diffusion barriers. One example for a thermally stable amorphous diffusion barrier is TaSiN [3].

Other materials with potential use as diffusion barriers are high entropy alloys (HEAs) and HEA nitrides (HEAN). Chang et al. found that with increasing number of elements within a diffusion barrier the resistance against Cu diffusion increased [16]. HEAs, in general, are alloys with a configurational entropy of at least 1.5R, where R is the gas

constant [17]. The most studied HEAN diffusion barriers are based on (AlCrTaTiZr)N [18–23]. With such films it was found that a 40 nm thick (AlCrTaTiZr)N film with a microstructure consisting of nanocrystals embedded in an amorphous matrix had the best diffusion barrier properties and prevented barrier failure up to 900 °C [18]. Additionally, (CrHfTiVZr)N diffusion barriers with an amorphous structure have been investigated and prevented barrier failure up to at least 800 °C [24].

The aim of this study is to evaluate the suitability of (MoNbTaW)N-based HEANs to act as diffusion barriers within microelectronic systems. For this purpose, six different stacks including a 20 nm thick (MoNbTaW)N-based diffusion barrier, alloyed with a fifth element (Ti, V, Cr, Mn, Zr or Hf), were deposited using high power impulse magnetron sputtering (HiPIMS). Subsequent to the deposition, the films were annealed at temperatures up to 950 °C for 30 min. The barrier failure was assessed by X-ray diffraction (XRD), resistance measurements and surface imaging.

2 EXPERIMENTAL DETAILS

For the synthesis of the refractory HEAN diffusion barrier films equimolar MoNbTaTiW, MoNbTaVW, CrMoNbTaW, MnMoNbTaW, MoNbTaWZr and HfMoNbTaW targets with a diameter of 76 mm were used. The targets were manufactured by powder metallurgical methods by Plansee Composite Materials GmbH (Lechbruck, Germany). A Cu target was used for the Cu films. The films were deposited on polished 325 µm thick B-doped (100) Si substrates (21 mm × 7 mm) using a lab-scale deposition system equipped with an unbalanced magnetron source. Acetone and then ethanol were used to clean the substrates in an ultrasonic bath before deposition. Afterwards, the substrates were placed in front of the magnetron source at a distance of 150 mm and the chamber was evacuated to a base pressure of $9 \cdot 10^{-4}$ Pa or below, before Ar was introduced to establish the etching pressure of 3 Pa. The substrates were plasma etched for 10 min applying 800 V, 100 kHz and a pulse length of 1 µs. After etching 0.1 Pa of N_2 was introduced into the vacuum chamber and the Ar flow was adjusted to obtain a total pressure of 1 Pa. The HEAN diffusion barrier layers were deposited using HiPIMS with an average power of 400 W, a frequency of 100 Hz, and a duty cycle of 1 %. Here, the duty cycle is defined as the ratio between the pulse on-time (100 µs) and the total pulse duration (10000 µs). The deposition time was set to 2 minutes to achieve a film thickness of 20 nm. Then, 3 min after the HEAN deposition was finished

and without breaking the vacuum, the Cu deposition was made. HiPIMS with an average power of 400 W, a frequency of 100 Hz and a duty cycle of 2 % was used to deposit the Cu film. Additionally, 300 nm HEAN single-layer films were deposited on Si and a polyimide (PI) foil to analyze microstructure and chemical composition.

For annealing of the samples, a HTM Retz vacuum furnace was used which was evacuated to a pressure of $5 \cdot 10^{-4}$ Pa prior to the annealing sequence. In the first step, the vacuum furnace was heated up to 250 °C with a heating rate of 20 K/min. To allow the temperature to stabilize, a waiting period of 30 minutes was introduced at this temperature. In the second step, the vacuum furnace was heated up to the desired annealing temperature with the same heating rate and held at this temperature for 30 min. All Cu/HEAN bi-layers were annealed at 600, 650, 700, 800 and 900 °C. In addition, the Cu/(MoNbTaVW)N, Cu/(CrMoNbTaW)N and Cu/(MnMoNbTaW)N bi-layers were annealed at 850 °C, and the Cu/(MoNbTaTiW)N, Cu/(MoNbTaWZr)N and Cu/(HfMoNbTaW)N bi-layers at 950 °C. A different sample was used for each annealing temperature.

The microstructure of the as deposited single-layer HEAN films on Si and of the HEAN in the bi-layers before and after annealing was investigated by XRD measurements using a Bruker-AXS D8 Advance diffractometer equipped with Cu-K_α radiation and parallel optics. The measurements were performed in Bragg-Brentano geometry. Besides revealing details about the films' microstructure in as-deposited state, these measurements allowed to check for the formation of new phases during annealing, in particular Cu_3Si which is typically a sign for barrier failure. Further, the resistance was measured after annealing using a Jandel Model RM2 cylindrical four-point probe, as well to check for barrier failure. Surface images were recorded using a Keyence 3D confocal laser scanning microscope, VK-X1100 Series, to monitor general changes in the surface appearance of the bi-layer films. Selected surface areas were imaged with a Tescan Magna scanning electron microscope (SEM) using the secondary electron signal. From some features within these areas the chemical composition was analyzed by energy-dispersive X-ray (EDX) spectroscopy using a Bruker Type XFlash 6-60 detector which was attached to the SEM. The chemical composition of the single-layer HEAN films on PI was measured by EDX using a detector by Oxford Instrument attached to a Tescan Clara SEM.

3 RESULTS AND DISCUSSION

3.1 HIGH ENTROPY ALLOY NITRIDE FILMS

The results of the EDX measurements to determine the chemical composition of the HEAN single-layer films are summarized in Table 1. All films have a N content below 50 at.%, which would be the stoichiometric composition for most binary transition metal nitrides with face-centered cubic (fcc) structure. The lowest N content was found for the (MnMoNbTaW)N film, which has a N concentration of 29.3 at.%. The N concentration of the (CrMoNbTaW)N film is about 10 at.% higher. All other films have a N concentration of above 40 at.%. The chemical composition of the metal elements within the films slightly depends on the mass of the different elements. All films show a slightly lower concentration of the heavier elements, W and Ta, as well as Hf in the case of the (HfMoNbTaW)N film. The reason for the lower concentration of the heavy elements is the different angular emission of the heavier elements, as found by Xia et al. [25] for MoNbTaVW films.

Table 1: Chemical composition of the HEA nitride films as measured by EDX. All values are in at.%.

	Mo	Nb	Ta	W	Ti	V	Cr	Mn	Zr	Hf	N
(MoNbTaTiW)N	11.5	10.8	9.0	10.0	13.7						45.1
(MoNbTaVW)N	12.6	11.9	9.9	11.1		12.8					41.8
(CrMoNbTaW)N	13.7	12.5	10.3	11.6			13.4				38.5
(MnMoNbTaW)N	15.5	14.9	12.1	13.2				15.0			29.3
(MoNbTaWZr)N	12.3	12.6	8.8	10.2					12.1		43.9
(HfMoNbTaW)N	13.1	12.2	10.0	10.8						8.9	45.0

The microstructure of the single-layer HEAN films was analyzed by XRD as shown in Figure 1. All HEAN films, independent of the N concentration within the film, have a fcc, NaCl-like structure. The intensity of the (111) peak of all films, except (MnMoNbTaW)N, is higher compared to the intensity of the (200) peak and in addition for those films the (200) peak is also wider compared to (111) peak. In the case of the (MoNbTaTiW)N and (MoNbTaWZr)N films the (200) peak is hardly visible.

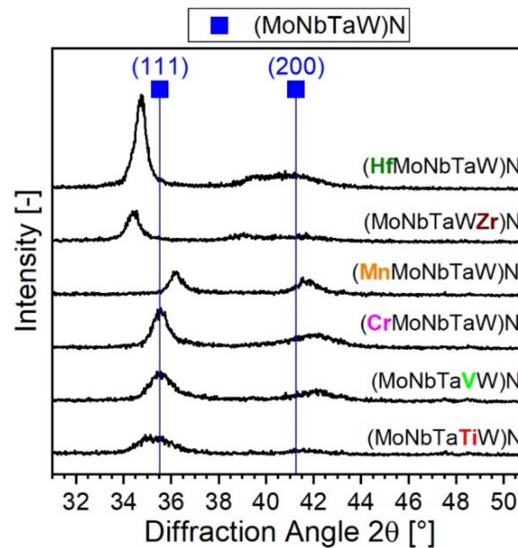

Figure 1: X-ray diffractograms of the as-deposited HEAN single-layer films.

3.2 Microstructure of As-Deposited Bi-Layer Films

In Figure 2 the microstructure of the Cu films deposited on top of the different (MoNbTaW)N-based diffusion barriers is compared to the microstructure of a Cu film deposited directly on the (100) Si substrate. According to the diffractograms, the microstructure of the Cu films in as-deposited state is only slightly affected by the underlying diffusion barrier. On the left-hand side of the Cu (111) peak a small shoulder is visible, which can be attributed to the (200) peak of the (MoNbTaW)N-based diffusion barrier. For most of the bi-layers a small (111) (MoNbTaW)N peak is also visible. However, both peaks associated to the (MoNbTaW)N-based phase show a low intensity regardless of the bi-layer indicating a low crystallinity of these phases. This can be understood by their low thickness of about 20 nm [26,27].

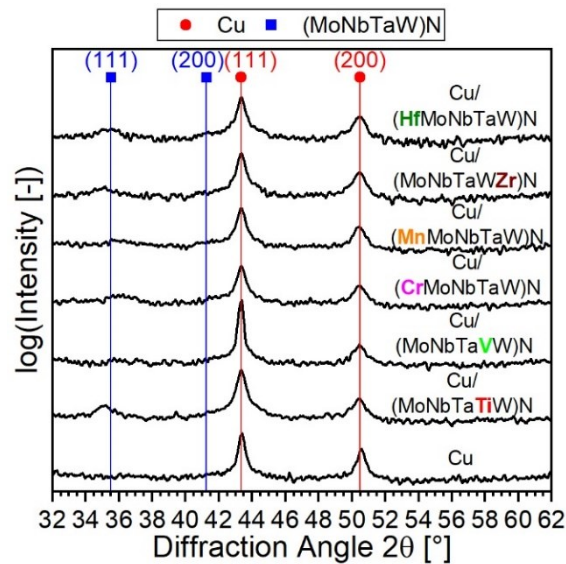

Figure 2: X-ray diffractograms of the as-deposited Cu single layer and Cu/HEAN bi-layers films on (100) Si substrate.

3.3 Diffusion Barrier Performance

The electrical resistance of all as-deposited bi-layers is similar as shown in Figure 3. In addition, potential changes of the electrical resistance were assessed after each annealing step. After annealing at 600 °C, the electrical resistance of all bi-layers decreases which can be attributed to grain growth and defect annihilation. It remains largely constant up to an annealing temperature of 800 °C. After annealing at 850 °C the resistance of the bi-layers containing (MoNbTaVW)N, (CrMoNbTaW)N and (MnMoNbTaW)N significantly increases, indicating barrier failure. The resistance of those films further increases after annealing at 900 °C. In contrast, after annealing at 900 °C the resistance of the bi-layer containing (MoNbTaTiW)N remains constant at a low value which is interpreted that the barrier is still intact. The bi-layers containing (MoNbTaWZr)N or (HfMoNbTaW)N show an intermediate value after annealing at 900 °C, indicating a partial failure. The resistance of the Cu/(MoNbTaWZr)N bi-layer remains constant within the measurement error after annealing at 950 °C, while the resistance of the Cu/(HfMoNbTaW)N bi-layer further increases. After annealing at 950 °C the resistance of the bi-layer containing (MoNbTaTiW)N strongly increases, typically associated to barrier failure.

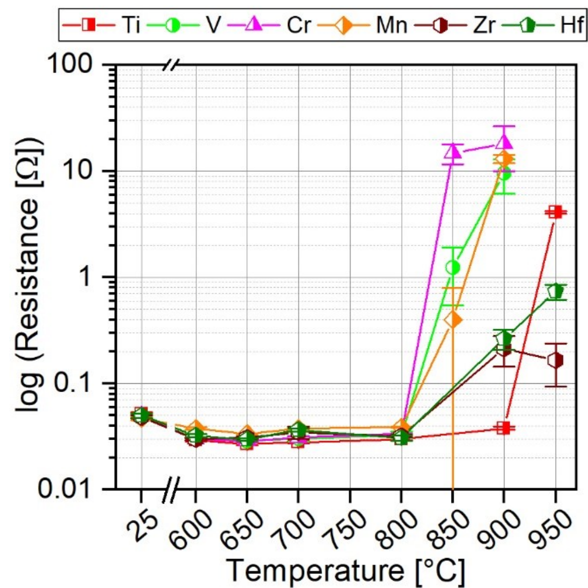

Figure 3: The electrical resistance of the bi-layer films as a function of annealing temperature.

Figure 4a shows the X-ray diffractograms of the Cu/(MoNbTaVW)N bi-layer after annealing at the different temperatures. With increasing annealing temperature up to 800 °C the intensity of the (200) Cu peak increases and both Cu peaks get sharper. The (111) (MoNbTaVW)N peak is not visible within the diffractogram of the as-deposited film, but after annealing at 600 °C, indicating the formation of a crystalline structure. From 600 to 800 °C the (111) (MoNbTaVW)N peak shifts slightly towards higher diffraction angles which is associated to a reduction of the lattice constant. After annealing at 850 °C, both Cu peaks significantly lose intensity, while the (MoNbTaVW)N peaks disappear. Instead, Cu_3Si peaks emerge, a typical indication for barrier failure. The failure temperature determined from the X-ray diffractograms is in good agreement with that obtained from the resistance measurements after annealing (see Figure 3). The shoulder visible on the right-hand side of the (111) Cu peak at 800 °C and below is most likely related to a surface oxide and not to Cu_3Si as it is already visible in the as-deposited state. After annealing at 900 °C all Cu peaks vanished indicating that the entire Cu reacted with Si to Cu_3Si. Furthermore, after annealing the Cu/(MoNbTaVW)N bi-layer at 850 °C (MoNbTaVW)Si_2 peaks, indicated by $MoSi_2$ within the X-ray diffractogram in Figure 4a, can be found. The existence of a silicide phase containing the metals of the HEAN diffusion barrier indicates that the diffusion barrier has reacted with the Si substrate.

The phases found after annealing of the bi-layers containing (CrMoNbTaW)N or (MnMoNbTaW)N are similar to those of the Cu/(MoNbTaVW)N bi-layer and

summarized in Figure 4c. The main difference is that for the (CrMoNbTaW)N containing bi-layer the Cu peaks vanished after annealing at 850 °C. The observation explains the high resistance value of this bi-layer after annealing at this temperature (see Figure 3). In general, the result for the failure temperature of the Cu/(CrMoNbTaW)N and Cu/(MnMoNbTaW)N bi-layers obtained by XRD (Figure 4c) and resistance measurements (Figure 3) are in good agreement.

Similar to other bi-layers, for Cu/(HfMoNbTaW)N the Cu (200) peak increases in intensity and both Cu peaks becomes sharper after annealing at 600 °C, as compared to the as-deposited bi-layer (see Figure 4b). However, in this case the Cu peaks remain largely unchanged up to the highest annealing temperature of 950 °C. A minor contribution of peaks associated to Cu_3Si is visible after annealing at 900 °C, indicating the onset of the barrier failure. While the shape of the (111) (HfMoNbTaW)N peak remains largely unchanged up to the highest annealing temperature of 950 °C, the peak shifts towards higher diffraction angles with increasing temperature. No HEA silicide phase formation was observed in this case.

The bi-layer containing (MoNbTaWZr)N shows almost identical results as the Cu/(HfMoNbTaW)N bi-layer based on the X-ray diffractograms after annealing and, hence, the occurring phases are summarized in Figure 4c. The Cu/(MoNbTaTiW)N bi-layer also shows similar results, with the difference that peaks associated to Cu_3Si are only observed at the maximum annealing temperature of 950 °C. This result agrees with the resistance measurements (see Figure 3), where also no resistance increase could be noticed for the Cu/(MoNbTaTiW)N bi-layer after annealing up to 900 °C.

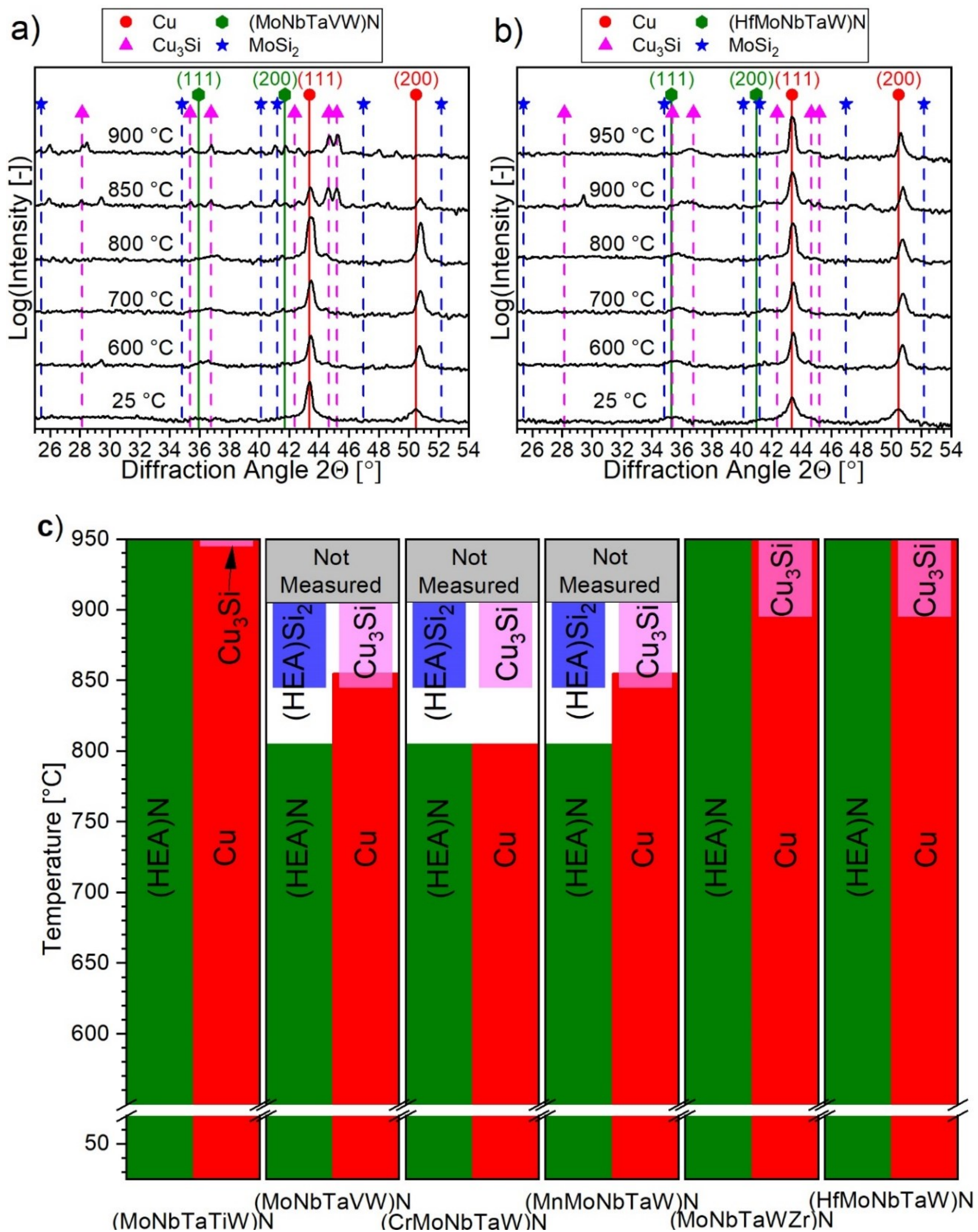

Figure 4: X-ray diffractograms of the bi-layer films using a) (MoNbTaVW)N and b) (HfMoNbTaW)N. c) Schematic overview of the phase evolution with annealing temperature derived from XRD measurements for all studied bi-layer films.

In Figure 5 the combined optical and laser intensity images of the surface of all studied bi-layer films after annealing at elevated temperatures is shown. Similar to the XRD and resistance measurements, the same two groups can be distinguished. The first group comprises the Cu/(MoNbTaVW)N, Cu/(CrMoNbTaW)N and Cu/(MnMoNbTaW)N bi-layers and the second the remaining ones. Regardless of the group classification, all bi-layer films are still intact after annealing at 800 °C.

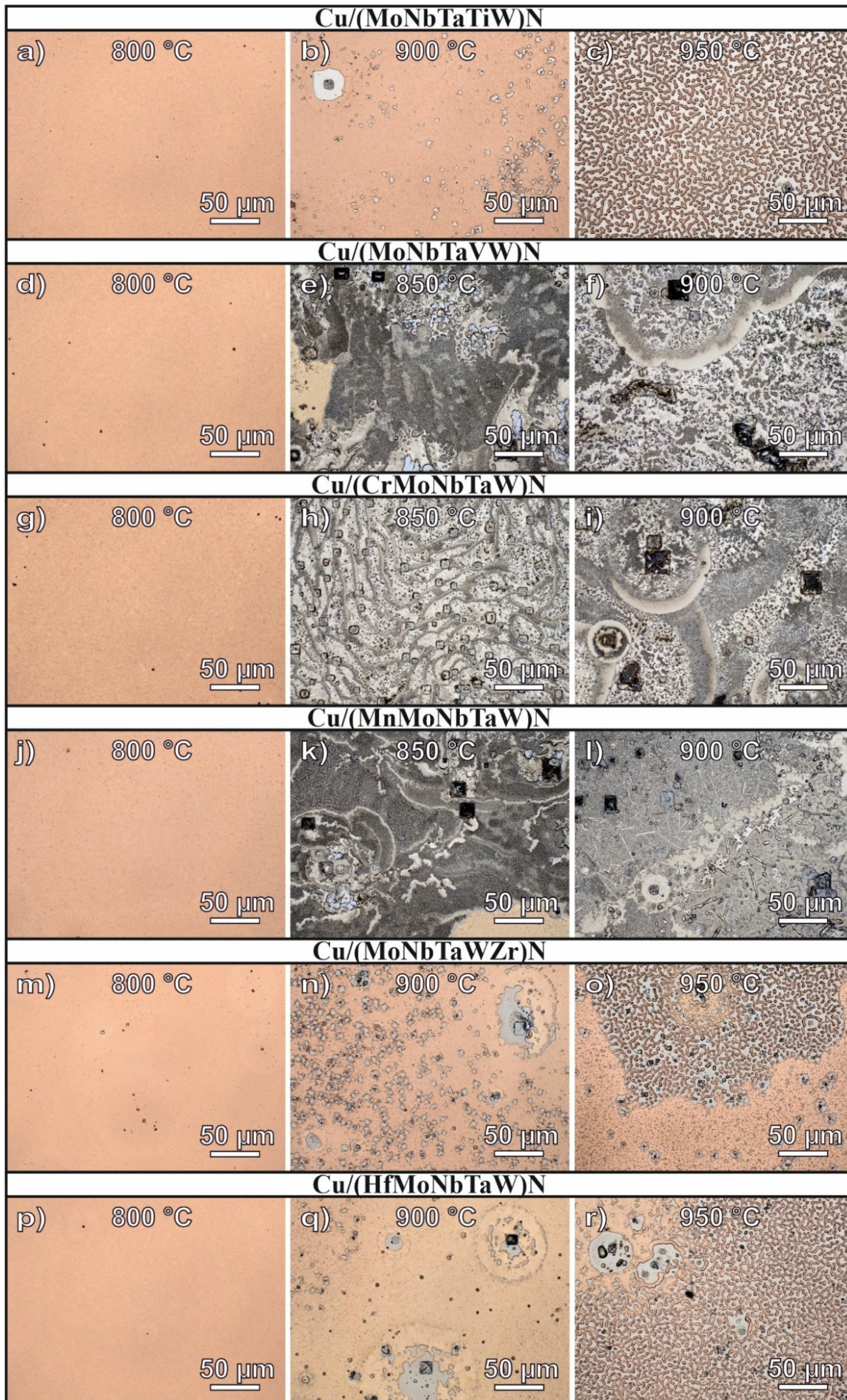

Figure 5: Combined optical and laser intensity images of all bi-layer films after annealing at elevated temperature.

After annealing of the bi-layers from the first group at 850 °C (Figure 5e, h and k), surface first appear that are most likely caused by a reaction of the bi-layer with the substrate. In contrast to our previous study [28], where the barrier failure of the metallic HEA films started locally, a more global failure covering almost the whole surface is encountered for the HEAN films in the current case. Further details about the change in surface appearance can be derived from a combined SEM+EDX analysis. In Figure 6a, a Cu_3Si can be seen beside a MoNbTaVW-containing phase. According to the XRD results, a $(MoNbTaVW)Si_2$ phase should already be present at this temperature, but due to the strong Si signal from the substrate in the EDX spectra, these results are ambiguous in this respect. The presence of a non-continuous (MoNbTaVW)N layer, that is undetected by XRD, cannot be completely excluded. High resolution analysis techniques, such as transmission electron microscopy, would be necessary to fully characterize the film chemistry after annealing, but are beyond the scope of the current work. Here, the focus was on identifying the onset of barrier failure which is clearly visible in the recorded surface images. A distinct surface feature is shown in Figure 6b of a Cu_3Si phase inside and surrounding a square-shaped hole. Such holes are most likely the remnants of Cu_3Si crystals shaped as square-based pyramids similar to the ones observed in our previous work [28]. As the melting temperature of Cu_3Si is about 850 °C [29], the Cu_3Si phase most probably melted during annealing. After annealing at 900 °C, the surface images of the bi-layers from the first group (Figure 5f, i and l) remain largely unchanged as compared to annealing at 850 °C. The higher resolution SEM image in Figure 6c reveals that, in addition to Cu_3Si, a needle-like structure can also be seen. These needles can be attributed to the $(HEA)Si_2$ phase.

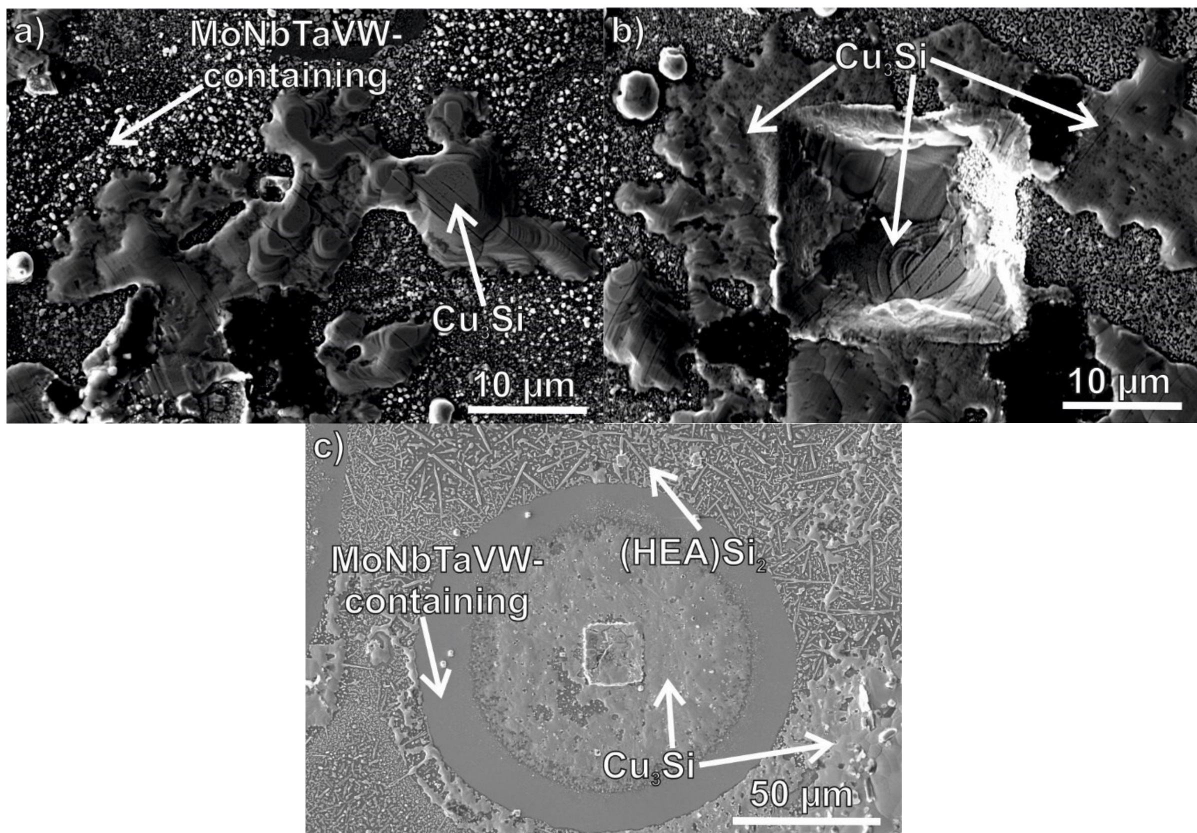

Figure 6: Secondary electron SEM images of the surface of Cu/(MoNbTaVW)N after annealing at a,b) 850 °C and c) 900 °C. EDX spectra (not shown) were recorded to determine the chemical composition of points of interest in order to locate the phases formed during annealing (XRD analysis served as reference for phase identification).

After annealing the bi-layers from the second group at 900 °C (Figure 5b, n and q), the Cu film remains undamaged in most parts. Only a few black or gray squares can be seen that are sometimes surrounded by a ring, where the lowest number was observed on the surface of the Cu/(MoNbTaTiW)N bi-layer. The combined SEM+EDX analysis (Figure 7a) revealed that these black squares are Cu_3Si crystals surrounded by an elevated Cu ring. Inside the Cu rings, the HEAN layer becomes visible for all three bi-layers. In addition, dewetting of the Cu layer seems to occur in the area around the Cu_3Si crystals as well as other regions exposing the HEAN layer. After annealing of these bi-layers at 950 °C (Figure 5c, o and r) the dewetting of the Cu layer increased significantly. The dewetted Cu can be clearly seen in the SEM surface image of the (HfMoNbTaW)N containing bi-layer in Figure 7b. In contrast, the number of spots related to the formation of Cu_3Si seems to increase only slightly. These observations allow the conclusion that the bi-layers containing (MoNbTaTiW)N, (MoNbTaWZr)N or (HfMoNbTaW)N fail only partly due to diffusion of Cu or Si through the diffusion barrier, but mainly by dewetting of the Cu layer. For device stability in microelectronics the use of an additional adhesion layer on top of this diffusion barrier would be necessary, to

fully benefit from the good interdiffusion barrier properties of these HEAN. Certain alloying elements like Ru have been shown to improve the adhesion of the diffusion barrier and the Cu layer [30].

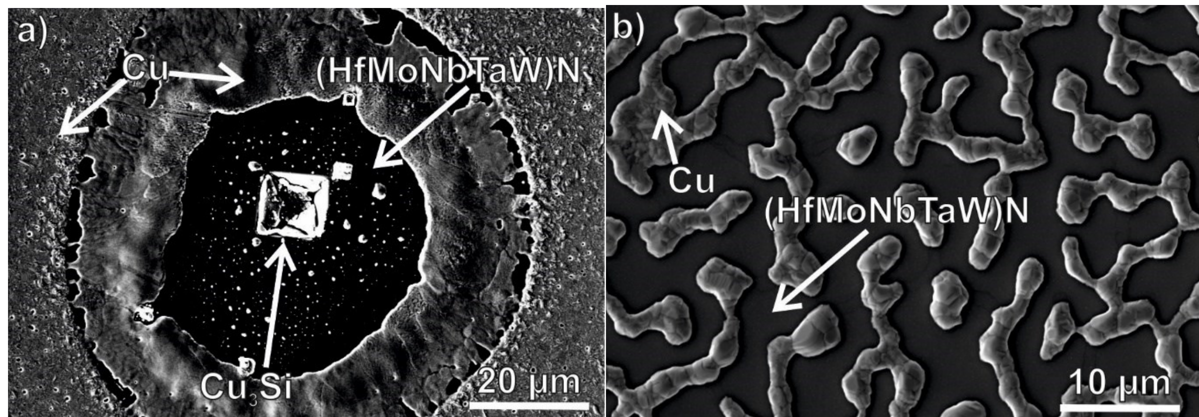

Figure 7: Secondary electron SEM images of the surface of Cu/(HfMoNbTaW)N after annealing at a) 900 °C and b) 950 °C. EDX spectra (not shown) were recorded to determine the chemical composition of points of interest in order to locate the phases formed during annealing annealing (XRD analysis served as reference for phase identification).

Summarizing the experimental results, two different failure mechanisms can be identified for the two groups of bi-layers. For the first group comprising (Cu/(MoNbTaVW)N, Cu/(CrMoNbTaW)N and Cu/(MnMoNbTaW)N) interdiffusion and formation of Cu_3Si are responsible for the barrier failure, and for the second group including (Cu/(MoNbTaTiW)N, Cu/(MoNbTaWZr)N and Cu/(HfMoNbTaW)N) mainly dewetting of the Cu layer with only limited interdiffusion and formation of Cu_3Si occurs. As the N concentration of (MoNbTaVW)N is similar to the N concentration of the films of the second group, it seems unlikely that the difference in diffusion barrier performance can be explained by difference in the N concentration (Table 1). Further studies including a N content variation would be necessary to fully understand the influence of the N concentration on the diffusion barrier performance of those HEAN films. However, when comparing the formation enthalpies of the binary nitrides of the fifth alloying elements (Ti, V, Cr, Mn, Zr or Hf) shown in Table 2, it can be noticed that those of the first group have an enthalpy higher than -100 kJ/mol and those of the second group lower than -150 kJ/mol [31]. In general, the more negative the formation enthalpy for the nitride, the more stable the bond and, evidently, the more difficult for Cu or Si to diffuse through the barrier. Based on this finding, a rule for HEAN-based diffusion barriers can be derived: The formation enthalpy of all binary nitrides should be as low as possible. For example, the (MoNbTaTiW)N diffusion barrier, which showed the best performance in this work, could be further improved by substituting

Mo and W as they have a high binary nitride formation enthalpy (see Table 2). Instead, alloying with Zr and Hf to form a (HfNbTaTiZr)N diffusion barrier should result in an even better barrier performance. However, in case of metal diffusion barriers Ti, Zr and Hf tend to diffuse out of the diffusion barriers into Cu triggering an early barrier failure [28]. The formation of strong bonds to N in the nitride phase seems to hinder this effect. A similar behavior was found for WTiN, where the N incorporation to form WTiN also prevented the Ti out-diffusion from the barrier layer [7].

Table 2: The formation enthalpy E_F of the different binary transition metal nitrides used within this study [31].

	NbN	MoN	TaN	WN		
E_F [kJ/mol]	-124	-46	-118	-30		
	TiN	VN	CrN	MnN	ZrN	HfN
E_F [kJ/mol]	-155	-86	-40	-59	-185	-169

The diffusion barriers of both groups only fail when exposed to temperatures exceeding 800 °C, either due to interdiffusion (1st group) or dewetting of the Cu top layer (2nd group). Compared to their metal counterparts [28], the highest temperature with active barrier performance was increased by up to 250 °C, e.g. from 550 °C for metallic MoNbTaWZr to 800 °C for nitride (MoNbTaWZr)N. Such temperatures have also been reported for other HEAN diffusion barriers in literature [20,22,24,32,33]. While the barriers discussed in those studies were all amorphous and, hence, without fast diffusion paths, the barriers studied in this work are crystalline with potentially fast diffusion along the grain boundaries. Therefore, a possible further improvement of the diffusion barrier performance could be achieved by synthesizing the refractory HEAN from this work in an amorphous state. The highest temperature HEA-based diffusion barriers operated without failure was found to be 900 °C [18,19], the same temperature the barriers of the second group achieved and even at 950 °C no significant Cu_3Si formation after annealing was noticed, only dewetting of Cu. This means that another way of improving the barrier performance is due to enhancing the adhesion between the HEAN barriers and Cu, e.g. by introducing an adhesion layer.

4 CONCLUSIONS

A series of (MoNbTaW)N-based thin films was deposited by HiPIMS to evaluate their suitability to serve as diffusion barriers in microelectronics. After annealing in vacuum at different temperatures, two failure mechanisms could be identified: (1) interdiffusion of Cu and Si to form Cu_3Si occurring at 850 °C and above in the case of (MoNbTaVW)N, (CrMoNbTaW)N and (MnMoNbTaW)N and (2) dewetting of the Cu film on top of the diffusion barriers (MoNbTaTiW)N, (MoNbTaWZr)N and (HfMoNbTaW)N at 900 °C. The latter is considered a failure as it is expected to lead to a potential device failure, even though the barriers remained largely intact. The improved barrier performance of these layers correlates with the low formation enthalpy of the binary nitride phases of the metals present in the layer. One conclusion that could be determined is that more stable metal-nitrogen bonds in the HEAN diffusion barrier are beneficial for improved barrier performance. A further improvement of HEAN diffusion barrier performance is expected by selecting metals with stable binary nitrides, in particular Hf, Nb, Ta, Ti and Zr, to form the HEAN phase. Other contributions to potentially improve the barrier performance comprise the synthesis of amorphous films to hinder fast diffusion along grain boundaries in polycrystalline films like in the present case as well as enhancing the adhesion between the HEAN diffusion barrier and the Cu layer. In general, HEAN films are promising candidates to serve as diffusion barriers in Cu metallization which is frequently applied in microelectronics.

ACKNOWLEDGEMENTS

The authors acknowledge the funding from the Austrian Research Promotion Agency (FFG) (project number: 871687, PowerHEA). G.C. Gruber wishes to thank Prof. C. Mitterer (Montanuniversität Leoben, Austria) for the inspiring discussions.

REFERENCES

[1] IEEE, Proceedings of the IEEE 1998 International Interconnect Technology Conference, Hyatt Regency Hotel, San Francisco, CA, June 1-3,1998, IEEE, Piscataway New Jersey, 1998.

[2] Dang R.L.M., Shigyo N., Coupling Capacitances for Two-Dimensonal Wires, IEEE Electron Device Letters (1981) 196–197.

[3] D. Gupta, Diffusion processes in advanced technological materials, William Andrew Pub, Norwich N.Y., 2005.

[4] M.-A. Nicolet, Diffusion barriers in thin films, Thin Solid Films 52 (1978) 415–443. https://doi.org/10.1016/0040-6090(78)90184-0.

[5] H. Ono, T. Nakano, T. Ohta, Diffusion barrier effects of transition metals for Cu/M/Si multilayers (M=Cr, Ti, Nb, Mo, Ta, W), Appl. Phys. Lett. 64 (1994) 1511–1513. https://doi.org/10.1063/1.111875.

[6] Q. Wang, Z. Fan, S. Liang, Thermal stability of nanocrystalline W-Ti diffusion barrier thin films, Sci. China Technol. Sci. 53 (2010) 1049–1055. https://doi.org/10.1007/s11431-009-0402-z.

[7] M. Fugger, M. Plappert, C. Schäffer, O. Humbel, H. Hutter, H. Danninger, M. Nowottnick, Comparison of WTi and WTi(N) as diffusion barriers for Al and Cu metallization on Si with respect to thermal stability and diffusion behavior of Ti, Microelectronics Reliability 54 (2014) 2487–2493. https://doi.org/10.1016/j.microrel.2014.04.016.

[8] I. Souli, V.L. Terziyska, J. Keckes, W. Robl, J. Zechner, C. Mitterer, Effect of growth conditions on interface stability and thermophysical properties of sputtered Cu films on Si with and without WTi barrier layers, Journal of Vacuum Science & Technology B, Nanotechnology and Microelectronics: Materials, Processing, Measurement, and Phenomena 35 (2017) 22201. https://doi.org/10.1116/1.4975805.

[9] A. Gupta, H. Wang, A. Kvit, G. Duscher, J. Narayan, Effect of microstructure on diffusion of copper in TiN films, Journal of Applied Physics 93 (2003) 5210–5214. https://doi.org/10.1063/1.1566472.

[10] M.B. Chamberlain, Diffusion of copper in thin TiN films, Thin Solid Films 91 (1982) 155–162. https://doi.org/10.1016/0040-6090(82)90429-1.

[11] M. Mühlbacher, G. Greczynski, B. Sartory, F. Mendez-Martin, N. Schalk, J. Lu, L. Hultman, C. Mitterer, TiN diffusion barrier failure by the formation of Cu 3 Si investigated by electron microscopy and atom probe tomography, Journal of Vacuum Science & Technology B, Nanotechnology and Microelectronics: Materials, Processing, Measurement, and Phenomena 34 (2016) 22202. https://doi.org/10.1116/1.4942003.

[12] M. Mühlbacher, A.S. Bochkarev, F. Mendez-Martin, B. Sartory, L. Chitu, M.N. Popov, P. Puschnig, J. Spitaler, H. Ding, N. Schalk, J. Lu, L. Hultman, C. Mitterer, Cu diffusion in single-crystal and polycrystalline TiN barrier layers: A high-resolution experimental study supported by first-principles calculations, Journal of Applied Physics 118 (2015) 85307. https://doi.org/10.1063/1.4929446.

[13] M. Mühlbacher, G. Greczynski, B. Sartory, N. Schalk, J. Lu, I. Petrov, J.E. Greene, L. Hultman, C. Mitterer, Enhanced Ti0.84Ta0.16N diffusion barriers, grown by a hybrid sputtering technique with no substrate heating, between Si(001) wafers and Cu overlayers, Sci. Rep. 8 (2018) 5360. https://doi.org/10.1038/s41598-018-23782-9.

[14] T. Oku, E. Kawakami, M. Uekubo, K. Takahiro, S. Yamaguchi, M. Murakami, Diffusion barrier property of TaN between Si and Cu, Applied Surface Science 99 (1996) 265–272. https://doi.org/10.1016/0169-4332(96)00464-3.

[15] N. Fréty, F. Bernard, J. Nazon, J. Sarradin, J.C. Tedenac, Copper Diffusion Into Silicon Substrates Through TaN and Ta/TaN Multilayer Barriers, Journal of Phase Equilibria & Diffusion 27 (2006) 590–597. https://doi.org/10.1361/154770306X153602.

[16] S.-Y. Chang, C.-E. Li, Y.-C. Huang, H.-F. Hsu, J.-W. Yeh, S.-J. Lin, Structural and thermodynamic factors of suppressed interdiffusion kinetics in multi-component high-entropy materials, Sci. Rep. 4 (2014) 4162. https://doi.org/10.1038/srep04162.

[17] B.S. Murty, J.-W. Yeh, S. Ranganathan, High-entropy alloys, Butterworth-Heinemann an imprint of Elsevier, London, Oxford, Amsterdam, San Diego, 2014.

[18] D.-S. Chen, M.-K. Chen, S.-Y. Chang, Multiprincipal-Element AlCrTaTiZr-Nitride Nanocomposite Film of Extremely High Thermal Stability as Diffusion Barrier for Cu Metallization, ECS Trans. 19 (2009) 751–762. https://doi.org/10.1149/1.3122130.

[19] C. Jiang, R. Li, X. Wang, H. Shang, Y. Zhang, P.K. Liaw, Diffusion Barrier Performance of AlCrTaTiZr/AlCrTaTiZr-N High-Entropy Alloy Films for Cu/Si Connect System, Entropy (Basel) 22 (2020). https://doi.org/10.3390/e22020234.

[20] R. Li, B. Qiao, H. Shang, J. Zhang, C. Jiang, W. Zhang, Multi-component AlCrTaTiZrMo-nitride film with high diffusion resistance in copper metallization, Journal of Alloys and Compounds 748 (2018) 258–264. https://doi.org/10.1016/j.jallcom.2018.03.084.

[21] S.-Y. Chang, C.-Y. Wang, C.-E. Li, Y.-C. Huang, 5 nm-Thick $(AlCrTaTiZrRu)N_{0.5}$ Multi-Component Barrier Layer with High Diffusion Resistance for Cu Interconnects, Nanosci Nanotechnol Lett 3 (2011) 289–293. https://doi.org/10.1166/nnl.2011.1155.

[22] S.-Y. Chang, C.-E. Li, S.-C. Chiang, Y.-C. Huang, 4-nm thick multilayer structure of multi-component (AlCrRuTaTiZr)N as robust diffusion barrier for Cu interconnects, Journal of Alloys and Compounds 515 (2012) 4–7. https://doi.org/10.1016/j.jallcom.2011.11.082.

[23] R. Li, T. Chen, C. Jiang, J. Zhang, Y. Zhang, P.K. Liaw, Applications of High Diffusion Resistance Multi- component AlCrTaTiZrRu/(AlCrTaTiZrRu)N 0.7 Film in Cu Interconnects, Adv. Eng. Mater. 22 (2020) 2000557. https://doi.org/10.1002/adem.202000557.

[24] S.-C. Liang, D.-C. Tsai, Z.-C. Chang, T.-N. Lin, M.-H. Shiao, F.-S. Shieu, Thermally Stable TiVCrZrHf Nitride Films as Diffusion Barriers in Copper Metallization, Electrochem. Solid-State Lett. 15 (2012) H5. https://doi.org/10.1149/2.012201esl.

[25] A. Xia, A. Togni, S. Hirn, G. Bolelli, L. Lusvarghi, R. Franz, Angular-dependent deposition of MoNbTaVW HEA thin films by three different physical vapor deposition methods, Surface and Coatings Technology 385 (2020) 125356. https://doi.org/10.1016/j.surfcoat.2020.125356.

[26] R. Daniel, K.J. Martinschitz, J. Keckes, C. Mitterer, The origin of stresses in magnetron-sputtered thin films with zone T structures, Acta Materialia 58 (2010) 2621–2633. https://doi.org/10.1016/j.actamat.2009.12.048.

[27] G.C. Gruber, A. Lassnig, S. Zak, C. Gammer, M.J. Cordill, R. Franz, Synthesis and structure of refractory high entropy alloy thin films based on the MoNbTaW system, Surface and Coatings Technology 439 (2022) 128446. https://doi.org/10.1016/j.surfcoat.2022.128446.

[28] G.C. Gruber, M. Kirchmair, S. Wurster, M.J. Cordill, R. Franz, A new design rule for high entropy alloy diffusion barriers in Cu metallization, Journal of Alloys and Compounds 953 (2023) 170166. https://doi.org/10.1016/j.jallcom.2023.170166.

[29] K. Sufryd, N. Ponweiser, P. Riani, K.W. Richter, G. Cacciamani, Experimental investigation of the Cu-Si phase diagram at x(Cu)0.72, Intermetallics 19 (2011) 1479–1488. https://doi.org/10.1016/j.intermet.2011.05.017.

[30] Z. Li, Y. Tian, C. Teng, H. Cao, Recent Advances in Barrier Layer of Cu Interconnects, Materials (Basel) 13 (2020) 5049. https://doi.org/10.3390/ma13215049.

[31] H. Aghajani, M.S. Motlagh, Effect of temperature on surface characteristics of nitrogen ion implanted biocompatible titanium, J. Mater. Sci. Mater. Med. 28 (2017) 29. https://doi.org/10.1007/s10856-016-5843-x.

[32] S.-Y. Chang, C.-Y. Wang, M.-K. Chen, C.-E. Li, Ru incorporation on marked enhancement of diffusion resistance of multi-component alloy barrier layers, Journal of Alloys and Compounds 509 (2011) L85-L89. https://doi.org/10.1016/j.jallcom.2010.11.124.

[33] R. Li, M. Li, C. Jiang, B. Qiao, W. Zhang, J. Xu, Thermal stability of AlCrTaTiZrMo-nitride high entropy film as a diffusion barrier for Cu metallization, Journal of Alloys and Compounds 773 (2019) 482–489. https://doi.org/10.1016/j.jallcom.2018.09.283.